DYNAMICS OF THIN FILMS NEAR SINGULARITIES UNDER THE INFLUENCE OF NON-NEWTONIAN RHEOLOGY

A Dissertation

Submitted to the Faculty

of

Purdue University

by

Vishrut Garg

In Partial Fulfillment of the

Requirements for the Degree

of

Doctor of Philosophy

December 2018

Purdue University

West Lafayette, Indiana

THE PURDUE UNIVERSITY GRADUATE SCHOOL
STATEMENT OF DISSERTATION APPROVAL

Dr. Osman A. Basaran, Chair

Davidson School of Chemical Engineering

Dr. Doraiswami Ramkrishna

Davidson School of Chemical Engineering

Dr. Michael T. Harris

Davidson School of Chemical Engineering

Dr. Anil K. Bajaj

School of Mechanical Engineering

Approved by:

Dr. John A. Morgan

Head of the School Graduate Program

To

Nana, my first and favorite maths teacher,

Mummy, Papa, and Shreyas,

and my dearest friends, Prasun and Shruti.

ACKNOWLEDGMENTS

I would like to thank my advisor, Prof. Osman Basaran, for these past five years at Purdue University. Under his guidance, I have grown tremendously as a researcher, a writer, a presenter, a scholar, and finally as a person. I am grateful for his unwavering support and constant encouragement that helped me overcome many seemingly unassailable roadblocks in research, and tackle unforeseen administrative hurdles. He has imbued in me a constant pursuit for rigor and quality in every task I undertake, and it will stay with me as I begin my professional career. It has been an honor to be part of one of the finest research groups in fluid dynamics.

I would also like to thank Prof. Doraiswami Ramkrishna, Prof. Michael Harris, and Prof. Anil K. Bajaj for serving on my committee and providing valuable critique and direction for my research work. I would also like to thank Prof. Ramkrishna for cultivating in me a love for mathematical analysis through his excellent courses on reaction engineering, linear operators and stochastics. His approach to reactor design and kinetics was enlightening for me both as a student and a teaching assistant, and I thoroughly enjoyed both experiences.

I would like to thank Dr. George Harriott and Dr. Sanjay Mehta of Air Products and Chemicals, Inc. for providing me with the opportunity to work as a graduate intern and experience industrial research. Working with Dr. Harriott was an especially rewarding experience, as I got to experience first hand how the theoretical methods that we learned in our research can be successfully applied in industry.

I am fortunate to be part of a research group that boasts of such highly successful alumni who are always ready to provide guidance and collaborate with current students, long after they have graduated themselves. I am thankful to Dr. Pradeep

Bhat for his insight and discussions on viscoelastic flows. While my time here never overlapped with Dr. Krishnaraj Sambath, he provided me with invaluable guidance and constructive criticism during my job applications, for which I am grateful. I am extremely fortunate to have spent three years in the company of Dr. Sumeet Thete, who served as a mentor, a friend, and a guide, from my first day here at Purdue. Sumeet's limitless knowledge of the field of fluid dynamics helped guide my work in thin films and viscoelastic flows, and I am indebted to him for teaching me the concepts of asymptotic analysis. Dr. Christopher Anthony's expertise in the computational aspect of our work was invaluable to my research, and his experience with elliptic meshes and algebraic surfaces helped me in solving some of the most challenging problems in this thesis. Apart from research, Chris motivated me to take up long distance running and then cycling, and hanging onto his wheel while riding into the strong Indiana headwinds is a memory I will always cherish. I am thankful to Dr. Pritish Kamat for his helpful criticism and insight on surfactant-laden flows, and for his cheerful company during every APS conference. I wish to thank Brayden Wagoner for teaching me how to conduct high-quality experiments and for our numerous discussions that encouraged me to refine my ideas and take them to conclusion. I am also grateful to him for his help during especially challenging times, and for hosting me while I was between apartments during the final months of my doctoral studies. Finally, I wish to thank Lihui Wang and Hansol Wee for the discussions and company in the office, and for forcing me to be sure of my concepts so that I could pass them on to them.

I would also like to thank Bev Johnson for her helpful guidance and assured handling of all administrative affairs during graduate school. I am also grateful for all the help I received from Corwin Green. I am grateful for the assistance of Jeff Valley and Nick Humpfrey during our lab transfer and when I conducted experiments. Finally, I want to thank Courtney Eddy and Christina Wilson for helping me out with all administrative and financial tasks.

I was fortunate to make many friends here at Purdue during these five years. Their company and support softened the blow of being two continents away from family and helped me adjust to the American culture rapidly. I am thankful to my classmates John Di Iorio, Sydney Hollingshead, Michael Cordon, and Jiangfeng Liu for all the good times during that first year when courses and homework were our biggest worries, and for sharing with me their own experiences of graduate life as we embarked upon our different research projects. I am thankful to Ravi Joshi for being a great roommate and someone I could always count on. I cherish my time spent in the townhouse with Atish, Ashish Vora and Sumeet. I am thankful to the Purdue cycling club for providing me with a hobby I will hopefully pursue for life. I am especially thankful to Jason Sohn for hosting me during the final months of graduate school, and Mark Zhao for encouraging me to get out and ride. Finally, I am thankful to William Snyder from the Purdue Photography Club, who was my mentor during my initial foray into cycling photography, and kindled in me a love for film photography that I will continue to pursue with dogged determination.

Finally, this journey would have been impossible without the support of my family. I am grateful for my aunt's help during the most challenging time of my Ph.D., and her encouragement as a professor at IIT Delhi that set me on the path of science. I am truly fortunate to have the unconditional and unwavering support of Prasun and Shruti, who have been and are always there for me, to celebrate the best, endure the worst, and forever encourage me to see the silver lining. Lastly, I would not be here without the hard work and sacrifice of my parents and my brother Shreyas, and am grateful for their unconditional love from across the world.

TABLE OF CONTENTS

Page

LIST OF FIGURES

Figure Page

Figure Page

Figure Page

Figure Page

Figure Page

Figure Page

Figure Page

Figure Page

Figure Page

ABSTRACT

Garg, Vishrut PhD, Purdue University, December 2018. Dynamics of Thin films near Singularities under the influence of non-Newtonian Rheology. Major Professors: Osman A. Basaran.

Free surface flows where the shape of the interface separating two fluids is unknown *apriori* are an important area of interest in fluid dynamics. The study of free surface flows such as the breakup and coalescence of drops, and thinning and rupture of films lends itself to a diverse range of industrial applications, such as inkjet printing, crop spraying, foam and emulsion stability, and nanolithography, and helps develop an understanding of natural phenomena such as sea spray generation in oceans, or the dynamics of tear films in our eyes. In free surface flows, *singularities* are commonly observed in finite time, such as when the radius of a thread goes to zero upon pinchoff or when the thickness of a film becomes zero upon rupture. Dynamics in the vicinity of singularities usually lack a length scale and exhibit self-similarity. In such cases, universal scaling laws that govern the temporal behavior of measurable physical quantities such as the thickness of a film can be determined from asymptotic analysis and verified by high-resolution experiments and numerical simulations. These scaling laws provide deep insight into the underlying physics, and help delineate the regions of parameter space in which certain forces are dominant, while others are negligible. While the majority of previous works on singularities in free-surface flows deal with Newtonian fluids, many fluids in daily use and industry exhibit non-Newtonian rheology, such as polymer-laden, emulsion, foam, and suspension flows.

The primary goal of this thesis is to investigate the thinning and rupture of thin films of non-Newtonian fluids exhibiting deformation-rate-thinning (power-law) rheology due to attractive intermolecular van der Waals forces. This is accom-

plished by means of intermediate asymptotic analysis and numerical simulations which utilize a robust Arbitrary Eulerian-Lagrangian (ALE) method that employs the Galerkin/Finite-Element Method for spatial discretization. For thinning of sheets of power-law fluids, a significant finding is the discovery of a previously undiscovered scaling regime where capillary, viscous and van der Waals forces due to attraction between the surfaces of the sheet, are in balance. For thinning of supported thin films, the breakdown of the lubrication approximation used almost exclusively in the past to study such systems, is shown to occur for films of power-law fluids through theory and confirmed by two dimensional simulations. The universality of scaling laws determined for rupture of supported films is shown by studying the impact of a bubble immersed in a power-law fluid with a solid wall.

Emulsions, which are fine dispersions of drops of one liquid in another immiscible liquid, are commonly encountered in a variety of industries such as food, oil and gas, pharmaceuticals, and chemicals. Stability over a specified time frame is desirable in some applications, such as the shelf life of food products, while rapid separation into its constituent phases is required in others, such as when separating out brine from crude oil. The timescale over which coalescence of two drops of the dispersed phase occurs is crucial in determining emulsion stability. The drainage of a thin film of the outer liquid that forms between the two drops is often the rate limiting step in this process. In this thesis, numerical simulations are used to decode the role played by fluid inertia in causing drop rebound, and the subsequent increase in drainage times, when two drops immersed in a second liquid are brought together due to a compressional flow imposed on the outer liquid. Additionally, the influence of the presence of insoluble surfactants at the drop interface is studied. It is shown that insoluble surfactants cause a dramatic increase in drainage times by two means, by causing drop rebound for small surfactant concentrations, and by partially immobilizing the interface for large surfactant concentrations.

1. INTRODUCTION

1.1 Background and Motivation

Many situations in everyday life, such as crop dusting, the breakup of a sheet of water on a car's windshield into drops, sea spray generated by air bubbles rising to the surface of the oceans, or the gradual separation of food products such as butter or milk into its constituent fluids, involve the motion of "free surfaces" or deformable interfaces between two fluids. The additional energy of fluid molecules at these interfaces between either a gas and a liquid, or two liquids, leads to motion in the bulk fluids and is responsible for the occurrence of several fascinating phenomena. The simplest example of a free surface flow, the dripping of a leaky faucet due to surface tension of the drop causing pinchoff, displays rich dynamics as flow properties are altered [1, 2]. While a comprehensive understanding of the underlying fluid dynamics is justified from a purely scientific perspective, continued and widespread interest in this problem is also a result of a variety of industrial applications involving drop generation, such as inkjet printing [3], crop spraying [4], or tablet printing in pharmaceuticals [5].

The nonlinear partial differential equations that govern fluid mechanics, developed by Euler and Navier, become irregular when the solution develops a vanishingly small length scale [6]. In free surface flows, such *singularities* are commonly observed in finite time, such as when the radius of a thread goes to zero upon pinchoff [7], the thickness of a film falls to zero upon rupture [8], or when two drops come together and touch at a point [9]; the radius of the bridge that connects them is initially zero. As the dynamics are governed by local scales, the solutions in the vicinity of singularities are independent of the influence of initial or boundary conditions [10], and thus reveal

the true structure of the equations. As a result, these solutions display two remarkable features: (1) Self-similarity − the solutions repeat themselves in time and space [10], and (2) Universality − an identical solution is obtained for different initial and boundary conditions. Self-similarity in the vicinity of singularities in free surface flows has been studied in much detail, beginning with the work of Keller and Miksis [11] on wedge retraction. Since then, the self-similar behavior of thread pinchoff [7, 12–16], breakup of sheets [17–20], rupture of supported films [21, 22], healing of films [23], coalescence of drops [9,24,25], and finally, coalescence of gas bubbles [26,27] has been explored in detail. Scaling laws that result from self-similarity provide insight into the dominant forces operating in the system in a given regime, and help delineate the regions of parameter space in which certain forces are dominant, while others are negligible. Indeed, self-similar analyses have been used to determine when inertia becomes significant in drop formation from a nozzle [16], which helps predict when the formation of undesirable satellite drops, or "fines" will occur. Self-similar analyses have also been used to determine the mechanism behind the occurrence of microthread cascades in surfactant-laden thread pinchoff [28], and predict when inertia becomes significant in film rupture [22], leading to the breakdown of the lubrication approximation [29] used almost exclusively to study supported film dynamics. They have also provided insight in many practical applications, e.g. the inherent self-similarity of gas flow in pipelines has been exploited to accurately detect the location of leaks, while Taylor [10] accurately predicted the radius of shock waves.

While the pinchoff of Newtonian threads has been studied for over 300 years, beginning with the works of Savart [4], pinchoff studies for fluids with non-Newtonian rheology is a relatively young field with the pioneering studies conducted by Middleman [30]. Dissolved polymer molecules lead to additional elastic stresses in the fluid, commonly referred to as viscoelastic stresses [31], and are responsible for novel phenomena, such as the formation of a beads-on-a-string structure [32] and blistering patterns [33]. Numerical studies of pinchoff of viscoelastic threads [32,34] have always assumed that the concentration of polymer molecules is constant along its length, and

do not predict the formation of the aforementioned blistering pattern. Recent experiments [35] and analytical studies [36] show that the effect of polymer migration is significant, and a probable reason for the blistering pattern observed during pinchoff.

Thin liquid films of thickness 1μm or below are known to be unstable to long wavelength perturbations due to intermolecular forces [37, 38]. This instability can lead to rupture of the film and subsequent dewetting, to form patterns of drops on a substrate, or in the case of free films, lead to coalescence of the phase separated by the film. In the past two decades, as micro and nano lithography techniques have evolved, interest in thin film dynamics has grown rapidly due to the advent of applications such as substrate patterning due to self-assembly [39], droplet generation [40], the dynamics of tear films [41], foam stability [42], aerosol generation [43], and the stability of bubbles in micro/nanochannels [44]. Many of the fluids involved in these applications exhibit non-Newtonian rheology, as a result of dissolved polymers [45], emulsions [46], or particles [47]. Non-Newtonian rheology can have a dramatic impact on the dynamics of thin films, such as the dewetting of seemingly stable films due to residual stresses [48]. While the influence of non-Newtonian rheology on the self-similar dynamics of thread pinchoff has been studied in great detail [49–51], its impact on thin film rupture is less well understood.

Emulsions, which are fine dispersions of drops of one liquid in another immiscible liquid, are commonly encountered in a variety of industries ranging from food [52] to oil and gas [53] to pharmaceuticals [54] to chemicals [55]. Stability over a specified time frame is desirable in some applications, such as the shelf life of food products [56], while rapid separation into its constituent phases is required in others, like separating brine from crude oil [53]. The timescale over which coalescence of two drops of the dispersed phase occurs is crucial in determining emulsion stability. The drainage of a thin film of the outer liquid that forms between the two drops is often the rate limiting step in this process. Additionally, the presence of surface-active agents in emulsions due to naturally occurring impurities [53], or by design [57], strongly affects coalescence dynamics and the overall properties of the emulsion [58]. The presence

of surfactants during drop coalescence of two drops leads to a dramatic increase in the timescale of coalescence [59], and similarly, longer rest times during coalescence of a drop with its bulk phase at a flat liquid/liquid interface [60] in comparison to the clean interface case.

1.2 Thesis goals

Motivated by recent experimental [35] and analytical studies [36] on viscoelastic thread pinchoff, the first goal of this thesis is to numerically study the nature of polymer molecule migration along the thread by utilizing constitutive equations developed by Bhave et al. [61], along with the slender-jet approximation for the Cauchy momentum and continuity equations [62]. It is also desirable to understand the effect of inertia on the extent of migration, as the presence of inertia is crucial for the formation of the well known beads-on-a-string structure [32].

The second goal of this thesis is to understand the effect of deformation-rate-thinning rheology on the thinning and rupture of thin films, driven by attractive intermolecular forces. This class of film flows has a rich history, with the self-similar dynamics of the thinning of free films [17, 19], as well as films supported by a solid substrate [21], well established for Newtonian liquids. Motivated by applications in oil and gas, cosmetics, personal care products, and food products, where the fluids exhibit non-Newtonian rheology [51, 63], and a recent work by Thete et al. [18] who discovered a novel scaling regime for the breakup of sheets of non-Newtonian fluids, we examine the effect of power-law rheology on the self-similar dynamics of film rupture. In addition to exploring systems where we initially begin with perturbing a liquid film of uniform thickness, it is desirable to explore the self-similar dynamics of systems where thin films are initially absent, but eventually form as two interfaces approach each other, such as when a bubble impacts a solid wall, to demonstrate the universality of the self-similar dynamics of film thinning.

The third goal of this thesis is to develop an understanding of flow-induced coalescence of two drops in a second liquid. A recent work by Sambath [64] revealed that

the drops rebound before coalescing on subsequent approach when inertial effects are significant, and drainage times no longer adhere to the simple scaling laws derived for flow in the Stokes limit [65]. The goal of this work is to decode the role played by fluid inertia in causing drop rebound, and subsequent increase in drainage times. Motivated by applications in the oil and gas industry, where the presence of surface-active asphaltames and emulsifiers in crude oil emulsions hinders quick separation of brine from oil, a further objective of this work is to study flow-induced coalescence in the presence of surfactants.

1.3 Thesis scope

All chapters in this thesis deal with free surface flows that are incompressible and isothermal throughout the duration of the physical process being studied. The numerical analyses performed in each chapter treat the fluids as a continuum which are governed by the continuity and Cauchy momentum equations. The physical processes are studied until molecular length scales are reached, and no further investigation of the discrete dynamics at molecular length scales are considered. All numerical analysis was performed using a Galerkin/Finite element method for discretization [66] with adaptive time-stepping [67]. For three-dimensional axisymmetric or two-dimensional flows, elliptic mesh techniques [68] were used with the addition of moving algebraic surfaces, which ensure accurate resolution of dynamics over scales spanning up to 9 orders of magnitude.

Numerical analyses of viscoelastic thread pinchoff utilized constitutive equations for the elastic stress and a transport equation for polymer concentration developed through kinetic theory by Bhave et al. [61]. Their model was shown to be identical to similar models which account for polymer migration and accurately capture physical phenomena in polymer flows [69].

The studies involving thinning of films of deformation-rate-thinning fluids utilized the Ostwald-de-Waele relationship to describe the dependence of the instantaneous fluid viscosity on the local deformation rate. This approximation of the generalized

Newtonian fluid or yield stress fluids was shown to accurately describe dynamics near singularities in the experiments of Savage et al. [70] and Huisman, Friedman, and Taborek [51].

Numerical work where intermolecular forces become significant utilized the disjoining pressure approximation developed by Lifshitz [71] for two unbounded parallel flat surfaces. The effects of the curvature of films on the expression for this pressure [72] are neglected, as they are sub-dominant in the vicinity of singularities.

Numerical works concerning surfactant-laden flows are performed under the assumption that surfactants are insoluble in the bulk phase, which was observed for copolymers [59], long-chain alcohols [73] and when bulk diffusion timescale is much larger than the timescale of coalescence [74].

1.4 Thesis outline

1.4.1 Pinchoff of slender threads of non-homogeneous polymer solutions

The pinchoff of threads of fluids with dissolved polymers is encountered in several applications, such as high-quality inkjet printing and the spraying of pesticides [31]. As a result of the dissolved polymers, additional elastic stresses are present in the fluid. As capillary forces cause the formation of a neck connecting drops on either ends, extensional flow in the neck region stretches the polymer chains and causes buildup of elastic stress. These resist pinchoff and cause the formation of a beads on a string structure [32], where cylindrical threads of uniform thickness connect spherical drops. Recent experiments [33, 35] have shown that once the threads become sufficiently thin, they are subject to instabilities that destroy its uniformity and result in a "blistering" pattern. This could be the result of inhomogenity in polymer concentration along the length of the thread [35,36], which has been hitherto ignored in numerical studies of viscoelastic thread pinchoff.

The work in this chapter considers pinchoff of viscoelastic threads where concentration variation along the length of the thread is considered by utilizing the

constitutive equations developed by Bhave et al. [61] for stress-induced migration of polymer chains. The slender-jet approximation [36] is utilized to reduce the spatially three-dimensional axisymmetric governing system of equations to one dimension. Remarkably, it is observed that polymer concentration rises in the neck as pinchoff occurs, due to gradients in chain mobility between the highly stretched chains in the neck (low mobility) and the relaxed chains in the drops (high mobility). Additional migration to the neck is observed when inertia effects are significant, as a result of formation of satellite drops. Lastly, the extent of migration and concentration of the neck region is observed to be directly proportional to the elasticity, and inversely proportional to the diffusivity of the polymeric fluid.

1.4.2 Self-similarity and scaling transitions during thinning of sheets of power-law fluids

Thin liquid sheets, or free films, with two free surfaces, are common in a variety of daily life situations such as foam and emulsion flows, sea sprays, and crop spraying. When the thickness of the sheet is of the order of several hundred nanometers, van der Waals attraction between the two free surfaces can cause spontaneous thinning and rupture of the sheet despite the presence of stabilizing capillary pressure. Past studies [17, 19] discovered that film rupture dynamics are self-similar in the vicinity of the space-time singularity when film thickness becomes zero, and determined the scaling regimes for Newtonian fluids as a function of the dimensionless Ohnesorge number $Oh \equiv \mu_0/\sqrt{\rho h_0 \sigma}$, where μ_0, ρ, σ and h_0 are the viscosity, density, surface tension and initial thickness of the film respectively. Motivated by applications such as personal care products, foam flows, and tear substitutes, the existing Newtonian studies are extended to consider the effect of deformation-rate-thinning or power-law rheology. A recent work by Thete et. al [18] showed that thinning dynamics for films of $Oh \sim 1$ undergo a transition from the power-law inertial viscous (PLIV) regime where inertial, viscous, and van der Waals forces are in balance, to a rheology independent inertial-capillary (IC) regime as the power-law exponent n is reduced

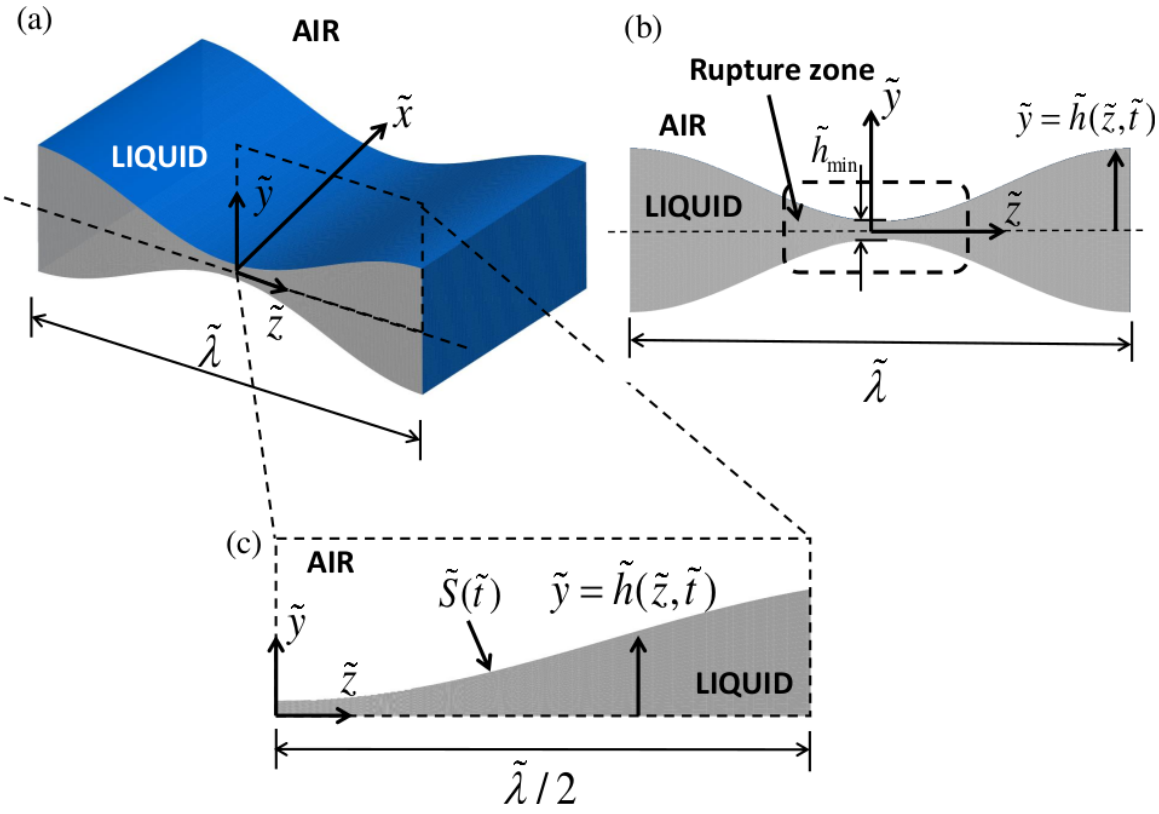

Figure 1.1. **Thinning and rupture of sheets of power-law fluids**: (a) Perspective view of a free film surrounded by air corresponding to one wavelength $\tilde{\lambda}$ of the imposed perturbation. (b) A cross-sectional view of the film and location of the "rupture zone", where dynamics are expected to be self-similar as the film approaches the space-time singularity. (c) The computational domain taken on account of symmetry.

below $n = 6/7$, where inertial, capillary, and van der Waals forces are in balance.

Taking inspiration from similar studies for pinchoff of threads power-law fluids [49–51,70], intermediate asymptotic analyses and numerical simulations are performed to develop a thorough understanding of the thinning dynamics and transitions that occur between different scaling regimes in the parameter space comprised of both the Ohnesorge number Oh and power-law exponent n. For thinning in the Stokes limit, it is shown that the dynamics lie in the power-law viscous (PLV) regime, such that van

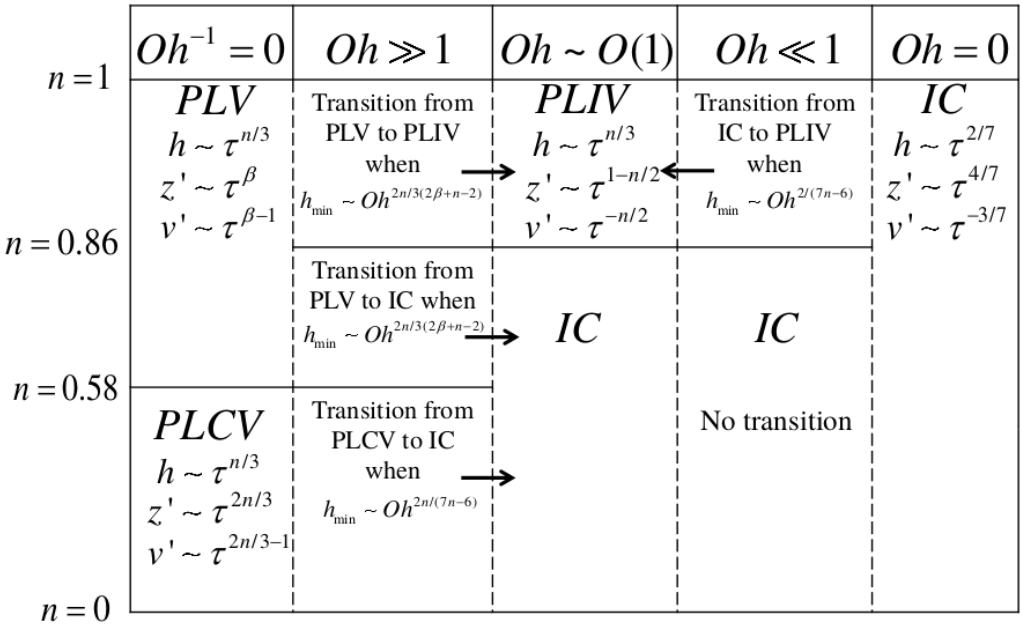

Figure 1.2. **Thinning and rupture of sheets of power-law fluids**: Phase diagram summarizing scaling laws for self-similar dynamics of thinning and rupture of sheets of power-law fluids as a function of Ohnesorge number Oh and power-law exponent n. The phase diagrams delineates the region of the parameter space where the dynamics lie in the power-law viscous (PLV), power-law capillary viscous (PLCV), power-law inertial viscous (PLIV) and inertial-capillary (IC) regimes, and when transitions between regimes are expected to occur. Here h is the film thickness, z' is the lateral length scale or lateral extent of the rupture zone, v' denotes the velocity in the lateral direction, and τ is time remaining to rupture. For the PLV regime, the scaling exponent β for the axial length scale is seen to increase as n decreases, with its values lying between $0.387 \leq \beta \leq 0.26$.

der Waals and viscous forces are in balance while capillary forces are negligible all the way till the sheet ruptures. As the self-similarity is of the second kind, the scaling exponent for the axial length scale is determined analytically by solving ordinary differential equations in the similarity space obtained by a similarity transformation. It is further shown that below a critical value of n, the assumptions of the PLV regime break down, and capillary forces enter the dominant force balance, leading to

a hitherto undiscovered power-law capillary viscous (PLCV) regime. On the other end of the spectrum, films with vanishing zero-deformation-rate viscosity μ_0 thin in the IC regime, as the viscosity of the fluid plays no role. Finally, for real fluids with finite Oh, the aforementioned inertial or viscous regimes are shown to be transitory, with the dynamics eventually transitioning to a late-stage PLIV or IC regime, based on the value of n. The inter-regime transition points are determined analytically and are in good agreement with numerical results. The chapter is concluded by presenting a phase map (figure 1.2) of the scaling regimes and transitions, plotted in the space of the Ohnesorge number Oh and power-law exponent n.

1.4.3 Self-similar rupture of thin films of power-law fluids on a substrate

Thin films supported by a solid substrate are ubiquitous in daily life and industry. Interest in the controlled thinning and rupture of supported films has grown in recent years due to advances in lithography techniques, leading to the advent of applications such as substrate patterning due to self-assembly [39], droplet generation [40], and tear film substitutes [41]. A comprehensive understanding of the rate at which thinning occurs is crucial for such applications, e.g. it helps determine the spacing of the patterns manufactured on the substrate. In many of these applications, the fluids are non-Newtonian in nature and exhibit deformation-rate-thinning power-law rheology as a result of dissolved polymers. Motivated by Zhang and Lister [21] who discovered self-similarity in the thinning of Newtonian supported films, the effect of power-law rheology on supported film rupture is studied here.

In the first part of the chapter, use is made of the slenderness of the film and the lubrication approximation is applied to the equations of motion to derive a spatially one-dimensional nonlinear evolution equation for film thickness. The variation with time remaining until rupture of the film thickness, the lateral length scale, fluid velocity, and viscosity is determined analytically and confirmed by numerical simulations for both line rupture and point rupture. The self-similarity of the numerically computed film profiles in the vicinity of the location where the film thickness is a min-

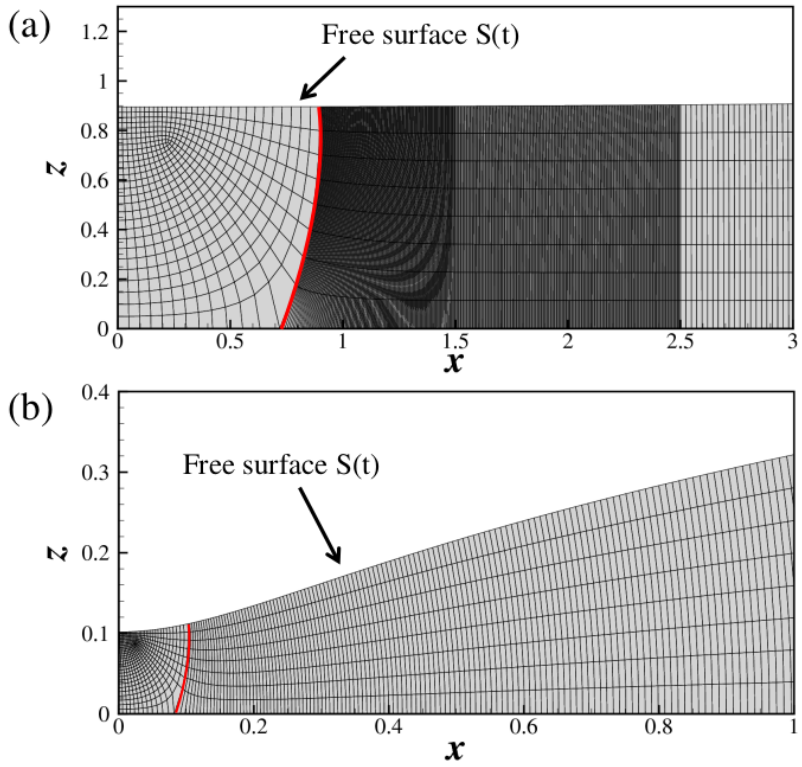

Figure 1.3. **Thinning and rupture of supported films of power-law fluids**: Close-up view of an illustrative (coarse) mesh generated for 2D simulations. (a) Elements are initially densely packed near $h_{\min}$ and as the film thins, (b) the mesh points are seen to concentrate near the rupture zone. The dynamic algebraic surface is shown by the red curve.

imum is demonstrated by rescaling of the transient profiles with the scales deduced from theory. It is then shown that in contrast to films of Newtonian fluids undergoing rupture for which inertia is always negligible, inertia can become important during thinning of films of power-law fluids in certain situations. The critical conditions for which inertia becomes important and the lubrication approximation is no longer valid are determined analytically. In the second part of the chapter, thinning and rupture of thin films of power-law fluids in situations when inertia is important are simulated by solving numerically the spatially two-dimensional, transient Cauchy momentum and continuity equations. Elliptic mesh generation [68] modified to include dynamic

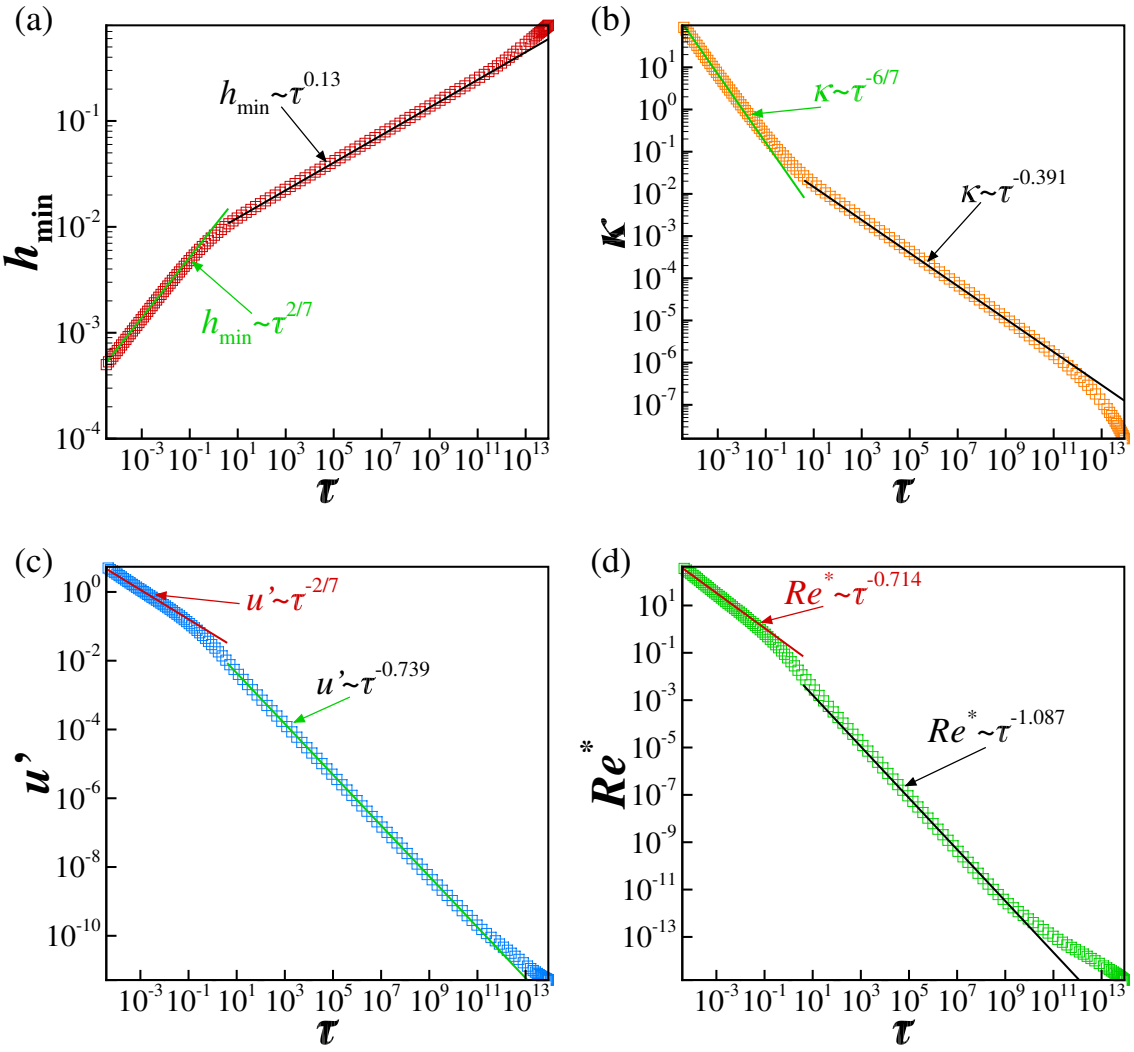

Figure 1.4. **Thinning and rupture of supported films of power-law fluids**: Effect of power-law rheology on the scaling behavior of variables in the rupture zone and change of scaling during thinning of a power-law film of $Oh = 1.18$, $A^* = 7.37 \times 10^{-7}$, and $n = 0.60$ undergoing line rupture: simulations (data points) and scaling theory predictions (straight lines with indicated dependencies on time remaining until rupture τ). Variation with time to rupture τ of (a) minimum film thickness h_{min}, (b) curvature κ evaluated at the lateral location of h_{min}, (c) lateral velocity u' evaluated at lateral location where $h = 1.05h_{min}$, and (d) modified Reynolds number Re^* evaluated at that lateral location. The occurrence of a change of scaling and a transition from the viscous regime to the inertial regime is clear as $\tau \to 0$ from the plots depicting the temporal evolution of all four variables in the figure.

algebraic surfaces is used to accurately resolve dynamics over a spatial range of 9 orders of magnitude. It is shown that as such films continue to thin, a change of scaling occurs from a regime in which van der Waals, capillary, and viscous forces are important to one where the dominant balance of forces is between van der Waals, capillary, and inertial forces while viscous force is negligible.

1.4.4 Impact of bubbles immersed in a power-law fluid with a solid wall

The phenomenon of bubbles interacting with other bubbles or surfaces is observed in a plethora of natural processes and industrial applications. For example, bubbles bursting at the surface of seas produce marine aerosols which affect local air quality [75] and rain formation [76]. In industry, bubble collisions with solid walls play a crucial role in the flow of foams and bubbly liquids in pipes and in other situations where solid surfaces are present [77]. Additionally, the understanding of bubble collisions with solid particles is essential for applications like tar-sands processing [78], where the recovery of bitumen is aided by aeration, mineral extraction and plastic separation through froth flotation [79, 80] and convective heat transfer [81].

In this chapter, the impact of bubbles immersed in both Newtonian and power-law liquids with a solid wall due to buoyancy was explored. For mm sized bubbles immersed in liquids of water-like viscosity, it was observed that bubbles that are two times its radius R or less away from the wall do not rebound from the wall as the approach velocity is very low, in contrast to most studies that consider approach of bubbles at terminal velocity and observe several rebounds before final attachment. However, if acceleration due to gravity is increased artificially, the bubbles were observed to undergo multiple rebounds.

For a 1 mm sized bubble approaching a solid wall when the initial separation is one bubble diameter, the final stages of attachment due to van der Waals driven rupture of the film between the bubble and the wall were analyzed theoretically and numerically for bubbles immersed in power-law liquids. For Newtonian outer liquids, or power-law liquids with a value of the power-law exponent n close to 1, the dynamics

in the vicinity of the singularity (when the separation becomes zero) are self-similar such that capillary, van der Waals and viscous forces are in balance. However, for power-law liquids of sufficiently small n values, inertia can become important as their viscosity falls rapidly. The critical minimum separation below which inertia will be important and the lubrication approximation is no longer valid was determined analytically. Simulation results showed that below this value a transition to a rheology independent inertial scaling regime occurs, signifying that viscous forces are negligible while inertial, capillary and van der Waals forces are in balance in this regime. A phase diagram was constructed to describe when inertia will become important for all possible values of n. The self-similar behavior observed for bubble impact in this chapter is identical to the self-similar behavior determined for rupture of supported films in chapter 4, thus demonstrating a salient feature of self-similarity: universality of the scaling regimes. Thus, bubble or drop impact can be used in the future as an ideal system to study self-similarity and scaling of two-layer systems, or surfactant-laden flows.

1.4.5 Flow-induced coalescence of two equal-sized liquid drops immersed in a second liquid

Emulsions, which are fine dispersions of drops of one liquid in another immiscible liquid, are commonly encountered in a variety of industries ranging from food [52] to oil and gas [53] to pharmaceuticals [54] to chemicals [55]. The competing mechanisms of coalescence and breakup of the dispersed drops decide the fate, and thus, the final quality and properties of the emulsion. The dynamics of the collision and coalescence of two drops are studied separately by usually assuming no influence from other drops and particles present in the emulsion. Most studies of drop coalescence focus on determining the drainage time, or time taken from when the drop centers are separated by a drop diameter to when their interfaces touch. This drainage time can be incorporated into population balance models to accurately determine the drop

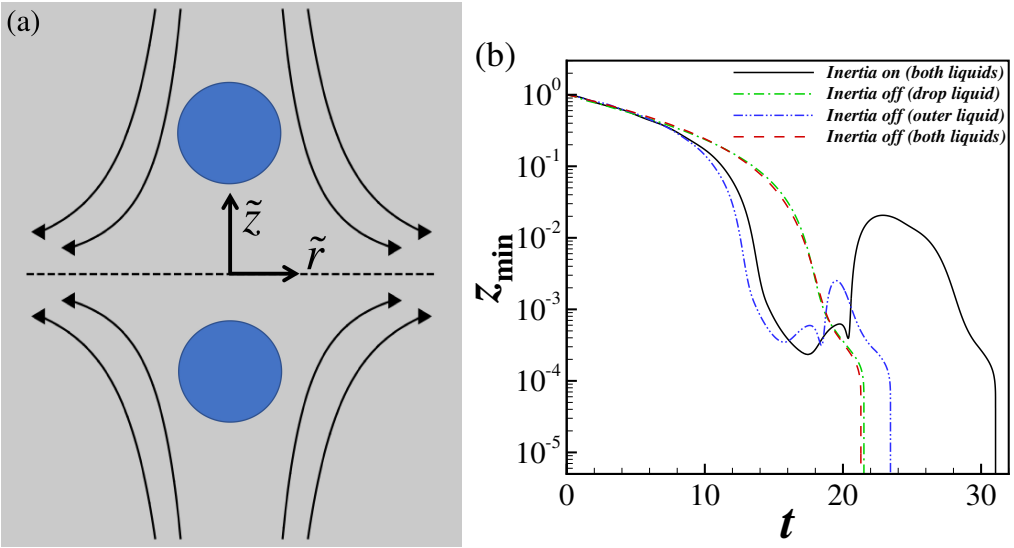

Figure 1.5. **Flow-induced drop coalescence in a second liquid**: Sketch of the problem setup. (b) Result from 2D simulation for $Oh = 0.023$, $m_2 = 1$, $d_2 = 1$, $U_\infty = 0.05$, and $A^* = 10^{-10}$ showing the variation with time t of half the minimum axial separation between the drops z_{min} when inertia is selectively turned off for either liquid 1 or liquid 2. Drop fluid inertia is crucial for the occurrence of drop rebound, as coalescence dynamics in its absence resemble those of creeping flow conditions.

size distribution in coalescers, separators, reactors etc. Until recently, most studies of pre-coalescence dynamics considered coalescence in creeping flow conditions. Recent work by Sambath [64] on the flow-induced head-on collision and coalescence of two equal sized drops in a compressional flow demonstrated that for coalescence in moderate Reynold's number flows, the drops rebound on first approach before coalescing on the second approach, as inertia plays a game-changing role in delaying coalescence. Sambath [64] further showed that drainage times computed for such cases do not conform to the scaling theories developed in previous works for creeping flow conditions.

In this chapter, the results of Sambath [64] are revisited in order to decode the role fluid inertia plays in causing drop rebound. Through Galerkin finite element simulations it is shown that a larger pressure develops in the film that forms between the colliding drops when fluid inertia is considered, leading to a large normal force

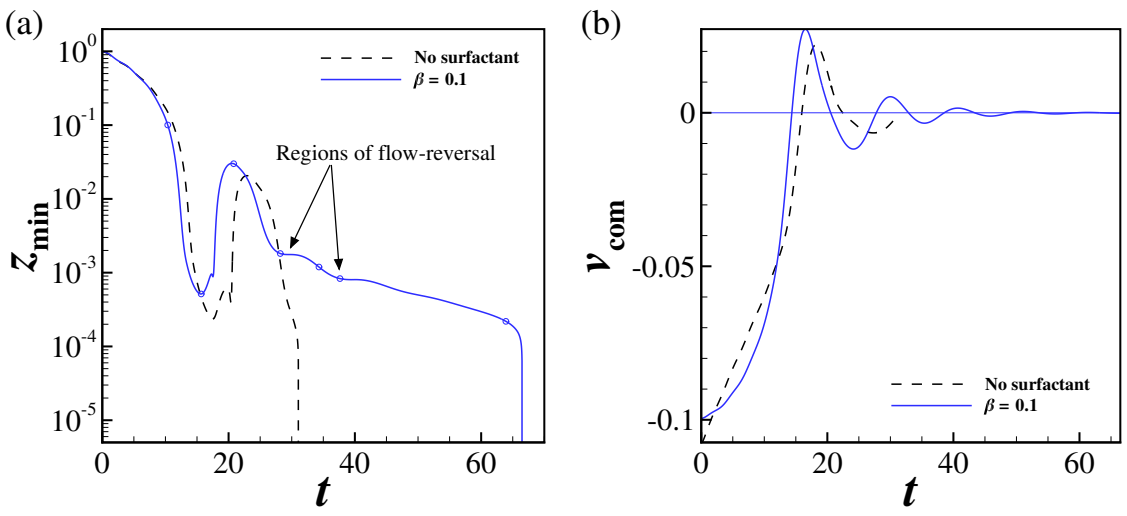

Figure 1.6. **Flow-induced coalescence in the presence of insoluble surfactants**(a) Time evolution of half the minimum axial separation between the drops' interfaces z_{min} for a surfactant-free case (black line) and a surfactant-laden case (blue line). (b) Velocity of center of mass of the drop for the corresponding cases in (a). Parameter values are $Oh = 0.023$, $m_2 = 1$, $d_2 = 1$, $U_\infty = 0.05$, $A = 10^{-10}$, $\Gamma_0 = 0.1$, $\beta = 0.1$ and $Pe = 1000$.

due to pressure. This opposes drop motion and causes the drops to rebound, before viscous drag pulls the drops together for a second approach and eventual coalescence. It is further shown that the inertia of the drop fluid is crucial for rebound, as selectively excluding drop fluid inertia from the governing equations leads to Stokes flow like behavior, even though inertia is present in the outer liquid. Lastly, it is shown that fluid viscosity plays a substantial role in rebound dynamics, as drop rebound is amplified if the outer liquid is less viscous than the drop liquid and can even result in no coalescence, while rebound is suppressed if the outer liquid is more viscous, as viscous drag pulling the drops together dominates over the normal force pushing them apart.

1.4.6 Flow-induced coalescence of two equal-sized liquid drops immersed in a second liquid in the presence of insoluble surfactants

Here the problem of two coalescing drops in a compressional flow is modified to account for the presence of insoluble surfactants at the liquid-liquid interface. It has been observed experimentally that the presence of surfactants during the coalescence of two drops leads to a dramatic increase in drainage times [59], and similarly, longer rest times during coalescence of a drop with its bulk phase at a flat liquid/liquid interface [60] in comparison to the clean interface case. Moreover, the presence of surfactants due to added chemicals and naturally occurring asphaltames in crude oil processing creates large bottlenecks during separation of oil from brine. Previous work always considered flow-induced coalescence of surfactant laden drops in creeping flow conditions [74, 82–84].

In this chapter, flow-induced coalescence of two equal-sized drops of radius R laden with insoluble surfactants is studied when $Re \sim O(1)$, where $Re = \mu_2(GR)R/\sigma_0$ is the Reynold's number and μ_2, G and σ_0 are the viscosity of the outer liquid, strain rate of the imposed flow and clean interface tension of the liquid-liquid interface. A study of the effect of the imposed strain rate, and surfactant parameters on drainage times is presented. Drop rebound due to addition of surfactants is observed for smaller surfactant concentrations and low surfactant strength. This mechanism is explored in further detail, and it is shown that as drainage of the film between the drops occurs, it causes transport of surfactant out of the film. This leads to buildup of Marangoni stress that opposes drainage, which causes flow-reversal and subsequent drop rebound. The significance of drop inertia is clear, as artificially "turning off" inertia predicts monotonic decrease of drop separation and predicts shorter drainage times. Following rebound, interface velocity is reduced and drainage is further slowed by partial immobilization due to Marangoni stress. Thus, two mechanisms of drainage delay act during surfactant coalescence in moderate Re flows, drop rebound and partial interface immobilization. Finally, the addition of surfactants to cases with larger Re, where drop rebound due to inertial effects for the clean interface case is

known to occur [64] results in remarkable behavior. Drop rebound is amplified due to addition of surfactant (figure1.6), and multiple instances of flow-reversal are observed. As surfactant drains out of the film, Marangoni stress builds up, thereby reversing flow and restoring surfactant in the film, before the cycle is repeated. This phenomena is reminiscent of microthread cascades observed in surfactant laden thread pinchoff [28], and similar behavior was observed experimentally for surfactant laden water in oil films [85].

1.5 List of References

[1] Bala Ambravaneswaran, Hariprasad J Subramani, Scott D Phillips, and Osman A Basaran. Dripping-jetting transitions in a dripping faucet. *Phys. Rev. Let.*, 93(3):034501, 2004.

[2] Hariprasad J. Subramani, Hak Koon Yeoh, Ronald Suryo, Qi Xu, Bala Ambravaneswaran, and Osman A. Basaran. Simplicity and coplexity in a dripping faucet. *Phys. Fluids*, 18(3):032106–1–032106–13, 2006.

[3] Osman A Basaran. Small-scale free surface flows with breakup: Drop formation and emerging applications. *AIChE Journal*, 48(9):1842–1848, 2002.

[4] Jens Eggers and Emmanuel Villermaux. Physics of liquid jets. *Reports on Progress in Physics*, 71(3):036601, 2008.

[5] Cory Berkland, Kyekyoon Kevin Kim, and Daniel W Pack. Fabrication of plg microspheres with precisely controlled and monodisperse size distributions. *Journal of controlled release*, 73(1):59–74, 2001.

[6] Jens Eggers and Marco A Fontelos. The role of self-similarity in singularities of partial differential equations. *Nonlinearity*, 22(1):R1, 2008.

[7] A. U. Chen, P. K. Notz, and O. A. Basaran. Computational and experimental analysis of pinch-off and scaling. *Phys. Rev. Lett.*, 88(17):174501, 2002.

[8] J. Becker, G. Grün, R. Seemann, H. Mantz, K. Jacobs, K. R. Mecke, and R. Blossey. Complex dewetting scenarios captured by thin-film models. *Nat. Mat.*, 2(1):59–63, 2003.

[9] J. D. Paulsen, J.C. Burton, S. R. Nagel, S. Appathuri, M. T. Harris, and O. A. Basaran. The inexorable resistance of inertia determines the initial regime of drop coalescence. *Proc. Nat. Acad. Sci.*, 109(18):6857–6861, 2002.

[10] G. I. Barenblatt. *Scaling, Self-similarity, and Intermediate Asymptotics: Dimensional Analysis and Intermediate Asymptotics*. Cambridge University Press, New York, 1996.

[11] Joseph B Keller and Michael J Miksis. Surface tension driven flows. *SIAM J. App. Math.*, 43(2):268–277, 1983.

[12] Jens Eggers. Universal pinching of 3d axisymmetric free-surface flow. *Phys. Rev. Lett.*, 71:3458–3460, Nov 1993.

[13] Demetrios T Papageorgiou. Analytical description of the breakup of liquid jets. *J. Fluid Mech.*, 301:109–132, 1995.

[14] Michael P Brenner, John R Lister, and Howard A Stone. Pinching threads, singularities and the number 0.0304... *Phys. Fluids*, 8(11):2827–2836, 1996.

[15] Richard F Day, E John Hinch, and John R Lister. Self-similar capillary pinchoff of an inviscid fluid. *Phys. Rev. Let.*, 80(4):704, 1998.

[16] J. R. Castrejón-Pita, A. A. Castrejón-Pita, S. S. Thete, K. Sambath, I. M. Hutchings, J. Hinch, J. R. Lister, and O. A. Basaran. Plethora of transitions during breakup of liquid filaments. *Proc. Natl. Acad. Sci. USA*, 112(15):4582–4587, 2015.

[17] D. Vaynblat, J. R. Lister, and T. P. Witelski. Rupture of thin viscous films by van der Waals forces: Evolution and self-similarity. *Phys. Fluids*, 13(5):1130–1140, 2001.

[18] S. S. Thete, C. Anthony, O. A. Basaran, and P. Doshi. Self-similar rupture of thin free films of power-law fluids. *Phys. Rev. E*, 92(2):023014, 2015.

[19] S. S. Thete, C. Anthony, P. Doshi, M. T. Harris, and O. A. Basaran. Self-similarity and scaling transitions during rupture of thin free films of Newtonian fluids. *Phys. Fluids*, 28(9):092101, 2016.

[20] Vishrut Garg, Sumeet S Thete, Christopher R Anthony, Brayden W Wagoner, and Osman A Basaran. Self-similarity and scaling transitions in breakup of sheets of power-law fluids. *Unpublished*, 2019.

[21] W. W. Zhang and J. R. Lister. Similarity solutions for van der Waals rupture of a thin film on a solid substrate. *Phys. Fluids*, 11(9):2454–2462, 1999.

[22] Vishrut Garg, Pritish M Kamat, Christopher R Anthony, Sumeet S Thete, and Osman A Basaran. Self-similar rupture of thin films of power-law fluids on a substrate. *J. Fluid Mech.*, 826:455–483, 2017.

[23] Zhong Zheng, Marco A Fontelos, Sangwoo Shin, and Howard A Stone. Universality in the nonlinear leveling of capillary films. *Phys. Rev. Fluids*, 3(3):032001, 2018.

[24] Jens Eggers, John R Lister, and Howard A Stone. Coalescence of liquid drops. *J. Fluid Mech.*, 401:293–310, 1999.

[25] L Duchemin, Jens Eggers, and C Josserand. Inviscid coalescence of drops. *J. Fluid. Mech.*, 487:167–178, 2003.

[26] J. P. Munro, C. R. Anthony, O. A. Basaran, and J. R. Lister. Thin-sheet flow between coalescing bubbles. *J. Fluid Mech.*, 773:R3, 2015.

[27] Christopher R Anthony, Pritish M Kamat, Sumeet S Thete, James P Munro, John R Lister, Michael T Harris, and Osman A Basaran. Scaling laws and dynamics of bubble coalescence. *Phys. Rev. Fluids*, 2(8):083601, 2017.

[28] Pritish M Kamat, Brayden W Wagoner, Sumeet S Thete, and Osman A Basaran. Role of marangoni stress during breakup of surfactant-covered liquid threads: Reduced rates of thinning and microthread cascades. *Phys. Rev. Fluids*, 3(4):043602, 2018.

[29] L. G. Leal. *Advanced Transport Phenomena: Fluid Mechanics and Convective Transport Processes*. Cambridge University Press, New York, 2007.

[30] Stanley Middleman. Stability of a viscoelastic jet. *Chem. Eng. Sci.*, 20(12):1037 – 1040, 1965.

[31] Gareth H McKinley. Visco-elasto-capillary thinning and break-up of complex fluids. 2005.

[32] P. P. Bhat, S. Appathurai, M. T. Harris, M. Pasquali, G. H. McKinley, and O. A. Basaran. Formation of beads-on-a-string structures during break-up of viscoelastic filaments. *Nat. Phys.*, 6(8):625–631, 2010.

[33] R Sattler, Christian Wagner, and Jens Eggers. Blistering pattern and formation of nanofibers in capillary thinning of polymer solutions. *Phys. Rev. Let.*, 100(16):164502, 2008.

[34] Christian Clasen, Jens Eggers, Marco A Fontelos, Jie Li, and Gareth H McKinley. The beads-on-string structure of viscoelastic threads. *J. Fluid Mech.*, 556:283–308, 2006.

[35] R Sattler, S Gier, Jens Eggers, and Christian Wagner. The final stages of capillary break-up of polymer solutions. *Phys. Fluids*, 24(2):023101, 2012.

[36] J Eggers. Instability of a polymeric thread. *Phys. Fluids*, 26(3):033106, 2014.

[37] G. F. Teletzke, H. T. Davis, and L.E. Scriven. How liquids spread on solids. *Chem. Eng. Comm.*, 55(1-6):41–82, 1987.

[38] Jacob N Israelachvili. *Intermolecular and surface forces*. Academic press, 2011.

[39] Yueying Wu, Jason D Fowlkes, Philip D Rack, Javier A Diez, and Lou Kondic. On the breakup of patterned nanoscale copper rings into droplets via pulsed-laser-induced dewetting: competing liquid-phase instability and transport mechanisms. *Langmuir*, 26(14):11972–11979, 2010.

[40] Daigo Yamamoto, Chika Nakajima, Akihisa Shioi, Marie Pierre Krafft, and Kenichi Yoshikawa. The evolution of spatial ordering of oil drops fast spreading on a water surface. *Nature Comm.*, 6:7189, 2015.

[41] R. J. Braun. Dynamics of the tear film. *Ann. Rev. Fluid Mech.*, 44:267–297, 2012.

[42] Anthony M Anderson, Lucien N Brush, and Stephen H Davis. Foam mechanics: spontaneous rupture of thinning liquid films with plateau borders. *J. Fluid. Mech.*, 658:63–88, 2010.

[43] Peter S Stewart, Jie Feng, Laura S Kimpton, Ian M Griffiths, and Howard A Stone. Stability of a bi-layer free film: simultaneous or individual rupture events? *J. Fluid Mech.*, 777:27–49, 2015.

[44] A Alizadeh Pahlavan, L Cueto-Felgueroso, AE Hosoi, GH McKinley, and R Juanes. Thin films in partial wetting: stability, dewetting and coarsening. *J. Fluid. Mech.*, 845:642–681, 2018.

[45] Rabibrata Mukherjee and Ashutosh Sharma. Instability, self-organization and pattern formation in thin soft films. *Soft Matter*, 11(45):8717–8740, 2015.

[46] Clara Vernay, Laurence Ramos, and Christian Ligoure. Bursting of dilute emulsion-based liquid sheets driven by a marangoni effect. *Phys. Rev. Let.*, 115(19):198302, 2015.

[47] Elisabeth Guazzelli and Jeffrey F Morris. *A physical introduction to suspension dynamics*, volume 45. Cambridge University Press, 2011.

[48] Günter Reiter, Moustafa Hamieh, Pascal Damman, Séverine Sclavons, Sylvain Gabriele, Thomas Vilmin, and Elie Raphaël. Residual stresses in thin polymer films cause rupture and dominate early stages of dewetting. *Nature Mat.*, 4(10):754, 2005.

[49] P. Doshi and O. A. Basaran. Self-similar pinch-off of power law fluids. *Phys. Fluids*, 16(3):585–593, 2004.

[50] R. Suryo and O. A. Basaran. Local dynamics during pinch-off of liquid threads of power law fluids: Scaling analysis and self-similarity. *J. Non-Newtonian Fluid Mech.*, 138(2):134–160, 2006.

[51] F. M. Huisman, S. R. Friedman, and P. Taborek. Pinch-off dynamics in foams, emulsions and suspensions. *Soft Matter*, 8(25):6767–6774, 2012.

[52] Stig Friberg, Kare Larsson, and Johan Sjöblom. *Food emulsions*, volume 132. CRC Press, 2003.

[53] Peter K Kilpatrick. Water-in-crude oil emulsion stabilization: Review and unanswered questions. *Energy & Fuels*, 26(7):4017–4026, 2012.

[54] Rudolf Heusch. Emulsions. *Ullmann's Encyclopedia of Industrial Chemistry*, 1987.

[55] D Moinard-Checot, Y Chevalier, S Briançon, H Fessi, and S Guinebretière. Nanoparticles for drug delivery: Review of the formulation and process difficulties illustrated by the emulsion-diffusion process. *Journal of nanoscience and nanotechnology*, 6(9-10):9–10, 2006.

[56] Sanjeev Kumar, G Narsimhan, and D Ramkrishna. Coalescence in creaming emulsions. existence of a pure coalescence zone. *Industrial & engineering chemistry research*, 35(9):3155–3162, 1996.

[57] Peter Van Puyvelde, Sachin Velankar, Jan Mewis, Paula Moldenaers, and KU Leuven. Effect of marangoni stresses on the deformation and coalescence in compatibilized immiscible polymer blends. *Polymer Engineering & Science*, 42(10):1956–1964, 2002.

[58] Xiaofan Li and C Pozrikidis. The effect of surfactants on drop deformation and on the rheology of dilute emulsions in stokes flow. *J. Fluid. Mech.*, 341:165–194, 1997.

[59] Yosang Yoon, Adam Hsu, and L Gary Leal. Experimental investigation of the effects of copolymer surfactants on flow-induced coalescence of drops. *Phys. Fluids*, 19(2):023102, 2007.

[60] TD Hodgson and DR Woods. The effect of surfactants on the coalescence of a drop at an interface. ii. *Journal of Colloid and Interface Science*, 30(4):429–446, 1969.

[61] Aparna V Bhave, Robert C Armstrong, and Robert A Brown. Kinetic theory and rheology of dilute, nonhomogeneous polymer solutions. *J. Chem. Phys.*, 95(4):2988–3000, 1991.

[62] J. Eggers and T. F. Dupont. Drop formation in a one-dimensional approximation of the Navier-Stokes equation. *J. Fluid Mech.*, 262:205–221, 1994.

[63] S. W. Hasan, M. T. Ghannam, and N. Esmail. Heavy crude oil viscosity reduction and rheology for pipeline transportation. *Fuel*, 89(5):1095–1100, 2010.

[64] Krishnaraj Sambath. *Dynamics of Drop Disintegration and Coalescence with and without Electric Fields*. PhD thesis, Purdue University, August 2013.

[65] JM Frostad, J Walter, and LG Leal. A scaling relation for the capillary-pressure driven drainage of thin films. *Phys. Fluids*, 25(5):052108, 2013.

[66] Patrick K. Notz and Osman A. Basaran. Dynamics and breakup of a contracting liquid filament. *J. Fluid Mech.*, 512:223–256, 2004.

[67] Philip M Gresho, Robert L Lee, Robert L Sani, and TW Stullich. Time-dependent fem solution of the incompressible navier–stokes equations in two-and three-dimensions. Technical report, California Univ., 1978.

[68] K. N. Christodoulou and L. E. Scriven. Discretization of free surface flows and other moving boundary problems. *J. Comput. Phys.*, 99(1):39–55, 1992.

[69] Antony N Beris and Vlasis G Mavrantzas. On the compatibility between various macroscopic formalisms for the concentration and flow of dilute polymer solutions. *J. Rheol.*, 38(5):1235–1250, 1994.

[70] J. R. Savage, M. Caggioni, P. T. Spicer, and I. Cohen. Partial universality: pinch-off dynamics in fluids with smectic liquid crystalline order. *Soft Matter*, 6(5):892–895, 2010.

[71] Igor Ekhiel'evich Dzyaloshinskii, EM Lifshitz, and Lev Petrovich Pitaevskii. General theory of van der waals forces. *Physics-Uspekhi*, 4(2):153–176, 1961.

[72] Bing Dai, L Gary Leal, and Antonio Redondo. Disjoining pressure for nonuniform thin films. *Phys. Rev. E*, 78(6):061602, 2008.

[73] Ying-Chih Liao, Elias I Franses, and Osman A Basaran. Deformation and breakup of a stretching liquid bridge covered with an insoluble surfactant monolayer. *Phys. Fluids*, 18(2):022101, 2006.

[74] Allan K Chesters and Ivan B Bazhlekov. Effect of insoluble surfactants on drainage and rupture of a film between drops interacting under a constant force. *J. Col. Int. Sci.*, 230(2):229–243, 2000.

[75] Colin D O'Dowd and Gerrit De Leeuw. Marine aerosol production: a review of the current knowledge. *Philosophical Transactions of the Royal Society of London A: Mathematical, Physical and Engineering Sciences*, 365(1856):1753–1774, 2007.

[76] DC Blanchard and AH Woodcock. Bubble formation and modification in the sea and its meteorological significance. *Tellus*, 9(2):145–158, 1957.

[77] E Canot, Laurent Davoust, M El Hammoumi, and D Lachkar. Numerical simulation of the buoyancy-driven bouncing of a 2-d bubble at a horizontal wall. *Theoretical and computational fluid dynamics*, 17(1):51–72, 2003.

[78] Vince Wallwork, Zhenghe Xu, and Jacob Masliyah. Bitumen recovery with oily air bubbles. *The Canadian journal of chemical engineering*, 81(5):993–997, 2003.

[79] A. Nguyen and H. J. Schulze. *Colloidal Science of Flotation*. CRC Press, Boca Raton, Florida, 2003.

[80] Yue Zhao, Yan-Peng Li, Jia Huang, Jun Liu, and Wen-Ke Wang. Rebound and attachment involving single bubble and particle in the separation of plastics by froth flotation. *Separation and Purification Technology*, 144:123–132, 2015.

[81] DB Donoghue, A Albadawi, YMC Delauré, AJ Robinson, and DB Murray. Bubble impingement and the mechanisms of heat transfer. *International Journal of Heat and Mass Transfer*, 71:439–450, 2014.

[82] Leslie Y Yeo, Omar K Matar, E Susana Perez de Ortiz, and Geoffrey F Hewitt. Film drainage between two surfactant-coated drops colliding at constant approach velocity. *J. Col. Int. Sci.*, 257(1):93–107, 2003.

[83] Bing Dai and L Gary Leal. The mechanism of surfactant effects on drop coalescence. *Phys. Fluids*, 20(4):040802, 2008.

[84] Carolina Vannozzi. Coalescence of surfactant covered drops in extensional flows: effects of the interfacial diffusivity. *Phys. Fluids*, 24(8):082101, 2012.

[85] Orlin D Velev, Theodor D Gurkov, and Rajendra P Borwankar. Spontaneous cyclic dimpling in emulsion films due to surfactant mass transfer between the phases. *J. Col. Int. Sci.*, 159(2):497–501, 1993.

2. PINCHOFF OF SLENDER THREADS OF NON-HOMOGENEOUS POLYMER SOLUTIONS

2.1 Introduction

The study of a liquid jet or thread emanating from a nozzle and its subsequent breakup into drops is a problem of great practical implication in industry with a rich history of 300 years. Applications include inkjet printing, deposition of reagents on diagnostic prints, DNA arraying and manufacture of particles and microcapsules [1]. Improving and optimizing diesel engine technology is another important field where understanding the dynamics of liquid threads is essential [2]. In addition to their practical usefulness, threads are an ideal probe for liquid properties, such as surface tension, viscosity or non-Newtonian rheology [2].

The earliest experiments on liquid threads were performed by Savart [3], who noted that pinchoff of a thread was spontaneous, and independent of any external force or direction. This led him to hypothesize that some intrinsic property of the dynamics was responsible, rather than gravity as Marriote and da Vinci had earlier stated [2]. Plateau [4] recognized the contribution of surface tension by observing that long wavelength perturbations that reduce the surface area are favored. Lord Rayleigh [5] showed that this surface tension had to act against inertia, which opposed fluid motion over long distances. His linear stability analysis formally established that threads were unstable to small perturbations of wavelengths greater than its circumference. This effect is known as the Plateau-Rayleigh instability.

Goedde and Yuen [6] were the first to show the nonlinear nature of thread pinchoff and subsequent droplet formation by performing a set of experiments that directly measured the radius of the thread, rather than the difference between the swell and

neck radii as Donnelly and Glaberson [7] had done. However, it was only given a theoretical treatment when Eggers [8] realized that close to pinchoff, thickness of the neck that forms during pinchoff could be predicted at a given distance from the axial location of pinchoff, irrespective of the initial conditions of the experiment. He thus concluded that in the absence of a suitable length scale, the dynamics must be self similar. Formulating a one-dimensional (1D) approximation of the Navier Stokes equations [9], he derived the universal scaling law for the minimum neck radius close to pinchoff, now known as Eggers scaling. This approximation, known as the "slender-jet approximation" sees widespread use in dripping and jetting applications [2].

Many industrial processes involve fluids that are Non-Newtonian in nature, especially those containing dissolved polymer chains (making them viscoelastic) or particles. The study of viscoelastic free surface flows is a relatively young field. Middleman [10] stated that viscoelastic threads are less stable to perturbations than their Newtonian counterparts by performing a linear stability analysis. However, Goldin [11] observed that nonlinear effects that developed in the neck stabilized the pinchoff process and led to the formation of a "beads on string structure". Bousfield [12] simulated the infinitely extensible Oldroyd-B model [13] and showed that elastic stresses grow exponentially in the neck, while the thread never goes to pinchoff. This is in contrast to experimental observations, where viscoelastic threads, although delayed, usually breakup into droplets. Subsequent studies by Renardy [14] and Fontelos and Li [15] on finitely extensible Giesekus [16] and FENE threads have shown that close to pinchoff, a self-similar necking process develops where the radius decays linearly in time [17], as the extensional viscosity reaches a plateau value, and the thread behaves like a highly viscous Newtonian liquid. More recently, Oliveira [18] and Sattler [19] reported complex phenomenon occurring during the later stages of polymer thread pinchoff, as they observed that several instabilities developed in the thread and led to the formation of a "blistering pattern", with growth rates much higher than that expected for a Newtonian liquid of the corresponding extensional viscosity [20]. They hypothesized that a possible reason for this deviation could be axial

non-uniformity in the polymer concentration along the length of the thread [19, 21]. Polymer concentration is controlled by four mechanisms [22], namely, advection, diffusion, dispersion, and finally, stress-gradient induced migration. The final mechanism causes migration of polymer chains due to spatial variations in the elastic stress, and is accounted for by coupled equations for the elastic stress due to polymer chains, and variation of polymer chain concentration in the flow, the so-called "stress-density coupling" [22–26]. This phenomenon has been studied in detail in the past, for flow of polymeric liquids through microchannels [27, 28], in corrugated channels [22, 29], and in Taylor-Couette devices [30, 31]. However, past studies on viscoelastic thread pinchoff have always involved models that assume polymer concentration to be spatially uniform. Eggers [21] was the first to consider the effect of stress-density coupling on viscoelastic thread pinchoff, by performing a linear stability analysis.

Here, we examine the effects of stress-density coupling on the nonlinear dynamics of viscoelastic thread pinchoff. The number of polymer molecules in the primary drop and filament formed on thread pinchoff are compared to the Oldroyd-B model for various parameter values, to ascertain when stress density coupling becomes important. We take advantage of the slenderness of the thread and axisymmetric nature of the system to solve a 1D set of equations numerically, using a Galerkin Finite Element Method (GFEM) based algorithm. Governing equations for the flow of viscoelastic fluid, followed by the numerical methods employed to solve the set of 1D partial differential equations are specified in section 2.2. This is followed by a brief description of accuracy tests performed to validate the code developed with results published in literature in section 2.3. This is followed by results and their analyses in section 2.4 and finally, conclusions and outlook in section 2.5.

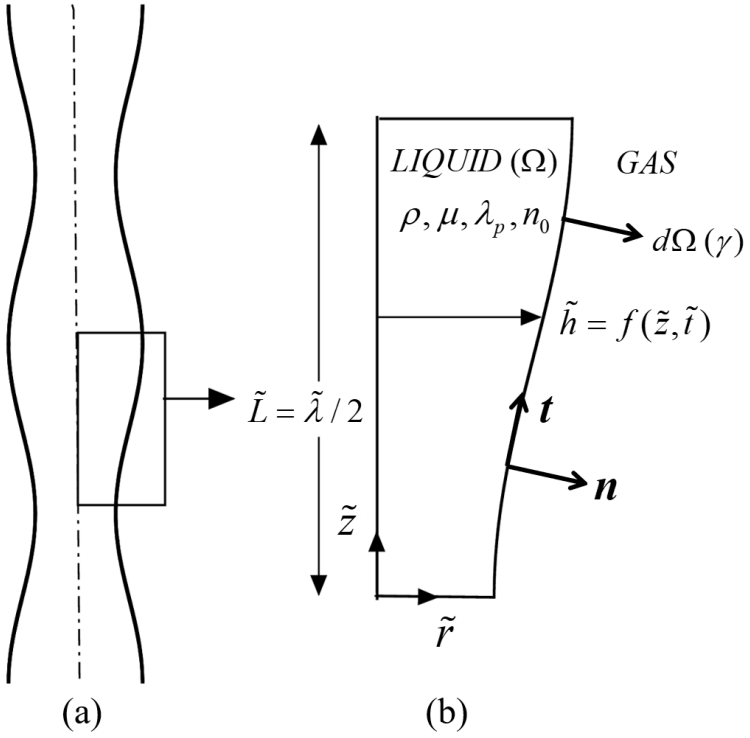

Figure 2.1. Diagram of (a) a slender viscoelastic thread, where a sinusoidal perturbation is applied to its interface. Owing to the symmetry of the system, only (b) half a wavelength of the thread is considered when studying pinchoff.

2.2 Mathematical Formulation

2.2.1 Governing equations

The system considered here is a section of an infinite perturbed thread of an incompressible, isothermal, viscoelastic fluid comprising of a dilute solution of polymers in a Newtonian solvent of constant density ρ, and viscosity μ. The unperturbed radius of the thread is R and a sinusoidal perturbation of amplitude ϵ and wavelength $\tilde{\lambda}$ is applied at time $\tilde{t} = 0$. The thread radius $\tilde{h}(\tilde{z})$ is then described by the following equation

$$\tilde{h} = R\left[\sqrt{1 - \frac{\epsilon^2}{2}} - \epsilon \cos\left(\frac{2\pi}{\tilde{\lambda}}\tilde{z}\right)\right] \tag{2.1}$$

As shown by Rayleigh [5,32], the thread is spontaneously unstable if $\tilde{\lambda} > 2\pi R$. Owing to the periodic nature of the perturbation and axisymmetric nature of the system, only half a wavelength of the thread is chosen as our problem domain, as illustrated in figure 2.1, such that the length of our domain is $\tilde{L} = \tilde{\lambda}/2$. The thread is surrounded by a passive gas such as air, and the pressure outside is set to be zero w.l.o.g. The surface tension γ of the interface $d\Omega$ is spatially uniform and constant in time. The effects of gravity are neglected on account of slenderness of the thread.

The problem variables are non-dimensionalised using the unperturbed thread radius as the length scale, $l_c \equiv R$, the inertio-capillary time as the characteristic time scale, $t_c \equiv (\rho R^3/\gamma)^{\frac{1}{2}}$, the ratio of these two scales as the characteristic velocity $v_c \equiv l_c/t_c$, capillary pressure as the characteristic stress scale, $p_c \equiv \gamma/R$, and average polymer number density n_0 as the characteristic polymer concentration. As a result of choosing these characteristic scales, the dynamics are governed by four dimensionless numbers, the Ohnesorge number, $Oh \equiv \mu/\sqrt{\rho R\gamma}$, which represents the ratio of the viscous force to the square root of the product of the inertial and capillary forces, the Deborah number, $De \equiv \lambda_p/t_c$, which represents the ratio of the relaxation time scale λ_p of polymer chains considered in this viscoelastic model, to the characteristic time scale for the system, the Peclet Number for polymer chain transport, $Pe \equiv l_c^2/Dt_c$, and finally, $\bar{N} \equiv Rn_0k_bT/\gamma$. This last dimensionless number $\bar{N}$ is a ratio of the force applied on polymer chains due to polymer migration to capillary forces in the system. In what follows, dimensionless counterparts of the corresponding dimensional variables are written without a tilde ($\sim$) over them.

The dimensionless forms of the mass and momentum balance governing the viscoelastic fluid are then given by

$$\nabla \cdot \mathbf{v} = 0 \tag{2.2}$$

$$\frac{\partial \mathbf{v}}{\partial t} + \mathbf{v} \cdot \nabla \mathbf{v} = \nabla \cdot \mathbf{T} \tag{2.3}$$

Here $\mathbf{T}$ represents the stress tensor which can be broken up into contributions from the isotropic, viscous and elastic stresses respectively as $\mathbf{T} = -p\mathbf{I} + \boldsymbol{\tau} + \boldsymbol{\sigma}$ where $\boldsymbol{\tau} = \mu\left(\nabla\mathbf{v} + (\mathbf{v})^T\right)$. The constitutive equation for elastic stress $\boldsymbol{\sigma}$ was derived by Bhave et al. [23] while considering each polymer chain as a Hookean dumbbell and accounting for spatial inhomogenity in the polymer chain distribution function. As a result, a mass balance to account for movement of polymer chains along the thread was added to the system of equations. These equations were reviewed by Beris and Mavrantzas [26] and found to be consistent with other models developed using a body tensor formulation [24], or a two-fluid Hamiltonian model [25], if third order gradients are omitted from both equations [21]. The coupled set of dimensionless equations for the elastic stress $\boldsymbol{\sigma}$ and polymer concentration n are given by

$$\frac{\boldsymbol{\sigma}}{De} + (\boldsymbol{\sigma})_{(1)} = \bar{N}n\left((\nabla\mathbf{v}) + (\nabla\mathbf{v})^T\right) + \bar{N}\boldsymbol{I}\left(\frac{1}{Pe}\nabla^2 n - \frac{Dn}{Dt}\right) + \frac{1}{Pe}\nabla^2\boldsymbol{\sigma} \tag{2.4}$$

$$\frac{Dn}{Dt} = -\frac{1}{Pe\bar{N}}\nabla\nabla : \boldsymbol{\sigma} + \frac{1}{Pe}\nabla^2 n \tag{2.5}$$

Here $()_{(1)}$ denotes the upper convected time derivative operator often found in continuum mechanics [13]. A mass and stress balance at the free surface $d\Omega$ leads to the application of the kinematic and traction boundary conditions

$$\mathbf{n}\cdot(\mathbf{v} - \mathbf{v}_s) = 0 \tag{2.6}$$

$$\mathbf{n}\cdot\mathbf{T} = 2H\mathbf{n} \tag{2.7}$$

Here $2H$ is twice the local mean curvature and can be evaluated by taking the dot product of the surface gradient with the unit normal vector $\mathbf{n}$ to the interface $d\Omega$, $2H = -\nabla_s\cdot\mathbf{n}$.

Finally, symmetry boundary conditions apply at the two ends of the thread $L = 0$ and $L = \lambda/2$, along with the requirement that no polymer chains can enter or exit the problem domain such that

$$\mathbf{t} \cdot \nabla_s n = 0 \tag{2.8}$$

where $\mathbf{t}$ is the unit tangent at the interface $d\Omega$.

For a system involving a slender thread such that its length is much larger than its thickness, the three-dimensional axisymmetric equations can be simplified by expanding the field variables, i.e. velocity, pressure, elastic stress and number density in a Taylor series in the radial coordinate r, as done by Eggers and Dupont for Newtonian threads [9]. The full expression for curvature is retained, rather than the asymptotically correct one, as it has proven to yield a more accurate description of the nonlinear free surface evolution [9, 33]. The "slender-jet" approximation for the governing set of equations (2.3) - (2.5) is then given by

$$\frac{\partial h^2}{\partial t} + \frac{\partial (h^2 v)}{\partial z} = 0 \tag{2.9}$$

$$\frac{\partial v}{\partial t} + v\frac{\partial v}{\partial z} + \frac{\partial (2H)}{\partial z} - \frac{3Oh}{h^2}\frac{\partial}{\partial z}(h^2 \frac{\partial v}{\partial z}) - \frac{1}{h^2}\frac{\partial}{\partial z}(h^2 \sigma) = 0 \tag{2.10}$$

$$\frac{\partial \sigma}{\partial t} + v\frac{\partial \sigma}{\partial z} - 2\frac{\partial v}{\partial z}\sigma - 2\bar{N} n \frac{\partial v}{\partial z} + \frac{\sigma}{De} + \bar{N}(\frac{\partial n}{\partial t} + v\frac{\partial n}{\partial z} - \frac{1}{Pe}\frac{\partial^2 n}{\partial z^2}) - \frac{1}{Pe}\frac{\partial^2 \sigma}{\partial z^2} = 0 \tag{2.11}$$

$$\frac{\partial n}{\partial t} + v\frac{\partial n}{\partial z} - \frac{1}{Pe}\frac{\partial^2 n}{\partial z^2} + \frac{1}{Pe\bar{N}}\frac{\partial^2 \sigma}{\partial z^2} = 0 \tag{2.12}$$

Here, the variables $h(z,t)$, $v(z,t)$, $\sigma(z,t)$, and $n(z,t)$ represent the neck radius, axial velocity, axial elastic stress (i.e. σ_{zz} from the elastic stress tensor $\boldsymbol{\sigma}$), and polymer concentration respectively. Equation (2.9) represents the 1D mass balance obtained from the kinematic boundary condition, equation (2.10) is the 1D form of the Cauchy Momentum equation, equation (2.11) is the constitutive equation for axial elastic stress, which is coupled with the convection diffusion equation (2.12) for polymer concentration.

The curvature $2H$ is given by

$$2H = \frac{1}{h\left(1+\left(\frac{\partial h}{\partial z}\right)^2\right)^{\frac{1}{2}}} - \frac{\frac{\partial^2 h}{\partial z^2}}{\left(1+\left(\frac{\partial h}{\partial z}\right)^2\right)^{\frac{3}{2}}} \tag{2.13}$$

As nonlinear effects are important close to pinchoff, diffusion and transport in equation (2.12) are not necessarily controlled by the same Onsager coefficient D_{tr} [34]. Thus, a diffusivity ratio A_{dif} is assumed, which modifies the constitutive equation (2.11) and convection diffusion equation (2.12) into the following form

$$\frac{\partial \sigma}{\partial t} + v\frac{\partial \sigma}{\partial z} - 2\frac{\partial v}{\partial z}\sigma - 2\bar{N}n\frac{\partial v}{\partial z} + \frac{\sigma}{De} + \bar{N}\left(\frac{\partial n}{\partial t} + v\frac{\partial n}{\partial z} - \frac{1}{Pe}\frac{\partial^2 n}{\partial z^2}\right) - A_{dif}\frac{1}{Pe}\frac{\partial^2 \sigma}{\partial z^2} = 0 \tag{2.14}$$

$$\frac{\partial n}{\partial t} + v\frac{\partial n}{\partial z} - \frac{1}{Pe}\frac{\partial^2 n}{\partial z^2} + A_{dif}\frac{1}{Pe\bar{N}}\frac{\partial^2 \sigma}{\partial z^2} = 0 \tag{2.15}$$

The boundary conditions (2.6) and (2.8) can be reduced to their 1D counterparts under the "slender-jet" approximation. Symmetry of the thread thickness $h(z,t)$, velocity $v(z,t)$, and axial elastic stress $\sigma(z,t)$ at the boundaries, along with no transport of polymer chains into or out of the thread requires that

At $z = 0$:

$$\frac{\partial h}{\partial z} = 0, \quad v = 0, \quad \frac{\partial \sigma}{\partial z} = 0, \quad \frac{\partial n}{\partial z} = 0 \tag{2.16}$$

At $z = L$:

$$\frac{\partial h}{\partial z} = 0, \quad v = 0, \quad \frac{\partial \sigma}{\partial z} = 0, \quad \frac{\partial n}{\partial z} = 0 \tag{2.17}$$

The system is initially quiescent, with the dimensionless form of equation (2.1) applied to the thread thickness $h(z,t)$ at time $t = 0$. The axial elastic stress $\sigma(z,t)$ is initially uniform and set to zero as the polymer chains are initially relaxed on account of no flow in the thread. The concentration is initially axially uniform and set equal to 1 along the length of the thread.

2.2.2 Numerical Methods

The system of one-dimensional nonlinear partial differential equations described above is simulated using either a Galerkin finite element or Streamline Upwind/Petrov Galerkin method, because of its accuracy [1] and ease with which boundary conditions can be applied. The domain is tessellated into elements, and variable values are evaluated within the elements using quadratic basis functions, resulting in a set of ordinary differential equations. For time integration, an implicit backward difference scheme is initially used to smoothen out aphysical initial conditions followed by a second order predictor corrector scheme involving the Adam's Bashforth Predictor and implicit trapezoid rule. Adaptive time stepping is essential for observing pinch off dynamics which occur at much smaller timescales. The non linear algebraic equations thus obtained are solved using Newton's method with a Jacobian that is evaluated analytically. The BANDED solver is used which utilizes the sparse nature of the Jacobian matrix. The codes are written in FORTRAN.

2.3 Code Validation

Volume and number of chains must be conserved to reflect accurate behavior, given only Neumann boundary conditions are applied on the system and thus fluxes at the boundaries are zero. These quantities were conserved all the way till pinchoff, with a maximum error of 0.1% between initial and final values.

In the limit of no stress density coupling, such that $A_{dif} = 0$, the system described above reduces to that of thread pinchoff of an infinitely extensible Oldroyd-B thread. The free surface profiles for the case of no stress density coupling were compared with the simulation results of Clasen et al. [35], and were seen to be an accurate reproduction, as is shown in figure 2.2. The red solid lines represent free surface profiles computed from our simulations, which match the free surface profiles of Clasen et al. [35], shown by the dashed black lines, at the specified dimensionless time instants. The case was run for aspect ratio $L = 2\pi$, $Oh = 0.79$, $De = 94.9$, $\bar{N} = 0.025$, $A_{dif} = 0$

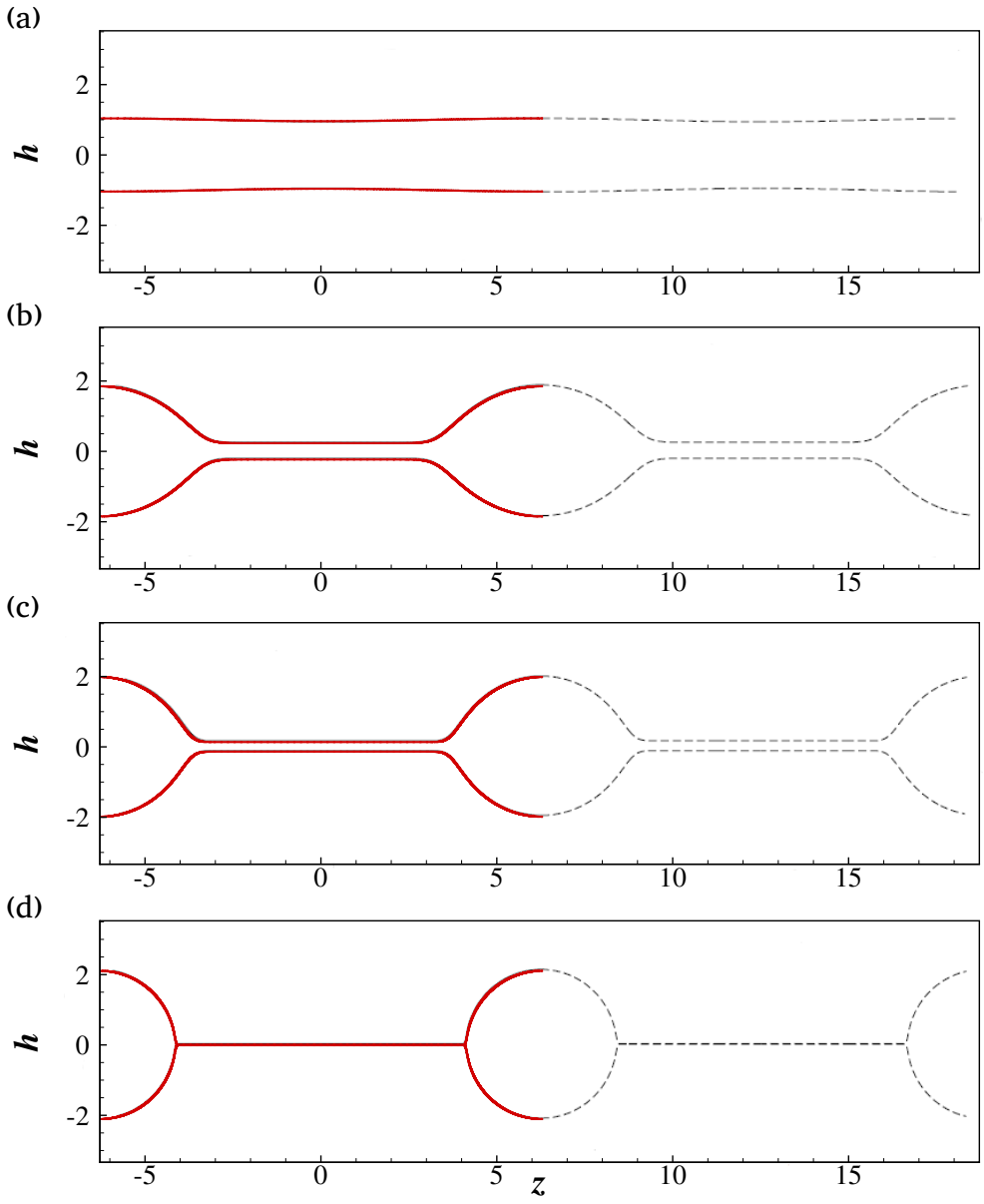

Figure 2.2. Series of interface profiles $h(z,t)$ for Oldroyd-B thread pinchoff compared with the simulation results of Clasen et al. [35]. Results of our numerical simulations are shown by the red solid lines, while those of Clasen et al. [35] are shown by the dashed black lines. The parameter values are $L = 2\pi$, $Oh = 0.79$, $De = 94.9$, $\bar{N} = 0.025$, $A_{dif} = 0$ and $Pe = 1000$. The dimensionless time instants for each profile are (a)0, (b)158.1, (c)316.2 , (d)948.7.

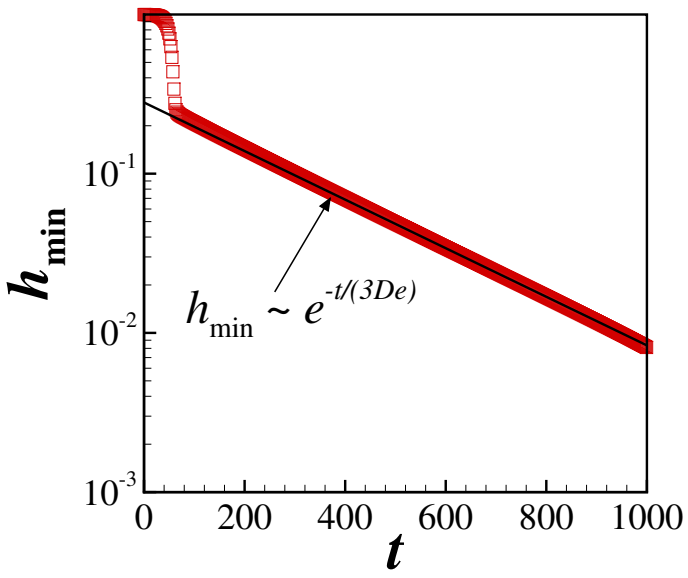

Figure 2.3. Evolution of minimum neck radius h_{min} with time t for Oldroyd-B thread pinchoff for the parameter values $L = 2\pi$, $Oh = 0.79$, $De = 94.9$, $\bar{N} = 0.025$, $A_{dif} = 0$ and $Pe = 1000$. The symbols represent the results of our numerical simulations while the line represents the best fit to the obtained data.

and $Pe = 1000$. Furthermore, our numerical methods were able to accurately demonstrate scaling behavior for the minimum neck radius h_{min}, as the evolution of h_{min} vs time was seen to obey the elasto-capillary scaling such that it varied with time as $h_{min} \sim e^{-t/3De}$ [14, 36], shown in figure 2.3. As such, we have demonstrated the accuracy of our numerical methods and proceed to study the evolution of polymer concentration as viscoelastic threads pinchoff, in the following section.

2.4 Results

The system of nonlinear partial differential equations specified in section 2.2 is solved numerically using the numerical methods outlined above, for a fixed value of $\bar{N} = 10^{-5}$, diffusivity ratio $A_{dif} = 10^{-8}$ and thread length $L = 4.0$, unless otherwise stated. Simulations advance in time until thread pinchoff occurs, which is defined to

occur when the minimum neck radius h_{min} reaches the value of 5×10^{-3}.

The evolution of polymer concentration with time is examined first, followed by an investigation into the significance of inertial effects on polymer concentration. The section is concluded by examining the effect of elasticity, or De, and polymer chain diffusivity Pe on the extent of polymer concentration variation.

2.4.1 Evolution of polymer concentration with time

Figure 2.4 shows the evolution in time of the thread thickness $h(z,t)$, axial velocity $v(z,t)$, and axial elastic stress $\sigma(z,t)$ profiles for capillary pinchoff of a viscoelastic thread such that $Oh = 0.5, De = 1.0, Pe = 1.0$. As thinning progresses, flow in the thread changes from unidirectional flow, represented by the dashed line in figure 2.4(b) (velocity values are positive along the length of the thread), to extensional flow, such that fluid is draining from the neck region, seen in figure 2.4(a), into a satellite drop on the left, and primary drop on the right. This extensional flow stretches the polymer chains, which leads to a buildup of elastic stress in the neck region, as seen in figure 2.4(c). The magnitude of this extensional flow in the neck increases as pinchoff is approached, while the flow remains unidirectional in the satellite and primary drop. Thus, large stress gradients are observed in the neck, while elastic stress remains negligible in the drops. These stress gradients induce an increase in polymer chain concentration in the neck such that a "concentration peak" is seen, while the primary and satellite drops are diluted. Figure 2.5 shows this spatial variation of the polymer concentration n at pinchoff ($h_{min} = 10^{-3}$).

Our results are in agreement with the experimental observations of Sattler et al. [19], who observed the formation of a concentrated neck for polyehtylenoxide (PEO) solutions, which subsequently formed a solid nanofiber. The observed phenomenon of polymer concentration in the neck region is counter-intuitive at first glance, as one would expect polymers to drain from the neck and move to regions of low stress in both the satellite and primary drop. However, it is known that the mobility of a polymer molecule is inversely proportional to the extent of chain extension [37]. Thus,

the mobility of polymer chains in the neck, where they are highly stretched due to extensional flow, is much lower than that of polymer chains in the drops, where they are relaxed and hence more mobile. This mobility gradient drives polymer migration to regions of low mobility, resulting in the counter-intuitive phenomenon of polymer concentration increasing in the neck. This was also observed for DNA flow through a square microchannel by Jendrejack et al. [27].

2.4.2 Effect of Inertia

Bhat et al. [38] showed that inertia is required for the formation of a small, satellite bead between two much larger main beads in viscoelastic threads. They also noted that the satellite drop thus formed is more spherical and has a larger volume than the Newtonian case, as elastic stresses delay pinch-off and enable more fluid to drain into the satellite drop. This is also evident here, when stress density coupling is added, but in this case the effect of satellite drop formation on polymer concentration is of specific interest. The parameter values are $L = 8.0$, $Oh = 0.5$, $De = 5.0$, and $Pe = 1000$, and two cases are compared, the first where the full set of equations are considered, such that inertial effects are included, and the second where inertial effects are artificially "turned off" by setting the left-hand side of the momentum equation (2.10) to zero. While in both cases (with and without inertia) concentration peaks are seen where the neck meets the primary drops (Corner region $C1$ as shown in figure 2.6), the concentration profile in the case with inertia is seen to have additional concentration peaks where the neck meets the satellite drop (corner region $C2$ as shown in figure 2.6). This is understandable, as the the polymer chains are highly stretched in the neck region, resulting in large elastic stress values in the neck as compared to low elastic stress in the satellite drop formed, where the polymer chains are in a relaxed state due to unidirectional flow. This sharp difference in elastic stress leads to polymer migration to corner region $C2$. The number of polymer chains that escape the primary drop when inertial effects are considered is observed to be 29.23 times higher than the number of chains that escape when inertial effects are neglected.

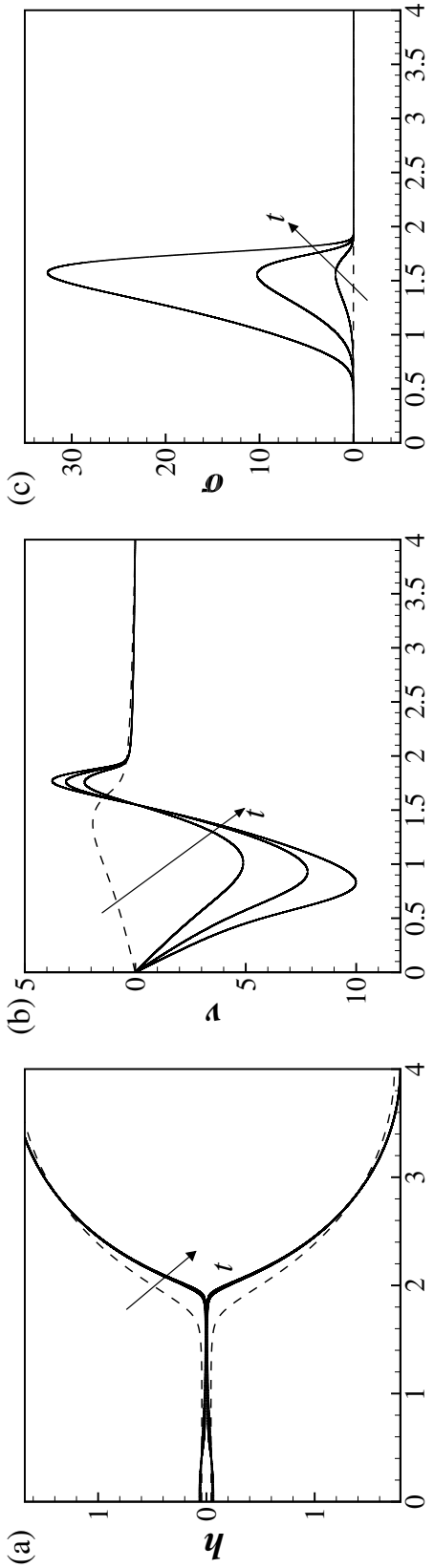

Figure 2.4. Spatial profiles of the (a) thread thickness $h(z,t)$, (b) axial velocity $v(z,t)$, and (c) axial elastic stress σ profiles at different time instants during capillary pinchoff of a viscoelastic thread such that $L = 4.0$, $Oh = 0.5$, $De = 1.0$, $\bar{N} = 10^{-5}$, $A_{dif} = 10^{-8}$, and $Pe = 1.0$. The earliest time instant at which the fluid in the thread is undergoing purely unidirectional flow is represented by the dashed line.

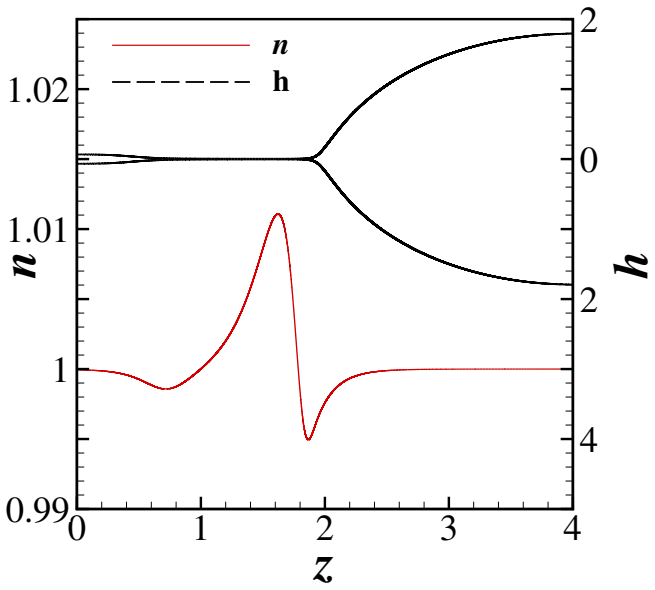

Figure 2.5. Polymer chain concentration n and thread thickness $h(z,t)$ profiles at the incipience of pinchoff for $L = 4.0$, $Oh = 0.5$, $De = 1.0$, $\bar{N} = 10^{-5}$, $A_{dif} = 10^{-8}$, and $Pe = 1.0$. It is clear that the neck is concentrated, while the satellite and primary drop are diluted.

Thus inertial effects play a significant role in deciding the eventual concentration of drops formed from viscoelastic thread pinchoff.

2.4.3 Effect of Elasticity

Figure 2.7 shows the effect of increasing the Deborah number De, or the elasticity of the polymer solution, on the extent of spatial variations in polymer concentration. The figure makes plain that polymer solutions with a higher elasticity result in more concentrated necks. Of particular interest is when De goes from 1.0 to 5.0, an additional concentration peak is observed. This is explained by observing the flow field snapshots for both cases at the incipience of pinch off. These are presented in figure 2.8. For $De = 1.0$, shown in figure 2.8(a), it is seen that the capillary pressure p is much higher than the elastic stresses σ that builds up due to the extensional flow in the neck. Thus, while the elasticity delays pinchoff, capillary forces dominate over

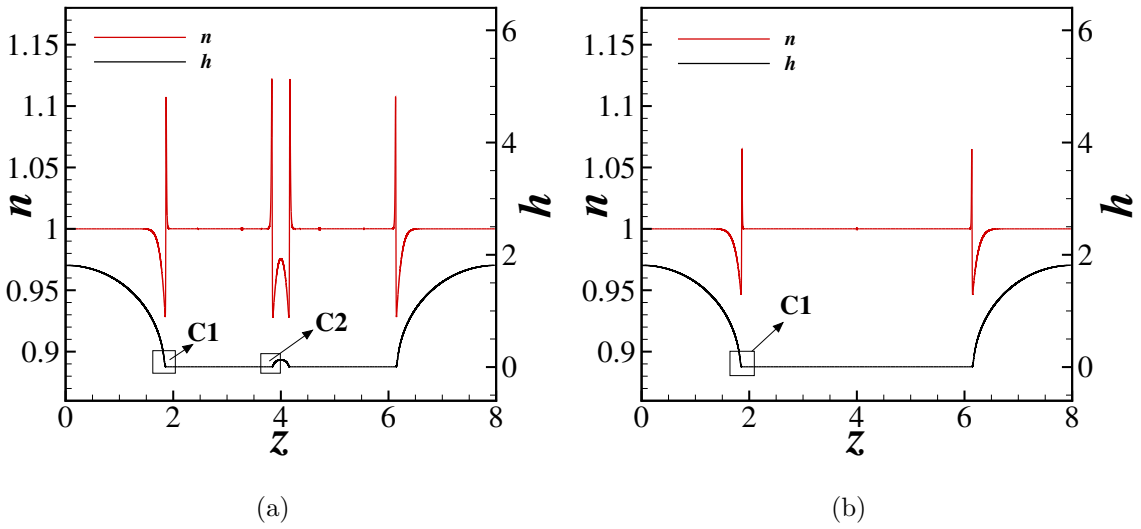

Figure 2.6. Concentration and shape profiles at the incipience of pinchoff for a viscoelastic thread with parameter values $L = 8.0$, $Oh = 0.5$, $De = 5.0$, $\bar{N} = 10^{-5}$, $A_{dif} = 10^{-8}$ and $Pe = 1000.0$ when (a) inertia is included, and when (b) inertia is excluded from the governing equations. It is seen that satellite drop formation, which occurs when inertia is included, leads to additional concentration peaks in corner region $C2$, which results in a larger number of polymer chains escaping the primary drop as compared to the Stokes flow case.

elastic stress and the thread breaks before formation of a long cylindrical microthread. In contrast, for $De = 5.0$, shown in figure 2.8(b), the elastic stresses dominate over capillary force, and a microthread of uniform thickness, with a more spherical satellite drop at the end, is formed. The polymer chains are stretched in this cylindrical microthread, while relaxed in the satellite drop, causing a high stress difference in the region where the satellite drop meets the microthread. Thus, an additional region of large negative stress gradients is present for polymer solutions with high elasticity, resulting in an additional concentration peak where the satellite drop meets the cylindrical microthread that is formed. In conclusion, for large enough De values, viscoelastic thread pinchoff will result in the formation of cylindrical microthreads

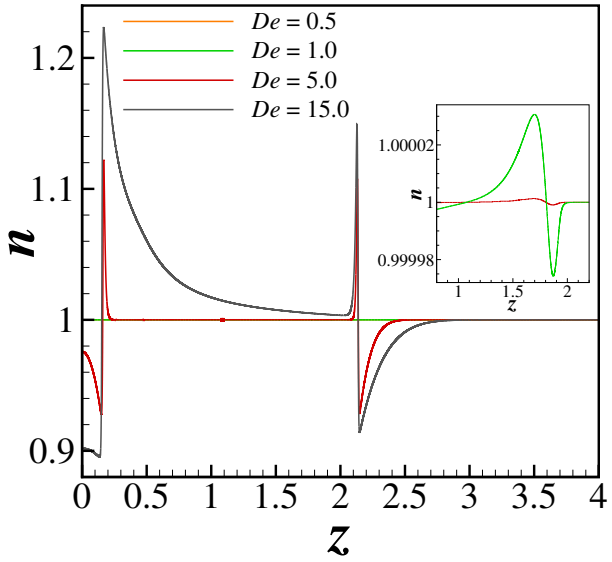

Figure 2.7. Variation of polymer concentration n profiles at the incipience of pinchoff with elasticity of the thread De. The extent of concentration variation changes by four orders of magnitude as De changes from 0.5 (shown in inset) to 5.0. Parameter values are $L = 4.0$, $Oh = 0.5$, $\bar{N} = 10^{-5}$, $A_{dif} = 10^{-8}$, and $Pe = 1000.0$.

with highly concentrated ends, while the primary and satellite drops formed will be dilute.

2.4.4 Effect of Diffusivity

The stress density coupling studied here is based on diffusion of elastic stress, as well as diffusion of the polymer chains themselves [21, 23]. Thus, it is imperative to study the effect of diffusivity on polymer concentration profiles. It is seen in figure 2.9 that an order of magnitude increase in the Peclet number Pe results in an order of magnitude decrease in the maximum concentration. This is expected, as the driving force for polymer migration is stress diffusion, which is inversely proportional to the Peclet number Pe, as seen in equation (2.15).

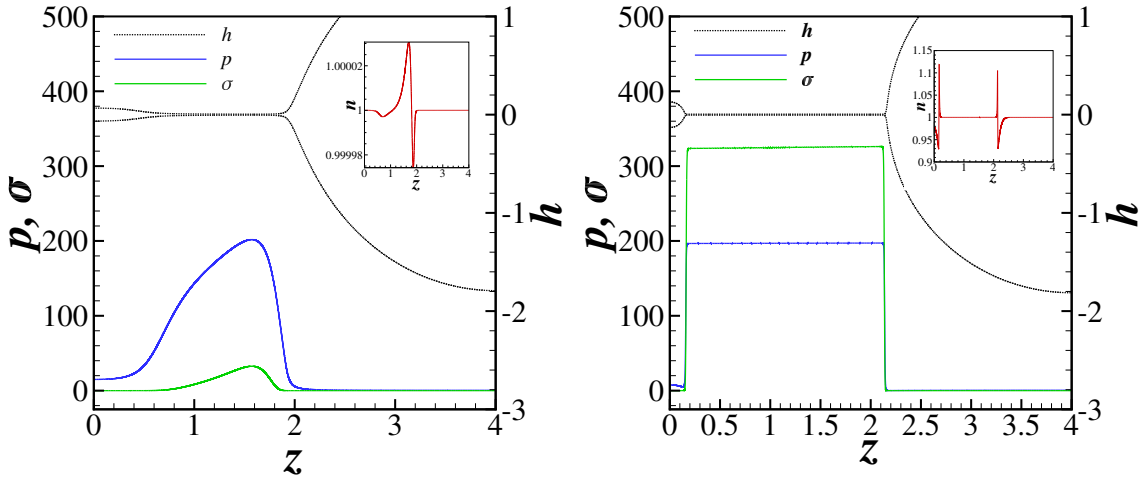

Figure 2.8. Spatial variation of capillary pressure p, axial elastic stress σ and the thread thickness $h(z,t)$ at the incipience of pinchoff for (a) $De = 1.0$ and (b) $De = 5.0$. The capillary pressure is higher than the elastic stress for (a), while the relationship is reversed for (b), which explains the formation of a cylindrical microthread for $De = 5.0$ and an additional concentration peak. Corresponding polymer concentration n profiles are shown in the inset for each figure. Parameter values are same as in figure 2.7.

2.5 Conclusions

In conclusion, we have added stress-density coupling to the system of equations used to study viscoelastic thread pinchoff using a Galerkin finite element method. It is observed that polymer chain concentration increases in the neck while the primary and satellite drop formed are dilute. Furthermore, we showed that inertial effects on polymer concentration profiles are significant, as a greater number of polymer chains are extracted from the primary drop when inertial effects are considered. Local dynamics were observed at the incipience of pinchoff for different Deborah numbers, to understand the change in concentration profiles with increasing elasticity. It was seen that more elasticity results in more concentration of polymer chains in the neck. Finally, we observed that since polymer concentration in the neck is driven primarily

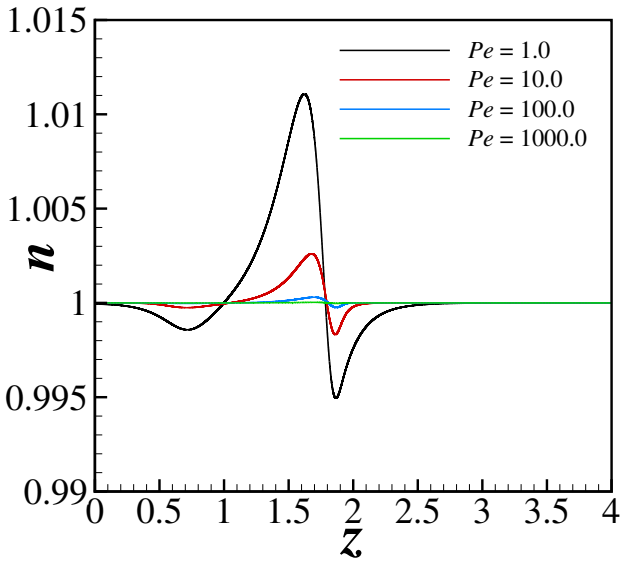

Figure 2.9. Variation of polymer concentration n profiles at the incipience of pinchoff with Peclet number Pe. An order of magnitude increase in Pe results in an order of magnitude decrease in the extent of spatial concentration variation. Parameter values are $L = 4.0$, $Oh = 0.5$, $De = 1.0$, $\bar{N} = 10^{-5}$, and $A_{dif} = 10^{-8}$.

by the existence of elastic stress gradients, migration is favored when the diffusivity of elastic stress is large, or when Pe number values are small.

The study conducted here is in the limit of a vanishingly small value of A_{dif}, the ratio between elastic stress diffusivity and polymer chain diffusivity. Thus, the results of this study consider the effects of nearly Oldroyd-B thread pinchoff on concentration profiles in the thread. However, for larger values of A_{dif}, polymer concentration changes will be more drastic, and significantly affect properties like polymer viscosity and elasticity locally. These local variations in polymer properties will in turn affect the dynamics of pinchoff. The derived set of equations in this chapter are able to capture this effect. However, due to the small gradients in concentration, which is a result of small A_{dif} values considered, the variation in local polymer properties for the scope of our study was negligible. Thus, how large values of A_{dif} affect the dynamics of viscoelastic thread pinchoff is expected to be an important area of future interest.

Appathurai [39] and Anthony [40] have shown that viscoelastic filaments display different dynamics from Newtonian filaments, as elastic stresses delay the mechanism of end-pinching causing filaments to retract into single drops, as opposed to multiple drops formed for Newtonian fluids. The effect of concentration gradients on the dynamics of end-pinching will provide a more realistic picture of the final fate of viscoelastic filaments in the future. Moreover, the eventual shape of filaments can be such that the slender-jet approximation fails, and a three-dimensional axisymmetric formulation of the problem will be required. The solution method described by Thete [41] where Streamline Upwind/Petrov Galerkin method is used for three-dimensional axisymmetric viscoelastic flows will provide an accurate understanding of viscoelastic filament dynamics, especially in the non-slender limit.

2.6 List of References

[1] Osman A Basaran. Small-scale free surface flows with breakup: Drop formation and emerging applications. *AIChE Journal*, 48(9):1842–1848, 2002.

[2] Jens Eggers and Emmanuel Villermaux. Physics of liquid jets. *Reports on Progress in Physics*, 71(3):036601, 2008.

[3] F. Savart. Mémoire sur la constitution des veines liquides lancées par des orifices circulaires en mince paroi. *Annales de chimie et de physique*, 53(337):15–86, 1833.

[4] J. Plateau. I. experimental and theoretical researches on the figures of equilibrium of a liquid mass withdrawn from the action of gravity.third series. *Philosophical Magazine Series 4*, 14(90):1–22, 1857.

[5] Lord Rayleigh. On the instability of jets. *Royal Society of London*, pages 4–12, 1878.

[6] E. F. Goedde and M. C. Yuen. Experiments on liquid jet instability. *J. Fluid Mech.*, 40:495–511, 2 1970.

[7] R. J. Donnelly and W. Glaberson. Experiments on the capillary instability of a liquid jet. *Proceedings of the Royal Society of London. Series A, Mathematical and Physical Sciences*, 290(1423):pp. 547–556, 1966.

[8] Jens Eggers. Universal pinching of 3d axisymmetric free-surface flow. *Phys. Rev. Lett.*, 71:3458–3460, Nov 1993.

[9] J. Eggers and T. F. Dupont. Drop formation in a one-dimensional approximation of the Navier-Stokes equation. *J. Fluid Mech.*, 262:205–221, 1994.

[10] Stanley Middleman. Stability of a viscoelastic jet. *Chem. Eng. Sci.*, 20(12):1037 – 1040, 1965.

[11] Michael Goldin, Joseph Yerushalmi, Robert Pfeffer, and Reuel Shinnar. Breakup of a laminar capillary jet of a viscoelastic fluid. *J. Fluid Mech.*, 38:689–711, 10 1969.

[12] DW Bousfield, Roland Keunings, G Marrucci, and MM Denn. Nonlinear analysis of the surface tension driven breakup of viscoelastic filaments. *J. Non-Newtonian Fluid Mech.*, 21(1):79–97, 1986.

[13] R Byron Bird, Robert C Armstrong, and Ole Hassager. Dynamics of polymeric liquids. vol. 1: Fluid mechanics. 1987.

[14] Michael Renardy. A numerical study of the asymptotic evolution and breakup of newtonian and viscoelastic jets. *J. Non-Newtonian Fluid Mech.*, 59(2-3):267–282, 1995.

[15] Marco A Fontelos and Jie Li. On the evolution and rupture of filaments in giesekus and fene models. *J. Non-Newtonian Fluid Mech.*, 118(1):1–16, 2004.

[16] H. Giesekus. A simple constitutive equation for polymer fluids based on the concept of deformation-dependent tensorial mobility. *J. Non-Newtonian Fluid Mech.*, 11(12):69 – 109, 1982.

[17] Gareth H McKinley. Visco-elasto-capillary thinning and break-up of complex fluids. 2005.

[18] Mónica SN Oliveira, Roger Yeh, and Gareth H McKinley. Iterated stretching, extensional rheology and formation of beads-on-a-string structures in polymer solutions. *J. Non-Newtonian Fluid Mech.*, 137(1-3):137–148, 2006.

[19] R Sattler, Christian Wagner, and Jens Eggers. Blistering pattern and formation of nanofibers in capillary thinning of polymer solutions. *Phys. Rev. Let.*, 100(16):164502, 2008.

[20] R Sattler, S Gier, Jens Eggers, and Christian Wagner. The final stages of capillary break-up of polymer solutions. *Phys. Fluids*, 24(2):023101, 2012.

[21] J Eggers. Instability of a polymeric thread. *Phys. Fluids*, 26(3):033106, 2014.

[22] Sophia Tsouka, Yannis Dimakopoulos, and John Tsamopoulos. Stress-gradient induced migration of polymers in thin films flowing over smoothly corrugated surfaces. *J. Non-Newtonian Fluid Mech.*, 228:79–95, 2016.

[23] Aparna V Bhave, Robert C Armstrong, and Robert A Brown. Kinetic theory and rheology of dilute, nonhomogeneous polymer solutions. *J. Chem. Phys.*, 95(4):2988–3000, 1991.

[24] Hans Christian Öttinger. Incorporation of polymer diffusivity and migration into constitutive equations. *Rheologica acta*, 31(1):14–21, 1992.

[25] Vlasis G Mavrantzas and Antony N Beris. Modeling of the rheology and flow-induced concentration changes in polymer solutions. *Phys. Rev. Let.*, 69(2):273, 1992.

[26] Antony N Beris and Vlasis G Mavrantzas. On the compatibility between various macroscopic formalisms for the concentration and flow of dilute polymer solutions. *J. Rheol.*, 38(5):1235–1250, 1994.

[27] Richard M Jendrejack, David C Schwartz, Juan J De Pablo, and Michael D Graham. Shear-induced migration in flowing polymer solutions: Simulation of long-chain dna in microchannels. *J. Chem. Phys.*, 120(5):2513–2529, 2004.

[28] Michael D Graham. Fluid dynamics of dissolved polymer molecules in confined geometries. *Annu. Rev. Fluid Mech.*, 43:273–298, 2011.

[29] Sophia Tsouka, Yannis Dimakopoulos, Vlasis Mavrantzas, and John Tsamopoulos. Stress-gradient induced migration of polymers in corrugated channels. *J. Rheol.*, 58(4):911–947, 2014.

[30] VG Mavrantzas, A Souvaliotis, and AN Beris. Pseudospectral calculations of stress-induced concentration changes in viscometric flows of polymer solutions. *Theoretical and Computational Fluid Dynamics*, 5(1):3–31, 1993.

[31] Michalis V Apostolakis, Vlasis G Mavrantzas, and Antony N Beris. Stress gradient-induced migration effects in the taylor–couette flow of a dilute polymer solution. *J. Non-Newtonian Fluid Mech.*, 102(2):409–445, 2002.

[32] Lord Rayleigh. Further observations upon liquid jets, in continuation of those recorded in the royal society's' proceedings' for march and may, 1879. *Proceedings of the Royal Society of London*, 34:130–145, 1882.

[33] B. Ambravaneswaran, E. D. Wilkes, and O. A. Basaran. Drop formation from a capillary tube: Comparison of one-dimensional and two-dimensional analyses and occurrence of satellite drops. *Phys. Fluids*, 14(8):2606–2621, 2002.

[34] Eugene Helfand and Glenn H Fredrickson. Large fluctuations in polymer solutions under shear. *Phys. Rev. Let.*, 62(21):2468, 1989.

[35] Christian Clasen, Jens Eggers, Marco A Fontelos, Jie Li, and Gareth H McKinley. The beads-on-string structure of viscoelastic threads. *J. Fluid Mech.*, 556:283–308, 2006.

[36] VM Entov and EJ Hinch. Effect of a spectrum of relaxation times on the capillary thinning of a filament of elastic liquid. *J. Non-Newtonian Fluid Mech.*, 72(1):31–53, 1997.

[37] Pierre-Gilles De Gennes and Pierre-Gilles Gennes. *Scaling concepts in polymer physics*. Cornell university press, 1979.

[38] P. P. Bhat, S. Appathurai, M. T. Harris, M. Pasquali, G. H. McKinley, and O. A. Basaran. Formation of beads-on-a-string structures during break-up of viscoelastic filaments. *Nat. Phys.*, 6(8):625–631, 2010.

[39] Santosh Appathurai. *Breakup and coalescence of liquid drops*. PhD thesis, Purdue University, 2012.

[40] Christopher R. Anthony. *Dynamics of retracting films and filaments near singularities*. PhD thesis, Purdue University, August 2017.

[41] Sumeet Suresh Thete. *Singularities in free surface flows*. PhD thesis, Purdue University, 2016.

3. SELF-SIMILARITY AND SCALING TRANSITIONS DURING THINNING OF SHEETS OF POWER-LAW FLUIDS

3.1 Abstract

Self-similarity and scaling transitions in van der Waals driven thinning and rupture of thin free films, or sheets of power-law fluids are analyzed for $0 < n \leq 1$, where n is the power-law exponent, and $0 \leq Oh \leq \infty$, where $Oh \equiv \mu_0/\sqrt{\rho h_0 \sigma}$ is the Ohnesorge number, and μ_0, ρ, h_0, and σ represent the zero-deformation-rate viscosity, density, initial film thickness, and surface tension of the sheet of power-law fluid. The variation with time remaining until rupture of the film thickness, lateral length scale, and lateral velocity is determined analytically through asymptotic analysis of the spatially one-dimensional partial differential equations for the film thickness and lateral velocity. The expected scaling regimes are then confirmed by numerical simulations of the spatially two-dimensional continuity and Cauchy momentum equations. For sheet rupture in the Stokes limit, and when $0.58 \leq n \leq 1$, it is shown that the dynamics lie in the power-law viscous (PLV) regime, such that van der Waals and viscous forces are in balance while capillary forces are negligible all the way till the sheet ruptures. As self-similarity is of the second kind in this regime, the values of the scaling exponent for the lateral length scale β are determined analytically by computing the similarity solution for thinning in the Stokes limit, and shown to be in excellent agreement with the values obtained from numerical simulations. It is then shown that in contrast to sheets of Newtonian fluids, capillary forces can become significant during thinning of sheets of power-law fluids in the Stokes limit if $n < 0.58$. The dynamics now lie in the so-called power-law capillary viscous (PLCV) regime where the dominant balance of forces is between capillary, viscous and van der Waals forces. Expectedly, when

$Oh \to 0$, or for sheets of inviscid fluids, the dynamics lie in the rheology independent inertial-capillary (IC) regime, as shown by Thete et al. [1] for Newtonian fluids, and the dominant force balance is between inertial, capillary and van der Waals forces. However, for sheets of real power-law fluids with finite Oh, a remarkably richer array of transitions than the corresponding Newtonian fluids [1] is observed. For sheets with $Oh \gg 1$ and $6/7 \leq n \leq 1$, it is shown that a thinning sheet begins in the PLV regime but eventually transitions to the power-law inertial viscous (PLIV) regime [2], where inertial, van der Waals, and capillary forces are in balance. However, for sheets with power-law exponents in the range $0.58 \leq n \leq 6/7$, while initial dynamics again lie in the PLV regime, viscous forces eventually fall out of the dominant force balance, and an eventual transition to the rheology-independent IC regime is observed. Finally, for highly viscous sheets with $0 < n \leq 0.58$, the initial dynamics lie in the PLCV regime instead, as capillary forces enter the force balance, but again eventually transition to the IC regime. For slightly viscous sheets, or when $Oh \ll 1$, the thinning sheet transitions from the IC regime to the PLIV regime when $6/7 \leq n \leq 1$. For all aforementioned transitions, the minimum film thickness at which the transition occurs as a function of Oh and n is estimated analytically, and observed to be in good agreement with our numerical simulations. Finally, for slightly viscous sheets or when $Oh \ll 1$ and $0 < n \leq 6/7$, viscous forces are always negligible and the sheet thins in the IC regime all the way till rupture without any scaling transitions.

3.2 Introduction

Thin fluid films are integral to our daily lives and many industrial applications. Thinning and rupture of free films or sheets, with two free surfaces, plays an important role in foam evolution [3], emulsion stability [4], and applications involving bubbles bursting at interfaces [5]. Similarly, the thinning dynamics of films supported by a solid substrate, with one free surface, are crucial in coating flows [6], tear film substitutes [7] and pattern formation [8].

If the thickness of such films is of or less than the order of a micrometer, long-range intermolecular forces become significant and influence thinning dynamics [9, 10]. For thin sheets, van der Waals attraction between the two free surfaces can cause spontaneous thinning and eventual rupture of the film despite the presence of stabilizing capillary pressure. This was observed experimentally by Debrégas, De Gennes, and Brochard-Wyart [11] while studying the bursting of bubbles at air-liquid interfaces. The sheet that formed between the bubble and the interface was seen to spontaneously rupture below a thickness of 70 nm due to van der Waals attraction. Similarly, for thin films on a substrate, van der Waals attraction between the liquid-gas interface and solid substrate can lead to spontaneous thinning and the subsequent formation of dry spots [12–14]. When these intermolecular forces are significant, they are accounted for by the addition of a disjoining pressure term to the set of governing equations [15].

Consider a fluid sheet of uniform thickness $2h_0$ surrounded by a passive gas such as air. The midplane of the sheet lies in the $\tilde{x} - \tilde{z}$ plane of a rectangular coordinate system and the $\tilde{y}$ axis is perpendicular to the midplane. Pressure variations due to gravity are negligible due to the thinness of the sheet. Next consider that the two surfaces of the sheet are perturbed such that the shape of the free surface above the $\tilde{x} - \tilde{z}$ plane is described by the equation

$$\tilde{h}(\tilde{z}) = h_0 \left[1 - \epsilon \cos\left(\frac{2\pi \tilde{z}}{\tilde{\lambda}} \right) \right] \tag{3.1}$$

with the shape of the free surface below given by the negative of equation (3.1). Here, $\epsilon \ll 1$ is the amplitude and $\tilde{\lambda}$ is the wavelength of the perturbation. Is is well known that the initial stages of thinning are governed by the competing influences of destabilizing van der Waals attraction and stabilizing capillary pressure [1]. Ruckenstein and Jain [16] performed a linear stability analysis for sheets and determined that wavelengths exceeding a critical value $\tilde{\lambda}_c$ are always unstable, where the critical value is given by

$$\tilde{\lambda}_c = \frac{8\pi^{3/2}\sigma^{1/2}{h_0}^2}{A_H^{1/2}} = 8\pi^{3/2}\frac{h_0}{d}h_0 \tag{3.2}$$

Here, σ is the surface tension, A_H is the Hamaker constant and $d \equiv (A_H/2\pi\sigma)^{1/2}$ is the molecular length scale for the particular liquid-gas system. Typically, $h_0 \gg d$, which implies that the critical wavelength for spontaneous rupture is much larger than the initial film thickness $\left(\tilde{\lambda}_c \gg h_0\right)$. Thus, thin free films or sheets are unstable to long-wavelength perturbations.

Erneux and Davis [17] made use of the long-wavelength nature of the problem and solved a set of one-dimensional (1D) partial differential equations (PDEs) for the film thickness and lateral velocity as a function of lateral space coordinate $\tilde{z}$ and time $\tilde{t}$ for Newtonian sheet rupture. They determined that non-linear effects led to acceleration of thinning and resulted in rupture times well below those predicted by linear theory. Film rupture dynamics are self-similar in the vicinity of the space-time singularity when film thickness $\tilde{h} = 0$, at the lateral location $\tilde{z} = \tilde{z}_R$, and at time $\tilde{t} = \tilde{t}_R$, and thus independent of initial and boundary conditions imposed on the film [18]. Ida and Miksis [19] explored the self-similar dynamics of thinning of a viscous Newtonian sheet, and determined that the dominant force balance is between viscous and van der Waals forces, while inertial and capillary forces are subdominant. Later, Vaynblat, Lister, and Witelski [20] solved numerically the set of 1D PDEs for both line or sheet rupture, and point or axisymmetric rupture, for Newtonian films with comparable viscosity and inertia, such that the Ohnesorge number $Oh = \mu_0/\sqrt{\rho h_0 \sigma} \sim O(1)$, where ρ is the density of the fluid, μ_0 is the viscosity, and Oh is a dimensionless group that denotes the ratio of viscous forces to the square root of the product of inertial and capillary forces. They determined analytically that the film thickness $\tilde{h}$, lateral length scale $\tilde{z}' \equiv \tilde{z} - \tilde{z}_R$, and lateral velocity $\tilde{v}$, vary with time remaining until rupture $\tilde{\tau} \equiv \tilde{t}_R - \tilde{t}$ as

$$\tilde{h} \sim \tilde{\tau}^{1/3}, \tilde{z}' \sim \tilde{\tau}^{1/2}, \tilde{v} \sim \tilde{\tau}^{-1/2} \tag{3.3}$$

respectively, where 1/3, 1/2 and $-1/2$ are referred to as the scaling exponents for this scaling regime, hereafter referred to as the inertial-viscous regime (IV regime). The dominant force balance in this regime is between inertial, viscous and van der Waals forces, while capillary forces are negligible. Vaynblat, Lister, and Witelski [20] also solved analytically the set of 1D ordinary differential equations (ODEs) obtained from the PDEs by means of a similarity transformation, and determined similarity solutions for the film thickness $\tilde{h}$ and lateral velocity $\tilde{v}$. They then demonstrated excellent agreement between self-similar solutions determined from the PDEs and analytical solutions of the aforementioned ODEs. More recently, Thete et. al [1] considered the dynamics of Newtonian sheets when the fluid had either infinitesimal inertia ($Oh^{-1} = 0$) or infinitesimal viscosity ($Oh = 0$). The authors demonstrated that in the limit of $Oh^{-1} = 0$, such that the sheet is undergoing Stokes flow, the dynamics lie in the viscous regime where the dominant force balance is between viscous and van der Waals forces, and capillary forces are always negligible. This leads to self-similarity of the second kind [18] and the scaling exponents are given by

$$\tilde{h} \sim \tilde{\tau}^{1/3}, \tilde{z}' \sim \tilde{\tau}^{0.26}, \tilde{v} \sim \tilde{\tau}^{-0.74} \tag{3.4}$$

In contrast, for inviscid sheets or when $Oh = 0$, the authors demonstrated that the dominant force balance is between inertial, van der Waals and capillary forces and the scaling exponents for this inertial-capillary (IC) regime are given by

$$\tilde{h} \sim \tilde{\tau}^{2/7}, \tilde{z}' \sim \tilde{\tau}^{4/7}, \tilde{v} \sim \tilde{\tau}^{-3/7} \tag{3.5}$$

Thete et al. [1] also obtained similarity solutions for both cases by analytically solving the ODEs in similarity space, and demonstrated excellent agreement with the similarity solutions obtained through numerical simulations of the PDEs. The authors then demonstrated that for real fluids with finite values of Oh, the dynamics initially lie in the inertial and viscous regimes for slightly viscous and highly viscous

sheets respectively, but will eventually transition to the IV regime shown by Vaynblat, Lister, and Witelski [20]. They determined analytically the film thickness at which these transitions from the initial regimes to a late-stage IV regime would occur and demonstrated good agreement with results from numerical simulations.

While the studies discussed above have focused on free film flows of Newtonian fluids, many industrial and everyday fluids exhibit complex rheology, due to dissolved polymers, particles, or other immiscible liquids. A common model utilized to describe the behavior of non-Newtonian fluids subject to deformation is the so called power-law fluid, which derives its name from the power-law dependence [21] of the viscosity $\tilde{\mu}$ on the deformation rate $\tilde{\dot{\gamma}}$ given by

$$\tilde{\mu}\left(\tilde{\dot{\gamma}}\right) = \mu_0 \left|2\tilde{m}\tilde{\dot{\gamma}}\right|^{n-1} \tag{3.6}$$

Here, μ_0 is the zero-deformation-rate viscosity, $\tilde{m}^{-1}$ the characteristic deformation rate, $0 < n \leq 1$ the power-law exponent ($n = 1$ corresponds to a Newtonian fluid) of the given fluid, and $\tilde{\dot{\gamma}}$ is the second invariant of the rate-of-deformation tensor $\tilde{\mathbf{D}}$

$$\tilde{\dot{\gamma}} = \left[\frac{1}{2}\left(\tilde{\mathbf{D}} : \tilde{\mathbf{D}}\right)\right]^{\frac{1}{2}} \tag{3.7a}$$

$$\tilde{\mathbf{D}} = \frac{1}{2}\left[\left(\tilde{\nabla}\tilde{\mathbf{v}}\right) + \left(\tilde{\nabla}\tilde{\mathbf{v}}\right)^{T}\right] \tag{3.7b}$$

where $\tilde{\mathbf{v}}$ is the fluid velocity. Experimental studies have shown that many common fluids exhibit power-law rheology [22–25]. A common example of thin film flow involving power-law fluid behavior is the tear film in our eye, which has large viscosity under low shear and forms a protective layer on the eye surface, but flows easily as its viscosity falls when subjected to high shear as we blink our eyes [7]. Common tear substitutes in the market involve deformation-rate-thinning fluids [26].

While the self-similar dynamics of thread pinchoff of power-law fluids have been studied extensively using analytical [27, 28], numerical [28–30] and experimental [23, 24] methods, the field of thin film rupture of power-law fluids was relatively unexplored until recently. Thete et al. [2] examined the rupture of sheets of power-law

fluids with $Oh \sim O(1)$ and demonstrated that for fluids with $6/7 \leq n \leq 1$, the dominant force balance is between inertial, van der Waals and viscous forces and the scaling exponents for this rheology dependent power-law inertial viscous (PLIV) regime are given by

$$\tilde{h} \sim \tilde{\tau}^{n/3}, \tilde{z}' \sim \tilde{\tau}^{1-n/2}, \tilde{v} \sim \tilde{\tau}^{-n/2} \tag{3.8}$$

However, when $0 < n \leq 6/7$, the authors demonstrated that viscous forces fall out of the dominant force balance, and the balance is now between inertial, van der Waals and capillary forces, leading to the IC regime from equation (3.5). In other words, for $0 < n \leq 6/7$ the fluid behaves as if it is inviscid as its viscosity drops rapidly on account of the low value of n, and the thinning dynamics are rheology independent. More recently, Garg et al. [31] demonstrated that a transition from a viscous to inertial regime occurs for thin films of power-law fluids on a substrate, and determined the critical parameter values at which this transition is seen. In their recent paper, Thete et al. [1] mentioned the need for a comprehensive study of the thinning of sheets of power-law fluids, to obtain a thorough understanding of the thinning dynamics and transitions that occur between different scaling regimes in the parameter space comprised of both the Ohnesorge number Oh and power-law exponent n, similar to already existing studies for pinchoff of threads of power-law fluids [30]. This is the main goal of this paper.

This paper is organized as follows. Section 3.3 describes in detail the problem under investigation and equations and boundary conditions governing the thinning of sheets. Furthermore, it describes succinctly the numerical methods utilized to solve the two-dimensional (2D) set of PDEs, and the set of 1D PDEs utilized for analytical investigation of self-similar dynamics. Section 3.4 analyses theoretically and computationally the thinning and rupture of sheets of power-law fluids when inertia is negligible, i.e. when the film is undergoing Stokes flow or $Oh^{-1} = 0$. Section 3.5 briefly explains why thinning dynamics in the inviscid limit, or when $Oh = 0$, will be identical for Newtonian and power-law sheets. Section 3.6 analyses thinning and rupture for sheets of real fluids where Oh is finite for the entire range of power-law

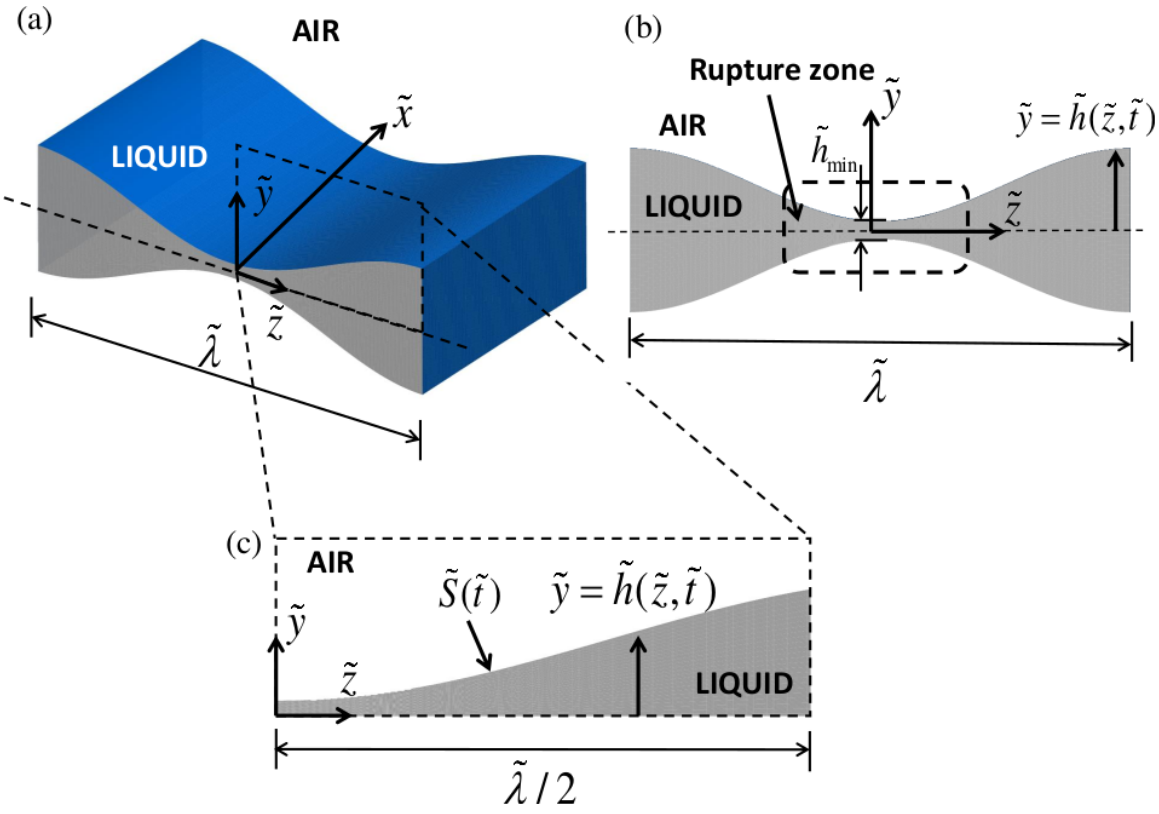

Figure 3.1. Line rupture of a free film. (a) Perspective view of a free film surrounded by air corresponding to one wavelength $\tilde{\lambda}$ of the imposed perturbation. (b) A cross-sectional view of the film and location of the "rupture zone", where dynamics are expected to be self-similar as the film approaches the space-time singularity. (c) The computational domain taken on account of symmetry.

exponent values $0 < n \leq 1$. In contrast to Newtonian films [1], a remarkably richer array of transitions is observed for power-law fluids, and corresponding transitions for highly viscous and slightly viscous sheets are explored in detail. Section 3.7 concludes the paper by summarizing the key results and outlines future avenues available for free film rupture using a similar approach to the one carried out in this paper.

3.3 Mathematical Formulation

The system is an isothermal free film or sheet of uniform thickness h_0 of an incompressible power-law fluid of constant density ρ and zero-deformation-rate viscosity of μ_0. The film is surrounded by a dynamically passive gas such as air, that exerts a constant pressure, set equal to zero w.l.o.g, and negligible viscous drag on the film. The Hamaker constant A_H for the fluid-gas system and surface tension of the interface σ are constant and spatially uniform. A rectangular coordinate system is chosen such that the origin is located halfway along the film's lateral length on its midplane, where $\tilde{x}$, $\tilde{y}$, and $\tilde{z}$ represent the translational, vertical and lateral coordinates respectively. The midplane of the film then coincides with the $\tilde{x} - \tilde{z}$ plane. A sinusoidal perturbation such that the film thickness $\tilde{h}$ is described by equation (3.1) is applied to the film surface at time $\tilde{t} = 0$, as shown in figure 3.1(a). As this perturbation is periodic in the lateral direction $\tilde{z}$, about the midplane $\tilde{y} = 0$, and translationally symmetric, it is sufficient to consider the spatial two-dimensional domain spanning half a wavelength of the perturbations ($0 \leq \tilde{z} \leq \tilde{\lambda}/2$), i.e. the domain is the region bounded above by the surface $\tilde{S}(\tilde{t})$ which is unknown a priori, bounded below by the midplane of the film located at ($0 \leq \tilde{z} \leq \tilde{\lambda}/2$, $\tilde{y} = 0$) and bounded on the sides by the symmetry planes located at $\tilde{z} = 0$ and $\tilde{z} = \tilde{\lambda}/2$ as shown in figure 3.1(c). The effect of gravity is assumed to be negligible on account of the film's thinness. In what follows, the spatially two-dimensional, transient Cauchy momentum and continuity equations that govern thinning and rupture of films of power-law fluids and the numerical methods utilized to solve these equations are described first. The remainder of the section describes the set of spatially one-dimensional transient PDEs (obtained by applying the long-wavelength approximation) that are utilized to analyze the self-similar behavior of sheet rupture analytically.

3.3.1 Two-dimensional governing equations and numerical methods

For numerical simulations, the problem variables are non-dimensionalized by using the undisturbed film thickness as the characteristic length $l_c = h_0$, the visco-capillary time as the characteristic time $t_c = \mu_0 h_0/\sigma$, the ratio of these two scales as the characteristic velocity $v_c = l_c/t_c$, zero-deformation-rate viscosity as the characteristic viscosity $\mu_c = \mu_0$, and the capillary pressure as the characteristic pressure $p_c = \sigma/h_0$. As a result of choosing these characteristic scales, the dynamics are governed by three dimensionless groups, the Ohnesorge number $Oh = \mu_0/(\rho\sigma h_0)^{1/2}$, which represents the ratio of the viscous force to square root of the product of the inertial and capillary force, the van der Waals number $A = A_H/48\pi\sigma {h_0}^2$, which represents the ratio of intermolecular forces to capillary forces, and the characteristic deformation rate $m^{-1} = t_c\tilde{m}^{-1}$. For the remainder of this paper, variables without a tilde ($\sim$) represent the dimensionless values of the corresponding variables with a tilde.

The dynamics of the fluid in the sheet are governed by the continuity and Cauchy momentum equations, which are given in dimensionless form by

$$\nabla \cdot \mathbf{v} = 0 \tag{3.9a}$$

$$\frac{1}{Oh^2}\left(\frac{\partial \mathbf{v}}{\partial t} + \mathbf{v}\cdot\nabla\mathbf{v}\right) = \nabla\cdot\mathbf{T} \tag{3.9b}$$

where $\mathbf{v} \equiv \tilde{\mathbf{v}}/v_c = v_y\mathbf{e_y} + v_z\mathbf{e_z}$ is the dimensionless fluid velocity, $t \equiv \tilde{t}/t_c$ is the dimensionless time, and $\mathbf{T} = -p\mathbf{I} + \mu\left(\nabla\mathbf{v} + (\nabla\mathbf{v})^T\right)$ is the dimensionless stress tensor, where $p = \tilde{p}/p_c$ is the dimensionless pressure, $\mu = |2m\dot{\gamma}|^{n-1}$ is the dimensionless viscosity, and $\nabla \equiv h_0\tilde{\nabla}$ is the dimensionless gradient operator.

The kinematic and traction boundary conditions are applied at the fluid-gas interface $S(t)$ to enforce mass conservation and to account for the discontinuity or jump in stress due to surface tension and van der Waals forces

$$\mathbf{n}\cdot(\mathbf{v} - \mathbf{v}_s) = 0 \tag{3.10a}$$

$$\mathbf{n}\cdot\mathbf{T} = 2H\mathbf{n} - \left(A/h^3\right)\mathbf{n} \tag{3.10b}$$

where $\mathbf{v}_s$ is the velocity of points on the interface $S(t)$, $\mathbf{n}$ is the unit normal vector to and $2H$ is twice the mean curvature of $S(t)$. Symmetry boundary conditions are applied at the two symmetry planes at $z = 0$ and $z = \lambda/2$, such that the lateral velocity and tangential stress are equal to zero. Finally, along the midplane at $y = 0$, the vertical velocity and tangential stress are zero on account of symmetry. The film is initially quiescent and the wavelength of the perturbation λ imposed on its surfaces is taken to be larger than the dimensionless critical wavelength given by $\lambda_c = 8\pi^{3/2}h_0/d$ such that the film is spontaneously unstable. As $h_0 \gg d$, the maximum lateral extent of the mesh is $3 - 5$ orders of magnitude larger than its vertical extent, and an accurate resolution of the highly disparate length scales is crucial.

The two-dimensional free surface flow described by the PDEs (3.9) subject to the aforementioned boundary and initial conditions is solved using a fully implicit, method of lines, arbitrary Lagrangian-Eulerian algorithm. The Galerkin/finite element method (G/FEM) is used for spatial discretization [32] with a finite difference implicit adaptive Adams Bashforth scheme for time integration [33]. The PDEs are converted to ODEs by G/FEM spatial discretization, while time integration reduces the system of ODEs to a system of nonlinear algebraic equations. These are solved using Newton's method with an analytically computed Jacobian. In order to capture the large deformation that the film's surface undergoes as well accurately resolve the highly disparate length scales, the elliptic mesh generation method [34, 35] is used to determine the vertical and lateral coordinates of each grid point in the moving, adaptive mesh simultaneously with the velocity and pressure unknowns in the fluid. Variants of this algorithm have been employed by our research group to successfully study hydrodynamic singularities that arise in thread pinchoff of both Newtonian and non-Newtonian fluids [30, 35–38], drop and bubble coalescence [39–41], and supported thin film rupture [31]. The reader is thus referred to these works for a complete description of the solution method and numerical implementation.

3.3.2 One-dimensional equations for asymptotic analysis

To study sheet dynamics analytically, the long-wavelength approximation [21, 42] can be invoked to reduce the system of 2D PDEs (3.9) to a set of 1D PDEs for the film thickness and lateral velocity. These PDEs have been derived by Thete et al. [2] for power-law fluids. The dimensionless form of the 1D PDEs for highly viscous sheets is given by

$$\frac{\partial h}{\partial t} + \frac{\partial \left(hv\right)}{\partial z} = 0 \tag{3.11a}$$

$$\frac{1}{Oh^2}\underbrace{\left(\frac{\partial v}{\partial t} + v\frac{\partial v}{\partial z}\right)}_{\text{Inertial (I)}} = \underbrace{\frac{\partial^3 h}{\partial z^3}}_{\text{Capillary (C)}} - \underbrace{\frac{\partial \left(h^{-3}\right)}{\partial z}}_{\text{van der Waals (vdW)}} + \underbrace{\frac{4}{h}\frac{\partial}{\partial z}\left(\mu_V h\frac{\partial v}{\partial z}\right)}_{\text{Viscous (V)}} \tag{3.11b}$$

where $z = \tilde{z}/l_z$ is the dimensionless lateral length, $t = \tilde{t}/t_V$ is the dimensionless time, $h\left(z,t\right)$ denotes the dimensionless film thickness, $v\left(z,t\right)$ denotes the dimensionless fluid velocity in the lateral or z direction and $\mu_V = \left|2m_1\partial v/\partial z\right|^{n-1}$. These equations were non-dimensionalized using $l_c = h_0$ as the characteristic length in the vertical direction, $l_z = \left(48\pi {h_0}^4\sigma/A_H\right)^{1/2}$ as the characteristic length in the lateral direction, $t_V = 48\pi {h_0}^3\mu_0/A_H$ as the characteristic time, and $v_V = l_z/t_V$ as the characteristic velocity. It follows from the non-dimensionalization described for the 2D PDEs described in section 3.3.1 that the characteristic times and characteristic deformation rates for the two non-dimensionalization schemes obey the following relation

$$t_V = t_c/A, \quad m_1 = mA \tag{3.12}$$

The forces that influence van der Waals driven rupture of sheets, namely inertial (I), capillary (C), van der Waals (vdW) and viscous (V) forces, are shown by symbols under the corresponding terms in equation (3.11b). Alternatively, for slightly viscous sheets the dimensionless form of the 1D PDEs is given by

$$\frac{\partial h}{\partial t} + \frac{\partial (hv)}{\partial z} = 0 \tag{3.13a}$$

$$\underbrace{\left(\frac{\partial v}{\partial t} + v\frac{\partial v}{\partial z}\right)}_{\text{Inertial (I)}} = \underbrace{\frac{\partial^3 h}{\partial z^3}}_{\text{Capillary (C)}} - \underbrace{\frac{\partial (h^{-3})}{\partial z}}_{\text{van der Waals (vdW)}} + \underbrace{\frac{4Oh}{h}\frac{\partial}{\partial z}\left(\mu_I h \frac{\partial v}{\partial z}\right)}_{\text{Viscous (V)}} \tag{3.13b}$$

where $z = \tilde{z}/l_z$ is the dimensionless lateral length, $t = \tilde{t}/t_I$ is the dimensionless time, $h(z,t)$ denotes the dimensionless film thickness, $v(z,t)$ denotes the dimensionless fluid velocity in the lateral or z direction and $\mu_I = |2m_2 \partial v/\partial z|^{n-1}$. These equations were non-dimensionalized using $l_c = h_0$ as the characteristic length in the vertical direction, $l_z = \left(48\pi {h_0}^4 \sigma/A_H\right)^{1/2}$ as the characteristic length in the lateral direction, $t_I = \left(\rho l_z^4/\sigma h_0\right)^{1/2}$ as the characteristic time, and $v_I = l_z/t_I$ as the characteristic velocity. For this case, the relation between characteristic times and deformation rates for the non-dimensionalization described in section 3.3.1 is given by

$$t_I = \frac{t_c}{OhA}, \quad m_2 = mOhA \tag{3.14}$$

3.4 Thinning dynamics in the Stokes limit

In this section, sheet rupture of power-law fluids is analyzed in the limit $Oh^{-1} = 0$, such that the sheet fluid has negligible inertia and is undergoing purely viscous or Stokes flow. The governing equations for this system are obtained by setting $1/Oh^2 = 0$ in equation (3.9b) and equation (3.11b). The 2D PDEs reduce to

$$\nabla \cdot \mathbf{v} = 0 \tag{3.15a}$$

$$\nabla \cdot \left[-p\mathbf{I} + \mu\left(\nabla \mathbf{v} + (\nabla \mathbf{v})^T\right)\right] = 0 \tag{3.15b}$$

while the 1D PDEs reduce to

$$\frac{\partial h}{\partial t} + \frac{\partial (hv)}{\partial z} = 0 \tag{3.16a}$$

$$\frac{\partial^3 h}{\partial z^3} - \frac{\partial (h^{-3})}{\partial z} + \frac{4}{h}\frac{\partial}{\partial z}\left(\mu_V h \frac{\partial v}{\partial z}\right) = 0 \tag{3.16b}$$

The film thickness and velocity profiles are expected to be self-similar in the vicinity of the lateral location where the film thickness is minimum as the singularity (z_R, t_R) is approached. The film thickness and lateral velocity in this so-called "rupture zone" as shown in figure 3.1(b), can be described by the similarity ansatz

$$h(z', \tau) \equiv \tau_v^{\alpha} H(\xi), \quad v(z', \tau) \equiv \tau_v^{\gamma} V(\xi), \quad \xi \equiv z'/\tau_v^{\beta} \tag{3.17}$$

where τ_v is the time remaining until rupture $\tau_v \equiv t_R - t$, ξ is the similarity variable, $z' \equiv z - z_R$ is the lateral extent of the rupture zone, α, β and γ are the scaling exponents for h, z' and v respectively, and $H(\xi)$ and $V(\xi)$ are the scaling functions for the film thickness profile and lateral velocity in similarity space. It should be noted that $\tau_v = A\tau$ where τ is time remaining to rupture according to the non-dimensionalization specified in the mathematical formulation presented for the 2D PDEs in section 3.3.1 and equation (3.12). Two different scaling regimes are possible for Stokes flow, depending on which forces are dominant as the sheet thins and approaches the singularity. It is clear that the dominant force balance will always include the van der Waals and viscous terms, as van der Waals forces are the driving forces for sheet rupture, while viscous stress will always be present for sheets undergoing Stokes flow. However, it is unknown a priori if the dominant force balance is between only these two forces, as observed by Thete et al. [1] for Newtonian fluids, or between all three forces present in the system. Substitution of equation (3.17) into equations (3.16a) and (3.16b) followed by a kinematic and dynamic balance yields the following relations for the scaling exponents

$$\alpha = n/3, \quad \gamma = \beta - 1 \tag{3.18}$$

The value of β can be determined through dimensional analysis alone if the self-similarity is of the first kind [18, 43], which occurs when all three forces in the system balance each other. However, if van der Waals forces are solely in balance with viscous forces, it leads to self-similarity of the second kind [18], where the value of β must be determined as part of the solution. In what follows in this section, it is first assumed

that the force balance for films of power-law fluids with values of power-law exponent n close to the Newtonian limit of $n = 1$ is solely between van der Waals and viscous forces, giving rise to the so-called "power-law viscous (PLV) regime".

3.4.1 Dynamics in the power-law viscous (PLV) regime

If the dominant force balance is solely between the driving van der Waals forces and viscous forces, the self-similarity is of the second kind [18], and the forces in the system vary with τ_v as

$$V \sim vdW \sim \tau_v^{-\beta-n}, \quad C \sim \tau_v^{n/3-3\beta} \tag{3.19}$$

It is clear from equation (3.19) that in this regime, capillary forces are negligible and will not feature in the dominant force balance if the condition $\beta < 2n/3$ is satisfied. The value of β is unknown and must be determined as part of the solution.

To examine the validity of our assumption that the proposed force balance in equation (3.19) and the resulting scaling regime holds true when n is close to the Newtonian limit, equations (3.15a) − (3.15b) are solved numerically subject to the boundary conditions and initial conditions as outlined in section 3.3 for $\lambda = 2\lambda_c$ so that the film is spontaneously unstable. Figure 3.2 shows the variation with time remaining until rupture τ for several quantities of interest for a sheet of power-law fluid undergoing Stokes flow such that $A = 9.21 \times 10^{-8}$, $m = 1/A$, and $n = 0.9$. The minimum film thickness h_{min}, or the minimum value of the axial coordinate of the fluid-gas interface $S(t)$, is observed to be always located at $z = 0$, for this case, and all following cases considered in this paper, such that the sheet ruptures symmetrically at $z_R = 0$, and $z' = z$. Figure 3.2(a) shows that h_{min} decreases with τ as $h_{min} = 0.0076\tau^{0.3} = 0.0076\tau^{0.9/3}$, which is in excellent agreement with the expected scaling exponent for the film thickness $h \sim \tau^{n/3}$ derived in equation (3.18). The scaling exponent for the lateral length scale z' is computed by tracking the location of the lateral location on the film interface $S(t)$ such that the film thickness h is some multiple of the minimum film thickness, which was taken to be $1.05h_{min}$ here. Figure

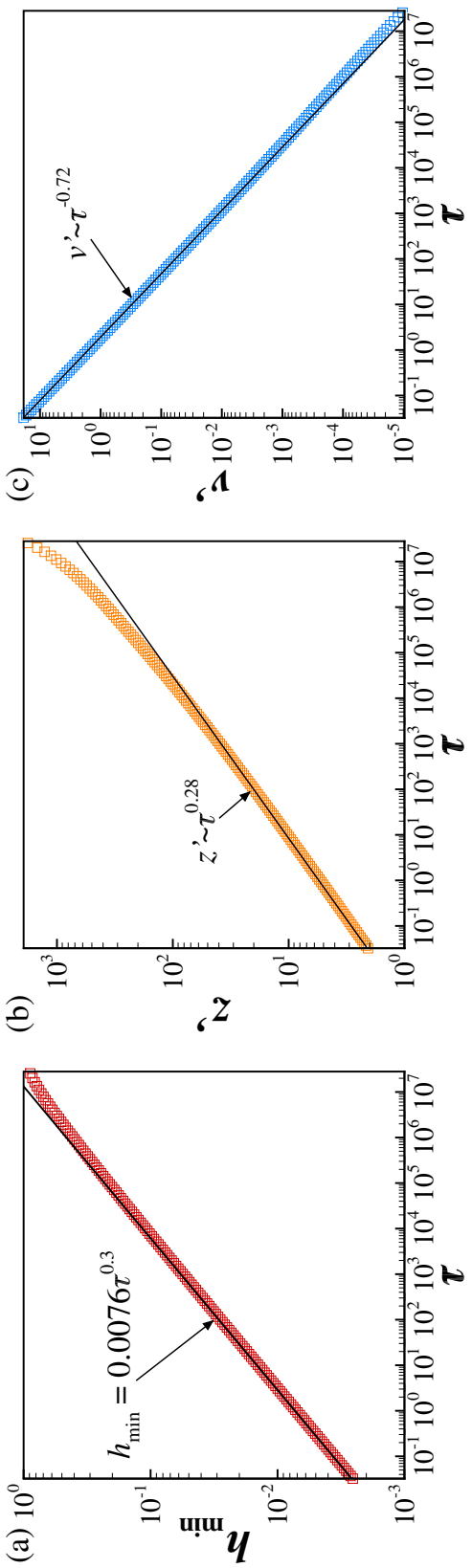

Figure 3.2. Scaling behavior of variables in the rupture zone during thinning of a sheet undergoing Stokes flow such that $A = 9.21 \times 10^{-8}$, $m = 1/A$, and $n = 0.9$. The variation with time to rupture τ for (a) minimum film thickness h_{min}, (b) lateral length scale z', evaluated at a lateral location where the film thickness is given by $h = 1.05 h_{min}$ and (c) lateral velocity v' evaluated at the same lateral location as that for z'. Simulation results are shown by the data points while the straight lines represent best fit to the data.

3.2(b) shows that the lateral length scale varies with time to rupture as $z' \sim \tau^{0.28}$, thus providing numerically the value of $\beta = 0.28$ for $n = 0.9$. Changing the value of this lateral location, e.g. from $1.05h_{min}$ to $1.1h_{min}$, had no effect whatsoever on the value of β determined from the simulation results and for the remainder of this paper, the lateral length scale and lateral velocity are always computed at the lateral location such that $h = 1.05h_{min}$. Figure 3.2(c) shows the variation with time until rupture of the lateral velocity v', which is also computed at the lateral location where $h = 1.05h_{min}$. The lateral velocity is seen to diverge as $v' \sim \tau^{-0.72}$, which is in excellent agreement with the expected scaling behavior of $v' \sim \tau^{\beta-1} \sim \tau^{0.28-1}$, and provides further support to the numerically obtained value of $\beta = 0.28$ for a fluid with a power-law exponent value of $n = 0.9$. The value of β obtained here is such that $\beta < 2n/3 = 0.6$, hence it is clear that the assumptions of the PLV regime are not violated, and capillary forces indeed fall out of the force balance.

The ODEs in similarity space governing the scaling functions $H(\xi)$ and $V(\xi)$ are obtained by substitution of the similarity ansatz (3.17) into the 1D PDEs (3.16a) - (3.16b), followed by neglecting capillary forces

$$-\frac{n}{3}H + \beta\xi\frac{dH}{d\xi} + \frac{d\,(HV)}{d\xi} = 0 \tag{3.20a}$$

$$\frac{3}{H^4}\frac{dH}{d\xi} + \frac{4}{H}\frac{d}{d\xi}\left[\left|2m_1\frac{dV}{d\xi}\right|^{n-1} H\frac{dV}{d\xi}\right] = 0 \tag{3.20b}$$

These ODEs are solved in the similarity space, in order to determine independently a value of β for a fluid with given n, a value of the pre-factor for the expression for h_{min}, and compare similarity solutions obtained from solutions of the PDEs with those obtained by solving these ODEs over the domain $-\infty < \xi < \infty$. The solution algorithm outlined below was first specified by Thete [44]. The kinematic boundary condition (3.20a) can be rearranged to give

$$\frac{H_\xi}{H} = \frac{n/3 - V_\xi}{V + \beta\xi} \tag{3.21}$$

where $(..)_\xi = d(..)/d\xi$. The denominator of the kinematic boundary condition vanishes when $V(\xi) = -\beta\xi$ at $\xi = \xi_0$. Thus, smooth solutions will only exist if the following regularity condition is satisfied

$$V_\xi(\xi_0) = \frac{n}{3}, \quad V(\xi_0) = -\beta\xi_0 \tag{3.22}$$

The far-field behavior of the scaling functions H and V can be determined by assuming that $H = P\xi^a$ and $V = Q\xi^b$ as $|\xi| \to \infty$, where P and Q are non-zero constants. In this limit, the h and v profiles evolve over significantly longer time-scales. Given this requirement, the exponents a and b can be determined from equation (3.17) and the far-field boundary conditions in similarity space are then given by

$$H \sim |\xi|^{n/3\beta}, \quad V \sim |\xi|^{1-1/\beta} \quad as \quad |\xi| \to \infty \tag{3.23}$$

In the limit of $n = 1$, these boundary conditions reduce to those derived by Thete et al. [1] for Newtonian sheets. Furthermore, the momentum equation (3.20b) can be integrated once to yield

$$\frac{8}{3}\left|2m_1\frac{dV}{d\xi}\right|^{n-1} H\frac{dV}{d\xi} - \frac{1}{H^2} = k_1 \tag{3.24}$$

where k_1 is a constant that is determined by substituting the regularity condition in equation (3.22) into equation (3.24), such that

$$k_1 = \frac{8}{9}n\theta H_0 - \frac{1}{H_0^2} \tag{3.25}$$

where $\theta = (2m_1 n/3)^{n-1}$. Following previous works [28, 45, 46] on self-similarity of second kind, it is helpful to consider expansions for H and V in a Taylor series about $\xi = \xi_0$ given by

$$H\left(\xi - \xi_0\right) = \sum_{k=0}^{\infty} H_k \left(\xi - \xi_0\right)^k \tag{3.26a}$$

$$V\left(\xi - \xi_0\right) = \sum_{k=0}^{\infty} V_k \left(\xi - \xi_0\right)^k \tag{3.26b}$$

These series expansions are substituted into equations (3.20a) and (3.24), and terms of order $(\xi - \xi_0)^{k-1}$ and $(\xi - \xi_0)^k$ are collected to obtain recurrence relations between series coefficients for H and V

$$[(k+1)H_0]\, V_{k+1} + \left[k\left(\frac{n}{3} + \beta\right)\right] H_k = Q_{k+1} \tag{3.27a}$$

$$\left[4\theta n k(k+1)H_0^4\right] V_{k+1} + \left[3 + \frac{4\theta n}{3} H_0^3\right] k H_k = R_k \tag{3.27b}$$

where Q_{k+1} and R_k are functions of β, H_{k-1}, V_k, and other lower order coefficients, given by

$$Q_{k+1} = \begin{cases} 0, & \text{for} \quad k = 1 \\ -(k+1)\sum_{i=2}^{k} V_i H_{k-i+1}, & \text{for} \quad k \geq 2 \end{cases}$$

$$R_{k+1} = \begin{cases} 0, & \text{for} \quad k = 1 \\ R_k\left(H_i^a H_j^b, \beta\right), & \text{for} \quad k \geq 2 \end{cases}$$

such that $ai + bj = k, i, j \neq 0$ and $i, j \leq k$.

It can be seen that $H = H_0$ and $V = -\beta\xi_0 + n\left(\xi - \xi_0\right)/3$ are exact solutions of the ODEs (3.20a) and (3.20b). Therefore, all higher order terms involving H_k, V_{k+1}, for $k \geq 1$, in the recurrence relations shown above will be zero. For non-trivial solutions of the ODEs to exist, the higher order coefficients must exist, or the determinant of the coefficient matrix that can be obtained from equations (3.27a) and (3.27b) should be zero for some $k = j$. Thus, the following expression for H_0 is obtained

$$H_0 = \left(\frac{9}{n\theta(4nj + 12\beta j - 4)}\right)^{1/3} \tag{3.28}$$

It is shown in appendix C.2 that this determinant also vanishes for values of $k = cj$ where c is a positive integer. Thus, the series expansions of equations (3.27a) and (3.27b) can be simplified to

$$H\left(\xi-\xi_0\right)=\sum_{k=0}^{\infty}H_{jk}\left(\xi-\xi_0\right)^{jk} \tag{3.29a}$$

$$V\left(\xi-\xi_0\right)=-\beta\xi_0+\sum_{k=0}^{\infty}V_{jk+1}\left(\xi-\xi_0\right)^{jk+1} \tag{3.29b}$$

Furthermore, equation (3.27a) can be rearranged for $k=j$ to give

$$V_{j+1}=-jH_j\left[\frac{\beta+n/3}{(j+1)H_0}\right] \tag{3.30}$$

Higher order coefficients such as H_{2j}, H_{3j}.. and V_{2j+1} etc. in equations (3.29a) and (3.29b) can be expressed in terms of H_0 and H_j. The similarity ODEs (3.20a) and (3.20b) are invariant if the variables are transformed such that $\xi\rightarrow-\xi$, $H\rightarrow H$, and $V\rightarrow-V$. This means that the scaling function H is even, while V is odd, and the film will always rupture symmetrically such that $z_R=0$ and thus, $\xi_0=0$. This was already observed in our simulations, as mentioned above. Thus, equations (3.20a) and (3.20b) need to be solved over the domain $0\leq\xi<\infty$ rather than $-\infty<\xi<\infty$ and j will always take even values. In addition, the ODEs are also invariant if $\xi\rightarrow\phi\xi$ and $V\rightarrow\phi V$ where ϕ is a non-zero constant, and the coefficient H_j can then be eliminated by setting $\phi=H_j^{1/j}$.

A shooting method for the axial exponent β is adopted in order to solve the ODEs (3.20a) and (3.20b), subject to the regularity condition (3.22) and far-field boundary condition (3.23) following the works of Doshi and Basaran [28] and Thete et al. [1], who coupled a shooting method with minimizing the error for a corresponding velocity integral. The final value of β is that which minimizes this error ε_v. In our case, this error is given by

$$\varepsilon_v=\left|\int_0^{\infty}\frac{dV}{d\xi}d\xi\right|=\int_0^{\infty}\left|\frac{3(1+k_1H^2)}{2^{n+2}m_1^{n-1}H^3}\right|^{1/n}d\xi=0 \tag{3.31}$$

The value of j was chosen to be 2 following the works of Doshi and Basaran [28] and Thete et al. [1]. Next, a value of β was taken and the values of H_0 and k_1 were

determined from equations (3.28) and (3.25) respectively. The initial values of H and V at $\xi = 10^{-4}$ were obtained from expansions (3.29a) and (3.29b) up to order ξ^j for H and ξ^{j+1} for V. A fourth-order Runge-Kutta scheme, ode45, in MATLAB was used to integrate the equations from $\xi = 10^{-4}$ to $\xi = L$, where L was varied from 50 to 2500 until the far field boundary conditions were always met at $\xi = L$. Following this, the error ε_v given by equation (3.31) was evaluated. This entire procedure was then repeated for a new value of β. Figure 3.3(a) shows the variation of this error ε_v with β, for a sheet of power-law exponent $n = 0.9$. The error is minimized for $\beta = 0.28$, which is in excellent agreement with the value of β obtained from the numerical simulations in figure 3.2(b). Moreover, the value of H_0 obtained from equation (3.28) for $\beta = 0.28$ and $j = 2$ is $H_0 = 0.986$. Since the film thickness is always at a minimum at $\xi = \xi_0 = 0$, it can be seen from equations (3.17) and (3.29a) that $h_{min} = H_0 \tau_v^{n/3} = H_0 A^{n/3} \tau^{n/3}$. Thus, for the value of H_0 obtained from solutions of the ODEs, the value of the pre-factor for h_{min} is $H_0 A^{n/3} = 0.0076$, which is in excellent agreement with the value obtained from numerical solutions as shown in figure 3.2(a).

In order to compare similarity solutions obtained from numerical solutions of the PDEs and solving the 1D ODEs by the shooting method specified above, the scaling function $H(\xi)$ is plotted along with the corresponding rescaled transient profile from the numerical simulations. The solutions of the ODEs are normalized in the following manner

$$\frac{h}{h_{min}} = \frac{H(\xi)}{H_0} \tag{3.32}$$

and plotted against ξ. The spatial profiles of the film thickness h obtained from numerical simulations, or axial coordinate of the fluid-gas interface $S(t)$ are similarly normalized in the following manner

$$\frac{h}{h_{min}} = \frac{y(S(t))}{y(S(t)|_{z=0})} \tag{3.33}$$

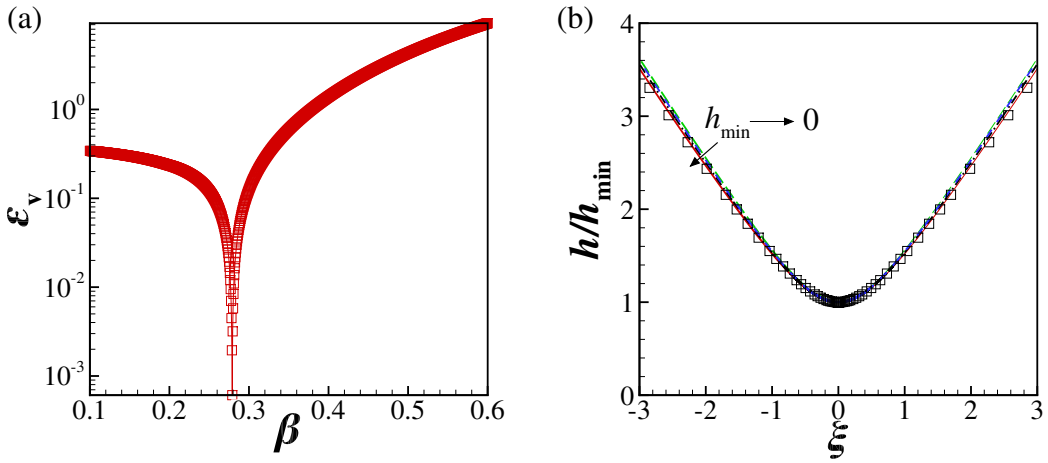

Figure 3.3. (a) Variation of the error ε_v in the velocity integral with the exponent for lateral length scale β for $n = 0.9$, which shows that error is minimized when $\beta = 0.28$. (b) Rescaled profiles of the fluid-gas interface obtained by numerically solving the transient PDEs represented by the lines for a sheet such that $A = 9.21 \times 10^{-8}$ and $m = 1/A$, and the normalized scaling function $H(\xi)$ obtained by solving the ODEs in similarity space represented by symbols are seen to overlap in the vicinity of rupture $z = 0$ for a sheet of power-law fluid undergoing Stokes flow when $n = 0.9$. The transient profiles shown are for instants when the minimum film thickness h_{min} lies between $h_{min} = 2 \times 10^{-4}$ and $h_{min} = 7 \times 10^{-3}$, such that each profile corresponds to an instant when the value of h_{min} is roughly half the value for the previous profile.

and plotted against $zh_0/l_z(h_{min}/H_0)^{3\beta/n}$ since

$$\xi = \frac{zh_0}{l_z \left[h_{min}/H_0\right]^{3\beta/n}} \tag{3.34}$$

where h_0/l_z is multiplied to account for the different lengthscales chosen for non-dimensionalization of the PDEs and ODEs. Figure 3.3(b) makes plain that the rescaled $H(\xi)$ profile from the ODE solutions and the corresponding transient profile from numerical simulations are in excellent agreement as they overlap in the vicinity of the singularity $z = 0$.

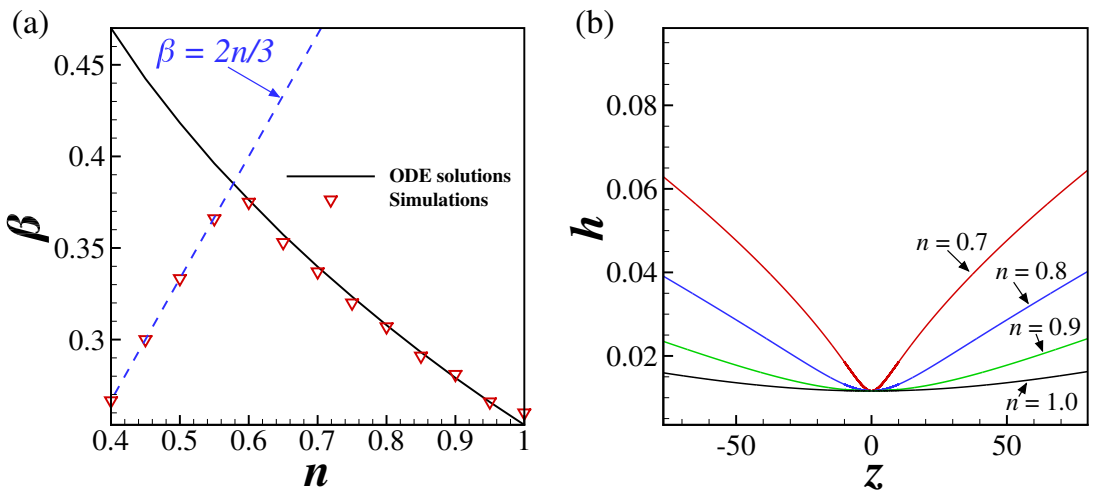

Figure 3.4. (a) Variation of the scaling exponent β for the lateral length scale with power-law exponent n obtained from solutions of the 1D ODEs by employing the shooting method described above for the PLV regime. The ∇ symbols represent corresponding values of β obtained from numerical simulations of the PDEs. (b) Surface profiles for films of power-law fluids undergoing thinning in the Stokes regime such that $A = 9.21 \times 10^{-8}$ and $m = 1/A$ when the minimum film thickness is $h_{min} = 1.12 \times 10^{-2}$. The values of the power-law exponent n are shown on the corresponding curves.

Figure 3.4(a) shows the variation of β values determined by solving the ODEs (3.20a) and (3.20b) using the shooting method outlined above for sheets undergoing Stokes flow with power-law exponents in the range $0.4 \leq n \leq 1$. Corresponding β values obtained from simulations of the PDEs for Stokes flow such that for $A = 9.21 \times 10^{-8}$ and $m = 1/A$ are in excellent agreement for $0.6 \leq n \leq 1$. However, for $n = 0.55$ and below, the values of β obtained from the solutions of the ODEs are no longer in agreement with the values obtained from solutions of the PDEs. Moreover, for $n < 0.58$, the values of β obtained from the ODE solutions are larger than $2n/3$, represented by the dashed line in figure 3.4(a), which means that capillary forces are no longer negligible in the dominant force balance. For example, for the value of $n = 0.5$, if it is assumed that the dynamics lie in the PLV regime and the value of

$\beta = 0.42$ from figure 3.4(a), then the variation with τ_v of the forces in the system can be determined from equation (3.19) and is given by

$$V \sim vdW \sim \tau_v^{-0.92}, \quad C \sim \tau_v^{-1.09} \tag{3.35}$$

Clearly, there is a contradiction, as capillary forces increase faster than the viscous and van der Waals forces as $\tau_v \to 0$, even though the assumptions of the PLV regime require that capillary forces are subdominant. Figure 3.4(b) shows the shape of the surface at $h_{min} = 1.12 \times 10^{-2}$ for sheets undergoing Stokes thinning when $A = 9.21 \times 10^{-8}$ and $m = 1/A$ and n values ranging from $0.7 - 1.0$. It is evident that as n decreases, the surface becomes more curved, which leads to larger capillary forces. As n decreases, the magnitude of viscous forces opposing van der Waals driven drainage of the film at $z = 0$ decreases faster with time. Van der Waals forces are thus able to rapidly drain the regions where initial film thickness was lower (as a sinusoidal perturbation was applied initially) and results in the larger curvature seen for low n values. Thus, while thinning in the Stokes limit of sheets of power-law fluids lies in the PLV regime for $0.58 \leq n \leq 1$, it is not valid for fluids with $n < 0.58$. Below this limit, capillary forces are present in the dominant force balance, leading to a new regime, which is termed hereafter as the "power-law capillary viscous regime" (PLCV). The remainder of this section explores thinning and rupture dynamics in the Stokes limit for fluids with power-law exponents in the range $0 < n \leq 0.58$.

3.4.2 Dynamics in the power-law capillary viscous (PLCV) regime

If the similarity ansatz (3.17) is substituted into the 1D PDEs (3.16a) and (3.16b) again, followed by a kinematic and dynamic balance such that all three forces, namely capillary, viscous, and van der Waals, are in the dominant force balance, the following relations for the scaling exponents are obtained

$$\alpha = n/3, \quad \beta = 2n/3, \quad \gamma = 2n/3 - 1 \tag{3.36}$$

Here β can be determined by dimensional analysis alone, as the self-similarity is of the first kind [43]. In this so-called "power-law capillary viscous" regime, the three forces in balance vary as $\tau_v \to 0$ as

$$C \sim V \sim vdW \sim \tau_v^{-5n/3} \tag{3.37}$$

Figure 3.5 shows the variation with time remaining until rupture τ for several quantities of interest for a power-law fluid sheet undergoing Stokes flow such that $A = 9.21 \times 10^{-8}$, $m = 1/A$, and $n = 0.5$. Figure 3.5(a) shows that h_{min} decreases with τ as $h_{min} \sim \tau^{0.5/3}$, which does not adequately confirm that dynamics lie in the PLCV regime, as $h \sim \tau^{n/3}$ for both the PLV and PLIV regimes. However, figures 3.5(b) and 3.5(c) show that the lateral length scale and velocity vary with time to rupture as $z' \sim \tau^{1/3} \sim \tau^{2(0.5)/3}$ and $v' \sim \tau^{-2/3} \sim \tau^{1/3-1}$ respectively, which are in excellent agreement with the expected value of $\beta = 2n/3$ and $\gamma = 2n/3 - 1$ from equation (3.36) respectively. Thus, the results of figure 3.5 make plain that the dynamics for $n = 0.5$ lie in the PLCV regime, where van der Waals, capillary, and viscous forces are in balance. Similar results are obtained numerically for the values of β for films of exponents ranging from $0.4 \leq n \leq 0.58$, shown in figure 3.4(a). All values lie on the line $\beta = 2n/3$, thus making plain that in this limit of n, the dynamics lie in the PLCV regime.

In conclusion, for power-law sheets with negligible inertia, the dynamics lie in the power-law viscous (PLV) regime for fluids with power-law exponents in the range $0.58 \leq n \leq 1$, such that the dominant force balance is between viscous and van der Waals forces, while capillary forces are negligible, and the scaling exponents are given by

$$h \sim \tau^{n/3}, z' \sim \tau^{\beta}, v \sim \tau^{\beta-1} \tag{3.38}$$

where the value of β increases as n decreases, as shown in figure 3.4(a). On the other hand, for sheets of power-law fluids with exponents in the range $0 < n \leq 0.58$, capillary forces are no longer negligible as viscous forces decrease faster for small n, and the dynamics lie in the power-law capillary viscous (PLCV) regime. The

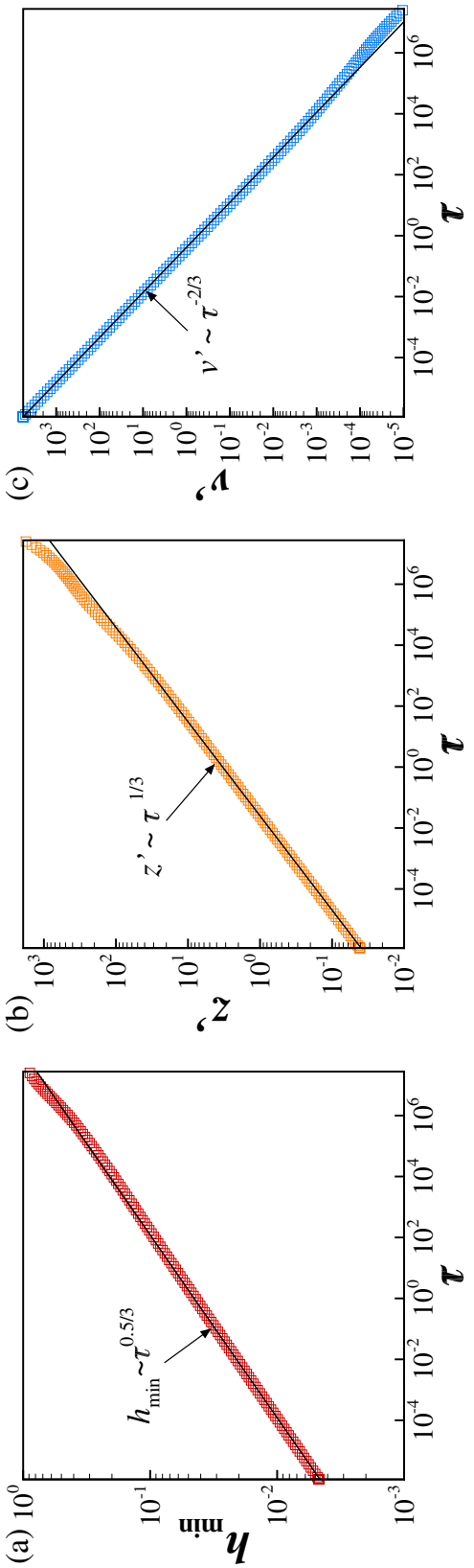

Figure 3.5. Scaling behavior of variables in the rupture zone during thinning of a sheet undergoing Stokes flow such that $A = 9.21 \times 10^{-8}$, $m = 1/A$, and $n = 0.5$. Simulation results are shown by the data points while the straight lines represent best fit to the data.

dynamic force balance for this regime is between the capillary, van der Waals and viscous forces, and the scaling exponents are given by

$$h \sim \tau^{n/3}, z' \sim \tau^{2n/3}, v \sim \tau^{2n/3-1} \tag{3.39}$$

3.5 Thinning dynamics in the inviscid limit

Thinning and rupture of sheets of power-law fluids in the inviscid limit can be studied computationally by setting $Oh = 0$ in equation (3.9b), and analyzed theoretically by setting $Oh = 0$ in equation (3.13b). However, as the fluid is inviscid, the dynamics are identical to that of sheets of Newtonian fluids in the inviscid limit. Thete et al. [1] have demonstrated that for Newtonian sheets, the dynamics lie in the IC regime given by equation (3.5), such that the dominant force balance is between inertial (I), capillary (C) and van der Waals forces (vdW). The forces vary with time to rupture τ as

$$I \sim C \sim vdW \sim \tau^{-10/7} \tag{3.40}$$

The authors also obtained similarity solutions of the 1D ODEs that govern the dynamics of inviscid sheets in the similarity space. Thus, the reader is referred to their works for a complete understanding of thinning dynamics in the inviscid limit.

3.6 Thinning dynamics for real fluids

In this section, the thinning dynamics of sheets of real fluids are explored, or when the value of Oh is finite. Scaling regimes in the Stokes limit observed in section 3.4 and the IC regime for inviscid films described in section 3.5 are expected to be transitory as the sheet approaches rupture, and fluid velocities increase, as seen for thread pinchoff [28–30], and Newtonian film rupture [1]. In what follows, thinning of sheets is analyzed first for highly viscous sheets of power-law fluids with $Oh \gg 1$, followed by slightly viscous sheets of power-law fluids with $Oh \ll 1$.

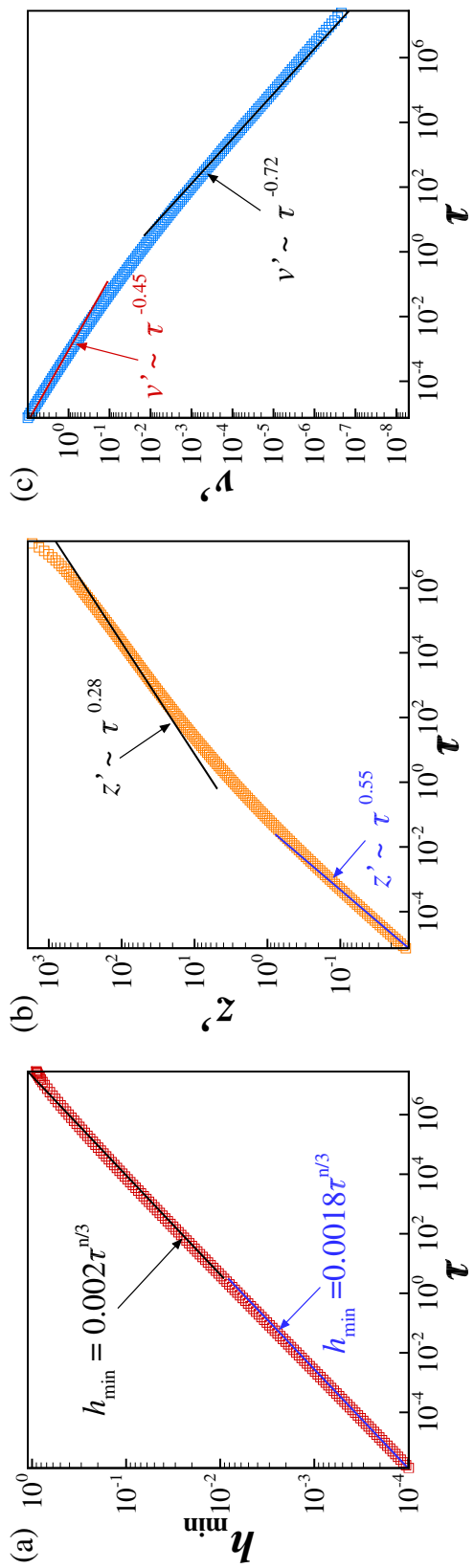

Figure 3.6. Scaling behavior of variables in the rupture zone during thinning of a sheet of power-law fluid such that $Oh = 50, A = 9.21 \times 10^{-8}$, $m = 1/A$, and $n = 0.9$. Simulation results are shown by the data points while the straight lines represent best fit to the data. A transition from the PLIV regime to the PLIV regime is observed.

3.6.1 Thinning of sheets of power-law fluids when $Oh \gg 1$

For sheets with $Oh \gg 1$, the initial dynamics are expected to lie in the corresponding Stokes flow regime for a given fluid of value n, described in section 3.4. However, it is useful to examine how inertial terms vary with time to rupture τ_v as the sheet approaches rupture. For a power-law fluid with $0.58 \leq n \leq 1$, it is expected from the results of section 3.4.1 that the initial dynamics will lie in the PLV regime. Thus, the variation with τ_v of inertial terms (I) in the momentum equation (3.11b) is given by

$$I \sim \frac{v}{t} \sim \frac{\tau_v^{\beta-1}}{\tau_v} \sim \tau_v^{\beta-2} \tag{3.41}$$

where τ_v is defined in section 3.3.2. It is clear from the values of β obtained for $0.58 \leq n \leq 1$ shown in figure 3.4(a), and the dominant force balance for the PLV regime in equation (3.19), that the inertial terms vary faster than the forces in balance for this regime. Thus, while the inertial terms might be initially negligible on account of large Oh values, such that thinning dynamics lie in the PLV regime, a transition to a regime where inertial forces feature in the dominant force balance is expected for real fluids with $Oh \gg 1$. To predict when this transition occurs, it is useful to define the instantaneous Reynolds number in the rupture zone, which is given by

$$Re = \frac{\rho \tilde{z} \tilde{v}}{\tilde{\mu}} = \frac{\rho l_z v_V}{\mu_0} \tau_v^{2\beta+n-2} = \frac{\tau_v^{2\beta+n-2}}{Oh^2} \tag{3.42}$$

where l_z and v_V are defined in section 3.3.2. From figure 3.4(a) it is clear that for the values of β determined for fluids with power-law exponents in the range $0.58 \leq n \leq 1$, the exponent $(2\beta + n - 2)$ is always negative, and thus Re is increasing as $\tau_v \to 0$. For the inertial terms to be significant, $Re \sim O(1)$, and this will occur when

$$\tau_v \sim Oh^{2/(2\beta+n-2)} \tag{3.43}$$

For power-law fluids with $Oh \sim O(1)$, Thete et al. [2] showed that the dynamics for fluids with a power-law exponent value in the range $6/7 \leq n \leq 1$ lie in the PLIV regime, where the inertial, viscous, and van der Waals forces are in balance, leading to scaling exponents given in equation (3.8). For fluids with $Oh \gg 1$ with a power-law exponent value in this range, the dynamics are thus expected to eventually transition from the initial PLV regime to a final PLIV regime when $Re \sim O(1)$. The value of the minimum film thickness, and lateral length scale at this instant is estimated by

$$h_{min,t} \sim Oh^{2n/3(2\beta+n-2)}, \quad z'_t \sim \frac{l_z}{h_0} Oh^{2\beta/(2\beta+n-2)} \tag{3.44}$$

Figure 3.6 shows the variation with τ of several quantities of interest for a sheet undergoing rupture of a fluid such that $Oh = 50, A = 9.21 \times 10^{-8}$, $m = 1/A$, and $n = 0.9$. Figure 3.6(a) shows that h_{min} decreases with τ as $h_{min} \sim \tau^{0.9/3} \sim \tau^{0.3}$ all the way till rupture. Since the scaling exponent for h is equal for both the PLV and PLIV regimes, this result is insufficient to demonstrate the expected transition. However, the pre-factor for the best fit line changes value at $h_{min} \sim 10^{-2}$, which is in excellent agreement with the expected value of $h_{min,t} \sim 1.2 \times 10^{-2}$ calculated from equation (3.44). Figure 3.6(b) shows the variation with τ of the scaling exponent for the lateral length scale z'. It initially varies with time to rupture as $z' \sim \tau^{0.28}$ which makes plain that the dynamics are in the PLV regime as the value of β agrees with that determined earlier in section 3.4.1 for $n = 0.9$. However, the dynamics are seen to clearly transition to a final asymptotic PLIV regime as $z' \sim \tau^{0.55} \sim \tau^{1-n/2}$ in the later stages of thinning. This transition is seen to occur at a value of $z' \approx 1 \times 10^1$, which is in good agreement with the expected value of $z'_t \sim (l_z/h_0) Oh^{2\beta/(2\beta+n-2)} \sim 5.7 \times 10^1$ from equation (3.44). This transition is also seen clearly in figure 3.6(c), where the lateral velocity initially varies with τ as $v' \sim \tau^{-0.72} \sim \tau^{\beta-1}$ but later varies as $v' \sim \tau^{-0.45} \sim \tau^{-n/2}$. Thus, for sheets of power-law fluids with $Oh \gg 1$ and $6/7 \leq n \leq 1$, thinning dynamics lie in the PLV regime initially, but eventually transition to the PLIV regime as the rupture singularity is approached.

For films with lower power-law exponents in the range $0.58 \leq n \leq 6/7$, initial dynamics are expected to again lie in the PLV regime. However, for fluids with $Oh \sim$

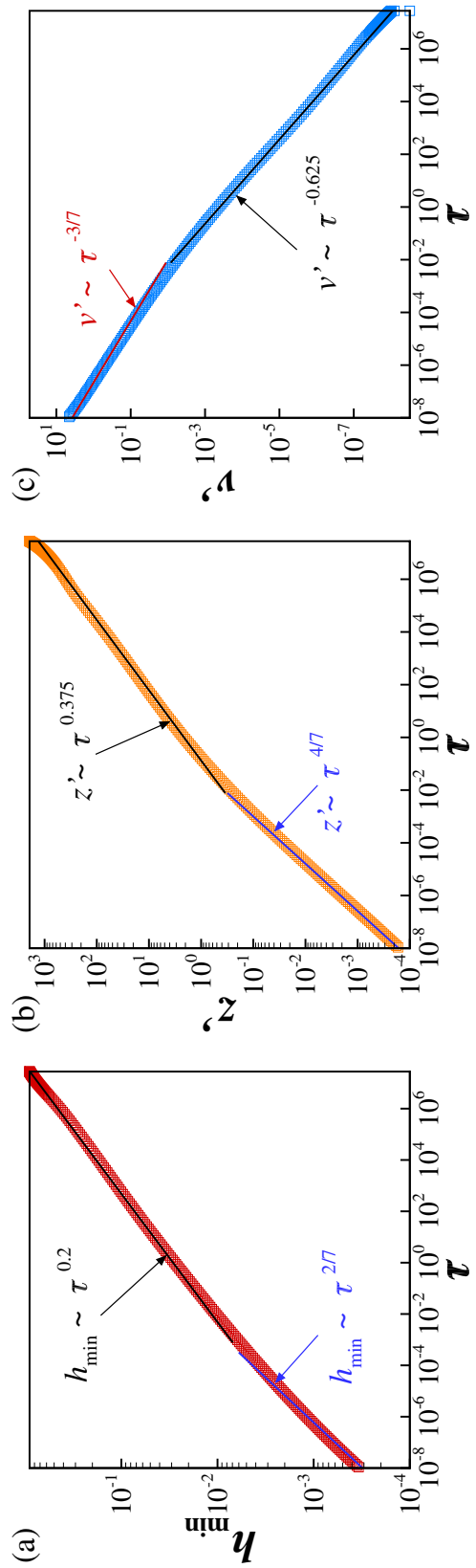

Figure 3.7. Scaling behavior of variables in the rupture zone during thinning of a sheet of power-law fluid such that $Oh = 1000, A = 9.21 \times 10^{-8}$, $m = 1/A$, and $n = 0.6$. Simulation results are shown by the data points while the straight lines represent best fit to the data. A transition from the PLV regime to the IC regime is observed.

$O(1)$, Thete et al. [2] showed that the dominant force balance changes when n lies in the range $0 < n \leq 6/7$. If one assumes nevertheless that thinning dynamics transition to the PLIV regime in the late stages of thinning, as seen above for $6/7 \leq n \leq 1$, the forces will vary with τ_v after this transition as

$$I \sim vdW \sim V \sim \tau_v^{-1-n/2}, \quad C \sim \tau_v^{11n/6-3} \tag{3.45}$$

Clearly, for $n < 6/7$, the capillary forces increase faster than the three forces in balance, eventually catching up and featuring in the dominant force balance. Thus, this PLIV regime is transitory, but the final dynamics will always lie in the IC regime where inertial, capillary, and van der Waals forces are in balance, as viscous forces fall out of the balance, and the scaling exponents are given by equation (3.5). It is therefore expected, that the dynamics for fluids with $Oh \gg 1$ and $0.58 \leq n \leq 6/7$ are expected to eventually transition from the initial PLV regime to a final IC regime as the film approaches rupture. When this transition occurs, the values of the minimum film thickness and lateral length scale can be estimated again, from equation (3.44) as the initial regimes in both cases are identical. Figure 3.7 shows the variation with τ of several quantities of interest for a sheet undergoing rupture for a fluid such that $Oh = 1000, A = 9.21 \times 10^{-8}$, $m = 1/A$, and $n = 0.6$. The minimum film thickness h_{min} is seen to initially vary with τ (figure 3.7(a)) as $h_{min} \sim \tau^{0.2} \sim \tau^{0.6/3}$ but later transitions to vary as $h_{min} \sim \tau^{2/7}$, signifying a transition to the IC regime. Corresponding transitions are observed for both the lateral length scale z' and lateral velocity v' in figures 3.7(b) and 3.7(c). Moreover, the transition for h_{min} is observed to occur at $h_{min} \approx 7 \times 10^{-3}$, which is in good agreement with $h_{min,t} \sim 1.33 \times 10^{-2}$ determined from equation (3.44). Similarly, the transition for z' is observed to occur at $z' \approx 6 \times 10^{-1}$, which is again in good agreement with $z'_t \sim 1.14 \times 10^{0}$ determined from equation (3.44). Thus, for sheets of power-law fluids with $Oh \gg 1$ and $0.58 \leq n \leq 6/7$, thinning dynamics transition from an initial PLV regime to a final IC regime, where the film essentially behaves like an inviscid fluid in the rupture zone.

Lastly, for sheets with power-law exponents in the range $0 < n \leq 0.58$, it was shown in section 3.4.2 that the dynamics lie in the PLCV regime for sheets undergoing

Stokes flow. The initial dynamics for a sheet with $Oh \gg 1$ and n values in this range are thus expected to initially thin in the PLCV regime, as opposed to the PLV regime seen for sheets with larger n values. For this regime $\beta = 2n/3$ and substituting this value into equation (3.41) one can obtain the variation with τ_v of the inertial terms

$$I \sim \frac{v}{t} \sim \frac{\tau_v^{2n/3-1}}{\tau_v} \sim \tau_v^{2n/3-2} \tag{3.46}$$

Clearly, for $n < 0.58$, it is clear from equations (3.37) and (3.46) that the inertial terms continue to increase faster than the capillary, van der Waals, and viscous forces that are in balance. A transition to a final asymptotic IC regime is expected as the film approaches rupture, as Thete et al. [2] have shown to be the case for films of $Oh \sim O(1)$. Again, we can find the value of τ_v at which $Re \sim O(1)$ and make use of the scaling exponents for the PLCV regime in equation (3.39) to estimate the minimum film thickness and lateral length scale at which this transition occurs

$$h_{min,t} \sim Oh^{2n/(7n-6)}, \quad z_t' \sim \frac{l_z}{h_0} Oh^{4n/(7n-6)} \tag{3.47}$$

Figure 3.8 shows the variation with τ of several quantities of interest for a sheet undergoing rupture for a fluid such that $Oh = 1000, A = 9.21 \times 10^{-8}$, $m = 1/A$, and $n = 0.5$. The minimum film thickness h_{min} is seen to initially vary with τ (figure 3.8(a)) as $h_{min} \sim \tau^{0.5/3}$ but later transitions to vary as $h_{min} \sim \tau^{2/7}$, signifying a transition to the IC regime. For the lateral length scale, the variation with τ (figure 3.8(b)) is seen to transition from $z' \sim \tau^{1/3} \sim \tau^{2n/3}$ for the PLCV regime to $z' \sim \tau^{4/7}$ for the IC regime. A corresponding transition is seen for the lateral velocity in figure 3.8(c). Moreover, the transition for h_{min} is observed to occur at $h_{min} \approx 4 \times 10^{-2}$, which is in good agreement with $h_{min,t} \sim 6.31 \times 10^{-2}$ determined from equation (3.47). Similarly, the transition for z' is observed to occur at $z' \approx 7 \times 10^{0}$, which is again in good agreement with $z_t' \sim 1.31 \times 10^{1}$ determined from equation (3.47). Thus, for sheets of power-law fluids with $Oh \gg 1$ and $0 < n \leq 0.58$, thinning dynamics transition from an initial PLCV regime to the final IC regime, where the film essentially behaves like an inviscid fluid in the rupture zone.

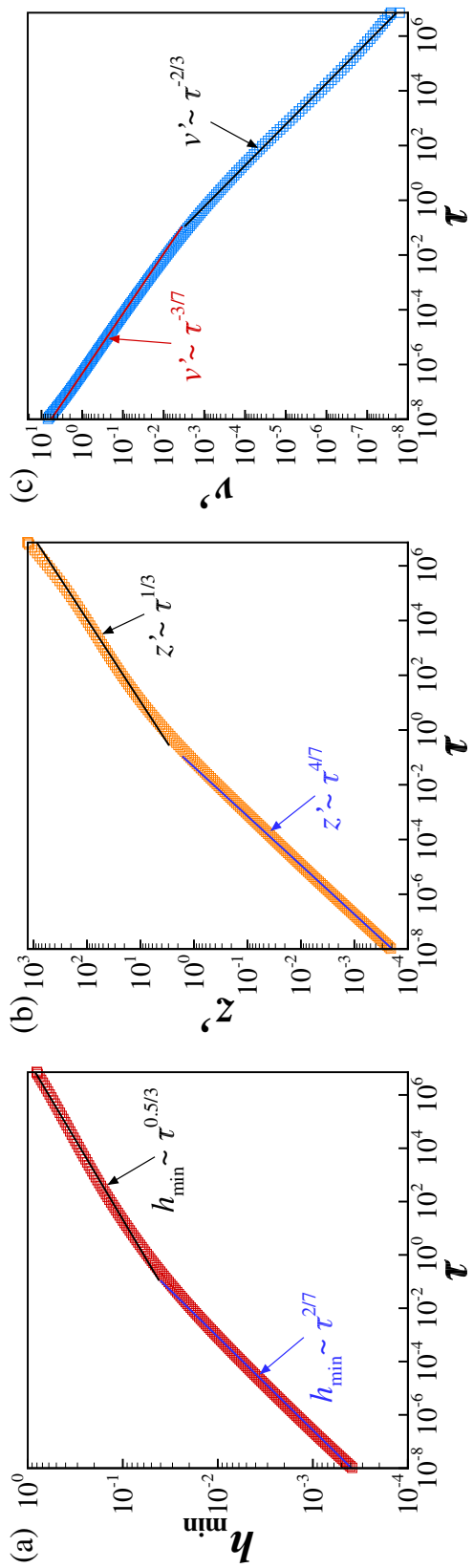

Figure 3.8. Scaling behavior of variables in the rupture zone during thinning of a sheet of power-law fluid such that $Oh = 1000, A = 9.21 \times 10^{-8}$, $m = 1/A$, and $n = 0.5$. Simulation results are shown by the data points while the straight lines represent best fit to the data. A transition from the PLCV to IC regime is observed.

3.6.2 Thinning of sheets of power-law fluids when $Oh \ll 1$

For sheets of power-law fluids with $Oh \ll 1$, the initial dynamics are expected to lie in the IC regime discussed in section 3.5 as viscous forces are negligible on account of low values of Oh. However, as the film starts to thin and fluid velocity in the rupture zone increases, viscous terms become significant. The viscous terms (V) in the momentum equation (3.13b) are found to vary with time to rupture τ_I in the inertial regime as

$$V \sim \mu \frac{v}{z^2} \sim \frac{\tau_I^{4/7-n}}{\tau_I^{8/7}} \sim \tau_I^{-n-4/7} \tag{3.48}$$

where τ_I is defined in section 3.3.2. From equations (3.40) and (3.48), it is clear that viscous forces will increase faster than the inertial, capillary and van der Waals forces in balance if $6/7 < n \leq 1$ as $\tau_I \to 0$. Thus, while viscous forces might be initially negligible, they are expected to become significant and be present in the dynamic force balance during the later stages of thinning. Thinning dynamics are expected to transition from the initial IC regime to the PLIV regime as $\tau \to 0$. The instantaneous Reynold's number for this case is given by

$$Re = \frac{\rho \tilde{z} \tilde{v}}{\tilde{\mu}} = \frac{\rho l_z v_I}{\mu_0} \tau^{n-6/7} = \frac{\tau_I^{(7n-6)/7}}{Oh} \tag{3.49}$$

It is clear that for $6/7 < n \leq 1$, the Re is decreasing as $\tau \to 0$, and thus viscous forces will not be negligible for the entire duration of thinning. Viscous forces are expected to become significant when $Re \sim O(1)$, which will occur when τ_I attains the following value

$$\tau_I \sim Oh^{7/(7n-6)} \tag{3.50}$$

The transition from the IC to PLIV regime is estimated to occur when the minimum film thickness h_{min} and lateral length scale z' reach the following values

$$h_{min,t} \sim Oh^{2/(7n-6)}, \quad z'_t \sim \frac{l_z}{h_0} Oh^{4/(7n-6)} \tag{3.51}$$

Figure 3.9 shows the variation with τ of several quantities of interest for a sheet of power-law fluid undergoing rupture such that $Oh = 0.08, A = 9.21 \times 10^{-8}$, $m = 1/A$, and $n = 0.97$. It makes plain that the minimum film thickness h_{min} initially varies with τ (figure3.9(a)) as $h_{min} \sim \tau^{2/7}$ in excellent agreement with the IC regime, but transitions in the later stages of thinning to vary as $h_{min} \sim \tau^{0.97/3} \sim \tau^{n/3}$, in agreement with the PLIV regime. Further, the lateral length scale z' is seen to vary with τ in figure 3.9(b) as $z' \sim \tau^{4/7}$ initially, which is again in excellent agreement with the IC regime, but transitions later to $z' \sim \tau^{0.515} \sim \tau^{1-n/2}$, in excellent agreement with the expected scaling exponent for the PLIV regime. Finally, figure 3.9(c) shows the corresponding transition for the lateral velocity v'. Moreover, the transition for h_{min} is observed to occur at $h_{min} \approx 4 \times 10^{-3}$, which is in good agreement with $h_{min,t} \sim 1.67 \times 10^{-3}$ determined from equation (3.49). Similarly, the transition for z' is observed to occur at $z' \approx 2 \times 10^{-2}$, which is again in good agreement with $z'_t \sim 9.21 \times 10^{-3}$ determined from equation (3.49). Thus, for sheet of power-law fluids with $Oh \ll 1$ and $6/7 < n \leq 1$, thinning dynamics transition from the IC regime to the PLIV regime, as viscous forces become significant once the fluid velocity increases in the rupture zone.

For sheets of power-law fluids with $Oh \ll 1$ and $0 < n \leq 6/7$, the dynamics are expected to stay in the IC regime throughout the duration of thinning, until the film ruptures. This is clear from equations (3.40) and (3.48), as the viscous forces will never increase faster than the inertial, capillary and van der Waals forces in balance. This is confirmed from numerical simulations, as shown in figure 3.10 for thinning of a sheet of power-law fluid such that $Oh = 0.08, A = 9.21 \times 10^{-8}$, $m = 1/A$, and $n = 0.6$. The variation with τ of h_{min}, z' and v' corresponds to the expected IC regime throughout the duration of thinning.

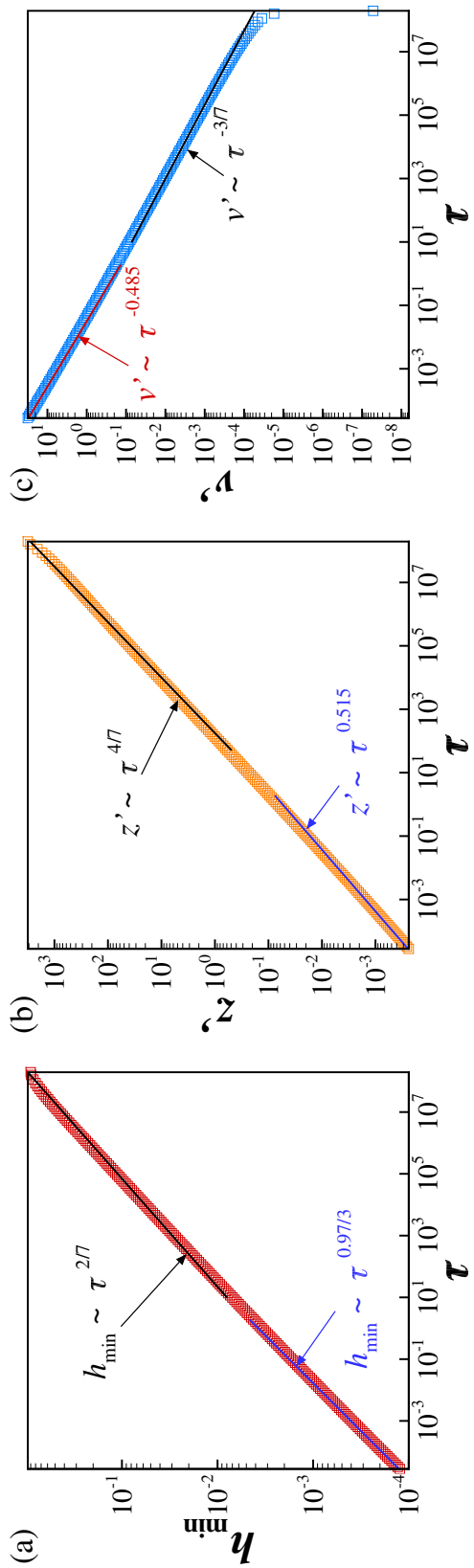

Figure 3.9. Scaling behavior of variables in the rupture zone during thinning of a sheet of power-law fluid such that $Oh = 0.08, A = 9.21 \times 10^{-8}$, $m = 1/A$, and $n = 0.97$. Simulation results are shown by the data points while the straight lines represent best fit to the data. A transition from the IC to the PLIV regime is observed.

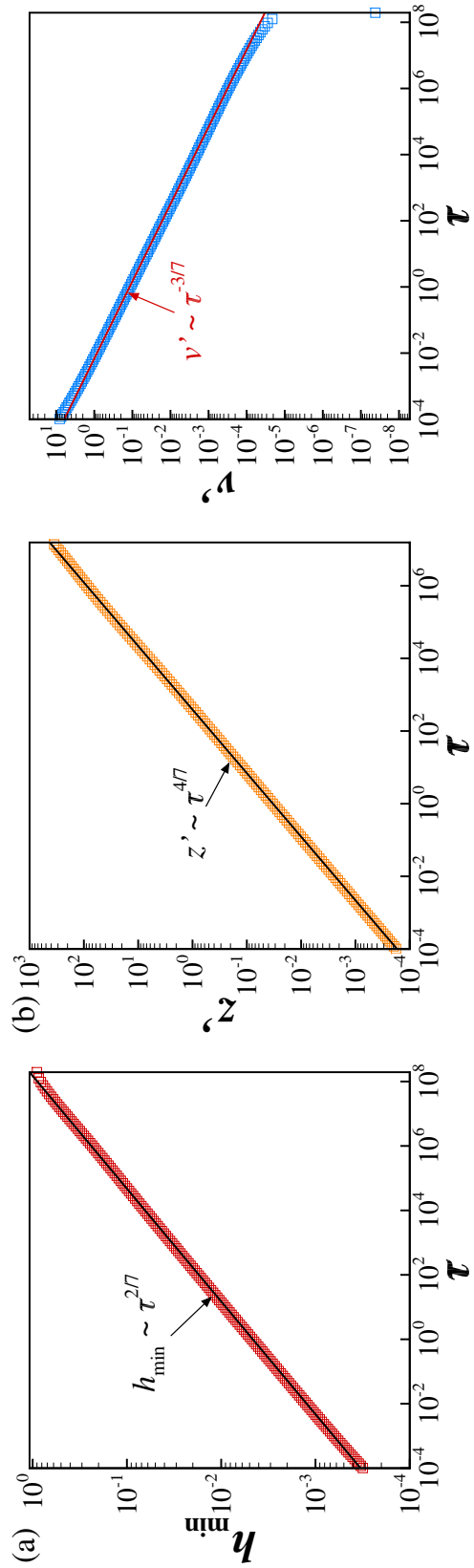

Figure 3.10. Scaling behavior of variables in the rupture zone during thinning of a sheet of power-law fluid such that $Oh = 0.08, A = 9.21 \times 10^{-8}$, $m = 1/A$, and $n = 0.6$. Simulation results are shown by the data points while the straight lines represent best fit to the data. The dynamics are observed to lie in the IC throughout the duration of thinning.

3.7 Conclusions and future outlook

In this paper, a comprehensive understanding of the local dynamics in the vicinity of the rupture singularity has been developed for sheets of power-law fluids thinning due to van der Waals forces. The plethora of scaling regimes and scaling transitions that are observed for sheets of power-law fluids over the entire parameter space spanned by the Ohnesorge number $0 \leq Oh \leq \infty$ and power-law exponent $0 < n \leq 1$ are summarized by means of a phase diagram in figure 3.11. For sheets undergoing Stokes flow such that $0.58 \leq n \leq 1$, the self-similarity is of the second kind and the value of the scaling exponent for lateral length scale β is determined as part of the solution of the 2D PDEs and shown to be in excellent agreement with the value determined from solution of 1D ODEs in similarity space for all values of $0.58 \leq n \leq 1$. Furthermore, for sheets with $0 < n \leq 0.58$, capillary forces are observed to become significant, and the dynamics lie in the previously unseen PLCV (power-law capillary viscous) regime where capillary, van der Waals and viscous forces are in balance. This scaling regime is never observed in thinning of Newtonian sheets as the viscous forces are always large enough to prevent capillary effects in the Stokes limit. Finally, for real fluids the viscous regimes discussed in section 3.4 or inertial regime discussed in section 3.5 are shown to be transitory, with the dynamics eventually transitioning to one of the scaling regimes described by Thete et al. [2] for sheets of power-law fluids with $Oh \sim O(1)$.

The long-wavelength nature of spontaneous van der Waals driven sheet rupture ensures that for sheets where the wavelength of perturbation is larger than the critical wavelength $\tilde{\lambda}_c$ described by equation (3.2), the slenderness approximation breaks after the minimum film thickness reaches the molecular length scale d, or after the continuum approximation has broken down. Thus, the long-wavelength approximation is valid all the way until rupture for spontaneous sheet rupture, and the results of a 1D Galerkin/finite element based algorithm were identical to the results obtained from solving the 2D PDEs using the algorithm specified in section 3.3.1. However, sheets

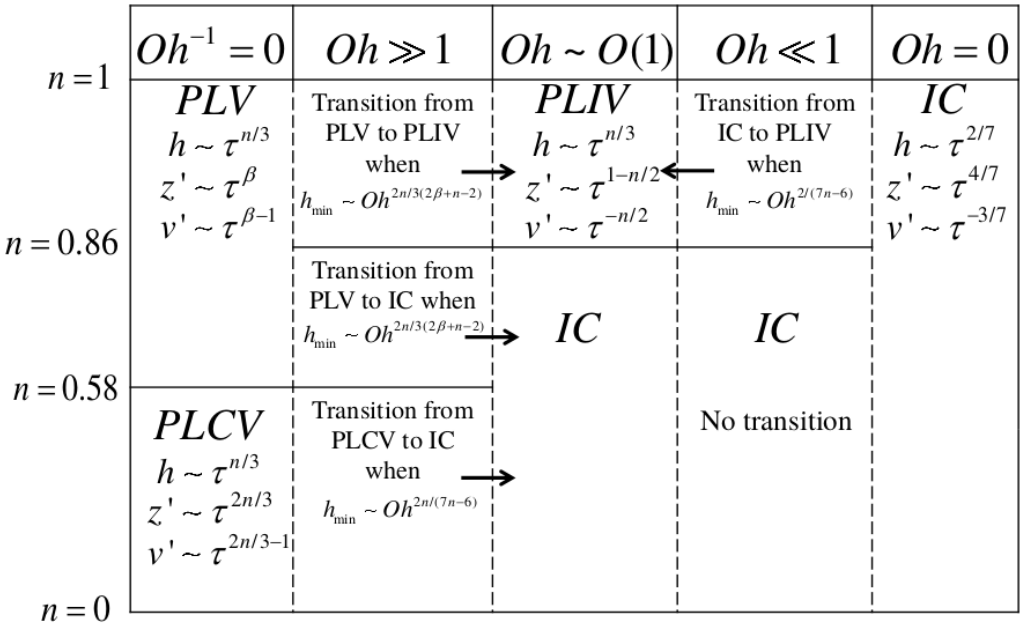

Figure 3.11. Phase diagram summarizing scaling laws for self-similar dynamics of thinning and rupture of sheets of power-law fluids as a function of Ohnesorge number Oh and power-law exponent n. The phase diagrams delineates the region of the parameter space where the dynamics lie in the power-law viscous (PLV), power-law capillary viscous (PLCV), power-law inertial viscous (PLIV) and inertial-capillary (IC) regimes, and when transitions between regimes are expected to occur. Here h is the film thickness, z' is the lateral length scale or lateral extent of the rupture zone, v' denotes the velocity in the lateral direction, and τ is time remaining to rupture. For the PLV regime, the scaling exponent β for the axial length scale is seen to increase as n decreases, with its values lying between $0.387 \leq \beta \leq 0.26$.

with a lateral extent much smaller than $\tilde{\lambda}_c$ are prone to rupture from finite amplitude perturbations [46], and it is shown in appendix C.1 that sheets with a lateral extent of $\tilde{\lambda}_c/25$ break for a finite amplitude perturbation and display the self-similar behavior expected for the parameter values of the given sheet. For such sheets, the slenderness approximation breaks down before the molecular length scale is reached, and the 2D algorithm specified in section 3.3.1 is essential to accurately capture the dynamics of thinning and rupture.

Experimental measurements of film thinning and rupture, similar to those conducted for thread pinchoff [24, 47] are still pending. The extremely small scales at which intermolecular forces become significant ($\sim$ 100 nm) makes accurately resolving the film thickness as a function of time challenging, as seen in recent experiments for rupture of soap films [48]. In the future, total internal reflection fluorescence (TIRF) microscopy [49] could possibly provide experimental confirmation of the scaling regimes detailed in this chapter.

In this paper, free film thinning and rupture has been considered for two-dimensional perturbations, as opposed to axisymmetric perturbations where the film ruptures at a point. Vaynblat, Lister and Witelski [20] state that sheet rupture is unstable to perturbations in the transverse direction, as capillary forces would be too weak to stabilize the film. Furthermore, Bernoff and Witelski [50] showed for the analogous problem of supported film rupture that axisymmetric rupture is stable to non-axisymmetric perturbations and asymtptotes to axisymmetric rupture. In other words, one expects that physically, the film will rupture at a point. We have solved the analogous problem of axisymmetric or point rupture of a free film numerically by means of the 2D algorithm specified in section 3.3.1, and scaling exponents for all regimes specified here are unchanged, except for the PLV regime described in section 3.4. This discrepancy is shown in appendix C.4 and will be addressed in a future publication.

Polymer thin films are ubiquitous in industrial applications [8], and experiments have shown that viscoelastic stresses that build up as a film thins can slow down or arrest rupture of polymer thin films [51]. A thorough stability analysis for free films in the future will provide crucial insight into the fate of sheets of polymeric fluids. Moreover, computational studies with the algorithm outlined here, augmented to account for the elasticity of the fluid, would provide a thorough understanding of the dynamics of polymer thin films, and the mechanism of slowdown of the thinning rate due to viscoelastic stresses.

3.8 List of References

[1] S. S. Thete, C. Anthony, P. Doshi, M. T. Harris, and O. A. Basaran. Self-similarity and scaling transitions during rupture of thin free films of Newtonian fluids. *Phys. Fluids*, 28(9):092101, 2016.

[2] S. S. Thete, C. Anthony, O. A. Basaran, and P. Doshi. Self-similar rupture of thin free films of power-law fluids. *Phys. Rev. E*, 92(2):023014, 2015.

[3] S. Cohen-Addad, R. Höhler, and O. Pitois. Flow in foams and flowing foams. *Ann. Rev. Fluid Mech.*, 45(1):241, 2013.

[4] Y. Yoon, F. Baldessari, H. D. Ceniceros, and L. G. Leal. Coalescence of two equal-sized deformable drops in an axisymmetric flow. *Phys. Fluids*, 19(10):102102, 2007.

[5] Peter S Stewart, Jie Feng, Laura S Kimpton, Ian M Griffiths, and Howard A Stone. Stability of a bi-layer free film: simultaneous or individual rupture events? *J. Fluid Mech.*, 777:27–49, 2015.

[6] Steven J Weinstein and Kenneth J Ruschak. Coating flows. *Annu. Rev. Fluid Mech.*, 36:29–53, 2004.

[7] R. J. Braun. Dynamics of the tear film. *Ann. Rev. Fluid Mech.*, 44:267–297, 2012.

[8] Rabibrata Mukherjee and Ashutosh Sharma. Instability, self-organization and pattern formation in thin soft films. *Soft Matter*, 11(45):8717–8740, 2015.

[9] P. G. De Gennes. Wetting: statics and dynamics. *Rev. Mod. Phys.*, 57(3):827, 1985.

[10] H. S. Kheshgi and L. E. Scriven. Dewetting: Nucleation and growth of dry regions. *Chem. Eng. Sci.*, 46(2):519–526, 1991.

[11] G Debrégeas, P-G De Gennes, and F Brochard-Wyart. The life and death of" bare" viscous bubbles. *Science*, 279(5357):1704–1707, 1998.

[12] G. Reiter. Dewetting of thin polymer films. *Phys. Rev. Lett.*, 68(1):75, 1992.

[13] T. G. Stange, D. F. Evans, and W. A. Hendrickson. Nucleation and growth of defects leading to dewetting of thin polymer films. *Langmuir*, 13(16):4459–4465, 1997.

[14] J. Becker, G. Grün, R. Seemann, H. Mantz, K. Jacobs, K. R. Mecke, and R. Blossey. Complex dewetting scenarios captured by thin-film models. *Nat. Mat.*, 2(1):59–63, 2003.

[15] G. F. Teletzke, H. T. Davis, and L.E. Scriven. How liquids spread on solids. *Chem. Eng. Comm.*, 55(1-6):41–82, 1987.

[16] E. Ruckenstein and R. K. Jain. Spontaneous rupture of thin liquid films. *J. Chem. Soc., Faraday Transactions 2: Molecular and Chemical Physics*, 70:132–147, 1974.

[17] Thomas Erneux and Stephen H Davis. Nonlinear rupture of free films. *Phys. Fluids A: Fluid Dynamics*, 5(5):1117–1122, 1993.

[18] G. I. Barenblatt. *Scaling, Self-similarity, and Intermediate Asymptotics: Dimensional Analysis and Intermediate Asymptotics*. Cambridge University Press, New York, 1996.

[19] Michael P Ida and Michael J Miksis. Thin film rupture. *Applied Mathematics Letters*, 9(3):35–40, 1996.

[20] D. Vaynblat, J. R. Lister, and T. P. Witelski. Rupture of thin viscous films by van der Waals forces: Evolution and self-similarity. *Phys. Fluids*, 13(5):1130–1140, 2001.

[21] W. M. Deen. *Analysis of Transport Phenomena*. Oxford University Press, New York, 1998.

[22] S. W. Hasan, M. T. Ghannam, and N. Esmail. Heavy crude oil viscosity reduction and rheology for pipeline transportation. *Fuel*, 89(5):1095–1100, 2010.

[23] J. R. Savage, M. Caggioni, P. T. Spicer, and I. Cohen. Partial universality: pinch-off dynamics in fluids with smectic liquid crystalline order. *Soft Matter*, 6(5):892–895, 2010.

[24] F. M. Huisman, S. R. Friedman, and P. Taborek. Pinch-off dynamics in foams, emulsions and suspensions. *Soft Matter*, 8(25):6767–6774, 2012.

[25] Daniel Bonn, Morton M Denn, Ludovic Berthier, Thibaut Divoux, and Sébastien Manneville. Yield stress materials in soft condensed matter. *Reviews of Modern Physics*, 89(3):035005, 2017.

[26] Laurent Jossic, Pauline Lefevre, Clement De Loubens, Albert Magnin, and Christophe Corre. The fluid mechanics of shear-thinning tear substitutes. *J. Non-Newtonian Fluid Mech.*, 161(1-3):1–9, 2009.

[27] M. Renardy. Similarity solutions for jet breakup for various models of viscoelastic fluids. *J. Non-Newtonian Fluid Mech.*, 104(1):65–74, 2002.

[28] P. Doshi and O. A. Basaran. Self-similar pinch-off of power law fluids. *Phys. Fluids*, 16(3):585–593, 2004.

[29] P. Doshi, R. Suryo, O. E. Yildirim, G. H. McKinley, and O. A. Basaran. Scaling in pinch-off of generalized Newtonian fluids. *J. Non-Newtonian Fluid Mech.*, 113(1):1–27, 2003.

[30] R. Suryo and O. A. Basaran. Local dynamics during pinch-off of liquid threads of power law fluids: Scaling analysis and self-similarity. *J. Non-Newtonian Fluid Mech.*, 138(2):134–160, 2006.

[31] Vishrut Garg, Pritish M Kamat, Christopher R Anthony, Sumeet S Thete, and Osman A Basaran. Self-similar rupture of thin films of power-law fluids on a substrate. *J. Fluid Mech.*, 826:455–483, 2017.

[32] J. Q. Feng and O. A. Basaran. Shear-flow over a translationally symmetrical cylindrical bubble pinned on a slot in a plane wall. *J. Fluid Mech.*, 275:351–378, 1994.

[33] E. D. Wilkes, S. D. Phillips, and O. A. Basaran. Computational and experimental analysis of dynamics of drop formation. *Phys. Fluids*, 11(12):3577–3598, 1999.

[34] K. N. Christodoulou and L. E. Scriven. Discretization of free surface flows and other moving boundary problems. *J. Comput. Phys.*, 99(1):39–55, 1992.

[35] Patrick K. Notz and Osman A. Basaran. Dynamics and breakup of a contracting liquid filament. *J. Fluid Mech.*, 512:223–256, 2004.

[36] P. P. Bhat, S. Appathurai, M. T. Harris, M. Pasquali, G. H. McKinley, and O. A. Basaran. Formation of beads-on-a-string structures during break-up of viscoelastic filaments. *Nat. Phys.*, 6(8):625–631, 2010.

[37] J. R. Castrejón-Pita, A. A. Castrejón-Pita, S. S. Thete, K. Sambath, I. M. Hutchings, J. Hinch, J. R. Lister, and O. A. Basaran. Plethora of transitions during breakup of liquid filaments. *Proc. Natl. Acad. Sci. USA*, 112(15):4582–4587, 2015.

[38] Pritish M Kamat, Brayden W Wagoner, Sumeet S Thete, and Osman A Basaran. Role of marangoni stress during breakup of surfactant-covered liquid threads: Reduced rates of thinning and microthread cascades. *Phys. Rev. Fluids*, 3(4):043602, 2018.

[39] J. D. Paulsen, J.C. Burton, S. R. Nagel, S. Appathuri, M. T. Harris, and O. A. Basaran. The inexorable resistance of inertia determines the initial regime of drop coalescence. *Proc. Nat. Acad. Sci.*, 109(18):6857–6861, 2002.

[40] J. P. Munro, C. R. Anthony, O. A. Basaran, and J. R. Lister. Thin-sheet flow between coalescing bubbles. *J. Fluid Mech.*, 773:R3, 2015.

[41] Christopher R Anthony, Pritish M Kamat, Sumeet S Thete, James P Munro, John R Lister, Michael T Harris, and Osman A Basaran. Scaling laws and dynamics of bubble coalescence. *Phys. Rev. Fluids*, 2(8):083601, 2017.

[42] L. G. Leal. *Advanced Transport Phenomena: Fluid Mechanics and Convective Transport Processes*. Cambridge University Press, New York, 2007.

[43] Michael P Brenner, John R Lister, and Howard A Stone. Pinching threads, singularities and the number 0.0304... *Phys. Fluids*, 8(11):2827–2836, 1996.

[44] Sumeet Suresh Thete. *Singularities in free surface flows*. PhD thesis, Purdue University, 2016.

[45] Demetrios T Papageorgiou. Analytical description of the breakup of liquid jets. *J. Fluid Mech.*, 301:109–132, 1995.

[46] JC Burton and P Taborek. Two-dimensional inviscid pinch-off: An example of self-similarity of the second kind. *Phys. Fluids*, 19(10):102109, 2007.

[47] Brayden W Wagoner, Sumeet S Thete, and Osman A Basaran. A new experimental method based on volume measurement for determining axial scaling during breakup of drops and liquid threads. *Phys. Fluids*, 30(8):082102, 2018.

[48] Lorene Champougny, Jonas Miguet, Robin Henaff, Frederic Restagno, Francois Boulogne, and Emmanuelle Rio. Influence of evaporation on soap film rupture. *Langmuir*, 34(10):3221–3227, 2018.

[49] Jérôme Boulanger, Charles Gueudry, Daniel Münch, Bertrand Cinquin, Perrine Paul-Gilloteaux, Sabine Bardin, Christophe Guérin, Fabrice Senger, Laurent Blanchoin, and Jean Salamero. Fast high-resolution 3d total internal reflection fluorescence microscopy by incidence angle scanning and azimuthal averaging. *Proc. Nat. Acad. Sci.*, 111(48):17164–17169, 2014.

[50] T. P. Witelski and A. J. Bernoff. Stability of self-similar solutions for van der Waals driven thin film rupture. *Phys. Fluids*, 11(9):2443–2445, 1999.

[51] Markus Rauscher, Andreas Muench, Barbara Wagner, and Ralf Blossey. A thin-film equation for viscoelastic liquids of jeffreys type. *The European Physical Journal E*, 17(3):373–379, 2005.

4. SELF-SIMILAR RUPTURE OF THIN FILMS OF POWER-LAW FLUIDS ON A SUBSTRATE

Note: This chapter is adapted from an article published in J. Fluid. Mech, 2017. Reprinted with Permission: Garg, V., Kamat, P., Anthony, C., Thete, S., & Basaran, O. (2017). Self-similar rupture of thin films of power-law fluids on a substrate. Journal of Fluid Mechanics, 826, 455-483, COPYRIGHT 2017, Cambridge University Press

4.1 Abstract

Thinning and rupture of a thin film of a power-law fluid on a solid substrate under the balance between destabilizing van der Waals pressure and stabilizing capillary pressure is analyzed. In a power-law fluid, viscosity is not constant but is proportional to the deformation rate raised to the $n-1$ power, where $0 < n \leq 1$ is the power-law exponent ($n = 1$ for a Newtonian fluid). In the first part of the paper, use is made of the slenderness of the film and the lubrication approximation is applied to the equations of motion to derive a spatially one-dimensional nonlinear evolution equation for film thickness. The variation with time remaining until rupture of the film thickness, the lateral length scale, fluid velocity, and viscosity is determined analytically and confirmed by numerical simulations for both line rupture and point rupture. The self-similarity of the numerically computed film profiles in the vicinity of the location where the film thickness is a minimum is demonstrated by rescaling of the transient profiles with the scales deduced from theory. It is then shown that in contrast to films of Newtonian fluids undergoing rupture for which inertia is always negligible, inertia can become important during thinning of films of power-law fluids

in certain situations. The critical conditions for which inertia becomes important and the lubrication approximation is no longer valid are determined analytically. In the second part of the paper, thinning and rupture of thin films of power-law fluids in situations when inertia is important are simulated by solving numerically the spatially two-dimensional, transient Cauchy momentum and continuity equations. It is shown that as such films continue to thin, a change of scaling occurs from a regime in which van der Waals, capillary, and viscous forces are important to one where the dominant balance of forces is between van der Waals, capillary, and inertial forces while viscous force is negligible.

4.2 Introduction

Thin liquid films are omnipresent in daily life and industry. Examples abound in coating flows [1], microfluidic devices [2], foam stability [3], and drop coalescence [4]. Understanding the dynamics of thin film rupture is central to many of these applications. For example, the formation of dry spots in cooling systems relying on thin-film flows driven by shear [5] can lead to loss of heat transfer efficiency. Premature rupture of the tear film in the eye can lead to dry-eye syndrome [6], a medical condition. The drainage of liquid films between gas bubbles and mineral particles is an important step in froth flotation [7].

In many of the aforementioned examples, the thickness of the film is of the order of or less than a micrometer and, therefore, long-range intermolecular forces become significant in deciding the fate of the film and its stability [9–11]. The dewetting of a solid surface by film thinning and rupture has been termed spinodal dewetting [12] and has been observed experimentally [8,13,14], as shown by the AFM scans of figure 4.1 from Becker et al. [8] that depict the rupture of a PS film on a silicon wafer. Contributions to the free energy of the thin film due to intermolecular interactions lead to the addition of a disjoining pressure term [15] to the fluid pressure.

Consider a liquid film of uniform thickness h_0 that completely wets the solid substrate on which it is lying and that is surrounded by a dynamically passive gas

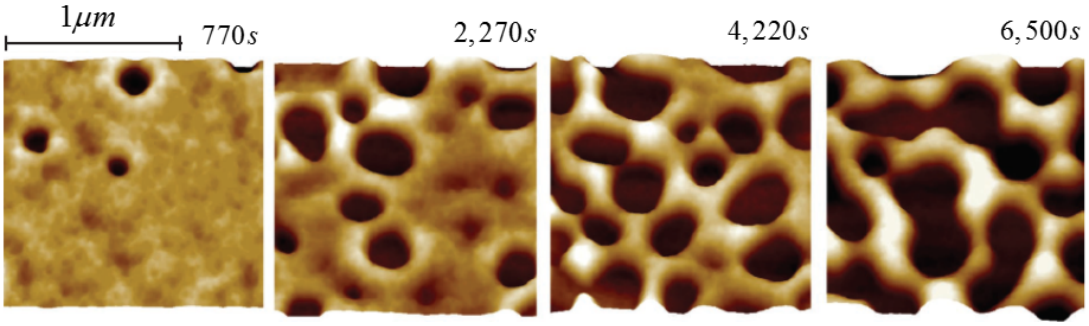

Figure 4.1. Temporal series of AFM scans recorded experimentally showing rupture of a 3.9 nm PS film on an oxidized Si wafer. For this system, the values of the Hamaker constant, surface tension, and viscosity are 2.2×10^{-20} J, 30.8 mN/m, and 12,000 Pa·s. The scale bar that is shown above the leftmost aimage applies to all four images. Adapted by permission from Macmillan Publishers Ltd: Nature Materials (Becker et al. [8]), copyright 2003.

such as air, as shown in figure 4.2. Next consider that the film's surface or the liquid-gas interface is perturbed so that the equation of the film's surface is given by $\tilde{z} = \tilde{h}(\tilde{\mathbf{x}}_{\mathrm{II}})$, with the $\tilde{z}$ coordinate measured in the direction perpendicular to the solid, $\tilde{h}$ is the local film thickness, and $\tilde{\mathbf{x}}_{\mathrm{II}} = \tilde{\mathbf{x}} - \tilde{z}\mathbf{e}_z$ is the two-dimensional position vector that lies in the plane of the solid, with $\tilde{\mathbf{x}}$ and $\mathbf{e}_z$ standing for the position vector and the unit vector in the $\tilde{z}$-direction. The pressure $\tilde{p}$ within a slightly perturbed film is then given by

$$\tilde{p} = \frac{A}{6\pi\tilde{h}^3} - \sigma\,\tilde{\nabla}_{\mathrm{II}}^2\tilde{h} \tag{4.1}$$

Here, the effect of gravity is neglected on account of the film's thinness, the pressure datum is taken to be that of the surrounding air, A is the Hamaker constant, σ is the surface tension, and $\tilde{\nabla}_{\mathrm{II}}$ is the two-dimensional gradient operator given by $\tilde{\nabla}_{\mathrm{II}} \equiv \tilde{\nabla} - \mathbf{e}_z\frac{\partial}{\partial\tilde{z}}$, with $\tilde{\nabla}$ standing for the usual gradient operator. Equation (4.1) makes plain that there are two competing effects in a deformed film: the first term, which corresponds to the van der Waals pressure, is destabilizing because it would cause flow from the troughs, or valleys, to the crests, or hills, and lead to further

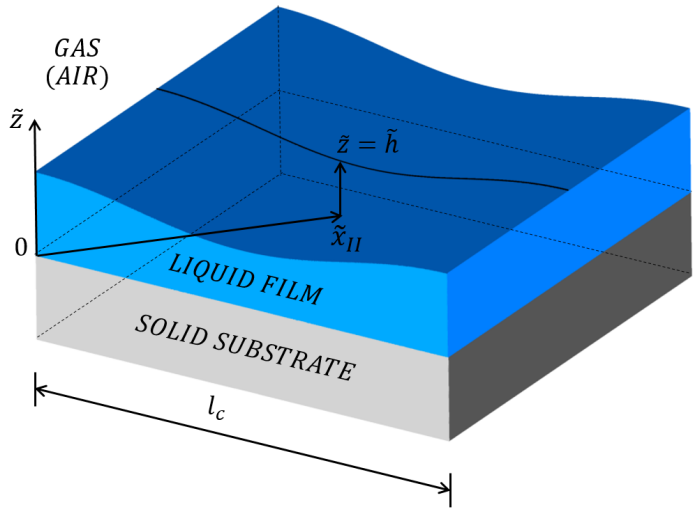

Figure 4.2. A thin film that is supported on a solid substrate and overlaid by a dynamically passive gas, e.g. air.

localized thinning of the film whereas the second term, which corresponds to the capillary or surface tension pressure, is stabilizing, because it would cause flow from the crests to the troughs and lead to healing of the film. Ruckenstein and Jain [16] developed a dynamic linear stability theory for an isothermal film on a horizontal plate, based on the Navier-Stokes equations in the lubrication or long-wavelength limit modified by the addition of a body force term to account for intermolecular van der Waals attractions. These authors thereby showed that perturbations or disturbances of wavelengths exceeding a critical value $\tilde{\lambda}_c$ are unstable where

$$\tilde{\lambda}_c = \left(\frac{8\pi^3\sigma}{A}\right)^{1/2} {h_0}^2 = 2\pi\frac{h_0}{d}h_0 \tag{4.2}$$

where $d \equiv (A/2\pi\sigma)^{1/2}$ is the molecular length scale. For the continuum approximation to be valid, $h_0 \gg d$, which implies that the critical wavelength is much larger than the film thickness and which justified their use of the lubrication approximation. These authors also calculated a rough estimate of the rupture time.

More recently, Williams and Davis [17] used long-wave theory to derive a nonlinear evolution equation for the thickness of a film of a Newtonian fluid as a function of the lateral space coordinate $\tilde{x}$ and time $\tilde{t}$. These authors reported that the rupture process is accelerated due to the nonlinear terms, thereby leading to rupture times much shorter than those predicted by linear theory. Zhang and Lister [18] solved this equation analytically and numerically to show that the lateral length scale $\tilde{x}' \equiv \tilde{x} - \tilde{x}_R$ and film thickness vary with time remaining to rupture $\tilde{\tau} \equiv \tilde{t}_R - \tilde{t}$, where $(\tilde{x}_R, \tilde{t}_R)$ give the location of the space-time singularity where the film ruptures, as $\tilde{x}' \sim \tilde{\tau}^{2/5}$ and $\tilde{h} \sim \tilde{\tau}^{1/5}$, respectively, where 2/5 and 1/5 are the scaling exponents, for both line and point rupture. These authors thereby demonstrated that during the rupture of Newtonian films, the dominant force balance is between van der Waals, viscous, and capillary forces. Since the relevant length and time scales in the vicinity of the rupture singularity are orders of magnitude smaller than similar variables in the far field, the dynamics in the vicinity of the rupture singularity is self-similar (see, e.g., Barenblatt [19] who discusses that self-similarity arises in problems that lack a length scale and Eggers [20, 21] on the closely related problem of capillary pinching of liquid jets). With the scaling exponents in hand, an ordinary differential equation can then be derived for the self-similar film profile in similarity space. Zhang and Lister [18] demonstrated that transient solutions for the film profile and certain other quantities obtained by solving the partial differential evolution equation can be collapsed onto self-similar profiles and are in excellent agreement with the self-similar profiles obtained by solving the afore-mentioned ordinary differential equation in similarity space.

While the studies discussed in the previous two paragraphs were concerned with Newtonian fluids, many fluids in industrial and everyday applications are non-Newtonian in nature. An important type of a non-Newtonian fluid is the so-called power-law fluid. It derives its name from the power-law dependence [22] of the viscosity $\tilde{\mu}$ on the deformation rate $\tilde{\dot{\gamma}}$ and is given by

$$\tilde{\mu}\left(\tilde{\dot{\gamma}}\right) = \mu_0 \left|2\tilde{m}\tilde{\dot{\gamma}}\right|^{n-1} \tag{4.3}$$

Here, μ_0 is the zero-deformation-rate viscosity of the fluid, $\tilde{m}^{-1}$ is the characteristic deformation rate, n, where $0 < n \leq 1$, is the power-law exponent or index ($n = 1$ corresponds to a Newtonian fluid), and $\tilde{\dot{\gamma}}$ is the second invariant of the rate-of-deformation tensor $\tilde{\mathbf{D}}$

$$\tilde{\dot{\gamma}} = \left[\frac{1}{2}\left(\tilde{\mathbf{D}} : \tilde{\mathbf{D}}\right)\right]^{\frac{1}{2}} \tag{4.4}$$

$$\tilde{\mathbf{D}} = \frac{1}{2}\left[\left(\tilde{\nabla}\tilde{\mathbf{v}}\right) + \left(\tilde{\nabla}\tilde{\mathbf{v}}\right)^{T}\right] \tag{4.5}$$

where $\tilde{\mathbf{v}}$ is the fluid velocity. It has been shown experimentally that many fluids in industrial applications and in every day use exhibit power-law rheology [23–26].

To date, extensive work has been done on the pinch-off singularity that arises during the breakup of threads or jets of power-law fluids. Scaling exponents and, in some cases, scaling functions or similarity profiles derived analytically [27–29] have been verified by comparison against numerical simulations [28–30] and experiments [25,26]. Previous works on thin films of power-law fluids on a substrate have dealt with the dynamics of films flowing down inclined planes [31], falling films [32], films on cylinders [33], films on rotating discs [34], and tear films [35] albeit without delving into the self-similar dynamics that arises during film rupture. Moreover, while the study of the dynamics of rupture of thin free films or sheets of Newtonian fluids by Vaynblat, Lister and Witelski [36] has recently been extended to power-law fluids by Thete et al. [37], studies have not been carried out to extend the pioneering study of Zhang and Lister [18] on rupture of supported films of Newtonian fluids to films of non-Newtonian fluids exhibiting power-law rheology. Filling this gap in knowledge on the rupture of supported films is the main goal of this work.

The organization of the paper is as follows. Section 4.3 describes in detail the problem under investigation and summarizes succinctly the equations and boundary conditions governing film thinning. Section 4.4 presents a derivation of the governing equations in the lubrication limit. Section 4.5 then derives and presents the nonlinear

evolution equation for the transient film profile for the case of two-dimensional or line rupture, and analyzes theoretically and computationally the rupture of a thin film of a power-law fluid. Section 4.6 provides a treatment that mirrors that of the previous section albeit for situations in which a film undergoes axisymmetric or point rupture. Section 4.7 determines the conditions for which inertia becomes important and the lubrication approximation is no longer valid. Section 4.8 summarizes the mathematical formulation of the problem for solving the equations governing film thinning without invoking the lubrication approximation and when inertia is important. This section presents the scaling exponents for the variation with time from rupture of the film thickness, the lateral length scale, and the lateral velocity that are expected in a thinning regime where inertia is important. In this section, the numerical method that is used to solve the transient, spatially two-dimensional set of partial differential equations comprised of the continuity and Cauchy momentum equations is also presented. In section 4.9, solutions obtained by solving the fully two-dimensional set of the aforementioned partial differential equations are presented and a transition from an initial thinning regime in which inertia is negligible to a final regime in which inertia is important is demonstrated. Section 4.10 concludes the paper by summarizing the results presented and outlining some possible future avenues for extending the analyses carried out in this work.

4.3 Problem statement

The system is an isothermal thin film of an incompressible power-law liquid of constant density ρ, non-constant viscosity $\tilde{\mu}$, and constant Hamaker constant A, as shown in figure 4.2. The film is initially quiescent and of uniform thickness h_0. The film overlays or sits on top of a homogeneous solid substrate. The liquid-solid surface of contact is taken to coincide with the $\tilde{x}\tilde{y}$-plane of a Cartesian coordinate system $(\tilde{x}, \tilde{y}, \tilde{z})$ or the $\tilde{r}\theta$-plane of a cylindrical polar coordinate system $(\tilde{r}, \theta, \tilde{z})$ with its origin located on that surface and with the $\tilde{z}$ coordinate measured in the direction perpendicular to the solid. The film is overlayed by a dynamically passive gas, e.g.

air, that exerts a constant pressure, set equal to zero w.l.o.g., on the film. The surface tension of the liquid-gas interface σ is spatially uniform and constant.

The flow within the film is governed by the continuity and Cauchy momentum equations

$$\tilde{\nabla} \cdot \tilde{\mathbf{v}} = 0 \tag{4.6}$$

$$\rho \left(\frac{\partial \tilde{\mathbf{v}}}{\partial \tilde{t}} + \tilde{\mathbf{v}} \cdot \tilde{\nabla} \tilde{\mathbf{v}} \right) = \tilde{\nabla} \cdot \tilde{\mathbf{T}} \tag{4.7}$$

Here, $\tilde{\mathbf{v}}$ is the velocity, $\tilde{t}$ is time, and $\tilde{\mathbf{T}} = -\tilde{p}\mathbf{I} + \tilde{\boldsymbol{\tau}}$ is the stress tensor with $\tilde{p}$ the pressure and $\tilde{\boldsymbol{\tau}}$ the viscous stress tensor. For a power-law liquid, $\tilde{\boldsymbol{\tau}} = 2\tilde{\mu}\tilde{\mathbf{D}}$. In equation (4.7) and the remainder of the paper, the effect of gravity on the dynamics is also taken to be negligible on account of the film's thinness.

Along the solid surface bounding the liquid film ($\tilde{z} = 0$), the liquid must obey no slip and no penetration or the adherence boundary condition

$$\tilde{\mathbf{v}} = \mathbf{0} \tag{4.8}$$

At the liquid-gas interface, the kinematic and traction boundary conditions are applied to enforce no mass transfer across the free surface $S(\tilde{t})$ and the jump in the traction vector due to surface tension and van der Waals forces:

$$\mathbf{n} \cdot (\tilde{\mathbf{v}} - \tilde{\mathbf{v}}_s) = 0 \tag{4.9}$$

$$\mathbf{n} \cdot \mathbf{T} = 2\tilde{H}\sigma\,\mathbf{n} - \frac{A}{6\pi\tilde{h}^3}\,\mathbf{n} \tag{4.10}$$

Here, $\tilde{\mathbf{v}}_s$ is the velocity of points on the interface $S(\tilde{t})$, and $\mathbf{n}$ is the unit normal vector to and $2\tilde{H}$ is twice the mean curvature of $S(\tilde{t})$.

In addition to the boundary conditions that have been imposed in the vertical direction, i.e. along the free surface $S(\tilde{t})$ and the solid substrate ($\tilde{z} = 0$), boundary conditions also need to be specified in the lateral direction. The latter are presented in the following sections when different rupture scenarios are analyzed. The mathematical statement of the problem is completed by the specification of initial conditions.

These too are provided in subsequent sections where the lateral boundary conditions are specified.

4.4 Film rupture in the lubrication limit

As the disturbances that cause the film to destabilize are of long wavelengths $\tilde{\lambda}$, advantage will be taken in this section of the fact that $\epsilon \equiv h_0/l_c \ll 1$, where $l_c = O(\tilde{\lambda})$ is the lateral or horizontal length scale, to simplify the governing Cauchy momentum and continuity equations by invoking the lubrication approximation [22, 38]. The process of simplification of the governing equations and the derivation of the lubrication equations is presented in the appendix 4.11.

The equations governing the flow within the film in dimensional form are then given by

$$-\tilde{\nabla}_{\mathrm{II}}\tilde{p} + \frac{\partial}{\partial \tilde{z}}\left(\tilde{\mu}\frac{\partial \tilde{\mathbf{v}}_{\mathrm{II}}}{\partial \tilde{z}}\right) = 0 \tag{4.11}$$

$$\frac{\partial \tilde{p}}{\partial \tilde{z}} = 0 \tag{4.12}$$

$$\frac{\partial \tilde{h}}{\partial \tilde{t}} + \tilde{\nabla}_{\mathrm{II}} \cdot \int_0^{\tilde{h}} \tilde{\mathbf{v}}_{\mathrm{II}}\, d\tilde{z} = 0 \tag{4.13}$$

where $\tilde{\mathbf{v}}_{\mathrm{II}} \equiv \tilde{\mathbf{v}} - \tilde{w}\mathbf{e}_z$ is the velocity parallel to the substrate and $\tilde{w}$ is the component of the velocity in the direction normal to it. As shown in the appendix 4.11, equations (4.11) and (4.12) follow from the horizontal and vertical components of the Cauchy momentum equation after invoking the lubrication approximation. It can be readily shown that in thin film flow, $\tilde{\dot{\gamma}}^2 = \frac{1}{4}\,(\partial \tilde{\mathbf{v}}_{\mathrm{II}}/\partial \tilde{z}) \cdot (\partial \tilde{\mathbf{v}}_{\mathrm{II}}/\partial \tilde{z})$ so that the viscosity of the film fluid is given by

$$\tilde{\mu}\left(\tilde{\dot{\gamma}}\right) = \mu_0 \left| \tilde{m}\left(\frac{\partial \tilde{\mathbf{v}}_{\mathrm{II}}}{\partial \tilde{z}} \cdot \frac{\partial \tilde{\mathbf{v}}_{\mathrm{II}}}{\partial \tilde{z}}\right)^{1/2} \right|^{n-1} \tag{4.14}$$

Equation (4.13) results when the continuity equation is integrated across the film thickness and is then combined with the kinematic boundary condition at the liquid-gas interface. In these equations and below, $\tilde{z} = \tilde{h}(\tilde{\mathbf{x}}_{\mathrm{II}}, \tilde{t})$ gives the location of the liquid-gas interface where $\tilde{h}$ is the instantaneous value of the local film thickness. As is the case with all lubrication flows, equation (4.12) shows that the pressure does not vary across the film and when this result is combined with the normal component of the traction boundary condition at the film's surface, it follows that the pressure within the film is given by equation (4.1). Equations (4.11)-(4.13) are solved subject to the following boundary conditions:

$$\tilde{\mathbf{v}}_{\mathrm{II}} = \mathbf{0} \qquad \text{at} \quad \tilde{z} = 0 \tag{4.15}$$

$$\frac{\partial \tilde{\mathbf{v}}_{\mathrm{II}}}{\partial \tilde{z}} = \mathbf{0} \qquad \text{at} \quad \tilde{z} = \tilde{h} \tag{4.16}$$

Equation (4.15) is the usual no slip boundary condition on the substrate and the free slip condition at the film's surface in equation (4.16) follows from the tangential component of the traction boundary condition in the lubrication limit.

Before solving the equations governing film thinning and rupture, it is advantageous to nondimensionalize the problem variables. This is accomplished by introducing the following characteristic scales for film thickness h_c, lateral length l_c, time t_c, pressure p_c, and lateral velocity u_c

$$h_c \equiv h_0 \tag{4.17}$$

$$l_c \equiv \frac{h_0^2}{d} = \frac{\tilde{\lambda}_c}{2\pi} \tag{4.18}$$

$$t_c \equiv \frac{12\pi^2 \mu_0 \sigma {h_0}^5}{A^2} = 3\left(\frac{\mu_0 h_0}{\sigma}\right)\left(\frac{h_0}{d}\right)^4 \tag{4.19}$$

$$p_c \equiv \frac{A}{6\pi h_0^3} = \frac{\sigma h_0}{3 l_c^2} \tag{4.20}$$

$$u_c \equiv \frac{l_c}{t_c} = \frac{1}{3}\left(\frac{\sigma}{\mu_0}\right)\left(\frac{d}{h_0}\right)^3 \tag{4.21}$$

With these scales, the dimensionless variables are then given by:

$$h \equiv \frac{\tilde{h}}{h_0}\,, \quad z \equiv \frac{\tilde{z}}{h_0}\,, \quad t \equiv \frac{\tilde{t}}{t_c} \tag{4.22}$$

$$\mathbf{x}_{\mathrm{II}} \equiv \frac{\tilde{\mathbf{x}}_{\mathrm{II}}}{l_c}\,, \quad \nabla_{\mathrm{II}} \equiv l_c \tilde{\nabla}_{\mathrm{II}}\,, \quad \lambda \equiv \frac{\tilde{\lambda}}{l_c} \tag{4.23}$$

$$p \equiv \frac{\tilde{p}}{p_c}\,, \quad \mathbf{v}_{\mathrm{II}} \equiv \frac{\tilde{\mathbf{v}}_{\mathrm{II}}}{u_c} \tag{4.24}$$

$$\mu \equiv \frac{\tilde{\mu}}{\mu_0}\,, \quad m \equiv \tilde{m}\frac{u_c}{h_0} \tag{4.25}$$

In equations (4.22)-(4.25), variables without tildes over them are the dimensionless counterparts of those with tildes.

In the following two sections, the governing equations (4.11)-(4.13), subject to the boundary conditions (4.15)-(4.16), written in dimensionless form will be solved first for the case of line rupture or when the rupture is two-dimensional and then for the case of point rupture or when the rupture is axisymmetric. In both cases, the initial conditions will entail subjecting a quiescent flat film to a periodic shape perturbation having a wavelength exceeding $\lambda_c \equiv \tilde{\lambda}_c/l_c = 2\pi$ and following the thinning of the film until rupture.

4.5 Two-dimensional or line rupture in the lubrication limit

In this section, the initially flat surface of the film is subjected to a sinusoidal shape perturbation that is translationally symmetric or invariant in the y-direction, where $y \equiv \tilde{y}/l_c$, and has wavelength λ in the lateral or x-direction, where $x \equiv \tilde{x}/l_c$, as shown in figure 4.3. Since the perturbation is two-dimensional in nature, equation (4.11) subjected to boundary conditions (4.15) and (4.16) is solved in Cartesian coordinates such that $\mathbf{v}_{\mathrm{II}} = u(x,z,t)\mathbf{e}_x$ and $\nabla_{\mathrm{II}} = \mathbf{e}_x \frac{\partial}{\partial x}$, where $\mathbf{e}_x$ is a unit vector in the x-direction, to arrive at the following expression for the dimensionless lateral velocity $u(x,z,t)$

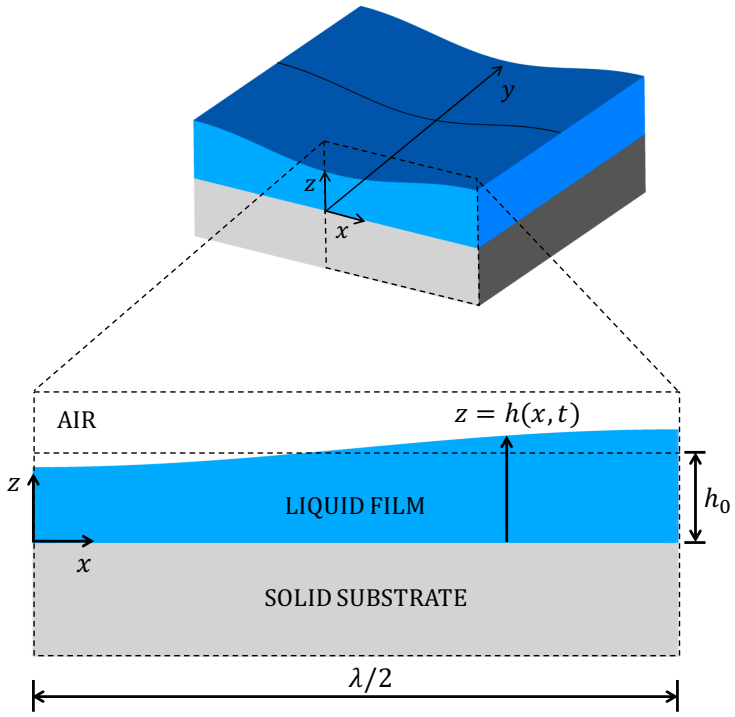

Figure 4.3. Line rupture. Top: perspective view of a film on a substrate showing the deformed interface over a lateral extent corresponding to one wavelength λ of the imposed perturbation. Bottom: a blowup or zoomed in cross-sectional view of the film over a lateral extent corresponding to a half of a wavelength of the imposed perturbation. Because of symmetry, the problem domain is $0 \leq x \leq \lambda/2$.

$$u(x,z,t) = \frac{n}{n+1}\frac{|\partial p/\partial x|}{\partial p/\partial x} m^{\frac{1}{n}-1} \left|\frac{\partial p}{\partial x}\right|^{1/n} \left[(h-z)^{1/n+1} - h^{1/n+1}\right] \tag{4.26}$$

where $h(x,t)$ is the dimensionless local film thickness. In arriving at equation (4.26), use is made of the fact that in Cartesian coordinates, the dimensionless viscosity (cf. equation (4.14)) and the dimensionless fluid pressure $p(x,t)$ are given by

$$\mu = \left|m\frac{\partial u}{\partial z}\right|^{n-1} \tag{4.27}$$

$$p(x,t) = \frac{1}{h^3} - 3\frac{\partial^2 h}{\partial x^2} \tag{4.28}$$

When the expression for u given by equation (4.26) is substituted into equation (4.13), a spatially one-dimensional (1D), nonlinear evolution equation results that governs the variation of the film thickness with the dimensionless lateral coordinate x and dimensionless time t

$$\frac{\partial h}{\partial t} - \frac{|\partial p/\partial x|}{\partial p/\partial x} m^{\frac{1}{n}-1} \frac{\partial}{\partial x}\left[\frac{n}{2n+1}\left|\frac{\partial p}{\partial x}\right|^{\frac{1}{n}} h^{\frac{1}{n}+2}\right] = 0 \tag{4.29}$$

Because of the periodic nature of the imposed perturbation, it is sufficient to solve the problem over the spatial domain spanning one half of the wavelength of the imposed perturbation, viz. $0 \leq x \leq \lambda/2$, as shown in figure 4.3. Hence, the 1D evolution equation is solved subject to the symmetry boundary conditions

$$\frac{\partial h}{\partial x} = \frac{\partial^3 h}{\partial x^3} = 0 \qquad \text{at} \quad x = 0,\, \lambda/2 \tag{4.30}$$

and initial condition

$$h(x, 0) = 1 - \delta \cos(2\pi x/\lambda) \tag{4.31}$$

where δ is the amplitude of the perturbation that is imposed to initiate the thinning of the film.

4.5.1 Scaling and self-similarity

The film profile is expected to be self-similar in the vicinity of the location where the film thickness is minimum as the rupture singularity (x_R, t_R) is approached. Hence, by the similarity ansatz, the film profile in the vicinity of the rupture point should have the functional form

$$h(x', \tau) = \tau^{\alpha} H(\eta), \qquad \eta = x'/\tau^{\beta} \tag{4.32}$$

where $\tau \equiv t_R - t$ is the dimensionless time remaining until rupture, $x' \equiv x - x_R$ is the lateral extent of this rupture zone, η is the similarity variable, α and β are the

scaling exponents for h and x', respectively, and $H(\eta)$ is the scaling function for the film profile in similarity space. Either (a) substituting equation (4.32) into equations (4.29), (4.27), and (4.28) and requiring that the resulting ordinary differential equation in similarity space be independent of time or (b) balancing the van der Waals (vdW), surface tension or capillary (ST), and viscous (V) stresses in equation (4.11) and equations (4.27) and (4.28) shows that the scaling exponents α and β are given by

$$\alpha = \frac{n}{n+4}, \qquad \beta = \frac{2n}{n+4} \tag{4.33}$$

It readily follows from the dimensionless form of equation (4.11) and equations (4.27) and (4.28) that the van der Waals (vdW), surface tension or capillary (ST), and viscous (V) stresses scale as

$$vdW \sim \left|\left|\frac{\partial}{\partial x}\left(\frac{1}{h^3}\right)\right|\right| \sim \frac{1}{x'h^3} \tag{4.34}$$

$$ST \sim \left|\left|\frac{\partial}{\partial x}\left(\frac{\partial^2 h}{\partial x^2}\right)\right|\right| \sim \frac{h}{x'^3} \tag{4.35}$$

$$V \sim \left|\left|\frac{\partial}{\partial z}\left(\mu\frac{\partial u}{\partial z}\right)\right|\right| \sim \left|\left|\frac{\partial}{\partial z}\left(\frac{\partial u}{\partial z}\right)^n\right|\right| \sim \frac{u^n}{z^{n+1}} \sim \frac{(x'/\tau)^n}{h^{n+1}} \tag{4.36}$$

where $||(\cdots)||$ stands for the magnitude of the quantity "$(\cdots)$". Therefore, with the scaling exponents given by equation (4.33), all three stresses can be seen to scale as $\tau \to 0$ as

$$vdW \sim ST \sim V \sim \tau^{-\frac{5n}{n+4}} \tag{4.37}$$

A noteworthy feature of the dynamics is that the scaling exponent for the lateral length scale β is twice that for the vertical length scale (or film thickness) β, viz. $\beta = 2\alpha$. The reason for this relationship between the two scaling exponents follows from the balance between the van der Waals and surface tension stresses (cf. equations (4.34) and (4.35). Initially, the lateral extent of the film is orders of magnitude larger than its thickness. As the film continues to thin and tends toward rupture, the rupture

zone shrinks and hence both the lateral and vertical length scales in the vicinity of the point of rupture tend to zero. Therefore, given the initial disparity in the two length scales, it accords with intuition that the lateral length scale should tend to zero faster than the film thickness. For future reference, it is worth noting that fluid viscosity in the thinning film scales as

$$\mu \sim \left|\left|\frac{\partial u}{\partial z}\right|\right|^{n-1} \sim \frac{(x'/\tau)^{n-1}}{z^{n-1}} \sim \tau^{\frac{4(1-n)}{n+4}} \tag{4.38}$$

In concluding this subsection, it is also worth noting that in the Newtonian limit ($n = 1$), the expressions in equation (4.33) for the scaling exponents take on the values of $\alpha = 1/5$ and $\beta = 2/5$ and all three stresses diverge as τ^{-1} (cf. equation (4.37), in agreement with previous work on rupture of Newtonian films [18].

4.5.2 Simulation of line rupture in the lubrication limit

The spatially fourth-order nonlinear evolution equation (4.29) subject to boundary conditions (4.30) and initial condition (4.31) with $\delta = 0.1$ is solved numerically using a Galerkin finite element-based method to verify the scaling exponents that have just been determined and to demonstrate the self-similarity of the film profiles in the rupture zone. We have used variants of this algorithm to successfully solve 1D long-wave evolution equations that arise in a variety of physical problems including dripping and jetting of Newtonian [39] as well as power-law fluids [40] from faucets, breakup of bridges of Newtonian [41] and power-law fluids [42], and rupture of sheets of Newtonian and power-law fluids [37], among others.The simulation results to be reported have been obtained using a value of $\lambda = 4\pi$. Use of larger values of the wavelength had no effect whatsoever on the values of the scaling exponents and the behavior of the solutions in the vicinity of the point of rupture.

Figure 4.4 shows at several instants in time computed profiles of a thinning film of power-law index of $n = 0.83$. In this situation and in all the other ones that have been considered, the minimum film thickness is always located at $x = 0$, viz. $h_{\min} = h(0, t)$, or the film always ruptures symmetrically at $x = 0$ so that $x_R = 0$ and $x' = x$.

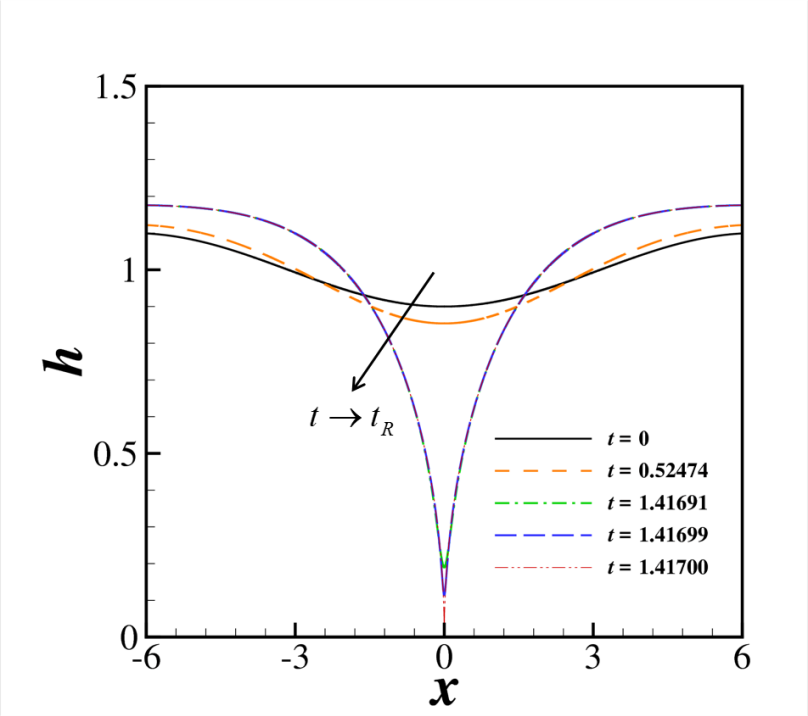

Figure 4.4. Computed instantaneous film profiles $h = h(x,t)$ as a function of the lateral coordinate x for a thinning film of power-law index of $n = 0.83$. Starting with a slightly deformed profile at $t = 0$, the interface profiles are seen to steepen as $t \to t_R$ and rupture nears. Here, the rupture time $t_R \doteq 1.41700$.

Figure 4.5 shows the computed variation with time remaining until rupture of several quantities of interest in the rupture zone for the film of power-law index of $n = 0.83$. The simulation results of figure 4.5(a) show that $h_{\min}$ decreases with τ as $h_{\min} \sim \tau^{0.172}$, a result that is in excellent agreement with the theoretical prediction (cf. equations (4.32) and (4.33)) that $h_{\min} \sim \tau^{n/(n+4)}\,|_{n=0.83} \equiv \tau^{0.172}$. The scaling of the lateral length has been determined in two different ways. The first method involves determining how the computed value of the film's curvature, $\partial^2 h/\partial x^2$, evaluated at $x = 0$ varies with τ and using this result, along with the known scaling for h, to determine the scaling for x. The curvature is expected to scale as

$$\frac{\partial^2 h}{\partial x^2} \sim \frac{h}{x^2} \sim \tau^{\alpha-2\beta} \sim \tau^{-\frac{3n}{n+4}} \tag{4.39}$$

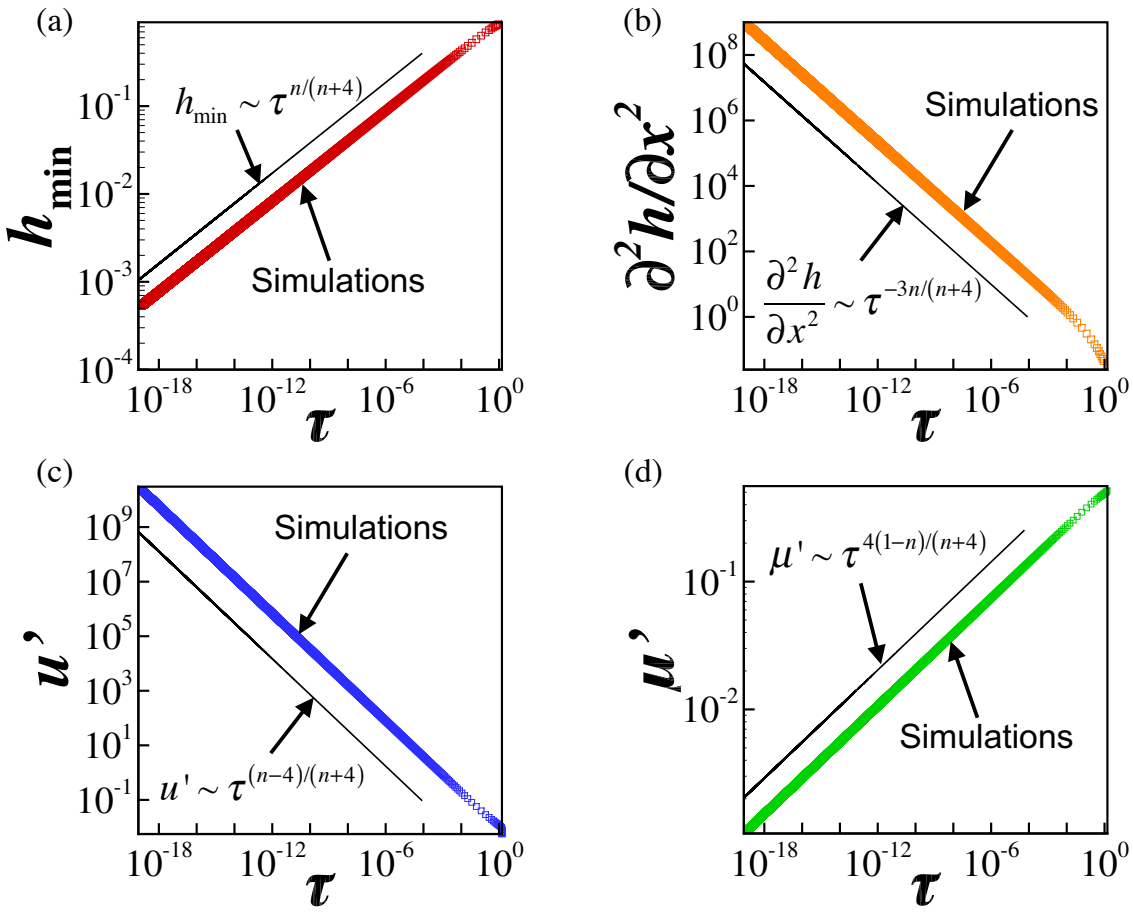

Figure 4.5. Scaling behavior of variables in the rupture zone during thinning of a film of power-law index of $n = 0.83$ undergoing line rupture: simulations (data points) and scaling theory predictions (straight lines with indicated dependencies on time remaining until rupture τ). Variation with τ of (a) minimum film thickness $h_{\min}$, (b) curvature $\partial^2 h/\partial x^2$ evaluated at $x = 0$, (c) lateral velocity u' evaluated at lateral location where $h = 1.001 h_{\min}$, and (d) viscosity μ' evaluated at that lateral location.

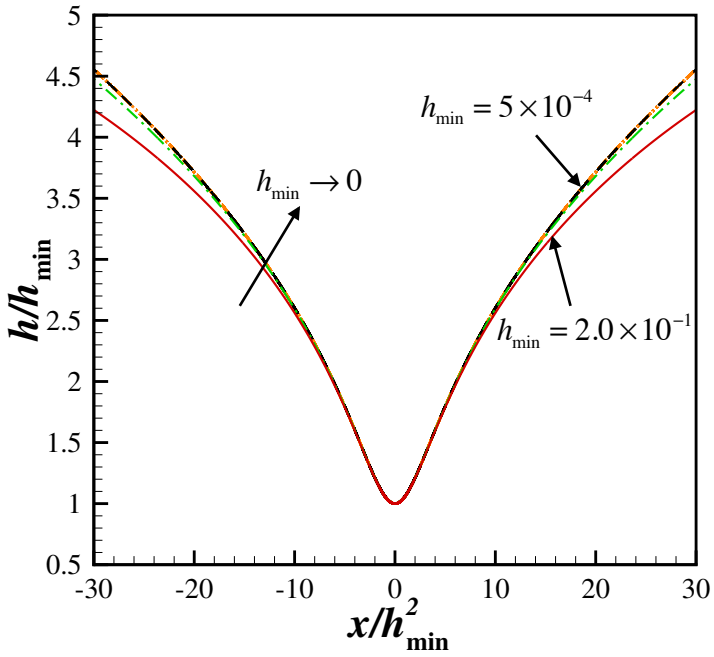

Figure 4.6. Rescaled interface shape $h/h_{\min}$ as a function of rescaled lateral coordinate $x/h_{\min}^2$ at several instants in time determined from simulations during thinning of a film of power-law index of $n = 0.83$ undergoing line rupture. The rescaled transient profiles are shown for values of $5 \times 10^{-4} \leq h_{\min} \leq 2.0 \times 10^{-1}$. Each rescaled interface shape corresponding to a successively smaller value of $h_{\min}$ is such that the value of the minimum film thickness is roughly half that of the previously shown rescaled profile. The rescaled profiles are seen to approach or collapse onto a similarity profile as $h_{\min} \to 0$.

Figure 4.5(b) shows the computed value of the curvature at $x = 0$ blows up with τ as $\frac{\partial^2 h}{\partial x^2}(0,t) \sim \tau^{-0.515}$, a result that is in excellent accord with the theoretical prediction of $\frac{\partial^2 h}{\partial x^2}(0,t) \sim \tau^{-3n/(n+4)}\,|_{n=0.83} \sim \tau^{-0.515}$. Since the value of the curvature predicted from simulations scales as $\tau^{-0.515}$, it is straightforward to combine this result with the simulation result that $h \sim \tau^{0.172}$ to determine that the lateral length scales as $x \sim \tau^{0.344}$. This result is also in excellent agreement with theory as it follows from equations (4.32) and (4.33) that when $n = 0.83$, the value of the lateral scaling ex-

ponent should be $2(0.172) = 0.344$. The second independent method for determining the scaling of the lateral length is based on monitoring the variation with τ of the lateral location at which the film thickness equals some multiple of the minimum film thickness, which is herein taken to be $1.001h_{\min}$. This latter method directly yields the value of the lateral scaling exponent. Reassuringly, the value of the lateral scaling exponent determined in this manner has been found to be identical to that determined by the first approach. Furthermore, changing the lateral location at which this determination is made, e.g. from $1.001h_{\min}$ to $1.002h_{\min}$, has no effect whatsoever on the value of the scaling exponent β determined from simulations. It is expected from theory that the lateral velocity u should scale as

$$u \sim \frac{x}{\tau} \sim \tau^{\beta-1} \sim \tau^{\frac{n-4}{n+4}} \tag{4.40}$$

Thus, when $n = 0.83$, the scaling exponent of the lateral velocity should equal -0.656. Figure 4.5 (c) shows that the lateral velocity u' computed at the lateral location x' where $h(x', t) = 1.001h_{\min}$ diverges with τ as $u' \sim \tau^{-0.656}$, in accord with theory.

Figure 4.5 (d) shows that the computed variation of the viscosity μ', calculated at lateral location x', with τ is seen to follow the scaling behavior that $\mu' \sim \tau^{0.141}$. This simulation result is also seen to accord nicely with theory in that it follows from equation (4.38) that $\mu \sim \tau^{4(1-n)/(n+4)}\,|_{n=0.83} \sim \tau^{0.141}$.

According to theory (cf. equations (4.32) and (4.33)), $h = \tau^{\alpha} H(\eta)$ and $\eta = x/\tau^{\beta} = x/\tau^{2\alpha}$. Therefore, it also follows from theory that $h_{\min} = \tau^{\alpha} H(0)$ and hence

$$\frac{h}{h_{\min}} = \frac{H(\eta)}{H(0)} \qquad \text{and} \qquad \eta = \frac{x}{[h_{\min}/H(0)]^2} \tag{4.41}$$

Therefore, to demonstrate the self-similarity of the computed film profiles, rescaled interface shapes $h/h_{\min}$ at certain instances in time determined from computations are plotted in figure 4.6 as a function of the rescaled coordinate $x/h_{\min}^2$, which is proportional to the similarity variable η. The rescaled shapes are seen to collapse nicely onto a single profile in the figure as $h_{\min} \to 0$, demonstrating the self-similarity

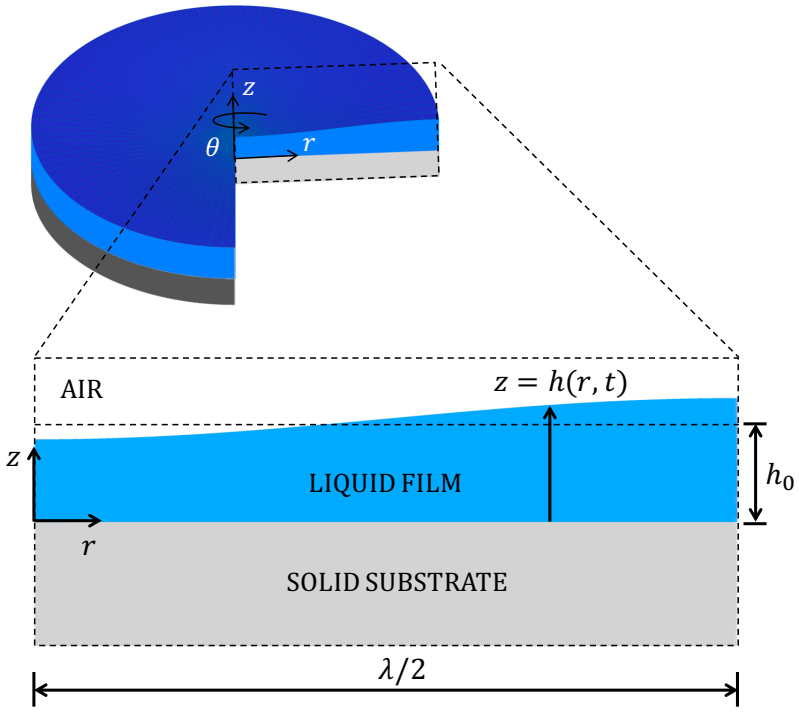

Figure 4.7. Point rupture. Top: perspective view of a film on a substrate showing the deformed interface over a lateral or radial extent corresponding to one half of a wavelength $\lambda/2$ of the imposed perturbation. Bottom: a blowup or zoomed in cross-sectional view of the film over a lateral extent corresponding to one half of a wavelength of the imposed perturbation. Here, the problem domain is $0 \leq r \leq \lambda/2$.

of the dynamics as the rupture singularity is approached. It is noteworthy that plotting the computed solutions in the manner indicated sidesteps the necessity of determining τ from simulations and therefore is preferable to plotting $h/h_{\min}$ as a function of η.

4.6 Axisymmetric or point rupture in the lubrication limit

In this section, the initially flat surface of the film is subjected to a sinusoidal shape perturbation that is axisymmetric or invariant in the θ-direction and has wavelength λ in the lateral (radial) or r-direction, where $r \equiv \tilde{r}/l_c$, as shown in figure

4.7. Since the perturbation is three-dimensional but axisymmetric in nature, equation (4.11) subjected to boundary conditions (4.15) and (4.16) is solved in cylindrical polar coordinates such that $\mathbf{v}_{\mathrm{II}} = u(r,z,t)\mathbf{e}_r$ and $\nabla_{\mathrm{II}} = \mathbf{e}_r\frac{\partial}{\partial r} + \mathbf{e}_\theta\frac{1}{r}\frac{\partial}{\partial\theta}$, where $\mathbf{e}_r$ and $\mathbf{e}_\theta$ are unit vectors in the r- and θ-directions, to arrive at the following expression for the dimensionless lateral velocity $u(r,z,t)$

$$u(r,z,t) = \frac{n}{n+1}\frac{|\partial p/\partial r|}{\partial p/\partial r}m^{\frac{1}{n}-1}\left|\frac{\partial p}{\partial r}\right|^{1/n}\left[(h-z)^{1/n+1} - h^{1/n+1}\right] \tag{4.42}$$

where $h(r,t)$ is the local film thickness. In arriving at equation (4.42), use is made of the fact that in cylindrical polar coordinates, the dimensionless viscosity (cf. equation (4.14)) and the dimensionless fluid pressure $p(r,t)$ are given by

$$\mu = \left|m\frac{\partial u}{\partial z}\right|^{n-1} \tag{4.43}$$

$$p = \frac{1}{h^3} - \frac{3}{r}\frac{\partial}{\partial r}\left(r\frac{\partial h}{\partial r}\right) \tag{4.44}$$

When the expression for u given by equation (4.42) is plugged into equation (4.13), a spatially one-dimensional (1D), nonlinear evolution equation results that governs the variation of the film thickness with the dimensionless lateral coordinate r and dimensionless time t

$$\frac{\partial h}{\partial t} - \frac{|\partial p/\partial r|}{\partial p/\partial r}m^{\frac{1}{n}-1}\frac{1}{r}\frac{\partial}{\partial r}\left[r\frac{n}{2n+1}\left|\frac{\partial p}{\partial r}\right|^{\frac{1}{n}}h^{\frac{1}{n}+2}\right] = 0 \tag{4.45}$$

Because of the periodic nature of the imposed perturbation, it is sufficient to solve the problem over the spatial domain spanning one half of the wavelength of the imposed perturbation, viz. $0 \le r \le \lambda/2$, as shown in figure 4.7. The 1D evolution equation is solved subject to the boundary conditions that

$$\frac{\partial h}{\partial r} = 0 \qquad \text{at} \quad r = 0 \quad \text{and} \quad r = \lambda/2 \tag{4.46}$$

$$Q = 0 \qquad \text{at} \quad r = 0 \quad \text{and} \quad r = \lambda/2 \tag{4.47}$$

where Q is the flow rate. Boundary conditions given by equation (4.47) are conveniently imposed in the Galerkin finite element formulation which through the usual integration by parts gives rise to end point terms at both $r = 0$ and $r = \lambda/2$ that are proportional to Q. Physically, imposing $Q = 0$ at $r = 0$ ensures that $r = 0$ is not a source or a sink of fluid. Imposing $Q = 0$ at $r = \lambda/2$ ensures that no fluid enters or leaves the computational domain at $r = \lambda/2$. The initial condition is given by

$$h(r, 0) = 1 - \delta \cos(2\pi r/\lambda) \tag{4.48}$$

where δ is once again the amplitude of the perturbation that is imposed to initiate the thinning of the film.

4.6.1 Scaling and self-similarity

Once again, the film profile is expected to be self-similar in the vicinity of the location where the film thickness is minimum as the space-time rupture singularity $(r = 0, t = t_R)$ is approached. Hence, the film profile in the vicinity of the rupture point $r = 0$ should have the functional form

$$h(r, \tau) = \tau^{\alpha} H(\eta), \qquad \eta = r/\tau^{\beta} \tag{4.49}$$

where $\tau \equiv t_R - t$ is the dimensionless time remaining until rupture, r, aside from being the radial coordinate, is the lateral extent of this rupture zone, η is the similarity variable, α and β are the scaling exponents for h and r, respectively, and $H(\eta)$ is the scaling function for the film profile in similarity space. Following the same approach as the one that was used to determine the scaling exponents in the case of line rupture, the scaling exponents α and β in equation (4.49) can be readily shown to be given by

$$\alpha = \frac{n}{n+4}, \qquad \beta = \frac{2n}{n+4} \tag{4.50}$$

From the dimensionless form of equation (4.11) and equations (4.43) and (4.44) and with the scaling exponents given by equation (4.50), the van der Waals (vdW), surface tension or capillary (ST), and viscous (V) stresses can be shown to scale as

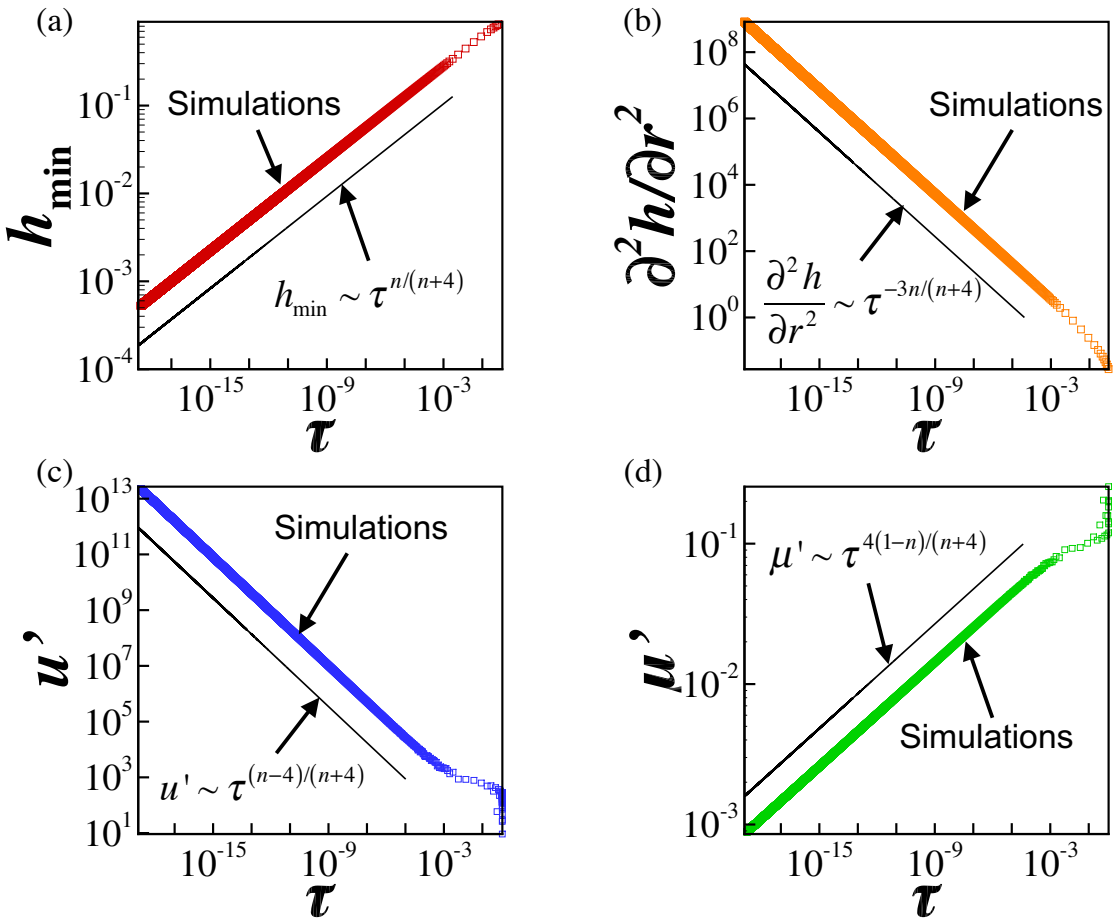

Figure 4.8. Scaling behavior of variables in the rupture zone during thinning of a film of power-law index of $n = 0.85$ undergoing point rupture: simulations (data points) and scaling theory predictions (straight lines with indicated dependencies on time remaining until rupture τ). Variation with τ of (a) minimum film thickness $h_{\min}$, (b) curvature $\partial^2 h/\partial r^2$ evaluated at $r = 0$, (c) lateral velocity u' evaluated at lateral location where $h = 1.001 h_{\min}$, and (d) viscosity μ' evaluated at that lateral location.

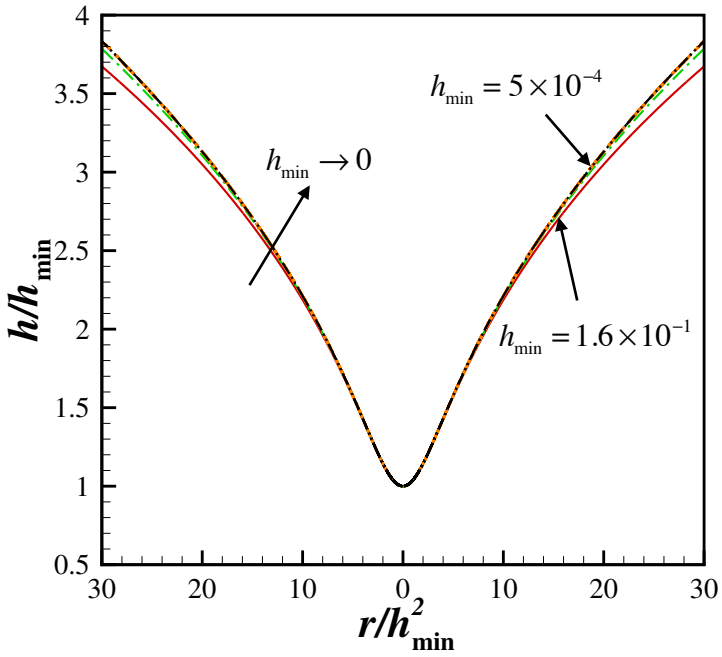

Figure 4.9. Rescaled interface shape $h/h_{\min}$ as a function of rescaled lateral coordinate $r/h_{\min}^2$ at several instants in time determined from simulations during thinning of a film of power-law index of $n = 0.85$ undergoing point rupture. The rescaled transient profiles are shown for values of $5 \times 10^{-4} \leq h_{\min} \leq 2.0 \times 10^{-1}$. Each rescaled interface shape corresponding to a successively smaller value of $h_{\min}$ is such that the value of the minimum film thickness is roughly half that of the previously shown rescaled profile. The rescaled profiles are seen to approach or collapse onto a similarity profile as $h_{\min} \to 0$.

$$vdW \sim \left|\left| \frac{\partial}{\partial r}\left(\frac{1}{h^3}\right) \right|\right| \sim \frac{1}{rh^3} \sim \tau^{-\frac{5n}{n+4}} \tag{4.51}$$

$$ST \sim \left|\left| \frac{\partial}{\partial r}\left[\frac{1}{r}\frac{\partial}{\partial r}\left(r\frac{\partial h}{\partial r}\right)\right] \right|\right| \sim \frac{h}{r^3} \sim \tau^{-\frac{5n}{n+4}} \tag{4.52}$$

$$V \sim \left|\left| \frac{\partial}{\partial z}\left(\mu\frac{\partial u}{\partial z}\right) \right|\right| \sim \left|\left| \frac{\partial}{\partial z}\left(\frac{\partial u}{\partial z}\right)^n \right|\right| \sim \frac{u^n}{z^{n+1}} \sim \frac{(r/\tau)^n}{h^{n+1}} \sim \tau^{-\frac{5n}{n+4}} \tag{4.53}$$

For future reference, it is worth noting that fluid viscosity in the thinning film scales as

$$\mu \sim \left|\left|\frac{\partial u}{\partial z}\right|\right|^{n-1} \sim \frac{(r/\tau)^{n-1}}{z^{n-1}} \sim \tau^{\frac{4(1-n)}{n+4}} \tag{4.54}$$

It is readily seen that in the Newtonian limit ($n = 1$), the expressions in equation (4.50) for the scaling exponents take on the values of $\alpha = 1/5$ and $\beta = 2/5$ and all three stresses diverge as τ^{-1} (cf. equations (4.51)-(4.53)), in agreement with previous work on rupture of Newtonian films [18].

4.6.2 Simulation of point rupture in the lubrication limit

The spatially fourth-order nonlinear evolution equation (4.45) subject to boundary conditions (4.46) and (4.47) and initial condition (4.48) with $\delta = 0.1$ is solved numerically using the same Galerkin finite element-based algorithm that has been employed earlier to simulate line rupture to verify the scaling exponents that have just been determined and to demonstrate the self-similarity of the film profiles in the rupture zone. In all of the simulations that have been carried out, it is found that the minimum film thickness is always located at $r = 0$, viz. $h_{\min} = h(0, t)$, and that the film always ruptures at $r = 0$.

Figure 4.8 shows the computed variation with time remaining until rupture of several quantities of interest in the vicinity of the rupture point for a thinning film of power-law index of $n = 0.85$. The results shown in parts (a)-(d) of this figure make plain that the computed variation with time remaining until rupture τ of the minimum film thickness, the curvature, lateral (radial) velocity, and viscosity are all in excellent accord with theory.

Figure 4.9 shows rescaled interface shapes $h/h_{\min}$ at certain instances in time determined from computations as a function of the rescaled coordinate $r/h_{\min}^2$ during thinning of a film of power-law index of $n = 0.85$. The rescaled shapes are seen to collapse nicely onto a single profile as $h_{\min} \to 0$, demonstrating the self-similarity of the dynamics as the film approaches rupture.

4.7 Breakdown of lubrication approximation and role of inertia

As discussed in standard books on fluid mechanics [22, 38] and shown in the appendix 4.11, two key assumptions that have been made in analyzing film rupture concern the applicability of the lubrication approximation. The first of these pertains to the validity of the long-wavelength approximation. As the initial aspect ratio of the film $\varepsilon(0) \equiv \epsilon \equiv h_0/l_c \ll 1$ (in this section, we use the notation $\varepsilon(\tilde{t})$ to denote the instantaneous aspect ratio of the film to distinguish it from the aspect ratio at the initial instant, ϵ), the use of the lubrication approximation is justified during the initial stages of the thinning. If $\tilde{h}(\tilde{t})$ and $\tilde{l}(\tilde{t})$ denote the film thickness and the lateral length scale at time $\tilde{t}$, the film aspect ratio at time $\tilde{t}$ is given by $\varepsilon(\tilde{t}) \equiv \tilde{h}_{\min}(\tilde{t})/\tilde{l}(\tilde{t})$. From the results of this paper, $\tilde{h}_{\min}(\tilde{t}) \sim h_0\tau^{n/(n+4)}$. The lateral length, however, scales as

$$\tilde{l}(\tilde{t}) \sim l_c\tau^{2n/(n+5)} \sim l_c\left[\frac{\tilde{h}_{\min}(\tilde{t})}{h_0}\right]^2 \tag{4.55}$$

$$\sim \frac{\left[\tilde{h}_{\min}(\tilde{t})\right]^2}{d} \tag{4.56}$$

Therefore, the aspect ratio at time $\tilde{t}$ is given by

$$\varepsilon(\tilde{t}) = \frac{\tilde{h}_{\min}(\tilde{t})}{\tilde{l}(\tilde{t})} \sim \frac{d}{\tilde{h}_{\min}(\tilde{t})} \tag{4.57}$$

Since the continuum approximation fails when the minimum film thickness becomes of the order of the molecular length scale, it is seen from the last equation that the long-wavelength approximation is valid throughout the thinning and fails at the same time as the continuum approximation does.

In order for the lubrication approximation to be valid, the film must not only be slender (as discussed in the previous paragraph) but the modified Reynolds number

Re^* which multiplies the inertial terms in the dimensionless Cauchy momentum equation (cf. [22] and the appendix 4.11) and is given by the product of the film aspect ratio and the Reynolds number Re, the ratio of inertial to viscous forces, must be small. Zhang and Lister [18] have shown that inertia remains negligible until rupture during thinning of films of Newtonian fluids. For power-law fluids, as the film's viscosity decreases due to the deformation-rate thinning rheology of such fluids, Re can grow and the possibility exists that the Re^* can become of order one or larger. The instantaneous value of Re^* can be calculated as

$$Re^*(\tilde{t}) = Re(\tilde{t})\,\varepsilon(\tilde{t}) = \frac{\rho\,\tilde{u}(\tilde{t})\,\tilde{h}(\tilde{t})}{\tilde{\mu}(\tilde{t})}\,\frac{\tilde{h}(\tilde{t})}{\tilde{l}(\tilde{t})} \tag{4.58}$$

$$= \frac{\rho h_0^2}{\mu_0 t_c}\tau^{(5n-8)/(n+4)} = \frac{1}{3}\frac{h_0}{l_\mu}\frac{1}{(h_0/d)^4}\tau^{(5n-8)/(n+4)} \tag{4.59}$$

where $l_\mu = \mu_0^2/\rho\sigma$ is the viscous length (see, e.g., Eggers [21]). Since $\tilde{h}_{\min}(\tilde{t}) \sim h_0\tau^{n/(n+4)}$, equation (4.59) can be used to determine the value of the minimum film thickness at which the modified Reynolds number becomes of order one, $Re^* \sim 1$:

$$\frac{\tilde{h}_{\min}}{d} \sim \left[\left(\frac{h_0}{l_\mu}\right)^{8(1-n)}\left(\frac{d}{l_\mu}\right)^{9n-8}\right]^{1/(8-5n)} \equiv \left[Oh^{16(n-1)}\left(\frac{d}{l_\mu}\right)^{9n-8}\right]^{1/(8-5n)} \tag{4.60}$$

where the ratio l_μ/h_0 is the square of the dimensionless group referred to as the Ohnesorge number Oh, viz. $Oh = \mu_0/\sqrt{\rho\sigma h_0}$. For a Newtonian fluid ($n = 1$), equation (4.60) reduces to

$$\frac{\tilde{h}_{\min}}{d} \sim \left(\frac{d}{l_\mu}\right)^{1/3} \tag{4.61}$$

Since typically $d < l_\mu$ (for example, whereas the molecular length scale is of the order of nanometers, the viscous length is about 14 nm for water, 200 μm for a 85% glycerol-water solution, and 2 cm for pure glycerol [43], $\tilde{h}_{\min}$ has to fall below the molecular

length scale for inertia to come into play for a Newtonian fluid. For power-law fluids, an interesting limit is that as $n \to 0$ in equation (4.60):

$$\frac{\tilde{h}_{\min}}{d} \sim \frac{h_0}{d} \tag{4.62}$$

Equation (4.62) shows that inertia would be important during the entire period of thinning for films of highly deformation-rate-thinning power-law fluids or ones having vanishingly small values of the power-law index n.

When neither $n = 1$ nor $n \to 0$ but $n \geq 8/9$, and if $h_0 < l_\mu$ and $d < l_\mu$, $\tilde{h}_{\min}$ will have to fall below d in order for inertia to become important during film thinning. Therefore, it is unlikely for inertia to become important during thinning of power-law films of power-law index of $n \geq 8/9$. If, however, $n \leq 8/9$ and $h_0 < l_\mu$ and $d < l_\mu$, it is possible that the modified Reynolds number can become of order one when $\tilde{h}_{\min}$ is greater than d. In particular, if the film fluid is acrylic paint [26], a power-law fluid with properties of $A = 10^{-19}$ J, $\sigma = 0.05$ N/m, $\mu_0 m^{\text{n-1}} = 35.6$ Pa·s^{n}, ρ =1,150 kg/m^3, and $n = 0.44$, and the initial film thickness $h_0 = 10^{-6}$ m (1 micrometer or 1,000 nanometers), inertia can become important once the normalized minimum film thickness reaches a value of $\tilde{h}_{\min}/d \sim 50.8$ or the minimum film thickess $\tilde{h}_{\min}$ falls below 28.6 nanometers. Hence, for power-law fluids of sufficiently small power-law index n, the possibility exists that inertia will become important before the continuum approximation breaks down.

Therefore, equation (4.60) can be used to determine for different films of power-law fluids the value of the scaled minimum film thickness $\tilde{h}_{\min}/d$ below which inertia will come into play during film thinning as a function of either (a) the ratio l_μ/h_0, the ratio d/h_0, and power-law index n, or equivalently (b) the Ohnesorge number $Oh = \sqrt{l_\mu/h_0} = \mu_0/\sqrt{\rho\sigma h_0}$ (a dimensionless group that equals the ratio of viscous force to the square root of the product of surface tension and inertial forces), the van der Waals number $A^* \equiv A/(6\pi\sigma {h_0}^2) = (1/3)(d/h_0)^2$ (a dimensionless group that represents the relative importance of intermolecular force to surface tension force), and power-law index n. The results of such an analysis can be used to construct a

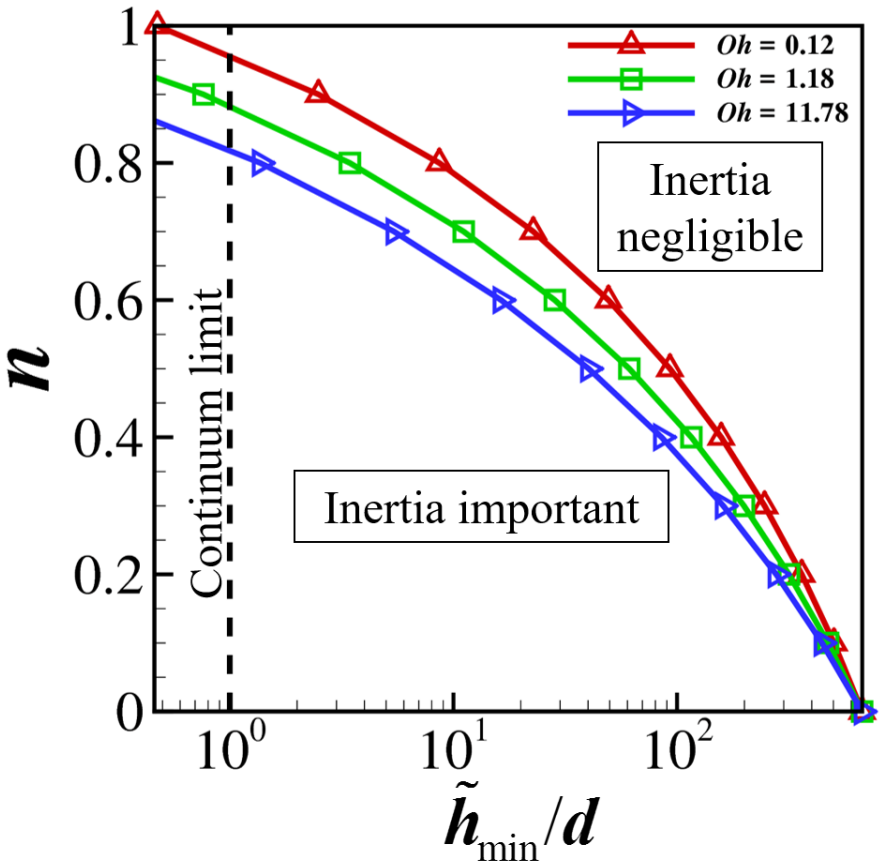

Figure 4.10. Phase diagram that shows for films of different power-law fluids each of which is characterized by a given value of Oh, A^*, and n whether inertia can become important during film thinning. Here, results are shown for three different values of the Ohnesorge number, $Oh = 0.12, 1.18$ and 11.78, at a fixed value of the ratio of van der Waals to surface tension force of $A^* = 7.37 \times 10^{-7}$, and over the entire range of possible values of the power-law index n. For a film of given n, the dynamics starts in a regime where inertia is negligible (in the region to the right of the curves in the figure) and, as the film continues to thin and $\tilde{h}_{\min}/d$ continues to decrease, the dynamics can undergo a transition from the inertialess regime to one where inertia is important if the value of $\tilde{h}_{\min}/d$ can attain a value that lies to the left of the appropriate curve in the figure and provided that the transition can occur before the continuum limit is reached (which is indicated by the vertical dashed line). It is clear that for sufficiently small values of the power-law index n, inertia becomes significant long before the continuum limit is reached.

phase diagram as in figure 4.10 that shows for a fixed value of $A^* = 7.37 \times 10^{-7}$ and Ohnesorge numbers spanning two orders of magnitude between about 0.1 and 10, the variation of the critical value of the normalized film thickness $\tilde{h}_{\min}/d$ at which inertia becomes important with the power-law index n. In accord with intuition, this figure makes it clear that for fixed n, the lower the value of Oh or the less viscous the film fluid, the larger is the value of the normalized film thickness at which inertia becomes important. Thus, the study of the dynamics of thinning of films of power-law fluids on a substrate is incomplete without considering the role of inertia, which is taken up in the following two sections.

4.8 Problem statement for analysis of film rupture with inertia and summary of approach used in two-dimensional simulations

In the remainder of the paper, the effect of inertia on thinning and rupture of a thin film of undisturbed thickness h_0 is determined by solving the spatially two-dimensional, transient Cauchy momentum and continuity equations (equations (4.7) and (4.6) in section 4.3). Given the equality of the scaling exponents governing the dynamics of thinning in the vicinity of the singularity in the planar (or two-dimensional rupture) and axisymmetric (point rupture) geometries, this more involved analysis requiring the solution of the free boundary problem comprised of a transient, nonlinear system of spatially two-dimensional partial differential equations is performed only for the case of line rupture. Therefore, in this situation, the dynamics is translationally-symmetric or invariant in the $\tilde{y}$-direction and the problem domain is the portion of the $(\tilde{x}, \tilde{z})$-plane that lies within the liquid film over a horizontal distance equal to one half the wavelength $\tilde{\lambda}/2$ of the initial perturbation that is imposed on the film's surface, i.e. the domain is the region that is bounded below by the solid substrate located at $(0 \leq \tilde{x} \leq \tilde{\lambda}/2, \tilde{z} = 0)$, bounded above by the free surface $S(\tilde{t})$, and bounded on the sides by the symmetry planes located at $\tilde{x} = 0$ and $\tilde{\lambda}/2$. Along the solid substrate, the adherence boundary condition given by equation (4.8) is imposed. At the film's surface, kinematic and traction boundary conditions given by equations (4.9) and

(4.10) are imposed. Along the two symmetry planes, the horizontal (lateral) velocity and the tangential stress are set equal to zero. At $\tilde{x} = 0$ and $\tilde{x} = \tilde{\lambda}/2$, symmetry requires that the free surface has zero slope at both locations.

In contrast to the previous sections where different characteristic lengths are employed in the horizontal and vertical directions, here a single characteristic length $h_c \equiv h_0$ is used to non-dimensionalize both the horizontal and vertical coordinates, viz. $x \equiv \tilde{x}/h_c$ and $y \equiv \tilde{y}/h_c$. As in the previous sections, here variables without tildes over them denote the dimensionless counterparts of those with tildes. Because the critical wavelength for instability $\tilde{\lambda}_c = 2\pi h_0^2/d$, the lateral extent of the film in the horizontal direction or the maximum value of the dimensionless x-coordinate can range between 10^3 and 10^5, thereby making the problem fall in the category of challenging multi-scale flow problems involving highly disparate length scales. In anticipation of computing solutions for which inertia is important, the inertio-capillary time is chosen as the characteristic time scale, viz. $t_c \equiv \sqrt{\rho h_0^3/\sigma}$, and the characteristic velocity is chosen as the ratio of the characteristic length and time scales, viz. $v_c \equiv h_c/t_c$. As characteristic pressure, viscosity and strain-rate scales, the same ones as those used in section 4.5 are adopted here. With the scales just introduced, the dynamics is then governed by two dimensionless groups: the Ohnesorge number $Oh \equiv \mu_0/\sqrt{\rho h_0 \sigma}$ and the dimensionless van der Waals number $A^* \equiv A/6\pi\sigma h_0^2$, both of which have already been introduced in the previous section.

As the rate at which viscosity falls with increasing deformation rate increases as n decreases, we expect the relative importance of inertia compared to viscous force to grow as a film thins for fluids of small n. A dominant balance argument in such cases reveals that inertial, capillary, and van der Waals forces are in balance as the film approaches rupture and gives to rise to an inertial scaling regime where the scaling exponents are independent of the power-law index n:

$$h \sim \tau^{2/7}, \quad x' \sim \tau^{4/7}, \quad u' \sim \tau^{-3/7} \tag{4.63}$$

Where h is the film thickness, x' is the lateral length scale, and u' is the lateral velocity scale. Thus, we expect to see a transition from the viscous scaling regime

given by equations (4.32) and (4.33) to this inertial scaling regime when the modified Reynold's number $Re^* = (u'h^2)/(Oh\mu' x')$ becomes $O(1)$ or larger.

The free surface flow comprised of the transient system of partial differential equations (4.6-4.7) and the aforementioned boundary and initial conditions is solved numerically using a fully implicit, method of lines (MOL), arbitrary Lagrangian-Eulerian (ALE) algorithm where the Galerkin/finite element method (G/FEM) is employed for spatial discretization and an adaptive finite difference method is used for time integration [44, 45]. As we have used variants of this algorithm to successfully analyze hydrodynamic singularities that arise in the breakup and coalescence of drops and/or filaments of both Newtonian and non-Newtonian fluids [30, 46–51], the reader is referred to these previous publications for details of the solution method used and computer implementation. A distinguished feature of the present and similar algorithms used in the aforementioned publications is highly adaptive finite element meshes that are generated using the method of elliptic mesh generation [52]. A coarse version of such meshes that have been used in the simulations is shown in Figure 4.11 where the elements and hence the mesh points are seen to concentrate near the rupture zone. A dynamic algebraic surface that moves in time based on the minimum film thickness h_{min} ensures that elements remain concentrated in the rupture zone to ensure accurate resolution of dynamics as h_{min} falls to molecular length scales.

4.9 Results for two-dimensional simulations with inertia

In this section, all the results that are reported have been obtained using the two-dimensional (2D) algorithm based on the finite element method that is described in the previous section. The section begins by presenting results on the thinning of a Newtonian film to benchmark the 2D algorithm and demonstrate the accuracy of predictions made with it. Thereafter, a set of results are presented for successively smaller values of n to highlight the thinning dynamics of films of power-law liquids. The simulation results to be reported have been obtained using an initial perturbation to the film surface having an amplitude of 0.1 and wavelength of $4\pi h_0/d$.

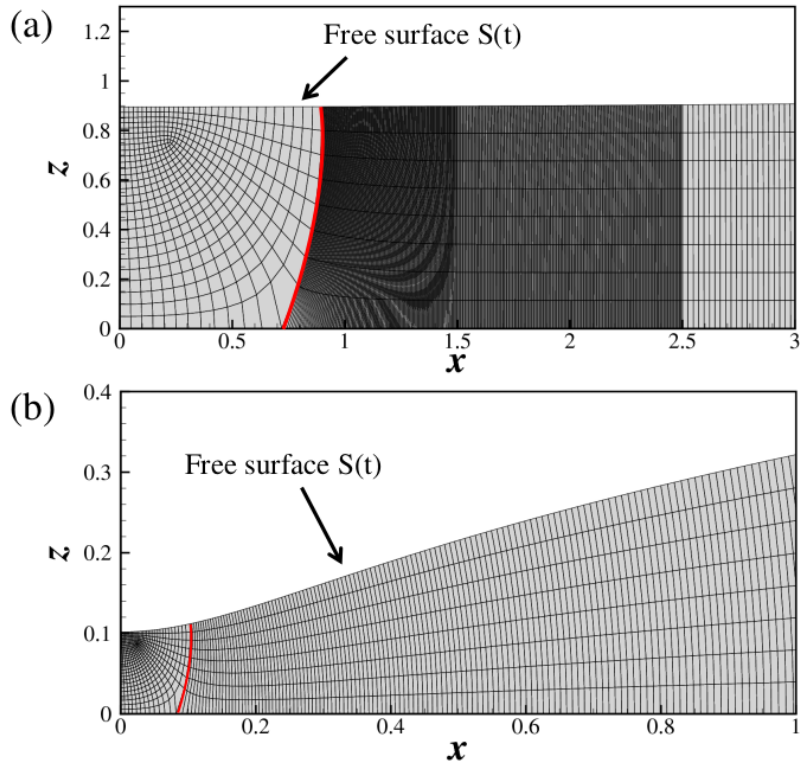

Figure 4.11. Close-up views of an illustrative coarse two-dimensional finite element mesh that has been constructed by elliptic mesh generation for 2D simulations. As the length of the domain in the lateral direction is 10,000, only the mesh in the vicinity of $h_{\min}$ is shown. The two parts of the figure show the mesh (a) at the initial instant when $h_{\min} = 0.9$ and (b) at a later time when $h_{\min} = 0.1$. The algorithm concentrates the elements more and more in the region close to the space-time singularity as the film thins and tends toward rupture. The dynamic algebraic surface is shown by the red curve.

Figure 4.12 shows the variation with time remaining until rupture τ of several quantities of interest in the rupture zone for a Newtonian film of $Oh = 1.18$ and $A^* = 7.37 \times 10^{-7}$. The simulation results depicted in figure 4.12(a) show that the minimum film thickness $h_{\min}$ decreases with τ as $h_{\min} \sim \tau^{1/5}$. Figure 4.12(b) shows the curvature evaluated at the lateral location where the film thickness is a minimum, $h_{\min}$, diverges with τ as $\kappa \sim \tau^{-3/5}$. As has already been shown previously by equation (4.39), the variation of κ with τ can be combined with the corresponding result for h

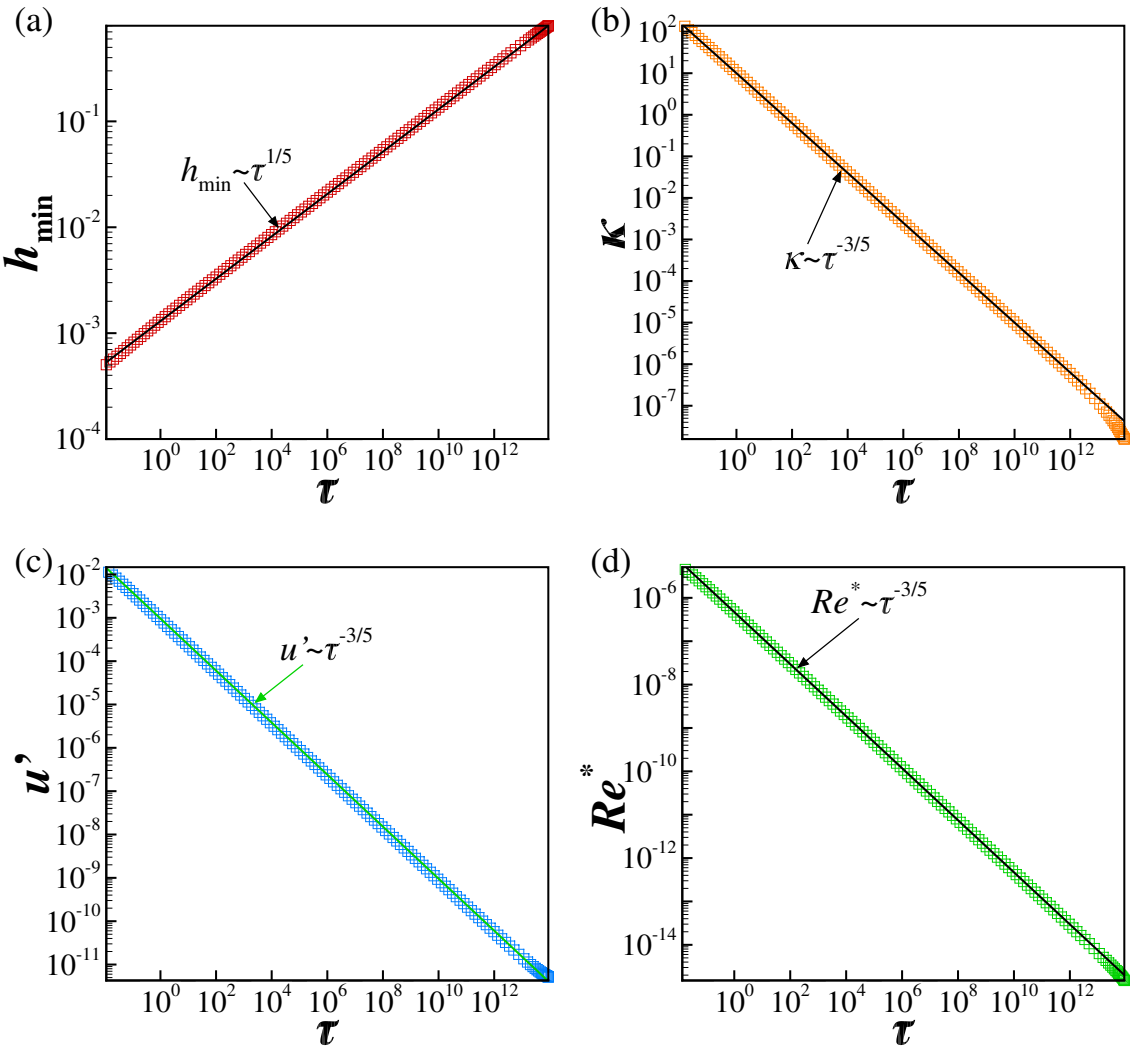

Figure 4.12. Scaling behavior of variables in the rupture zone during thinning of a Newtonian film with $Oh = 1.18$ and $A^* = 7.37 \times 10^{-7}$ undergoing line rupture: simulations (data points) and scaling theory predictions (straight lines with indicated dependencies on time remaining until rupture τ). Variation with τ of (a) minimum film thickness $h_{\min}$, (b) curvature κ evaluated at the lateral location of $h_{\min}$, (c) lateral velocity u' evaluated at lateral location where $h = 1.05h_{\min}$, and (d) Modified Reynold's number Re^* evaluated at that lateral location.

to infer that the lateral length scales as $x' \sim \tau^{2/5}$. Figure 4.12(c) shows that the lateral velocity u' computed at the film's surface at the lateral location where $h = 1.05h_{\min}$ diverges with τ as $u' \sim \tau^{-3/5}$. Reassuringly, this scaling result is unchanged if the lateral location at which u' is evaluated is changed: for example, the scaling exponent for u' is unchanged if u' is evaluated at $1.1h_{\min}$ instead of $1.05h_{\min}$. Figure 4.12(d) shows that the modified Reynold's number Re^* computed at the lateral location where u' is evaluated to diverge with τ as $Re^* \sim \tau^{-3/5}$. However, as shown in figure 4.12(d), the value of the modified Reynolds number remains small or $Re^* \ll 1$ all the way until rupture. Thus, all of the 2D simulation results reported for the Newtonian film of this paragraph are in excellent agreement with the predictions obtained from an analysis based on the 1D lubrication equations (cf. equations 4.32 and 4.33), which is to be expected since the lubrication approximation is valid during the entire period of thinning of a Newtonian film having the properties for which the 2D simulations have been carried out (see figure 4.10).

Figure 4.13 shows results of 2D simulations for the thinning of a power-law film of $n = 0.83$ and for which all the other conditions are identical to the Newtonian case discussed in the previous paragraph. For the power-law film, the simulations reveal that during virtually the entire period of thinning, the minimum film thickness, the curvature at the location where the film thickness is a minimum, and the lateral velocity all follow the power-law scalings predicted by lubrication theory, viz. $h_{\min} \sim \tau^{n/(n+4)} \mid_{n=0.83} \sim \tau^{0.172}$ (figure 4.13(a)), $\kappa \sim \tau^{-3n/(n+4)} \mid_{n=0.83} \sim \tau^{0.515}$ (figure 4.13(b)), and $u' \sim \tau^{(n-4)/(n+4)} \mid_{n=0.83} \sim \tau^{-0.656}$ (figure 4.13(c)), because the modified Reynolds number Re^* remains well below $O(1)$ (figure 4.13(d)) until $h_{\min}$ has decreased by three orders of magnitude. As inertia begins to become important during the final stages of thinning, the scaling exponent obtained from 2D simulations for the variation of $h_{\min}$ with τ transitions from a value of $n/(n+4) = 0.172$ to $2/7$, as shown in figure 4.13(a). To see this transition from a viscous power-law regime to an inertial regime more clearly, we next consider a case for a smaller value of n, where the transition is expected to occur for a value of $h_{\min}$ much larger than that in figure 4.13(a).

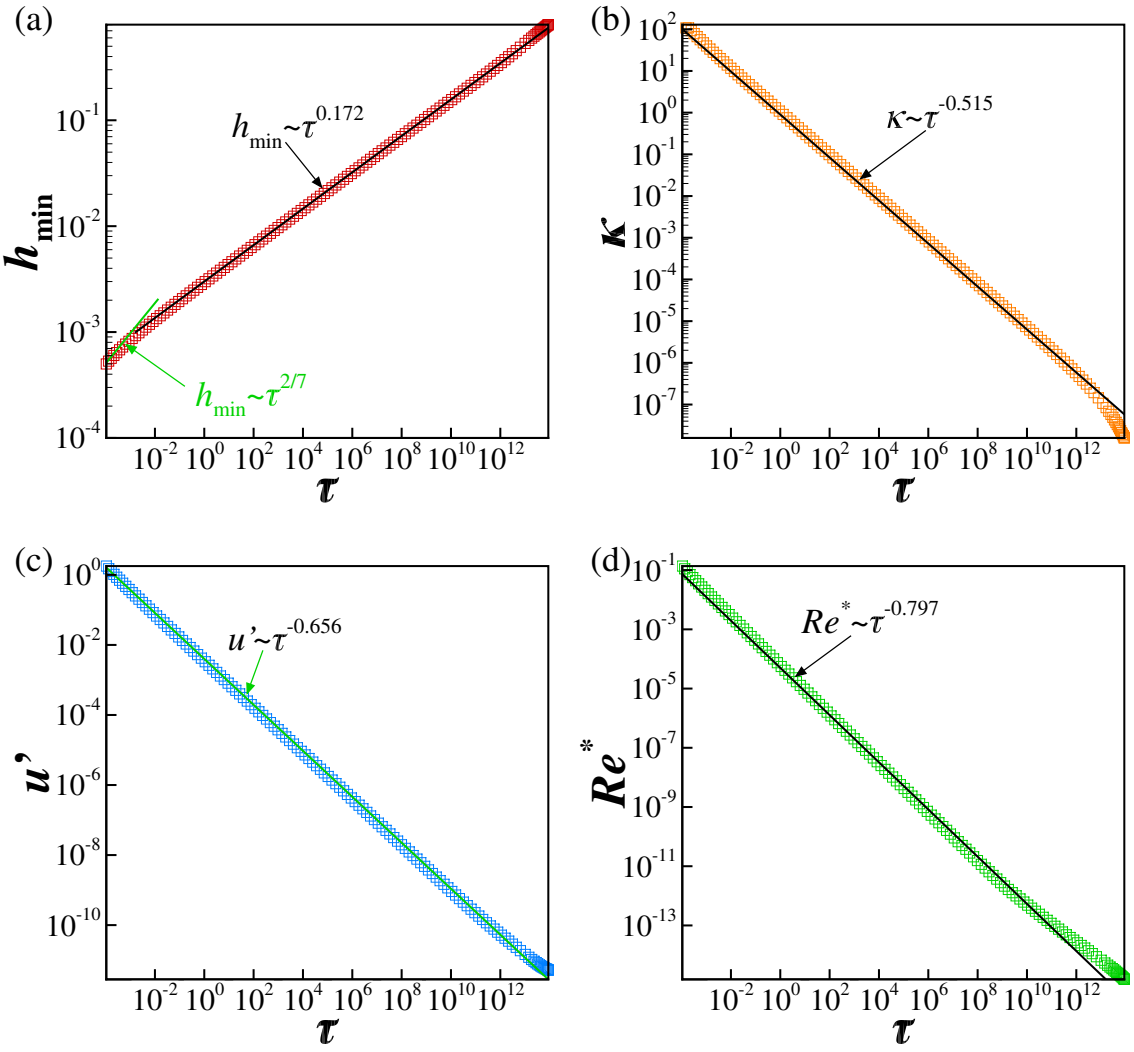

Figure 4.13. Effect of power-law rheology on the scaling behavior of variables in the rupture zone during thinning of a power-law film undergoing line rupture: simulations (data points) and scaling theory predictions (straight lines with indicated dependencies on time remaining until rupture τ). Here, $Oh = 1.18$, $A^* = 7.37 \times 10^{-7}$, and $n = 0.83$. Variation with τ of (a) minimum film thickness $h_{\min}$, (b) curvature κ evaluated at the lateral location of $h_{\min}$, (c) lateral velocity u' evaluated at lateral location where $h = 1.05h_{\min}$, and (d) modified Reynolds number Re^* evaluated at that lateral location.

Figure 4.14 shows results of 2D simulations for the thinning of a power-law film of $n = 0.6$ and for which all the other conditions are identical to the Newtonian film for which results of thinning are shown in figure 4.12 and the case of the power-law film of $n = 0.83$ discussed in the previous paragraph (figure 4.14). The results depicted in figure 4.14(a) unequivocally show that a change of scaling from the viscous regime where $h_{\min} \sim \tau^{n/(n+4)} \mid_{n=0.60} \sim \tau^{0.130}$) to the inertial regime that is independent of the power-law index and where $h_{\min} \sim \tau^{2/7}$. According to the simulation results depicted in figure 4.14(a), this transition occurs when $h_{\min} \approx O(10^{-2})$, a result that is in good agreement with the theoretical estimate of $h_{\min} \sim 4 \times 10^{-2}$ predicted by equation (4.60). Figures 4.14(b) and Figure 4.14(c) show the change of scaling that are exhibited by the curvature at the location where the film thickness is a mininum and the lateral velocity. That inertia becomes significant as the film thins and approaches rupture is made evident from figure 4.14(d), which shows the modified Reynolds number increasing monotonically as the thinning continues, and becoming $O(1)$ and signaling the transition from the viscous to the inertial regime. Using the expressions for the scaling estimates given by equation (4.63) for the variation of the film thickness, lateral length scale, and lateral velocity with τ, the modified Reynolds number in the inertial regime can be shown to vary with time remaining until rupture as $Re^* \sim \tau^{(5n-8)/7}$. The modified Reynolds number predicted from simulations is shown in figure 4.14(d) to be in excellent agreement with this scaling estimate.

4.10 Conclusion

In this paper, the van der Waals force-driven thinning and rupture films of power-law fluids lying on a solid substrate have been analyzed by two different means. When the film fluid is Newtonian (for which the power-law index $n = 1$) or the film is a deformation-rate-thinning fluid of power-law index that is close to one, the dynamics has been analyzed by solving a spatially one-dimensional, nonlinear evolution equation that results by application of the lubrication approximation. In such situ-

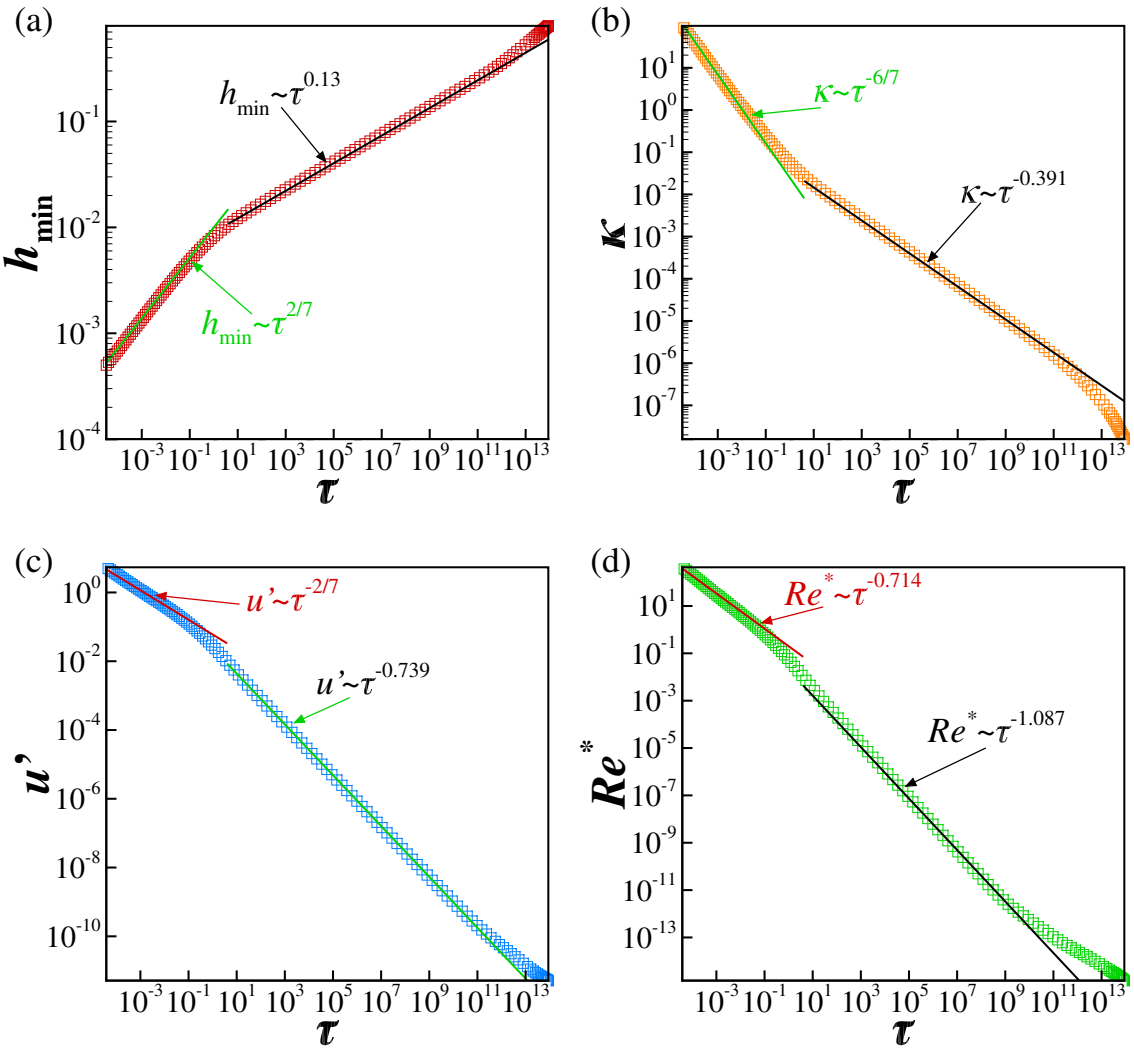

Figure 4.14. Effect of power-law rheology on the scaling behavior of variables in the rupture zone and change of scaling during thinning of a power-law film of $Oh = 1.18$, $A^* = 7.37 \times 10^{-7}$, and $n = 0.60$ undergoing line rupture: simulations (data points) and scaling theory predictions (straight lines with indicated dependencies on time remaining until rupture τ). Variation with τ of (a) minimum film thickness $h_{\min}$, (b) curvature κ evaluated at the lateral location of $h_{\min}$, (c) lateral velocity u' evaluated at lateral location where $h = 1.05h_{\min}$, and (d) modified Reynolds number Re^* evaluated at that lateral location. The occurrence of a change of scaling and a transition from the viscous regime to the inertial regime is clear as $\tau \to 0$ from the plots depicting the temporal evolution of all four variables in the figure.

ations, the dynamics has been studied both theoretically and numerically for both two-dimensional or line rupture as well as axisymmetric or point rupture. In both cases, the dynamics in the vicinity of the rupture singularity has been shown to be self-similar and for which the film thickness and the lateral length scale decrease as $\tau^{n/n+4}$ and $\tau^{2n/n+4}$, respectively, where τ is the dimensionless time remaining until rupture. During the thinning of such films, van der Waals, capillary (surface tension), and viscous forces remain in balance but inertia is negligible as the film tends toward rupture.

For power-law fluids of sufficiently small n, inertia can become important once the minimum film thickness falls below a critical value. The critical conditions for which inertia becomes important and the lubrication approximation is no longer valid have been determined analytically and a phase diagram has been constructed that depicts when inertia will become important during film thinning for fluids of any value of the power-law index n ($0 < n \leq 1$). To analyze film thinning and rupture when inertia may be important, a computational fluid dynamics (CFD) algorithm has been developed for solving the free boundary problem comprised of the transient, spatially two-dimensional Cauchy momentum and continuity equations. In situations where inertia is important, the film thickness and the lateral length scale have been shown to decrease as $\tau^{2/7}$ and $\tau^{4/7}$. During the thinning of such films, van der Waals, capillary, and inertial forces remain in balance but viscous force is negligible as the film tends toward rupture.

In the 2D simulations carried out in this paper, the entire domain is discretized into a set of curved quadrilateral elements. Solving the set of spatially two-dimensional partial differential equations (PDEs) governing film thinning and rupture is costly because a large number of elements or mesh points must be used in the lateral direction as the lateral extent of the film or the maximum value of the x-coordinate, $\lambda/2$, is three to five orders of magnitude larger than the undisturbed film thickness. Since the lateral velocity and the local Reynolds number decrease as one moves away from the rupture zone, an efficient computational scheme can be developed by dividing the

domain into two parts: in the first part, for $0 \leq x \leq L$, with $x' \ll L \ll \lambda/2$, and where inertia may be important, the domain is discretized into a set of 2D quadrilateral elements and the set of spatially 2D PDEs is solved and in the second part, for $L \leq x \leq \lambda/2$ and where inertia is insignificant, the domain is discretized into a set of 1D elements and the spatially 1D long-wavelength, or lubrication, equation is solved. The lateral location L where the two solutions are matched can be varied to minimize the error in the solution obtained with the hybrid algorithm compared to that obtained with the more expensive 2D algorithm alone. We leave the implementation of such a hybrid algorithm as a future goal of research on studies of the thinning and rupture of thin films on substrates.

As pointed out by Witelski and Bernoff [53] and Zhang and Lister [18] for Newtonian fluids, two-dimensional film rupture is unstable to perturbations in film thickness in the third direction. Since axisymmetric solutions are stable with respect to asymmetric perturbations, unstable thin films are generally expected to rupture at a point.

4.11 Appendix: governing equations in the lubrication limit

When the divergence of the stress tensor is evaluated, the Cauchy momentum equation can be rewritten as

$$\rho\left(\frac{\partial\tilde{\mathbf{v}}}{\partial\tilde{t}}+\tilde{\mathbf{v}}\cdot\tilde{\nabla}\tilde{\mathbf{v}}\right)=-\tilde{\nabla}\tilde{p}+\tilde{\mu}\tilde{\nabla}^2\tilde{\mathbf{v}}+\tilde{\nabla}\tilde{\mu}\cdot\tilde{\nabla}\tilde{\mathbf{v}}+\tilde{\nabla}\tilde{\mathbf{v}}\cdot\tilde{\nabla}\tilde{\mu} \tag{4.64}$$

In what follows, it proves convenient to decompose the fluid velocity and the gradient operator into two parts, one of which is parallel to the solid substrate and the other perpendicular to it, viz.

$$\tilde{\mathbf{v}}=\tilde{\mathbf{v}}_{\mathrm{II}}+\tilde{w}\,,\quad \tilde{\nabla}=\tilde{\nabla}_{\mathrm{II}}+\mathbf{e}_z\frac{\partial}{\partial\tilde{z}} \tag{4.65}$$

With these definitions, the continuity equation and the components of the Cauchy momentum equation in the direction parallel and perpendicular to the substrate can be written as

$$\tilde{\nabla}_{\mathrm{II}} \cdot \tilde{\mathbf{v}}_{\mathrm{II}} + \frac{\partial \tilde{w}}{\partial \tilde{z}} = 0 \tag{4.66}$$

$$\begin{aligned} \rho \left(\frac{\partial \tilde{\mathbf{v}}_{\mathrm{II}}}{\partial \tilde{t}} + \tilde{\mathbf{v}}_{\mathrm{II}} \cdot \tilde{\nabla}_{\mathrm{II}} \tilde{\mathbf{v}}_{\mathrm{II}} + \tilde{w} \frac{\partial \tilde{\mathbf{v}}_{\mathrm{II}}}{\partial \tilde{z}} \right) &= -\tilde{\nabla}_{\mathrm{II}} \tilde{p} + \tilde{\mu} \left(\tilde{\nabla}_{\mathrm{II}}^2 \tilde{\mathbf{v}}_{\mathrm{II}} + \frac{\partial^2 \tilde{\mathbf{v}}_{\mathrm{II}}}{\partial \tilde{z}^2} \right) \\ &\quad + \tilde{\nabla}_{\mathrm{II}} \tilde{\mu} \cdot \tilde{\nabla}_{\mathrm{II}} \tilde{\mathbf{v}}_{\mathrm{II}} + \frac{\partial \tilde{\mu}}{\partial \tilde{z}} \frac{\partial \tilde{\mathbf{v}}_{\mathrm{II}}}{\partial \tilde{z}} \\ &\quad + \tilde{\nabla}_{\mathrm{II}} \tilde{\mathbf{v}}_{\mathrm{II}} \cdot \tilde{\nabla}_{\mathrm{II}} \tilde{\mu} + \frac{\partial \tilde{\mu}}{\partial \tilde{z}} \tilde{\nabla}_{\mathrm{II}} \tilde{w} \end{aligned} \tag{4.67}$$

(4.68)

$$\begin{aligned} \rho \left(\frac{\partial \tilde{w}}{\partial \tilde{t}} + \tilde{\mathbf{v}}_{\mathrm{II}} \cdot \tilde{\nabla}_{\mathrm{II}} \tilde{w} + \tilde{w} \frac{\partial \tilde{w}}{\partial \tilde{z}} \right) &= -\frac{\partial \tilde{p}}{\partial \tilde{z}} + \tilde{\mu} \left(\tilde{\nabla}_{\mathrm{II}}^2 \tilde{w} + \frac{\partial^2 \tilde{w}}{\partial \tilde{z}^2} \right) \\ &\quad + \tilde{\nabla}_{\mathrm{II}} \tilde{\mu} \cdot \tilde{\nabla}_{\mathrm{II}} \tilde{w} + 2 \frac{\partial \tilde{\mu}}{\partial \tilde{z}} \frac{\partial \tilde{w}}{\partial \tilde{z}} + \frac{\partial \tilde{\mathbf{v}}_{\mathrm{II}}}{\partial \tilde{z}} \cdot \tilde{\nabla}_{\mathrm{II}} \tilde{\mu} \end{aligned} \tag{4.69}$$

In thin-film flow, the characteristic length scale in the vertical direction, h_0, is much smaller than that in the horizontal or lateral direction, l_c, so that the aspect ratio or slenderness of the film $\epsilon \equiv h_0/l_c \ll 1$. It then follows from the continuity equation (4.66) that if the characteristic velocity scales in the horizontal and vertical directions are given by v_c and w_c, then $w_c \sim \epsilon v_c$. If the characteristic time, pressure, and viscosity scales are taken to be $t_c = l_c/u_c$, $p_c = \mu_0 u_c l_c/h_0^2$, and μ_0, the continuity equation and the lateral and axial components of the Cauchy momentum equation in dimensionless form become

$$\nabla_{\mathrm{II}} \cdot \mathbf{v}_{\mathrm{II}} + \frac{\partial w}{\partial z} = 0 \tag{4.70}$$

$$\begin{aligned} Re\, \epsilon \left(\frac{\partial \mathbf{v}_{\mathrm{II}}}{\partial t} + \mathbf{v}_{\mathrm{II}} \cdot \nabla_{\mathrm{II}} \mathbf{v}_{\mathrm{II}} + w \frac{\partial v_{\mathrm{II}}}{\partial z} \right) &= -\nabla_{\mathrm{II}} p + \mu \left(\epsilon^2 \nabla_{\mathrm{II}}^2 \mathbf{v}_{\mathrm{II}} + \frac{\partial^2 \mathbf{v}_{\mathrm{II}}}{\partial z^2} \right) + \frac{\partial \mu}{\partial z} \frac{\partial \mathbf{v}_{\mathrm{II}}}{\partial z} \\ &\quad + \epsilon^2 \left(\nabla_{\mathrm{II}} \mu \cdot \nabla_{\mathrm{II}} \mathbf{v}_{\mathrm{II}} + \nabla_{\mathrm{II}} \mathbf{v}_{\mathrm{II}} \cdot \nabla_{\mathrm{II}} \mu + \frac{\partial \mu}{\partial z} \nabla_{\mathrm{II}} w \right) \end{aligned} \tag{4.71}$$

$$Re\,\epsilon\left(\frac{\partial w}{\partial t}+\mathbf{v}_{\mathrm{II}}\cdot\nabla_{\mathrm{II}}w+w\,\frac{\partial w}{\partial z}\right)=-\frac{1}{\epsilon^2}\frac{\partial p}{\partial z}+\mu\left(\epsilon^2\nabla_{\mathrm{II}}^2 w+\frac{\partial^2 w}{\partial z^2}\right)$$
$$+\nabla_{\mathrm{II}}\mu\cdot\left(\epsilon^2\nabla_{\mathrm{II}}w+\frac{\partial\mathbf{v}_{\mathrm{II}}}{\partial z}\right)+2\frac{\partial\mu}{\partial z}\frac{\partial w}{\partial z}\qquad(4.72)$$

where $Re = \rho u_c h_0/\mu_0$ is the Reynolds number and variables that appear without tildes over them are the dimensionless counterparts of those with tildes. Equations similar to equations (4.70), (4.71), and (4.72), albeit for Newtonian fluids and typically with lateral variation in a single direction, can be found in standard books in fluid mechanics and transport phenomena (cf. [22]). In the lubrication approximation, both the aspect ratio and the Reynolds number times aspect ratio must be small, viz. $\epsilon \ll 1$ and $Re\,\epsilon \ll 1$.

4.12 List of References

[1] Steven J Weinstein and Kenneth J Ruschak. Coating flows. *Annu. Rev. Fluid Mech.*, 36:29–53, 2004.

[2] V. S. Ajaev and G. M. Homsy. Modeling shapes and dynamics of confined bubbles. *Ann. Rev. Fluid Mech.*, 38:277–307, 2006.

[3] S. Cohen-Addad, R. Höhler, and O. Pitois. Flow in foams and flowing foams. *Ann. Rev. Fluid Mech.*, 45(1):241, 2013.

[4] Y. Yoon, F. Baldessari, H. D. Ceniceros, and L. G. Leal. Coalescence of two equal-sized deformable drops in an axisymmetric flow. *Phys. Fluids*, 19(10):102102, 2007.

[5] O. Kabov. Breakdown of a liquid film flowing over the surface with a local heat source. *Thermophysics and Aeromechanics*, 7(4):513–520, 2000.

[6] R. J. Braun. Dynamics of the tear film. *Ann. Rev. Fluid Mech.*, 44:267–297, 2012.

[7] A. Nguyen and H. J. Schulze. *Colloidal Science of Flotation*. CRC Press, Boca Raton, Florida, 2003.

[8] J. Becker, G. Grün, R. Seemann, H. Mantz, K. Jacobs, K. R. Mecke, and R. Blossey. Complex dewetting scenarios captured by thin-film models. *Nat. Mat.*, 2(1):59–63, 2003.

[9] P. G. De Gennes. Wetting: statics and dynamics. *Rev. Mod. Phys.*, 57(3):827, 1985.

[10] H. S. Kheshgi and L. E. Scriven. Dewetting: Nucleation and growth of dry regions. *Chem. Eng. Sci.*, 46(2):519–526, 1991.

[11] G. Reiter, A. Sharma, A. Casoli, M. David, R. Khanna, and P. Auroy. Thin film instability induced by long-range forces. *Langmuir*, 15(7):2551–2558, 1999.

[12] V. S. Mitlin. Dewetting of solid surface: Analogy with spinodal decomposition. *J. Col. Int. Sci.*, 156(2):491–497, 1993.

[13] G. Reiter. Dewetting of thin polymer films. *Phys. Rev. Lett.*, 68(1):75, 1992.

[14] T. G. Stange, D. F. Evans, and W. A. Hendrickson. Nucleation and growth of defects leading to dewetting of thin polymer films. *Langmuir*, 13(16):4459–4465, 1997.

[15] G. F. Teletzke, H. T. Davis, and L.E. Scriven. How liquids spread on solids. *Chem. Eng. Comm.*, 55(1-6):41–82, 1987.

[16] E. Ruckenstein and R. K. Jain. Spontaneous rupture of thin liquid films. *J. Chem. Soc., Faraday Transactions 2: Molecular and Chemical Physics*, 70:132–147, 1974.

[17] M. B. Williams and S. H. Davis. Nonlinear theory of film rupture. *J. Col. Int. Sci.*, 90(1):220–228, 1982.

[18] W. W. Zhang and J. R. Lister. Similarity solutions for van der Waals rupture of a thin film on a solid substrate. *Phys. Fluids*, 11(9):2454–2462, 1999.

[19] G. I. Barenblatt. *Scaling, Self-similarity, and Intermediate Asymptotics: Dimensional Analysis and Intermediate Asymptotics*. Cambridge University Press, New York, 1996.

[20] Jens Eggers. Universal pinching of 3d axisymmetric free-surface flow. *Phys. Rev. Lett.*, 71:3458–3460, Nov 1993.

[21] J. Eggers. Nonlinear dynamics and breakup of free-surface flows. *Rev. Mod. Phys.*, 69(3):865, 1997.

[22] W. M. Deen. *Analysis of Transport Phenomena*. Oxford University Press, New York, 1998.

[23] R. B. Bird, R. C. Armstrong, O. Hassager, and C. F. Curtiss. *Dynamics of Polymeric Liquids*. Wiley New York, 1977.

[24] S. W. Hasan, M. T. Ghannam, and N. Esmail. Heavy crude oil viscosity reduction and rheology for pipeline transportation. *Fuel*, 89(5):1095–1100, 2010.

[25] J. R. Savage, M. Caggioni, P. T. Spicer, and I. Cohen. Partial universality: pinch-off dynamics in fluids with smectic liquid crystalline order. *Soft Matter*, 6(5):892–895, 2010.

[26] F. M. Huisman, S. R. Friedman, and P. Taborek. Pinch-off dynamics in foams, emulsions and suspensions. *Soft Matter*, 8(25):6767–6774, 2012.

[27] M. Renardy. Similarity solutions for jet breakup for various models of viscoelastic fluids. *J. Non-Newtonian Fluid Mech.*, 104(1):65–74, 2002.

[28] P. Doshi, R. Suryo, O. E. Yildirim, G. H. McKinley, and O. A. Basaran. Scaling in pinch-off of generalized Newtonian fluids. *J. Non-Newtonian Fluid Mech.*, 113(1):1–27, 2003.

[29] P. Doshi and O. A. Basaran. Self-similar pinch-off of power law fluids. *Phys. Fluids*, 16(3):585–593, 2004.

[30] R. Suryo and O. A. Basaran. Local dynamics during pinch-off of liquid threads of power law fluids: Scaling analysis and self-similarity. *J. Non-Newtonian Fluid Mech.*, 138(2):134–160, 2006.

[31] S. Miladinova, G. Lebon, and E. Toshev. Thin-film flow of a power-law liquid falling down an inclined plate. *J. Non-Newtonian Fluid Mech.*, 122(1):69–78, 2004.

[32] B. S. Dandapat and A. Mukhopadhyay. Waves on the surface of a falling power-law fluid film. *Int. J. Non-linear Mech.*, 38(1):21–38, 2003.

[33] R. S. R. Gorla. Rupture of thin power-law liquid film on a cylinder. *J. Appl. Mech.*, 68(2):294–297, 2001.

[34] A. Arora and P. Doshi. Fingering instability in the flow of a power-law fluid on a rotating disc. *Phys. Fluids*, 28(1):013102, 2016.

[35] Y. L. Zhang, O. K. Matar, and R. V. Craster. Analysis of tear film rupture: effect of non-Newtonian rheology. *J. Col. Int. Sci.*, 262(1):130–148, 2003.

[36] D. Vaynblat, J. R. Lister, and T. P. Witelski. Rupture of thin viscous films by van der Waals forces: Evolution and self-similarity. *Phys. Fluids*, 13(5):1130–1140, 2001.

[37] S. S. Thete, C. Anthony, O. A. Basaran, and P. Doshi. Self-similar rupture of thin free films of power-law fluids. *Phys. Rev. E*, 92(2):023014, 2015.

[38] L. G. Leal. *Advanced Transport Phenomena: Fluid Mechanics and Convective Transport Processes*. Cambridge University Press, New York, 2007.

[39] B. Ambravaneswaran, S. D. Phillips, and O. A. Basaran. Theoretical analysis of a dripping faucet. *Phys. Rev. Lett.*, 85(25):5332, 2000.

[40] O. E. Yildirim and O. A. Basaran. Dynamics of formation and dripping of drops of deformation-rate-thinning and -thickening liquids from capillary tubes. *J. Non-Newtonian Fluid Mech.*, 136(1):17–37, 2006.

[41] X. Zhang, R. S. Padgett, and O. A. Basaran. Nonlinear deformation and breakup of stretching liquid bridges. *J. Fluid Mech.*, 329:207–246, 1996.

[42] O. E. Yildirim and O. A. Basaran. Deformation and breakup of stretching bridges of Newtonian and shear-thinning liquids: comparison of one-and two-dimensional models. *Chem. Eng. Sci.*, 56(1):211–233, 2001.

[43] J. Timmermans. *The Physico-Chemical Constants of Binary Systems in Concentrated Solutions*. Interscience, New York, 1960.

[44] E. D. Wilkes, S. D. Phillips, and O. A. Basaran. Computational and experimental analysis of dynamics of drop formation. *Phys. Fluids*, 11(12):3577–3598, 1999.

[45] Patrick K. Notz and Osman A. Basaran. Dynamics and breakup of a contracting liquid filament. *J. Fluid Mech.*, 512:223–256, 2004.

[46] A. U. Chen, P. K. Notz, and O. A. Basaran. Computational and experimental analysis of pinch-off and scaling. *Phys. Rev. Lett.*, 88(17):174501, 2002.

[47] P. P. Bhat, S. Appathurai, M. T. Harris, M. Pasquali, G. H. McKinley, and O. A. Basaran. Formation of beads-on-a-string structures during break-up of viscoelastic filaments. *Nat. Phys.*, 6(8):625–631, 2010.

[48] J. D. Paulsen, J.C. Burton, S. R. Nagel, S. Appathuri, M. T. Harris, and O. A. Basaran. The inexorable resistance of inertia determines the initial regime of drop coalescence. *Proc. Nat. Acad. Sci.*, 109(18):6857–6861, 2002.

[49] R. T. Collins, K. Sambath, M. T. Harris, and O. A. Basaran. Universal scaling laws for the disintegration of electrified drops. *Proc. Nat. Acad. Sci. USA*, 110(13):4905–4910, 2013.

[50] J. R. Castrejón-Pita, A. A. Castrejón-Pita, S. S. Thete, K. Sambath, I. M. Hutchings, J. Hinch, J. R. Lister, and O. A. Basaran. Plethora of transitions during breakup of liquid filaments. *Proc. Natl. Acad. Sci. USA*, 112(15):4582–4587, 2015.

[51] J. P. Munro, C. R. Anthony, O. A. Basaran, and J. R. Lister. Thin-sheet flow between coalescing bubbles. *J. Fluid Mech.*, 773:R3, 2015.

[52] K. N. Christodoulou and L. E. Scriven. Discretization of free surface flows and other moving boundary problems. *J. Comput. Phys.*, 99(1):39–55, 1992.

[53] T. P. Witelski and A. J. Bernoff. Stability of self-similar solutions for van der Waals driven thin film rupture. *Phys. Fluids*, 11(9):2443–2445, 1999.

5. IMPACT OF BUBBLES IMMERSED IN POWER-LAW FLUIDS WITH A SOLID WALL

5.1 Introduction

The phenomenon of bubbles interacting with other bubbles or surfaces is observed in a plethora of natural processes and industrial applications. For example, bubbles bursting at the surface of seas produce marine aerosols which affect local air quality [1] and rain formation [2]. Collisions of bubbles with liquid/gas and liquid/solid interfaces is the first stage for formation of foams [3]. In industry, bubble collisions with solid walls play a crucial role in the flow of foams and bubbly liquids in pipes and in other situations where solid surfaces are present [4]. Additionally, the understanding of bubble collisions with solid particles is essential for applications like tar-sands processing [5], where the recovery of bitumen is aided by aeration, mineral extraction and plastic separation through froth flotation [6, 7] and convective heat transfer [8].

If a bubble approaches a solid surface with sufficiently high kinetic energy, such that the Reynold's number $Re = 2\rho VR/\mu_0 \gg 1$, it rebounds multiple times before finally attaching to the solid surface [3, 9, 10]. Here, ρ and μ_0 are the density and viscosity of the liquid that the bubble is immersed in, while V and R are the velocity and radius of the bubble. Tsao and Koch [9] conducted extensive experiments on the interactions of high Re bubbles with a horizontal rigid wall, as well as oblique walls. They observed that bubbles approaching a horizontal wall always bounced when the Weber number $We = 2\rho V^2 R/\sigma > 0.3$, and determined the energy lost by the bubble as it bounced back from the wall. Subsequent experimental studies [3, 11, 12] have shown that larger bubbles or equivalently, bubbles approaching with a larger Re, or bubbles approaching from a greater distance, travel back a greater distance from the

wall upon rebound. Canot et al. [4] were the first to study this problem computationally, with a viscous approximation of the boundary element method (BEM). More recently, Albadawi et al. [13] used the volume of fluid (VOF) method to numerically simulate bubble impact with a solid wall and observed good agreement with the experiments of Zenit and Legendre [11] and Kosior et al. [12]. Finally, Chan and coworkers have used a simple force balance model for the bubble to understand the dynamics of bubble impact and rebound from solid walls in a series of papers [14–16].

Small bubbles, or bubbles that approach the solid wall with a low enough velocity such that $Re < 1$, do not rebound from the surface upon first approach as observed experimentally by Parkinson and Ralston [10]. As the bubble approaches the wall, a thin film between the bubble and solid surface is formed, which drains and finally ruptures if long range van der Waals forces are attractive in nature [17–19]. For bubbles approaching a solid surface in water, film rupture occurs if the surface is hydrophobic [20]. Lubrication theory has been used to study the drainage of the film during the final stages of bubble attachment to the solid wall [16, 18, 21] as the local Reynold's number in the film for bubbles immersed in Newtonian fluids is observed to be orders of magnitude smaller than the Reynold's number of the bubble. As the final stages of bubble attachment resemble supported thin film rupture due to van der Waals forces, it is expected that dynamics in the vicinity of the singularity, i.e. when the bubble attaches to the solid wall, will be self-similar. However, studies that examine the self-similar dynamics of the final stages of bubble attachment with solid walls in a similar manner to existing literature on self-similarity of thread pinchoff [22, 23], drop and bubble coalescence [24–26], free film rupture [27–30] and supported film rupture [31, 32] are lacking.

Furthermore, while the previous works on bubble impact with solid walls mentioned above dealt with Newtonian fluids, where the viscosity is constant, many fluids of practical importance in daily life and industrial applications exhibit non-Newtonian rheology. An important type of a non-Newtonian fluid is the so-called power-law fluid.

It derives its name from the power-law dependence [33] of the viscosity $\tilde{\mu}$ on the deformation rate $\tilde{\dot{\gamma}}$ and is given by

$$\tilde{\mu}\left(\tilde{\dot{\gamma}}\right) = \mu_0 \left|2\tilde{m}\tilde{\dot{\gamma}}\right|^{n-1} \tag{5.1}$$

Here, μ_0 is the zero-deformation-rate viscosity of the fluid, $\tilde{m}^{-1}$ is the characteristic deformation rate, n, where $0 < n \leq 1$, is the power-law exponent or index ($n = 1$ corresponds to a Newtonian fluid), and $\tilde{\dot{\gamma}}$ is the second invariant of the rate-of-deformation tensor $\tilde{\mathbf{D}}$

$$\tilde{\dot{\gamma}} = \left[\frac{1}{2}\left(\tilde{\mathbf{D}} : \tilde{\mathbf{D}}\right)\right]^{\frac{1}{2}} \tag{5.2}$$

$$\tilde{\mathbf{D}} = \frac{1}{2}\left[\left(\tilde{\nabla}\tilde{\mathbf{v}}\right) + \left(\tilde{\nabla}\tilde{\mathbf{v}}\right)^T\right] \tag{5.3}$$

where $\tilde{\nabla}$ is the gradient operator and $\tilde{\mathbf{v}}$ is the fluid velocity. It has been shown experimentally that many fluids in industrial applications and in every day use exhibit power-law rheology [34–37].

Previous works on flows of power-law fluids have focused on the self-similarity near singularities arising in thread pinchoff [22, 36–40] and film rupture [28, 30, 32]. It is instructive to note the recent work of Garg et al. [32], who showed that the dynamics of thinning of supported films of power-law fluids were self-similar in the vicinity of the rupture singularity. For power-law fluids with sufficiently large zero-deformation-rate viscosity μ_0 and power-law exponent n, van der Waals, capillary and viscous forces were in balance as the film thins, while inertia is negligible and the lubrication approximation is valid. The variation of the film thickness $\tilde{h}$, lateral length scale $\tilde{z}' \equiv \tilde{z} - \tilde{z}_R$ and lateral velocity $\tilde{v}'$ with time remaining to rupture $\tilde{\tau} \equiv \tilde{t}_R - \tilde{t}$, where $(\tilde{z}_R, \tilde{t}_R)$ denote the lateral location and time instant of the singularity, i.e. when the film thickness $\tilde{h} = 0$, is given by

$$\tilde{h} \sim \tilde{\tau}^{n/(n+4)}, \quad \tilde{z}' \sim \tilde{\tau}^{2n/(n+4)}, \quad \tilde{v}' \sim \tilde{\tau}^{(n-4)/(n+4)} \tag{5.4}$$

for both line or sheet rupture, and axisymmetric or point rupture. However, for films of power-law fluids with low values of μ_0 and n, the dynamics were shown to

transition to an inertial regime, where the lubrication approximation broke down. The dominant balance of forces is now between inertial, capillary and van der Waals forces, and the film thickness, lateral length scale and lateral velocity scale with $\tilde{\tau}$ as

$$\tilde{h} \sim \tilde{\tau}^{2/7}, \quad \tilde{z}' \sim \tilde{\tau}^{4/7}, \quad \tilde{v}' \sim \tilde{\tau}^{-3/7} \tag{5.5}$$

The critical values of fluid parameters for which this transition occurs were also determined analytically by Garg et al. [32] and good agreement with numerical simulations was observed for line rupture of supported thin films.

Motivated by these studies, in this chapter we study self-similarity of the final stages of bubble attachment to a solid wall when its velocity of approach is small enough such that rebound does not occur, for both Newtonian and power-law fluids. The chapter is organized as follows. Section 5.2 describes in detail the problem under investigation and equations and boundary conditions that govern bubble approach, impact and subsequent attachment to the wall. The numerical methods used to solve these equations along with additional meshing techniques employed to resolve the largely disparate lengthscales of the problem are also described in this section. Section 5.3 presents results for bubbles that approach a solid wall with a large approach velocity, and examines the conditions required for the bubble to rebound. Section 5.4 examines bubble impact when the approach velocity is low enough such that rebound effects are absent, and the bubble attaches to the wall on first approach. The self-similarity during the final stages of bubble attachment − when the film in between the bubble and wall is draining − is examined for bubbles immersed in both Newtonian and power-law liquids. Finally, section 5.5 consists of concluding remarks and identifies areas that will benefit from further study using the methods and results described in this chapter.

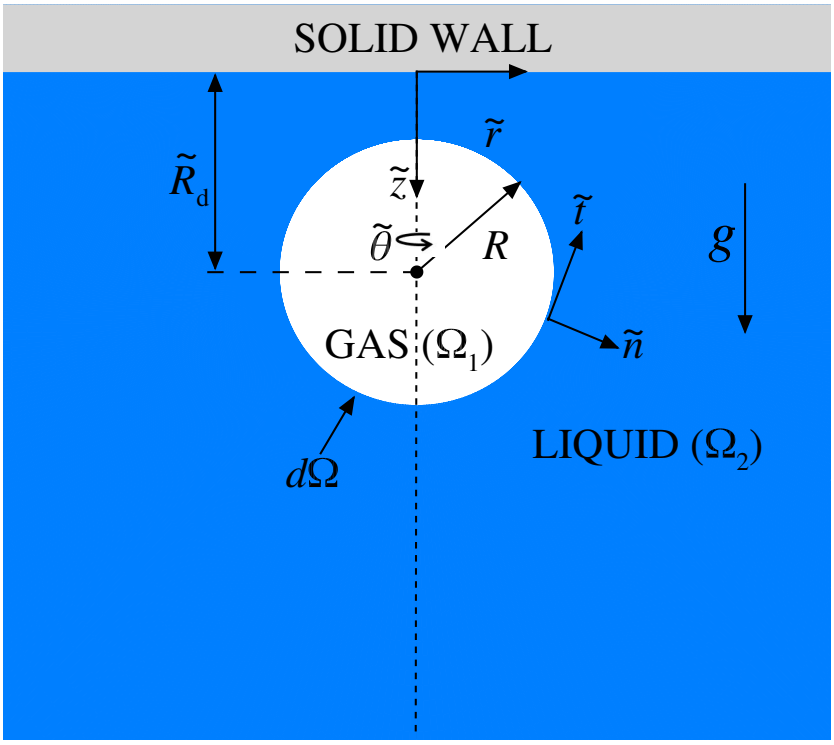

Figure 5.1. Sketch for impact of a gas bubble immersed in a power-law liquid with a solid wall. The initially spherical bubble of radius R is separated from the wall by a center to wall distance $\tilde{R}_d$. Buoyancy forces drive the bubble towards the horizontal wall.

5.2 Mathematical formulation

5.2.1 Problem Setup

The system consists of a single, initially spherical bubble of radius R of an incompressible gas of density ρ_1 and constant viscosity η_1, immersed in an incompressible power-law liquid of density ρ_2, non-constant viscosity $\tilde{\eta}$, rising due to buoyancy forces towards a horizontal, solid wall separated by a distance of $\tilde{R}_d$ from the center of mass of the bubble, as shown in figure 5.1. The system is isothermal and the interface tension σ of the gas-liquid interface $\partial\Omega$, and the Hamaker constant A_H for the gas-liquid-solid system, are spatially uniform and constant. In the following mathematical

formulation, a cylindrical coordinate system $(\tilde{r}, \tilde{\theta}, \tilde{z})$ is chosen with the $\tilde{z}$-axis running through the center of the bubble and the origin is located at the point where the $\tilde{z}$-axis meets the horizontal wall. Owing to the axially symmetric nature of the system, the problem can be reduced to half of the schematic shown in figure 5.1.

In this chapter, the problem variables are non-dimensionalized by choosing the radius of the bubble as the characteristic length scale $l_c = R$, the inertio-capillary time as characteristic time $t_c = \sqrt{\rho_2 R^3/\sigma}$, the ratio of these two scales at the characteristic velocity $v_c = l_c/t_c$, capillary pressure as the characteristic pressure/stress $p_c = \sigma/R$, and the zero-deformation-rate viscosity η_2 of the liquid as the characteristic viscosity $\eta_c = \eta_2$. The dynamics are then governed by the following dimensionless groups: the Ohnesorge number $Oh = \eta_2/\sqrt{\rho_2 \sigma R}$, which is the ratio of the viscous force to the square root of the product of the inertial and capillary forces, viscosity ratio $\beta = \eta_1/\eta_2$, which is the ratio of the viscosity of the gas to zero-deformation-rate viscosity of the liquid, density ratio $d_1 = \rho_1/\rho_2$, which is the ratio of the densities of the two fluids, the gravitational Bond number $G = ((\rho_2 - \rho_1)gR^2)/\sigma$, which is the ratio of buoyancy force to capillary force, where g is acceleration due to gravity, the dimensionless characteristic deformation rate $m = \tilde{m}/t_c$ of the outer liquid, and finally, the van der Waals number $A = A_H/(6\pi\sigma R^2)$, which is the ratio of long range van der Waals forces to capillary forces. In what follows, variables without a tilde $(\sim)$ denote the dimensionless counterparts of variables with tildes over them.

The dynamics in the region $\Omega_1(t)$, or the bubble, are governed by the continuity and Navier Stokes equations for dimensionless pressure $p_1 \equiv \tilde{p}_1/p_c$ and dimensionless velocity $\mathbf{v}_1 \equiv \tilde{\mathbf{v}}_1/v_c$, which in dimensionless form are given by

$$\nabla \cdot \mathbf{v}_1 = 0 \tag{5.6}$$

$$d_1 \left(\frac{\partial \mathbf{v}_1}{\partial t} + \mathbf{v}_1 \cdot \nabla \mathbf{v}_1 + G \right) = \nabla \cdot \mathbf{T}_1 \tag{5.7}$$

where $\mathbf{T}_1 \equiv -p_1\mathbf{I} + \beta_1 Oh\left[\nabla\mathbf{v}_1 + (\nabla\mathbf{v}_1)^T\right]$ is the dimensionless stress tensor. The dynamics in the region $\Omega_2(t)$, or the power-law liquid, are governed by the continuity and Cauchy momentum equations, which in dimensionless form are given by

$$\nabla \cdot \mathbf{v}_2 = 0 \tag{5.8}$$

$$\left(\frac{\partial \mathbf{v}_2}{\partial t} + \mathbf{v}_2 \cdot \nabla\mathbf{v}_2\right) = \nabla \cdot \mathbf{T}_i \tag{5.9}$$

where $\mathbf{T}_2 \equiv -p_2\mathbf{I} + \mu_2 Oh\left[(\nabla\mathbf{v}_2) + (\nabla\mathbf{v}_2)^T\right]$ is the dimensionless stress tensor, and μ_2 is the dimensionless viscosity given by $\mu_2 = |2m\dot{\gamma}|^{n-1}$.

The kinematic and traction boundary conditions are applied at the liquid-gas interface $d\Omega$ which is unknown a priori, to enforce mass conservation and account for the discontinuity in stress due to interface tension and van der Waals forces

$$\mathbf{n} \cdot (\mathbf{v}_i - \mathbf{v}_s) = 0 \tag{5.10}$$

$$\mathbf{n} \cdot (\mathbf{T}_2 - \mathbf{T}_1) = 2H\mathbf{n} - \frac{A}{h^3}\,\mathbf{n} \tag{5.11}$$

where $\mathbf{v}_s$ is the velocity of points on the interface $d\Omega$, $\mathbf{n}$ is the unit normal vector to and $2H$ is twice the mean curvature of $d\Omega$. Due to axisymmetry at $r = 0$, symmetry conditions are applied at this boundary. At the solid wall, the liquid must obey the no-slip and no penetration boundary condition, such that

$$\mathbf{v_2} = 0 \tag{5.12}$$

Finally, the liquid must become quiescent at distances infinitely far away from the bubble. The system is initially quiescent, such that $\mathbf{v}_i = 0$ at time $t = 0$.

5.2.2 Numerical Method

The two-dimensional interfacial flow described by the system of transient partial differential equations (5.8) - (5.9) subject to the aforementioned boundary and initial conditions is solved using a fully implicit, method of lines, arbitrary Lagrangian-Eulerian algorithm. The Galerkin/finite element method (G/FEM) is used for spatial

discretization [41] with a finite difference implicit adaptive Adams Bashforth scheme for time integration [42]. The partial differential equations are converted to ordinary differential equations by using the Galerkin/finite element method (G/FEM) for spatial discretization, while time integration reduces the system of ordinary different al equations to a system of nonlinear algebraic equations. In order to capture the large deformations that the gas-liquid interface undergoes as well accurately resolve the highly disparate lengthscales of the problem, the elliptic mesh generation method developed by Christodolou and Scriven [43] is used to determine the vertical and lateral coordinates of each grid point in the moving, adaptive mesh simultaneously with the velocity and pressure unknowns. A mixed interpolation scheme is used for the variables, as biquadratic basis functions are used to represent the mesh coordinates and velocity unknowns, while bilinear basis functions are used to represent the pressure unknowns. The resulting nonlinear algebraic equations are solved using Newton's method with an analytically computed Jacobian. Variants of this algorithm have been employed by our research group to successfully study hydrodynamic singularities that arise in thread pinchoff of both Newtonian and non-Newtonian fluids [22,44], drop and bubble coalescence [25,26], and supported thin film rupture [32]. The reader is referred to these works for a complete description of the solution method and numerical implementation.

For our simulations, the domain extent in the lateral r and axial z direction was fixed at a large but finite value of R_∞ for all simulations. On these surfaces at $r = R_\infty$ and $z = R_\infty$, a stress free boundary condition was imposed, such that $\mathbf{n}_2 \cdot \mathbf{T}_2 = 0$ where $\mathbf{n}_2$ is the outward pointing unit normal to the boundaries. Thus, $\mathbf{n}_2 = \mathbf{e}_r$ at $r = R_\infty$, and $\mathbf{n}_2 = \mathbf{e}_z$ at $z = R_\infty$. It was observed that changing the value of the lateral and axial extents beyond $R_\infty = 7$ resulted in insignificant change in the computed solutions, and thus, this value is used for all results presented in this chapter.

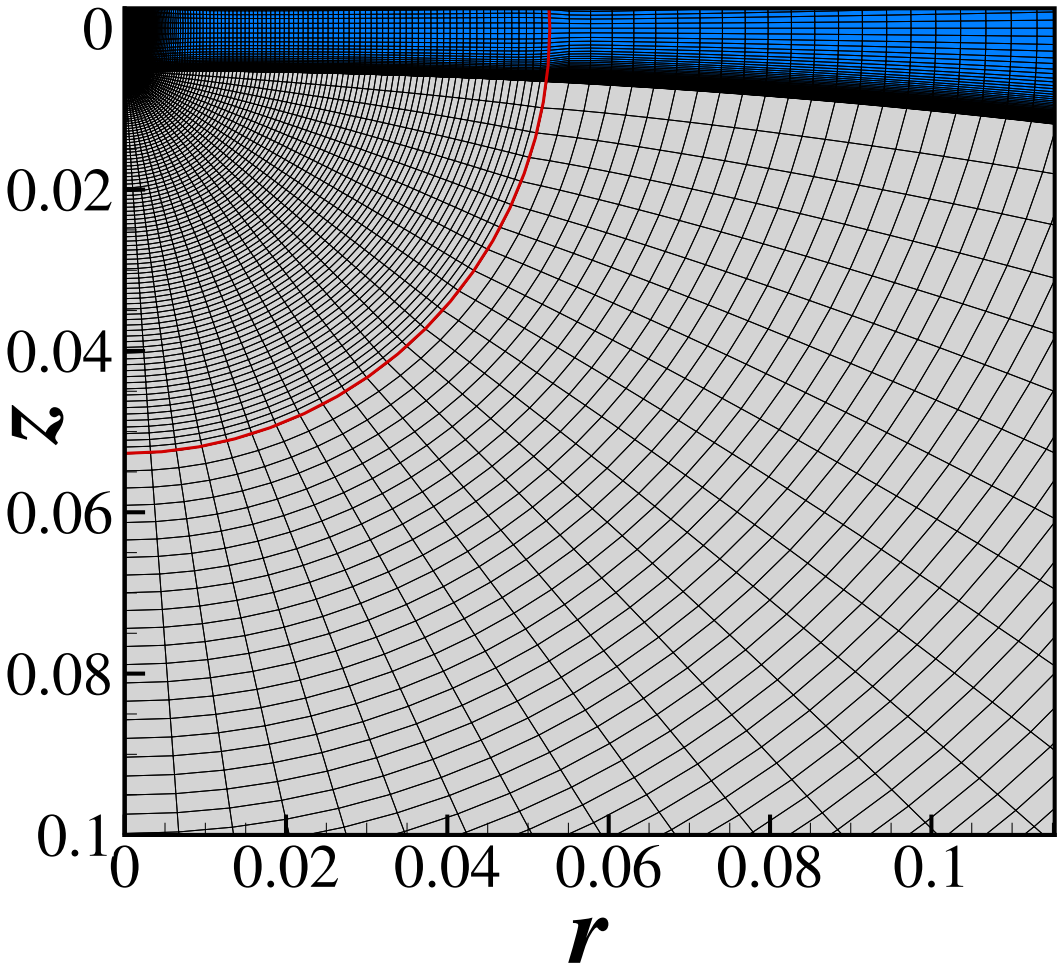

Figure 5.2. An example mesh showing the bubble as it approaches the solid wall at $z = 0$. The algebraic surface shown by the red curve here divides the mesh into two domains, such that elements are concentrated towards the tip of the bubble. This surface moves in time according to a specification defined by the value of the minimum separation of the interface from the wall $z_{min}(t)$. Simulations typically use a mesh two to five times denser than the one shown here.

5.2.3 Meshing techniques

In this problem two disparate lengthscales exist, the radius of the bubble which is $O(1)$, and the thickness of the film that forms between the bubble and solid wall during its approach, which ranges from $O(10^{-3})$ to $O(10^{-6})$ as the film thins and

ruptures. This large disparity in lengthscales requires concentrating elements in the film region as it thins, in order to accurately resolve scaling behavior as well as the macroscale dynamics of bubble approach. While the elliptic mesh equations developed by Christodoulou and Scriven [43] allow for use of functions to selectively concentrate elements, additional methods of mesh concentration are required for this problem. In the limit of small approach velocity, or in other words, for bubbles with low We number values, it is known that bubble deformation upon approach to the wall is negligible [10]. Thus, we define an artificial algebraic surface that surrounds the region of the film between the solid wall and bottom of the bubble and moves inwards with the bubble, such that elements can never cross this boundary. As the bubble approaches the wall, the imposition of this surface causes elements to concentrate in the region of the film where the separation of the bubble from the wall is minimum. This boundary is imposed as an ellipse where its parameters are specified solely by the minimum separation between the bubble and wall, denoted by z_{min}. The ellipse is always centered at the origin such that $(h, k) = (0, 0)$, where the equation of the ellipse is given by

$$\frac{(x-h)^2}{a^2} + \frac{(y-k)^2}{b^2} = 1 \tag{5.13}$$

and a and b depend on z_{min} in the following manner

$$a = \begin{cases} z_{min}, & \text{for} \quad z_{min} > 0.1 \\ 0.1, & \text{for} \quad 0.1 > z_{min} > 0.01 \\ 10 z_{min}, & \text{for} \quad 0.01 > z_{min} > 0.0005 \\ 0.005, & \text{for} \quad z_{min} < 0.0005 \end{cases}$$

$$b = \begin{cases} z_{min} + 0.2, & \text{for} \quad z_{min} > 0.1 \\ 3 z_{min}, & \text{for} \quad 0.1 > z_{min} > 0.1/3 \\ 0.1, & \text{for} \quad 0.1/3 > z_{min} > 0.01 \\ 10 z_{min}, & \text{for} \quad 0.01 > z_{min} > 0.0005 \\ 0.005, & \text{for} \quad z_{min} < 0.0005 \end{cases}$$

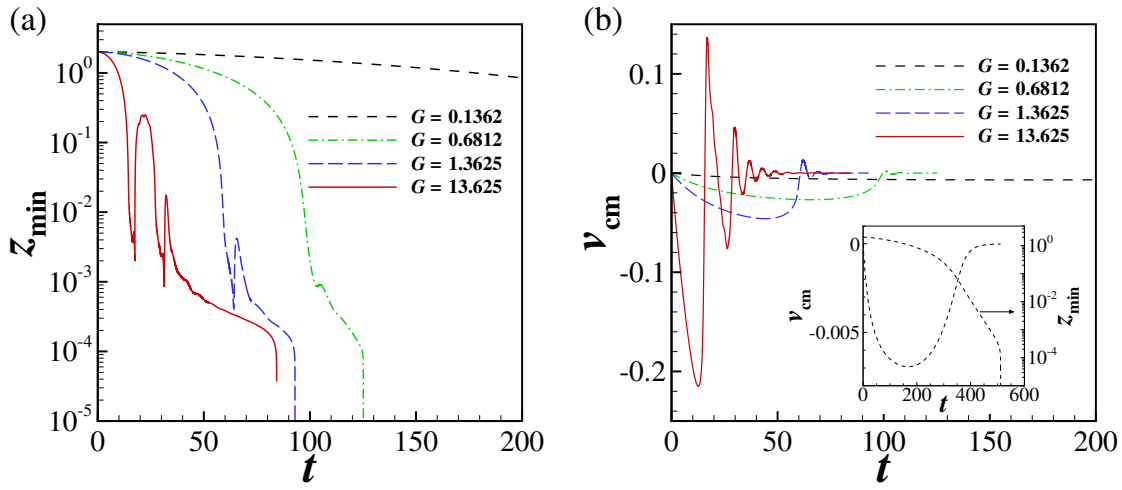

Figure 5.3. (a) Variation with time t of the minimum axial separation z_{min} of the bubble-liquid interface from the solid wall and (b) velocity of the center of mass of the bubble v_{cm} for an air bubble immersed in water approaching a solid wall such that $Oh = 3.7628 \times 10^{-3}$, $A = 10^{-10}$, $d_1 = 10^{-3}$, $\beta_1 = 10^{-3}$, $m = Oh\epsilon^5/A^2$ and $n = 1$ for $G = 0.1362$, 0.6812, 1.3625, and 13.625. The bubble is seen to rebound from the wall if the value of G is artificially increased from its physical value. The inset in (b) shows the variation of v_{cm} and z_{min} for the physical case, when $G = 0.1362$.

An example mesh is shown in figure 5.2. The position of this boundary is updated after the value of z_{min} is obtained for the current time step, so that the location of the nodes on the algebraic surface are never implicitly dependent on the node at $z = z_{min}$.

5.3 Bubble impact for large Re

In this section, the bubble is initially separated by $R_d = 3$ from the solid wall that it approaches due to buoyancy forces. Figure 5.3(a) shows the variation with time of the minimum axial separation between the bubble interface and the wall for an air bubble immersed in water approaching a hydrophobic solid wall for four cases such that parameter values are $Oh = 3.7628 \times 10^{-3}$, $A = 10^{-10}$, $d_1 = 10^{-3}$, $\beta_1 = 10^{-3}$, $m = Oh\epsilon^5/A^2$ and $n = 1$, while the value of the Bond number is artificially varied such that $G = 0.1362$, 0.6812, 1.3625, and 13.625. This is equivalent to artificially

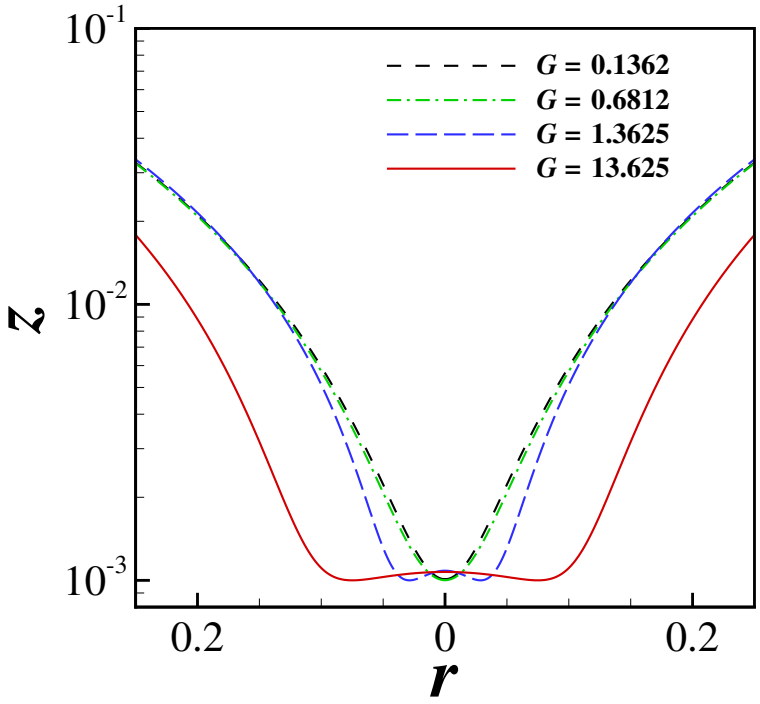

Figure 5.4. Interface shapes for four cases of an air bubble rising in water towards a hydrophobic solid wall such that parameter values are $Oh = 3.7628 \times 10^{-3}$, $A = 10^{-10}$, $d_1 = 10^{-3}$, $\beta_1 = 10^{-3}$, $m = Oh\epsilon^5/A^2$ and $n = 1$ and $G = 0.1362$, 0.6812, 1.3625, and 13.625. The interface shapes shown are for the time instant when $z_{min} = 1 \times 10^{-3}$ for each case. The interface deforms for larger values of G as pressure builds up in the film and pushes the bubble away, causing the observed rebound effects.

increasing acceleration due to gravity by a factor of 5, 10, and 100 respectively for the latter three cases. It is clear that for a mm sized bubble separated by three radii from a solid wall ($G = 0.1362$), the bubble attaches to the wall at first approach without any rebound. The corresponding variation of the velocity of the center of mass of the bubble v_{cm} is shown in figure 5.3(b). For $G = 0.1362$, the largest value of the Reynold's number attained is $Re = v_{cm}/Oh = 1.856$, or $Re \sim O(1)$. The Reynold's number is small, and no rebound of the bubble is seen. However, for larger values of G, the bubble accelerates to attain larger values of v_{cm} before approaching the wall, and rebound from the wall is seen in each of the three cases. For $G = 13.625$, the bubble

rebounds twice before finally attaching to the wall, as the maximum value of the Reynold's number attained is $Re = 57.133 \gg 1$ in this case. The dimensional terminal velocity $\tilde{v}_t$ for a bubble rising in a liquid is given by the Hadamard−Rybczynski equation [45, 46]

$$\tilde{v}_t = \frac{\rho_2 g R^2}{3\eta_2} \tag{5.14}$$

It is straightforward to show that the dimensionless terminal velocity is thus $v_t = G/3Oh = 12.069$ for a 1 mm air bubble rising in water. Thus it is clear that even an artificial value of G that is 100 times the physical value for a 1 mm air bubble in water is insufficiently small for the bubble to achieve terminal velocity if the initial separation is only $R_d = 3$, and a larger initial separation and/or larger value of G is required to observe the multiple rebounds seen by Tsao and Koch [9].

The bubble-liquid interface shapes at the time instant when $z_{min} = 1 \times 10^{-3}$ in the vicinity of the solid wall are shown for the aforementioned cases in figure 5.4. The interface does not deform for the physical case of $G = 0.1362$ or when $G = 0.6812$. Corresponding values of the largest Weber number $We = v_{cm}^2$ attained for these cases are 4.795×10^{-5} and 7.236×10^{-4} respectively. These are negligible compared to the values observed by Tsao and Koch [9] who observed multiple rebound for $We \sim O(1)$. In contrast, when $G = 1.3625$, a slight flattening of the interface is apparent from figure 5.4 and for the highest value of $G = 13.625$, the interface is significantly flattened at $z_{min} = 1 \times 10^{-3}$. The corresponding Weber numbers for these two cases are 2.116×10^{-3} and 4.618×10^{-2}. The flattening of the interface occurs when the pressure in the film region is of the same order of magnitude as the pressure inside the bubble. As a result, a large normal force opposes the motion of the bubble towards the solid wall and leads to rebound in these cases. This explains the absence of any deformation for the natural value of G, as the capillary forces are stronger than these normal forces due to pressure and maintain its spherical shape. Naturally, the extent of deformation is expected to be much larger if the bubble is initially separated from the wall by a distance large enough for it to attain terminal velocity.

In this section, we have established that for physical parameter values of a 1 mm sized air bubble immersed in water approaching a solid wall, a separation of $R_d < 3$ will result in monotonic decrease of the separation between the bubble and the wall without any shape deformation, until it finally attaches to the solid substrate. For the remainder of this chapter, we will explore the impact of bubbles when rebound effects and shape deformations are absent, or when $Re \sim O(1)$ and $We \ll 1$. Our goal is to examine the self-similarity of bubble approach once van der Waals forces become significant.

5.4 Bubble impact for low Re

5.4.1 Macroscopic behavior of bubbles

In this section, the bubble is always initially separated by one diameter ($R_d = 2$) from the solid wall. For bubbles of size 1 mm or below, it is expected that the bubble will not rebound from the wall for even low viscosity liquids such as water, as the maximum approach velocity attained by the bubble will be very low. Figure 5.5(a) shows the variation with time t of the velocity of the center of mass v_{cm} of the bubble, and minimum axial separation between the bubble and the wall z_{min}, for an air bubble immersed in water approaching a hydrophobic solid wall, such that parameter values are $Oh = 3.7628 \times 10^{-3}$, $G = 0.136$, $A = 10^{-10}$, $d_1 = 10^{-3}$, $\beta_1 = 10^{-3}$, $m = Oh\epsilon^5/A^2$ and $n = 1$. The value of z_{min} is seen to monotonically decrease to $O(10^{-4})$, before van der Waals forces become significant and the liquid film between the bubble and wall rapidly ruptures. The value of $|v_{cm}|$ increases as the bubble, initially at rest, accelerates due to buoyancy and approaches a near constant value before decreasing as $z_{min} \sim O(10^{-1})$. Below this value of z_{min}, the bubble slows down due to pressure build up in the liquid between the bubble and the wall. The instantaneous value of the Reynold's number for the bubble at the maximum value of $|v_{cm}|$ is $Re = 1.49$, while the local Weber number $We = |v_{cm}|^2 = 3.1 \times 10^{-5}$, which is extremely small. Figure 5.5(b) shows shapes of the gas-liquid interface at different instants of time as

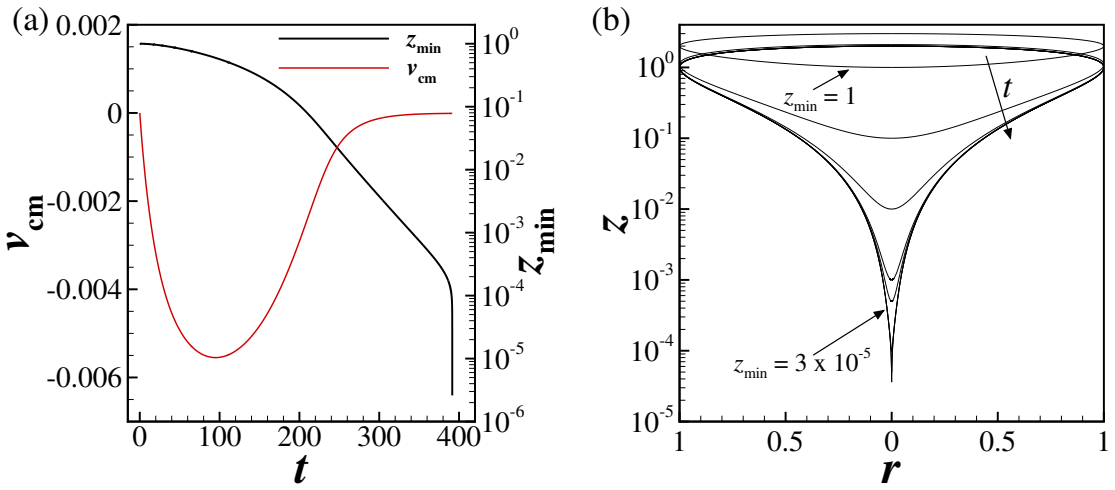

Figure 5.5. (a) Variation with time t of the velocity of the center of mass of the bubble v_{cm} and the minimum axial separation z_{min} of the bubble-liquid interface from the solid wall and (b) interface profiles at various time instants for an air bubble immersed in water approaching a solid wall such that $Oh = 3.7628 \times 10^{-3}$, $G = 0.136$, $A = 10^{-10}$, $d_1 = 10^{-3}$, $\beta_1 = 10^{-3}$, $m = Oh\epsilon^5/A^2$ and $n = 1$. Dimpling of the bubble interface is absent for such a low approach velocity and the point of attachment is always at $r = 0$.

the bubble approaches the wall and it is clear that dimpling of the surface is absent, and z_{min} is always located at $r = 0$, which is where the bubble eventually attaches to the wall.

Similar macroscopic behavior is observed if keeping all other parameters constant, the value of the power-law exponent for the outer liquid is reduced. Figure 5.6(a) shows the variation with time of z_{min}, while 5.6(b) shows the variation of v_{cm} with time for three cases, where $n = 1.0$, $n = 0.9$ and $n = 0.7$ respectively. These figures make plain that a lower value of power-law exponent for the outer fluid results in a higher approach velocity for the bubble, which results in a smaller total attachment time. This is expected as the viscous drag on the bubble falls rapidly for outer liquid with lower values of power-law exponents. However, lowering the power-law exponent does not lead to rebound, as the maximum values of the instantaneous Reynold's number are $Re = 1.74$ for $n = 0.9$, and $Re = 1.86$ for $n = 0.7$ respectively. Similarly,

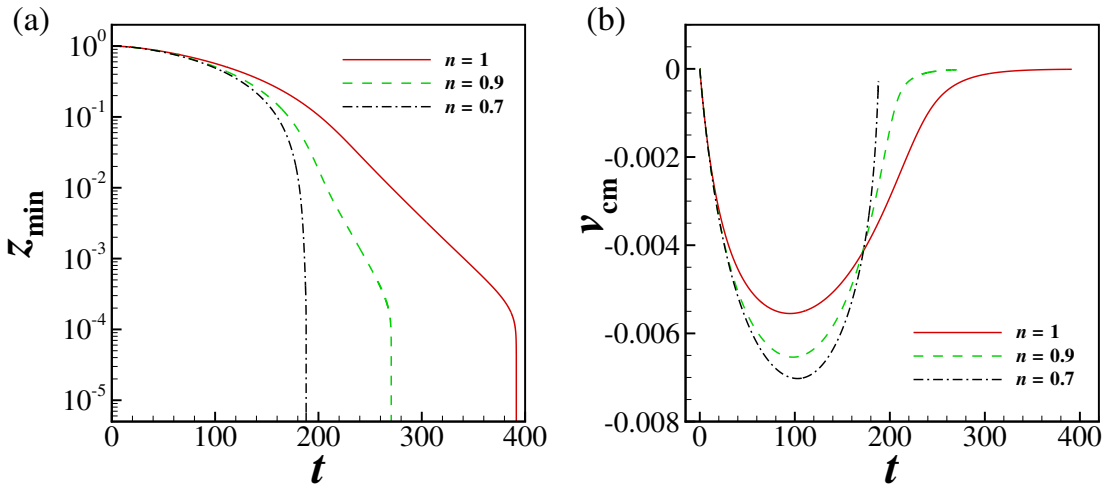

Figure 5.6. (a) Variation with time t of the minimum axial separation z_{min} of the bubble-liquid interface from the solid wall and (b) the velocity of the center of mass of the bubble v_{cm} for an air bubble immersed in a power-law liquid approaching a solid wall such that $Oh = 3.7628 \times 10^{-3}$, $G = 0.136$, $A = 10^{-10}$, $d_1 = 10^{-3}$, $\beta_1 = 10^{-3}$, $m = Oh\epsilon^5/A^2$ for three values of power-law exponents $n = 1$, 0.9 and 0.7.

deformation of the gas-liquid interface is negligible, as the maximum values of the instantaneous Weber numbers are $We = 4.27 \times 10^{-5}$ for $n = 0.9$ and 5.23×10^{-5} for $n = 0.7$ respectively. The macroscopic behavior of mm sized bubbles separated by one diameter from a solid wall shown here makes plain that this system is ideal for studying the scaling and self-similarity of axisymmetric rupture of supported liquid films due to van der Waals forces. This is explored in the remainder of this section.

5.4.2 Scaling and self-similarity during bubble impact

For bubbles that approach solid walls with low Re, the final stages of bubble attachment to the wall, where rapid thinning and rupture of the liquid film in between the bubble and wall occurs, resemble van der Waals driven axisymmetric or point rupture of supported thin films. As seen above, this driving force becomes significant only when $z_{min} \sim O(10^{-4})$, because intermolecular forces become significant for small

separations of $\sim$ 100 nm. Consequently, the characteristic scales for dynamics occurring in the liquid film are different from those originally specified for macroscopic approach of the bubble to the wall in section 5.2. An alternative approach to non-dimensionalization is to consider the initial film thickness h_0 at which van der Waals forces between the bubble and solid wall become significant as the vertical lengthscale in addition to the bubble radius R, which is now defined as the lateral lengthscale. Furthermore, if the characteristic stress is defined instead as $p_c = \eta_2 v_c R/h_0^2$, as viscous forces are expected to be significant in the film for low Re flow, the dimensionless equations governing the flow of the outer liquid are modified to

$$\nabla_{\rm II} \cdot \mathbf{v}_{\rm II} + \frac{\partial w}{\partial z} = 0 \tag{5.15}$$

$$Re_r \left(\frac{\partial \mathbf{v}_{\rm II}}{\partial t} + \mathbf{v}_{\rm II} \cdot \nabla_{\rm II} \mathbf{v}_{\rm II} + w \frac{\partial v_{\rm II}}{\partial z} \right) = -\nabla_{\rm II} p + \mu \left(\epsilon^2 \nabla_{\rm II}^2 \mathbf{v}_{\rm II} + \frac{\partial^2 \mathbf{v}_{\rm II}}{\partial z^2} \right) + \frac{\partial \mu}{\partial z} \frac{\partial \mathbf{v}_{\rm II}}{\partial z} + \epsilon^2 \left(\nabla_{\rm II} \mu \cdot \nabla_{\rm II} \mathbf{v}_{\rm II} + \nabla_{\rm II} \mathbf{v}_{\rm II} \cdot \nabla_{\rm II} \mu + \frac{\partial \mu}{\partial z} \nabla_{\rm II} w \right) \tag{5.16}$$

$$Re_r \left(\frac{\partial w}{\partial t} + \mathbf{v}_{\rm II} \cdot \nabla_{\rm II} w + w \frac{\partial w}{\partial z} \right) = -\frac{1}{\epsilon^2} \frac{\partial p}{\partial z} + \mu \left(\epsilon^2 \nabla_{\rm II}^2 w + \frac{\partial^2 w}{\partial z^2} \right) + \nabla_{\rm II} \mu \cdot \left(\epsilon^2 \nabla_{\rm II} w + \frac{\partial \mathbf{v}_{\rm II}}{\partial z} \right) + 2 \frac{\partial \mu}{\partial z} \frac{\partial w}{\partial z} \tag{5.17}$$

where the liquid velocity and gradient are decomposed into two parts, one which is parallel to the solid wall $\mathbf{v}_{\rm II} \equiv \tilde{\mathbf{v}}_{\rm II}/v_c$, while the other is perpendicular to the wall $w \equiv \tilde{w}/w_c$, such that

$$\mathbf{v}_2 = \mathbf{v}_{\rm II} + w \mathbf{e}_z \,, \quad \nabla = \nabla_{\rm II} + \mathbf{e}_z \frac{\partial}{\partial z} \tag{5.18}$$

and $Re_r \equiv \epsilon \rho_2 v_c h_0/\eta_2 \equiv \epsilon^2/Oh$ is the reduced Reynold's number, $\epsilon = h_0/R$ is the film aspect ratio, while it follows from the continuity equation that $w_c \sim \epsilon v_c$.

The profiles of the axial separation of the bubble and wall, denoted by $z_I(r,t)$, which is the axial coordinate z of the gas-liquid interface, and radial velocity $v(r,t)$ at the interface, are expected to be self-similar as the singularity r_S, t_S is approached, where the bubble attaches to the wall at $r = r_S$ at $t = t_S$, or the minimum separation

becomes zero. The separation and radial velocity in the vicinity of this singularity can be described by the similarity ansatz

$$z_I \equiv \tau^{\alpha} H(\eta), \quad v \equiv \tau^{\gamma} V(\eta), \quad \eta \equiv r'/\tau^{\beta} \tag{5.19}$$

where $\tau \equiv t_S - t$ is the time until attachment, η is the similarity variable, $r' \equiv r - r_S$ is the radial extent of the attachment zone, α, β and γ are scaling exponents for z_I, v and r' respectively, and $H(\eta)$ and $V(\eta)$ are the scaling functions for the separation and radial velocity in similarity space. It is evident from results presented above that the initial value of the reduced Reynold's number Re_r is negligibly small for the cases considered in this section. Indeed, for air bubbles in water, the value of $Re_r = 2.66 \times 10^{-6}$, signifying that the inertial terms in equations (5.16) and (5.17) can presumably be neglected, and the final stages of bubble impact could be described by a one-dimensional evolution equation, as was done in many previous works [16,18]. Substituting equation (5.19) into equations (5.16) and (5.17) and carrying out a kinematic and dynamic balance, in the absence of inertial forces, yields the scaling exponents of equation (5.4) shown by Garg et al. [32] for supported film rupture. The dynamic force balance for this regime is between capillary (C), van der Waals (vdW) and viscous (V) forces, and the forces increase with τ as

$$C \sim vdW \sim V \sim \tau^{-5n/(n+4)} \tag{5.20}$$

If lubrication theory is valid all the way until attachment, the dynamics will be described accurately by this scaling regime. To validate the scaling exponents and proposed balance of forces, bubble impact with a solid wall for bubbles approaching with low Re is simulated using the 3-D axisymmetric algorithm based on the finite-element method specified in section 5.2, by solving equations (5.8) and (5.9). The bubble is said to attach to the wall when the minimum separation has reached the molecular lengthscale and the continuum approximation breaks down, or when $z_{min} = d/R$. Figure 5.7 shows the variation with time to rupture τ of several quantities of interest in the region of minimum separation between the bubble and the

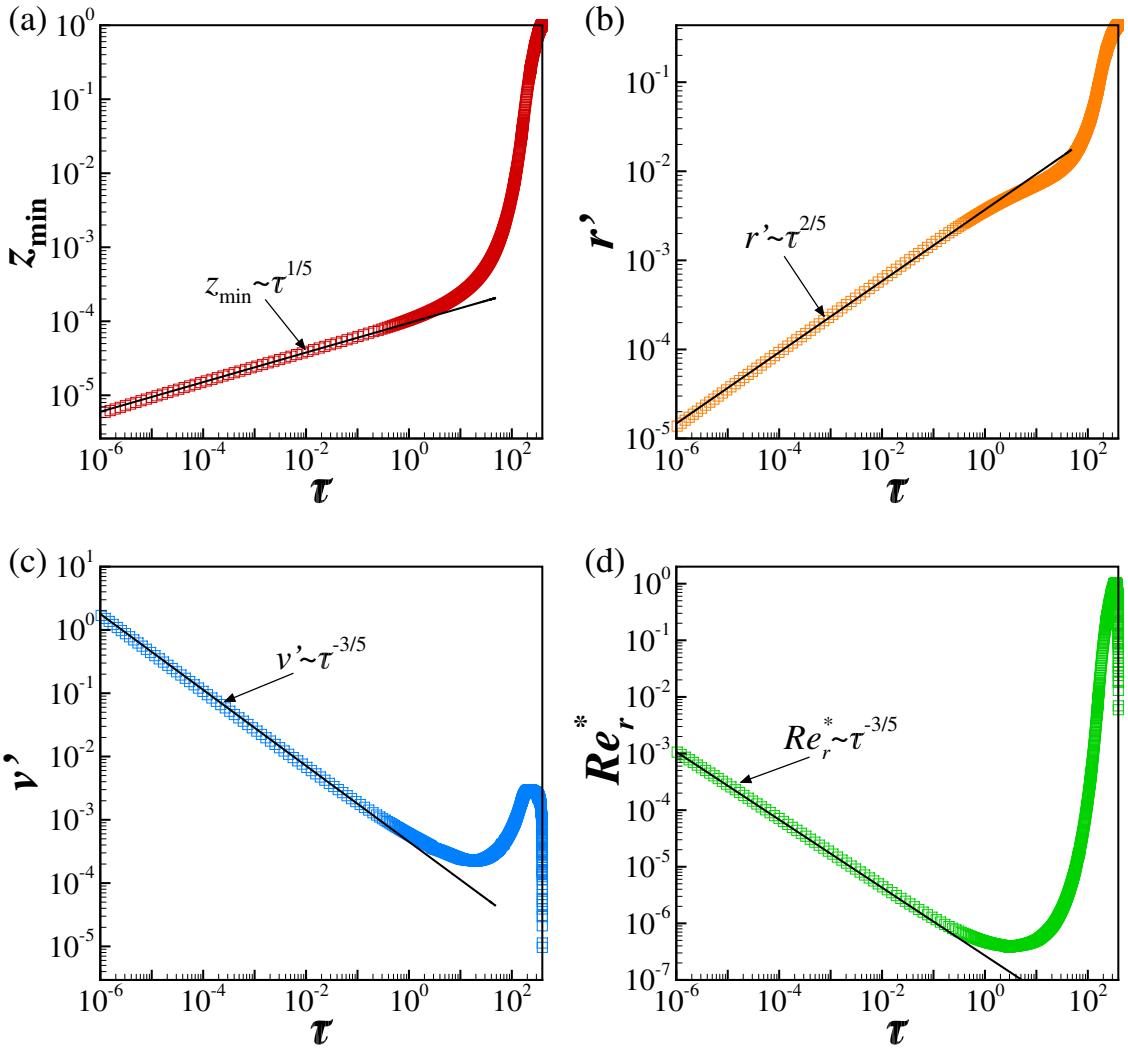

Figure 5.7. Variation with time remaining to rupture τ of (a) minimum axial separation z_{min} between the bubble-liquid interface and solid wall, (b) radial lengthscale r', computed as the radial coordinate r of the bubble-liquid interface at which the axial separation is given by $z_I = 1.05 z_{min}$ (c) radial velocity v' and (d) instantaneous Reynold's number Re_r^* computed at this same radial location for an air bubble immersed in water approaching a solid wall such that $Oh = 3.7628 \times 10^{-3}$, $G = 0.136$, $A = 10^{-10}$, $d_1 = 10^{-3}$, $\beta_1 = 10^{-3}$, $m = Oh\epsilon^5/(A^2)$ and $n = 1$. The symbols represent data points obtained from numerical simulations while the solid lines represent best fits to the data.

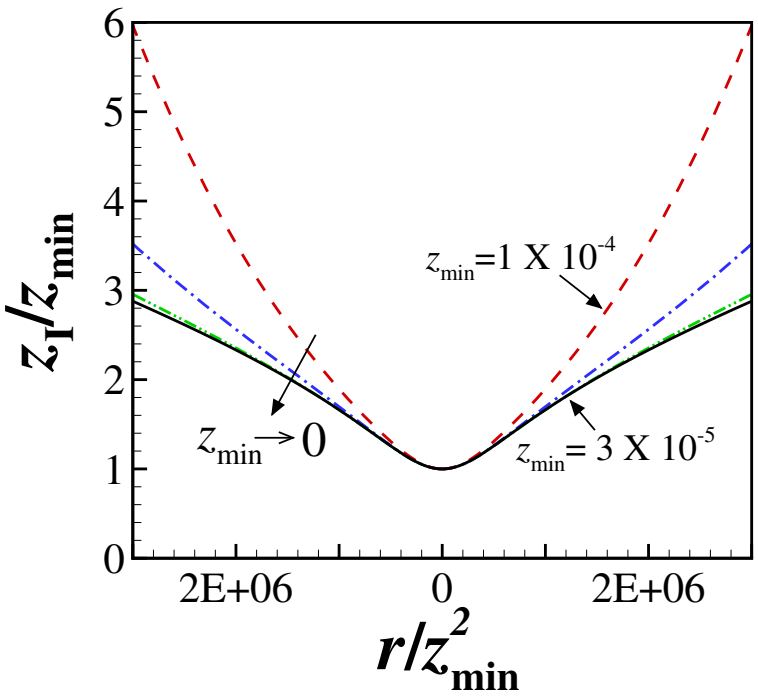

Figure 5.8. Rescaled bubble-liquid interface profiles z_I/z_{min} as a function of the rescaled radial coordinate r/z_{min}^2 for many instants of time determined from numerical simulations for an air bubble immersed in water approaching a solid wall such that $Oh = 3.7628 \times 10^{-3}$, $G = 0.136$, $A = 10^{-10}$, $d_1 = 10^{-3}$, $\beta_1 = 10^{-3}$, $m = Oh\epsilon^5/(A^2)$ and $n = 1$. The profiles are shown for $3 \times 10^{-5} \leq z_{min} \leq 1 \times 10^{-4}$ and each rescaled profile is plotted such that the corresponding value of z_{min} is approximately 2/3rd that of the previous rescaled profile. The profiles collapse onto a single similarity profile as $z_{min} \rightarrow 0$ in the vicinity of the point of attachment $r = 0$.

wall, for an air bubble immersed in water approaching a solid wall, such that parameter values are $Oh = 3.7628 \times 10^{-3}$, $G = 0.136$, $A = 10^{-10}$, $d_1 = 10^{-3}$, $\beta_1 = 10^{-3}$, $m = Oh\epsilon^5/(A^2)$ and $n = 1$. Figure 5.7(a) shows that the minimum separation z_{min} decreases with τ as $z_{min} \sim \tau^{1/5}$ once z_{min} falls below 10^{-4} all the way until the bubble attaches to the wall at $z_{min} = d/R = 1.73 \times 10^{-5}$. The simulation is allowed to run until $h_{min} = 5 \times 10^{-6}$, or beyond the continuum limit when $z_{min} = d/R$, in order to observe if inertia ever becomes significant. Figure 5.7(b) shows the variation with τ of the radial lengthscale r', which is computed by tracking the radial location where

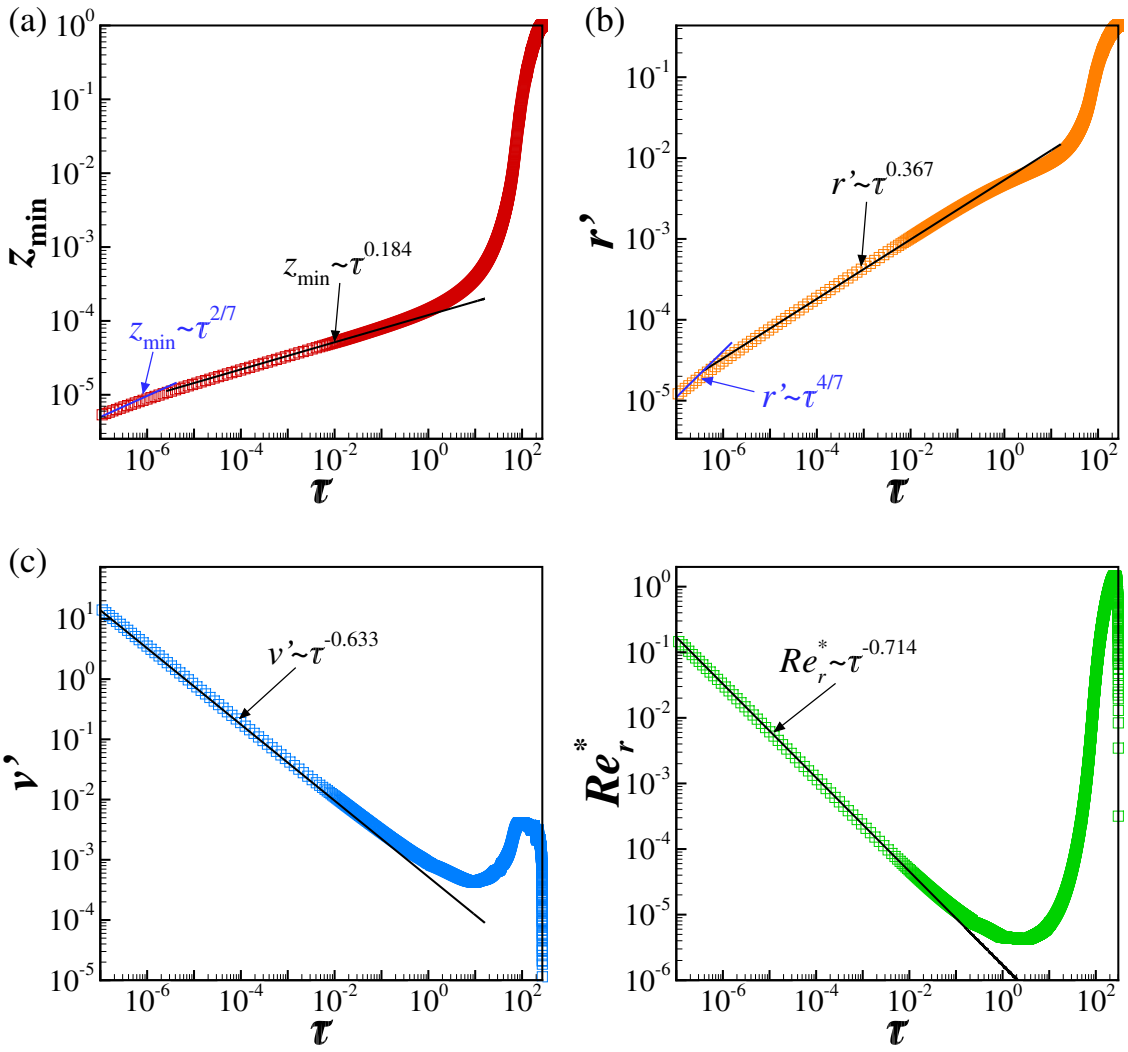

Figure 5.9. Variation with time remaining to rupture τ of (a) minimum axial separation z_{min} between the bubble-liquid interface and solid wall, (b) radial lengthscale r' (c) radial velocity v' and (d) instantaneous Reynold's number Re_r^* computed at the radial location of the bubble-liquid interface where $z_I = 1.05 z_{min}$ for an air bubble immersed in a power-law liquid approaching a solid wall such that $Oh = 3.7628 \times 10^{-3}$, $G = 0.136$, $A = 10^{-10}$, $d_1 = 10^{-3}$, $\beta_1 = 10^{-3}$, $m = Oh\epsilon^5/(A^2)$ and $n = 0.9$. The symbols represent data points obtained from numerical simulations while the solid lines represent best fits to the data.

the axial separation is some order one multiple of z_{min}, e.g., $z_I = 1.05 z_{min}$. The figure makes plain that $r' \sim \tau^{2/5}$ all the way until attachment. Changing the location at which r' was computed, for example using a value of the multiple other than 1.05 led to no change in the value of the scaling exponent obtained for r', for this result and all results presented hereafter in this chapter. Figure 5.7(c) shows that the radial velocity scale v' varies with τ as $v' \sim \tau^{-3/5}$. Again, v' is computed by tracking the radial velocity of the interface at the radial location where $z_I = 1.05 z_{min}$, and again, changing the value of this pre-factor leads to no change in the observed scaling exponent for v'. Thus, the observed scaling exponents are in excellent agreement with the expected exponents for the capillary-viscous regime from equation (5.4).

Figure 5.7(d) shows the instantaneous value of the Reynold's number $Re_r^* = v' {z_{min}}^2/(Oh\mu' r')$, where μ' is the dimensionless fluid viscosity (which remains 1 for water as it is a Newtonian fluid), computed at the radial location where $z_I = 1.05 z_{min}$. It is important to note that this value is obtained from numerical simulations where a single lengthscale $l_c = R$ is used, and not two lengthscales as specified above. Re_r^* is observed to vary with τ as $Re_r^* \sim \tau^{-3/5} \sim \tau^{(5n-8)/(n+4)}$, rising three orders of magnitude from a negligibly small value of 10^{-6} when van der Waals forces become significant, to 10^{-3} at the incipience of attachment. Thus, even though Re_r^* is increasing as the bubble approaches the wall, inertial forces are always negligible for air bubbles in water, and lubrication theory can be used to study the dynamics of the film for bubbles approaching with low Re.

Finally, similarity solutions for the interface profiles can be obtained by collapsing the transient profiles obtained from the numerical solutions. Figure 5.8 shows interface profiles at several time instants, rescaled by z_{min}, plotted against the radial length scale, rescaled by ${z_{min}}^2$, collapsing onto the single similarity solution in the vicinity of the eventual point of attachment. Thus, the impact with solid walls for bubbles approaching with low Re in Newtonian fluids is self-similar, with the dominant force balance between capillary, van der Waals and viscous forces. This regime is observed until $z_{min} = d/R$ and inertial effects are always negligible.

Figure 5.9 shows the variation with τ of these same quantities if the outer liquid is instead taken to be a power-law fluid of exponent $n = 0.9$ while all other parameters are kept constant. Again, simulation results are in excellent agreement with the expected scaling regime from equation (5.4) for $z_{min} < 10^{-4}$ until $z_{min} = d/R$. However, a transition is observed at $z_{min} \sim 6 \times 10^{-6} < d/R$ (figure 5.9(a)), and the variation with τ thereafter is described by $z_{min} \sim \tau^{2/7}$. A similar transition is seen for the radial lengthscale as shown in figure 5.9(b). The presence of these transitions suggest that inertial effects are playing a role, since the scaling exponents are independent of liquid rheology, and identical to those observed by Garg et al. [32] for their inertial regime described by equation (5.5). The value of the instantaneous Reynold's number (figure 5.9(d)) at this instant is $Re_r^* \sim 0.2$, which again suggests that inertial effects could be important, albeit once the continuum limit has broken down in this case. An inevitable question that arises is if inertial effects could be significant before the continuum limit is reached? As the viscosity of the liquid would decrease faster if its power-law exponent n were lower, one expects this to be the case for a sufficiently small value of n. To ascertain if this possibility exists, we first determine analytically when this transition is expected to occur.

5.4.3 Scaling and self-similarity in the presence of inertia

To determine if inertial effects become significant during bubble impact with a solid wall before the bubble attaches to the wall, it is useful to examine the instantaneous value of the pre-factor Re_r in the equations (5.16) and (5.17) that govern flow of the liquid in the film between the bubble and the wall. The variation with time of this pre-factor, denoted by Re_r^i to distinguish it from Re_r^* determined from numerical simulations, is given by

$$\begin{aligned} Re_r^i(\tilde{t}) = Re(\tilde{t})\,\varepsilon(\tilde{t}) &= \frac{\rho_2\,\tilde{u}(\tilde{t})\,\tilde{z}_I(\tilde{t})}{\tilde{\mu}(\tilde{t})}\,\frac{\tilde{z}_I(\tilde{t})}{\tilde{r}'(\tilde{t})} \\ &= \frac{1}{Oh}\frac{h_0^2}{R^2}\tau^{(5n-8)/(n+4)} \end{aligned} \tag{5.21}$$

Since $\tilde{z}_{min}(\tilde{t}) \sim h_0 \tau^{n/(n+4)}$, the ratio of the minimum separation to the molecular lengthscale $\tilde{z}_{min}/d$ at which $Re_r^i \sim O(1)$ can be determined from equation (5.21)

$$\frac{\tilde{z}_{\min}}{d} \sim \frac{h_0}{d}\left(\frac{1}{Oh}\frac{h_0^2}{R^2}\right)^{n/(8-5n)} \tag{5.22}$$

For a Newtonian fluid ($n = 1$), the value of $\tilde{z}_{min}/d$ is given by

$$\frac{\tilde{z}_{\min}}{d} \sim \frac{h_0}{d}\left(\frac{1}{Oh}\frac{h_0^2}{R^2}\right)^{1/3} \tag{5.23}$$

For an air bubble in water with an original size of 1 mm, van der Waals forces were seen to become significant at $h_0 = 2 \times 10^{-7}$m in the previous sub-section, and thus, the value is given by $\tilde{z}_{min}/d = 0.545$, which means that inertia becomes significant only after the separation is below the molecular lengthscale, and thus lubrication theory is valid for the entire duration of bubble impact and subsequent attachment. In contrast, for a hypothetical power-law fluid with $n \to 0$, the ratio is given by

$$\frac{\tilde{z}_{\min}}{d} \sim \frac{h_0}{d} \tag{5.24}$$

which signifies that inertial effects would be significant for the entire duration of bubble impact, and lubrication theory cannot be used to study dynamics in the film. For real power-law fluids, where values of n lie in between 0 and 1, the reduced Reynold's number can become of order one when $\tilde{z}_{min}$ is greater than d, and a transition to an inertial scaling regime should be observed when the value of the minimum separation falls below that given by equation (5.22). Indeed, for an air bubble of radius $R = 0.1$ mm approaching a solid wall in acrylic paint [37], a power-law fluid with $\rho_2 = 1150$ kg m^{-3}, $\eta_2 m^{n-1} = 35.6$ Pa s^n, $\sigma = 0.05$ N m^{-1}, $A = 10^{-19}$ J, and $n = 0.44$, if we assume that van der Waals effects became significant at $h_0 = 10^{-7}$m, inertia becomes significant at $\tilde{z}_{min}/d = 27.47$, or when the minimum separation falls below 15.4 nm. Thus, while inertia could be neglected and lubrication theory be used for studying the impact of bubbles immersed in Newtonian liquids, it becomes significant for power-law fluids before the continuum breaks down.

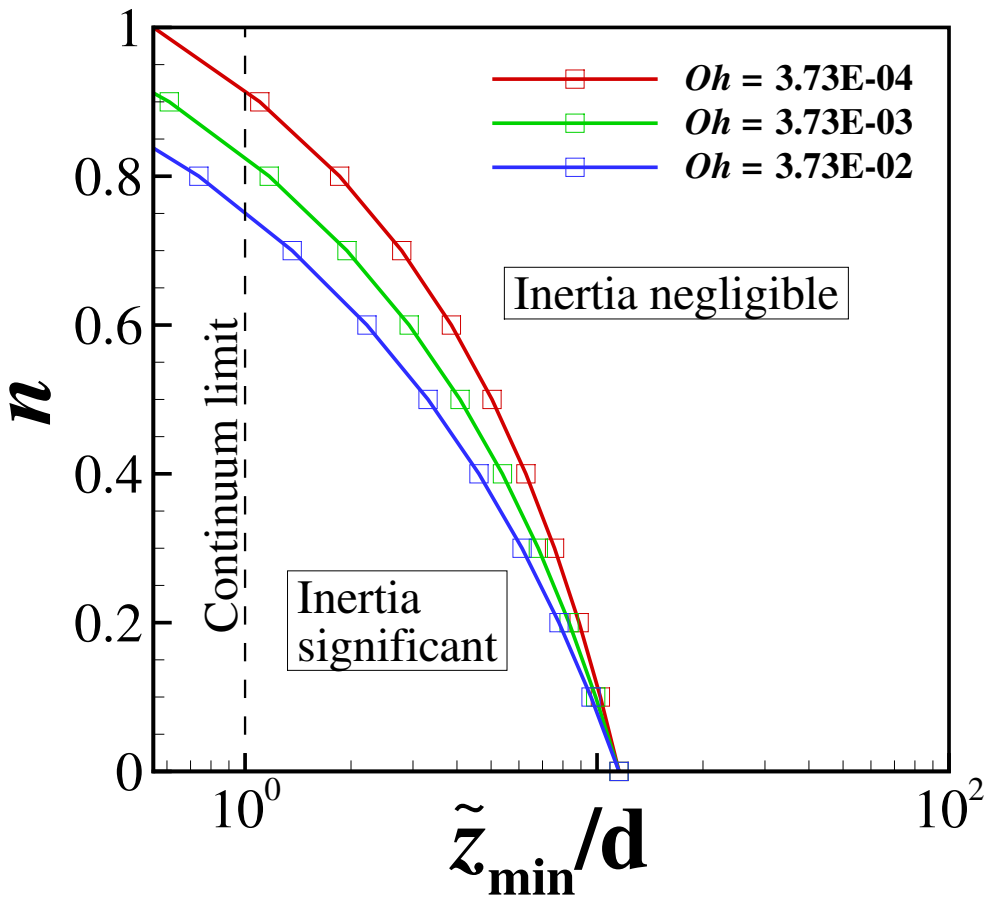

Figure 5.10. Phase diagram which shows when inertia can become important for $R = 1$ mm air bubbles approaching a solid wall in different power-law liquids where each liquid and solid combination is characterized by a given value of Oh, A and n. Here, the value of A is fixed at $A = 10^{-10}$ and the minimum initial separation at which van der Waals forces become important is taken to be $h_0 = 2 \times 10^{-4}R$. Results are shown for three values of Oh, and all the possible values of power-law exponent n. For an air bubble approaching a solid wall in a power-law liquid of fixed n, the normalized minimum axial separation $\tilde{z}_{min}/d$ begins at a high value of 10^5, in the region to the right of the curves shown in this figure, and decreases as the bubble approaches the wall. The curves show the value of $\tilde{z}_{min}/d$ at which the reduced Reynold's number becomes $O(1)$ (computed from equation (5.22)) and the dynamics undergo a transition from the capillary-viscous to the inertial regime.

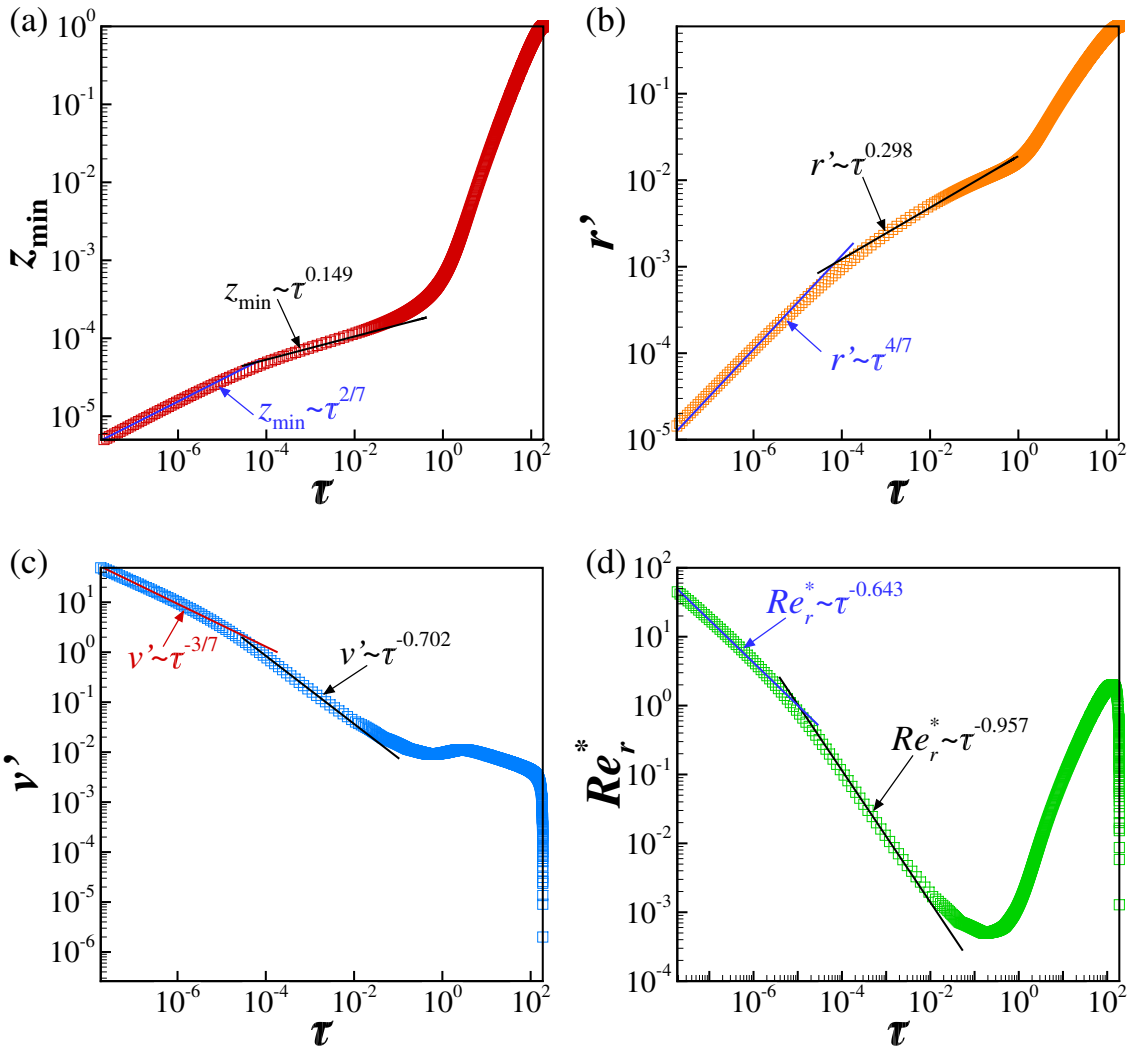

Figure 5.11. Change of scaling for an air bubble immersed in a power-law liquid approaching a solid wall such that $Oh = 3.7628 \times 10^{-3}$, $G = 0.136$, $A = 10^{-10}$, $d_1 = 10^{-3}$, $\beta_1 = 10^{-3}$, $m = Oh\epsilon^5/(A^2)$ and $n = 0.7$. Variation with time remaining to rupture τ of (a) minimum axial separation z_{min} between the bubble-liquid interface and solid wall, (b) radial lengthscale r' (c) radial velocity v' and (d) instantaneous Reynold's number Re_r^* computed at the radial location of the bubble-liquid interface where $z_I = 1.05 z_{min}$. The symbols represent data points obtained from numerical simulations while the solid lines represent best fits to the data.

For a fixed value of A, a phase diagram can be constructed, which shows the critical separation normalized by the molecular lengthscale, $\tilde{z}_{min}/d$ at which inertial effects become significant, as a function of the power-law exponent n. Figure 5.10 shows the phase diagram for $A = 10^{-10}$, and Oh values spanning two orders of magnitude, where the fluid with the least Oh represents bubble impact in water-like liquids while the larger Oh values resemble fluids like acrylic paint [37]. It is clear that inertia becomes important at a larger normalized separation for liquids with lower Oh for fixed n values, and liquids with lower n values for fixed Oh.

As the film drains from between the bubble and the solid wall, the rate at which its viscosity falls increases for power-law liquids with smaller values of n, and we expect inertial forces to grow in importance as compared to viscous forces as the film drains. The dominant force balance in such situations is between inertial (I), capillary (C) and van der Waals forces (vdW), while viscous forces (V) become negligible on account of falling viscosity. The scaling exponents for this inertial regime are then given by equation (5.5) while the variation with τ of the forces themselves is given by

$$I \sim C \sim vdW \ \tau^{-10/7}, \quad V \sim \tau^{-(5n+2)/7} \tag{5.25}$$

It is clear that for $n < 1$, the forces in balance blow up as $\tau \to 0$ much faster than the viscous forces. Thus, we expect to see a transition from the capillary viscous scaling regime given by equations (5.4) and (5.20) to this inertial regime when the instantaneous reduced Reynold's number Re_r^i given by equation (5.21) becomes $O(1)$ or larger.

Figure 5.11 shows the variation with τ of several quantities of interest for an air bubble approaching a solid wall in an outer power-law liquid of power-law exponent $n = 0.7$ where all other conditions are identical to the case of bubble approach discussed in the previous sub-section. Figure 5.11(a) shows that a change of scaling occurs as the bubble approaches the wall as the minimum separation, initially varying as $z_{min} \sim \tau^{0.149} \sim \tau^{n/(n+4)}|_{n=0.7}$, later varies as $z_{min} \sim \tau^{2/7}$, signifying that dynamics transition from the capillary-viscous regime to the inertial regime. This transition is observed at $z_{min} \approx 5 \times 10^{-5}$, which is in good agreement with the theoretical

estimate of $z_{min} = 3.37 \times 10^{-5}$ from equation (5.22), such that the ratio of the normalized minimum separation is $\tilde{z}_{min} \approx 2.89$. Figures 5.11(b) and 5.11(c) make plain that corresponding changes in scaling are observed for the radial lengthscale r' and radial velocity v' respectively, with scaling exponents obtained from the numerical simulations in excellent agreement with both the expected regimes from equations (5.4) and (5.5). It is clear that inertia becomes significant as $\tau \to 0$ from figure 5.11(d), as the Reynold's number Re_r^* becomes $O(1)$, signalling the transition from the capillary-viscous to inertial regime. Re_r^* is seen to initially vary as $Re_r^* \sim \tau^{-0.957} \sim \tau^{(5n-8)/(n+4)}|_{n=0.7}$ which is in excellent agreement with theoretical scaling estimate for the capillary-viscous regime predicted in equation (5.21). However, once Re_r^* becomes $O(1)$, it varies with τ as $Re_r^* \sim \tau^{-0.643} \sim \tau^{(5n-8)/7}|_{n=0.7}$, which is in excellent agreement with the theoretical scaling estimate for Re_r^* for the inertial regime, which can be obtained by using the scaling exponents for axial separation, radial lengthscale and radial velocity from equation (5.5).

In the previous paragraphs we have shown how the dynamics transition from the capillary-viscous to the inertial regime as the power-law exponent of the outer liquid is decreased. However, the occurrence of this transition is also dependent on the Ohnesorge number of the outer liquid, as shown in equation (5.22). Figure 5.12 explores the effect of increasing the zero-deformation-rate viscosity of the outer liquid by a factor of 10, while keeping all other parameters identical to those of the case described in the previous paragraph. Figure 5.12(a) makes plain that the change in scaling occurs closer to the continuum limit for this liquid, which is initially more viscous. Indeed, the transition from $z_{min} \sim \tau^{0.149} \sim \tau^{n/n+4}|_{n=0.7}$ to $z_{min} \sim \tau^{2/7}$ is observed at $z_{min} \approx 3 \times 10^{-5}$ which is in excellent agreement with the theoretical estimate of $z_{min} = 2.35 \times 10^{-5}$ from equation (5.22), but the normalized minimum separation is only $\tilde{z}_{min} \approx 1.36$. Moreover, figure 5.12(d) shows that Re_r^* only becomes $O(1)$ at the incipience of attachment. Thus, for more viscous outer liquids, the breakdown of lubrication theory much before the continuum limit is reached will only occur for power-law liquids with very small values of n.

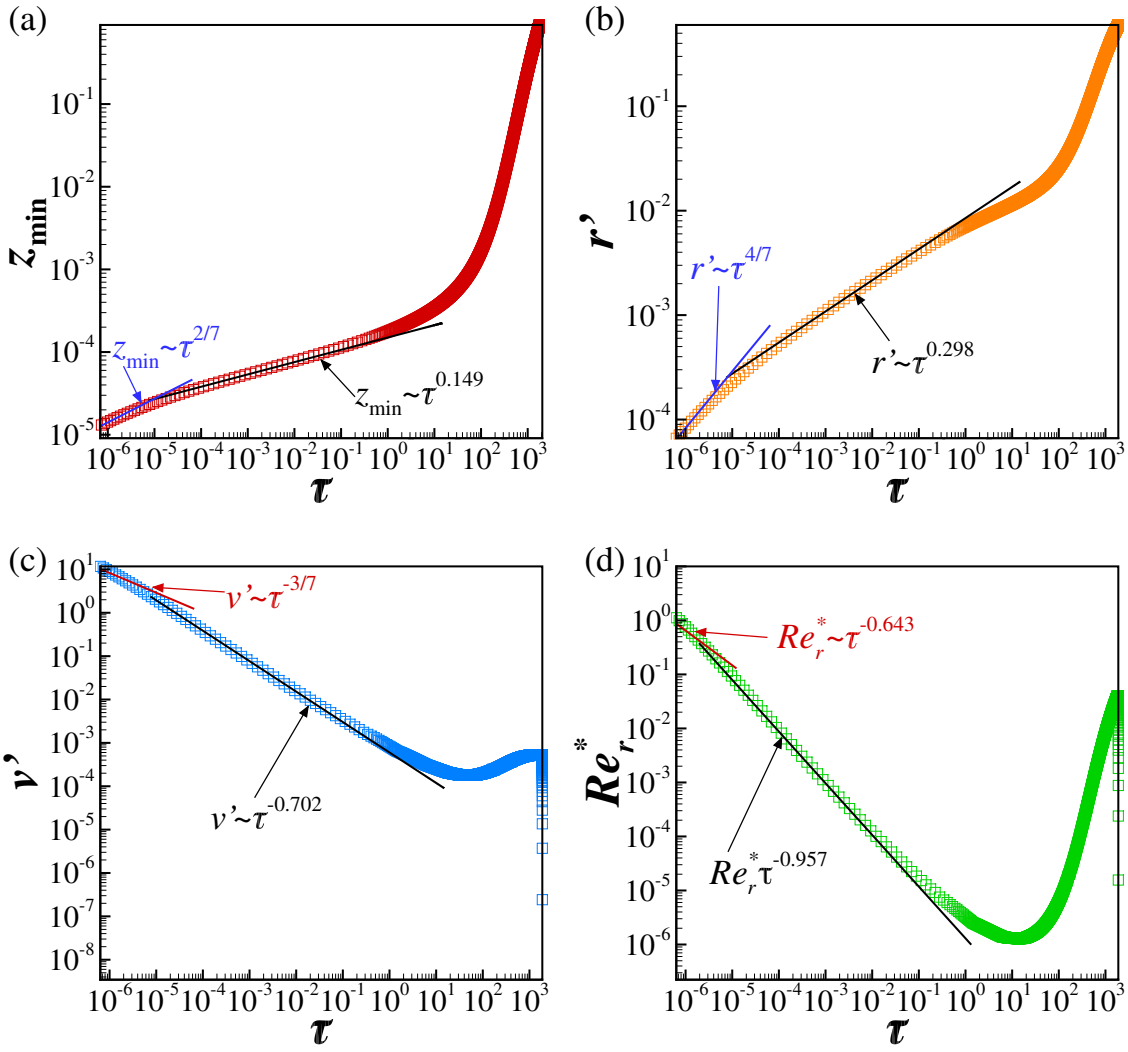

Figure 5.12. Effect of outer liquid viscosity on the scaling behavior of variable in the attachment zone, and change of scaling during approach of an air bubble towards a solid wall immersed in a power-law liquid such that $Oh = 3.7628 \times 10^{-2}$, $G = 0.136$, $A = 10^{-10}$, $d_1 = 10^{-3}$, $\beta_1 = 10^{-4}$, $m = Oh\epsilon^5/(A^2)$ and $n = 0.7$. Variation with time remaining to rupture τ of (a) minimum axial separation z_{min} between the bubble-liquid interface and solid wall, (b) radial length-scale r' (c) radial velocity v' and (d) instantaneous Reynold's number Re_r^* computed at the radial location of the bubble-liquid interface where $z_I = 1.05 z_{min}$. The symbols represent data points obtained from numerical simulations while the solid lines represent best fits to the data.

5.5 Conclusions and outlook

In this chapter, the impact of bubbles immersed in both Newtonian and power-law liquids with a solid wall due to buoyancy was explored. For mm sized bubbles immersed in liquids of water-like viscosity, it was observed that bubbles that are three times its radius or less away from the wall do not rebound from the wall as the Re of approach is very low. However, if the Bond number is increased artificially, the bubbles were observed to undergo multiple rebounds.

For a 1 mm sized bubble approaching a solid wall when the initial separation is one bubble diameter, the final stages of attachment due to van der Waals driven rupture of the film between the bubble and the wall were analyzed theoretically and numerically for bubbles immersed in power-law liquids. The dynamics are self-similar, lying in the viscous regime observed for supported film rupture if the power-law liquid was sufficiently viscous with a large power-law exponent. However, for power-law liquids of sufficiently small n values, inertia can become important as their viscosity falls rapidly. The critical minimum separation below which inertia will be important and the lubrication approximation is no longer valid was determined analytically, and simulation results showed that below this value a transition to an inertial scaling regime occurs, where viscous forces are negligible while inertial, capillary and van der Waals forces are in balance. A phase diagram was constructed to describe when inertia will become important for all possible values of n. Finally, the effect of the outer liquid's zero-deformation-rate viscosity on this transition was examined, and it was established that for liquids more viscous than water, the transition to the inertial regime will be observed for only very small values of power-law exponent n.

Typically, spontaneous thinning and rupture of liquid films has been studied by utilizing the lubrication approximation [47, 48], on account of the large disparity between its lateral extent and thickness. However, in situations where the lubrication approximation breaks down, e.g. power-law liquids, numerical studies have been challenging due to the complexity and cost of the multi-dimensional CFD algorithm

required to resolve these disparate lengthscales accurately. Through this chapter, we have established that the approach of bubbles towards solid walls is an ideal system for studying the dynamics of thinning of liquid films, as the results shown here are in agreement with those of Garg et al. [32] for thin films on solid substrates. The algorithm developed here considers the gas inside the bubble as an incompressible Newtonian fluid, but can be easily used in its current form to study the dynamics of thinning and rupture of two-layer systems supported by a solid substrate [49].

If a bubble approaches a solid wall at terminal velocity, or with a sufficiently large $Re \gg 1$, it will rebound before it finally attaches to the wall. Previous works have used simple force balance models [16] and lubrication theory [21] to determine the shape of the film that forms between the bubble and the solid wall. Studying high Re impact of bubbles with solid walls (as examined in section 5.3) is an area of active interest, as the algorithm described in this chapter can accurately capture film dynamics at the nanoscale as well as the macroscale dynamics of bubble rebound.

Moreover, the presence of surfactants at the bubble-liquid interface is unavoidable in experiments unless extreme care is taken to purge the experimental setup [16]. Previous studies for bubble impact consider the bubble as a deformable sphere, using a no-slip boundary condition at the interface to account for the presence of surfactants. The effect of surfactants at the bubble-liquid interface needs to be investigated in detail, as surfactants will be present in bubble-liquid systems in many daily life situations and industrial applications. Furthermore, the presence of surfactants causes a reduction in the rebound velocity when a bubble impacts a free surface [50]. A thorough computational analysis of the related problem of bubble impact on a free surface will provide a greater understanding of bubble collision dynamics in the presence of surfactants and make clear if current usage of a no-slip boundary condition is valid, and whether the interface is indeed "immobile" as assumed in past literature.

5.6 List of References

[1] Colin D O'Dowd and Gerrit De Leeuw. Marine aerosol production: a review of the current knowledge. *Philosophical Transactions of the Royal Society of London A: Mathematical, Physical and Engineering Sciences*, 365(1856):1753–1774, 2007.

[2] DC Blanchard and AH Woodcock. Bubble formation and modification in the sea and its meteorological significance. *Tellus*, 9(2):145–158, 1957.

[3] Jan Zawala, Marta Krasowska, T Dabros, and K Malysa. Influence of bubble kinetic energy on its bouncing during collisions with various interfaces. *The Canadian Journal of Chemical Engineering*, 85(5):669–678, 2007.

[4] E Canot, Laurent Davoust, M El Hammoumi, and D Lachkar. Numerical simulation of the buoyancy-driven bouncing of a 2-d bubble at a horizontal wall. *Theoretical and computational fluid dynamics*, 17(1):51–72, 2003.

[5] Vince Wallwork, Zhenghe Xu, and Jacob Masliyah. Bitumen recovery with oily air bubbles. *The Canadian journal of chemical engineering*, 81(5):993–997, 2003.

[6] A. Nguyen and H. J. Schulze. *Colloidal Science of Flotation*. CRC Press, Boca Raton, Florida, 2003.

[7] Yue Zhao, Yan-Peng Li, Jia Huang, Jun Liu, and Wen-Ke Wang. Rebound and attachment involving single bubble and particle in the separation of plastics by froth flotation. *Separation and Purification Technology*, 144:123–132, 2015.

[8] DB Donoghue, A Albadawi, YMC Delauré, AJ Robinson, and DB Murray. Bubble impingement and the mechanisms of heat transfer. *International Journal of Heat and Mass Transfer*, 71:439–450, 2014.

[9] Heng-Kwong Tsao and Donald L Koch. Observations of high reynolds number bubbles interacting with a rigid wall. *Phys. Fluids*, 9(1):44–56, 1997.

[10] Luke Parkinson and John Ralston. The interaction between a very small rising bubble and a hydrophilic titania surface. *The Journal of Physical Chemistry C*, 114(5):2273–2281, 2010.

[11] Roberto Zenit and Dominique Legendre. The coefficient of restitution for air bubbles colliding against solid walls in viscous liquids. *Phys. Fluids*, 21(8):083306, 2009.

[12] Dominik Kosior, Jan Zawala, Marta Krasowska, and Kazimierz Malysa. Influence of n-octanol and α-terpineol on thin film stability and bubble attachment to hydrophobic surface. *Physical Chemistry Chemical Physics*, 15(7):2586–2595, 2013.

[13] A Albadawi, DB Donoghue, AJ Robinson, DB Murray, and YMC Delauré. On the assessment of a vof based compressive interface capturing scheme for the analysis of bubble impact on and bounce from a flat horizontal surface. *International Journal of Multiphase Flow*, 65:82–97, 2014.

[14] Evert Klaseboer, Rogerio Manica, Maurice HW Hendrix, Claus-Dieter Ohl, and Derek YC Chan. A force balance model for the motion, impact, and bounce of bubbles. *Phys. Fluids*, 26(9):092101, 2014.

[15] Rogerio Manica, Evert Klaseboer, and Derek YC Chan. Force balance model for bubble rise, impact, and bounce from solid surfaces. *Langmuir*, 31(24):6763–6772, 2015.

[16] Rogerio Manica, Evert Klaseboer, and Derek YC Chan. The hydrodynamics of bubble rise and impact with solid surfaces. *Advances in colloid and interface science*, 235:214–232, 2016.

[17] G. F. Teletzke, H. T. Davis, and L.E. Scriven. How liquids spread on solids. *Chem. Eng. Comm.*, 55(1-6):41–82, 1987.

[18] Cheng-Yuan Lin and JC Slattery. Thinning of a liquid film as a small drop or bubble approaches a fluid–fluid interface. *AIChE Journal*, 28(5):786–792, 1982.

[19] Leonard R Fisher, Emma E Mitchell, David Hewitt, John Ralston, and Joe Wolfe. The drainage of a thin aqueous film between a solid surface and an approaching gas bubble. *Colloids and Surfaces*, 52:163–174, 1991.

[20] Luke Parkinson and John Ralston. Dynamic aspects of small bubble and hydrophilic solid encounters. *Advances in colloid and interface science*, 168(1-2):198–209, 2011.

[21] Maurice HW Hendrix, Rogerio Manica, Evert Klaseboer, Derek YC Chan, and Claus-Dieter Ohl. Spatiotemporal evolution of thin liquid films during impact of water bubbles on glass on a micrometer to nanometer scale. *Phys. Rev. Let.*, 108(24):247803, 2012.

[22] R. Suryo and O. A. Basaran. Local dynamics during pinch-off of liquid threads of power law fluids: Scaling analysis and self-similarity. *J. Non-Newtonian Fluid Mech.*, 138(2):134–160, 2006.

[23] J. R. Castrejón-Pita, A. A. Castrejón-Pita, S. S. Thete, K. Sambath, I. M. Hutchings, J. Hinch, J. R. Lister, and O. A. Basaran. Plethora of transitions during breakup of liquid filaments. *Proc. Natl. Acad. Sci. USA*, 112(15):4582–4587, 2015.

[24] Jens Eggers, John R Lister, and Howard A Stone. Coalescence of liquid drops. *J. Fluid Mech.*, 401:293–310, 1999.

[25] J. D. Paulsen, J.C. Burton, S. R. Nagel, S. Appathuri, M. T. Harris, and O. A. Basaran. The inexorable resistance of inertia determines the initial regime of drop coalescence. *Proc. Nat. Acad. Sci.*, 109(18):6857–6861, 2002.

[26] Christopher R Anthony, Pritish M Kamat, Sumeet S Thete, James P Munro, John R Lister, Michael T Harris, and Osman A Basaran. Scaling laws and dynamics of bubble coalescence. *Phys. Rev. Fluids*, 2(8):083601, 2017.

[27] D. Vaynblat, J. R. Lister, and T. P. Witelski. Rupture of thin viscous films by van der Waals forces: Evolution and self-similarity. *Phys. Fluids*, 13(5):1130–1140, 2001.

[28] S. S. Thete, C. Anthony, O. A. Basaran, and P. Doshi. Self-similar rupture of thin free films of power-law fluids. *Phys. Rev. E*, 92(2):023014, 2015.

[29] S. S. Thete, C. Anthony, P. Doshi, M. T. Harris, and O. A. Basaran. Self-similarity and scaling transitions during rupture of thin free films of Newtonian fluids. *Phys. Fluids*, 28(9):092101, 2016.

[30] Vishrut Garg, Sumeet S Thete, Christopher R Anthony, Brayden W Wagoner, and Osman A Basaran. Self-similarity and scaling transitions in breakup of sheets of power-law fluids. *Unpublished*, 2019.

[31] W. W. Zhang and J. R. Lister. Similarity solutions for van der Waals rupture of a thin film on a solid substrate. *Phys. Fluids*, 11(9):2454–2462, 1999.

[32] Vishrut Garg, Pritish M Kamat, Christopher R Anthony, Sumeet S Thete, and Osman A Basaran. Self-similar rupture of thin films of power-law fluids on a substrate. *J. Fluid Mech.*, 826:455–483, 2017.

[33] W. M. Deen. *Analysis of Transport Phenomena*. Oxford University Press, New York, 1998.

[34] R. B. Bird, R. C. Armstrong, O. Hassager, and C. F. Curtiss. *Dynamics of Polymeric Liquids*. Wiley New York, 1977.

[35] S. W. Hasan, M. T. Ghannam, and N. Esmail. Heavy crude oil viscosity reduction and rheology for pipeline transportation. *Fuel*, 89(5):1095–1100, 2010.

[36] J. R. Savage, M. Caggioni, P. T. Spicer, and I. Cohen. Partial universality: pinch-off dynamics in fluids with smectic liquid crystalline order. *Soft Matter*, 6(5):892–895, 2010.

[37] F. M. Huisman, S. R. Friedman, and P. Taborek. Pinch-off dynamics in foams, emulsions and suspensions. *Soft Matter*, 8(25):6767–6774, 2012.

[38] O. E. Yildirim and O. A. Basaran. Deformation and breakup of stretching bridges of Newtonian and shear-thinning liquids: comparison of one-and two-dimensional models. *Chem. Eng. Sci.*, 56(1):211–233, 2001.

[39] P. Doshi, R. Suryo, O. E. Yildirim, G. H. McKinley, and O. A. Basaran. Scaling in pinch-off of generalized Newtonian fluids. *J. Non-Newtonian Fluid Mech.*, 113(1):1–27, 2003.

[40] P. Doshi and O. A. Basaran. Self-similar pinch-off of power law fluids. *Phys. Fluids*, 16(3):585–593, 2004.

[41] J. Q. Feng and O. A. Basaran. Shear-flow over a translationally symmetrical cylindrical bubble pinned on a slot in a plane wall. *J. Fluid Mech.*, 275:351–378, 1994.

[42] E. D. Wilkes, S. D. Phillips, and O. A. Basaran. Computational and experimental analysis of dynamics of drop formation. *Phys. Fluids*, 11(12):3577–3598, 1999.

[43] K. N. Christodoulou and L. E. Scriven. Discretization of free surface flows and other moving boundary problems. *J. Comput. Phys.*, 99(1):39–55, 1992.

[44] Patrick K. Notz and Osman A. Basaran. Dynamics and breakup of a contracting liquid filament. *J. Fluid Mech.*, 512:223–256, 2004.

[45] JS Hadamard. Mouvement permanent lent d'une sphere liquid et visqueuse dans un liquide visqueux. *CR Hebd. Seances Acad. Sci. Paris*, 152:1735–1738, 1911.

[46] Witold Rybczynski. Uber die fortschreitende bewegung einer flussigen kugel in einem zahen medium. *Bull. Acad. Sci. Cracovie A*, 1:40–46, 1911.

[47] Alexander Oron, Stephen H Davis, and S George Bankoff. Long-scale evolution of thin liquid films. *Reviews of modern physics*, 69(3):931, 1997.

[48] R. V. Craster and O. K. Matar. Dynamics and stability of thin liquid films. *Rev. Mod. Phys.*, 81(3):1131, 2009.

[49] Subhadarshinee Sahoo, Akash Arora, and Pankaj Doshi. Two-layer spin coating flow of newtonian liquids: A computational study. *Computers & Fluids*, 131:180–189, 2016.

[50] Shiyan Wang, Tianqi Guo, Sadegh Dabiri, Pavlos P Vlachos, and Arezoo M Ardekani. Effect of surfactant on bubble collisions on a free surface. *Phys. Rev. Fluids*, 2(4):043601, 2017.

6. FLOW-INDUCED COALESCENCE OF TWO EQUAL-SIZED LIQUID DROPS IMMERSED IN A SECOND LIQUID

6.1 Introduction

Emulsions, which are fine dispersions of drops of one liquid in another immiscible liquid, are commonly encountered in a variety of industries ranging from food [1] to oil and gas [2] to pharmaceuticals [3] to chemicals [4]. The competing mechanisms of coalescence and breakup of the dispersed drops decide the fate, and thus, the final quality and properties of the emulsion. While droplet breakup has been investigated thoroughly both theoretically and experimentally [5], the coalescence of two drops immersed in an immiscible liquid is still poorly understood. The dynamics of the collision and coalescence of two drops are studied separately by usually assuming no influence from other drops and particles present in the emulsion. Such studies on coalescence of two drops can again be sub-categorized into two parts: (a) pre-coalescence dynamics − events leading up to the contact of two drops − and (b) post-coalescence dynamics, or the events following contact as the drops merge into one large drop due to capillary forces [6–8]. These constitute either sides of the hydrodynamic singularity event when the two drops come in contact.

Pre-coalescence dynamics of a drop pair consists of three steps. First, the two drops approach each other due to a driving force, e.g. gravitational, electric, or buoyancy forces, or due to imposed flow of the external liquid. As the drops get closer, a thin film of outer liquid forms between the approaching drops, which then begins to drain as the driving force pushes the drops further towards each other. Finally, once the film thickness is below some critical value, van der Waals forces of attraction destabilize and rupture the film, leading to coalescence of the drops [9]. The param-

eters influencing this process are: (a) fluid properties (for Newtonian liquids, these include the densities of the two liquids ρ_1 and ρ_2, viscosities μ_1 and μ_2, tension of the interface separating the two liquids σ, and the Hamaker constant A_H for the system), (b) flow properties (such as strain rate of imposed flow G, electric fields E, and the offset of approaching drops θ), and (c) interface rheological effects (such as surfactant concentration and charge distribution along the interface). Extensive experimental studies of flow-induced coalescence in the Stokes limit of two equal-sized drops in a four-roll Taylor mill setup [10] were conducted by Leal and coworkers [11–15]. Through these experiments, they observed that the dependence of drainage time t_d − defined as the time elapsed between the instant when the center-to-center distance between the drops is twice their undeformed radius R to when the drops make contact − on the capillary number Ca, in a head-on collision (as seen in figure 6.1) could be described by the scaling relation $t_d G \sim Ca^m$. Here, G is the strain rate of the imposed compressional flow and $Ca \equiv \mu_2 GR/\sigma$, where μ_2 is the viscosity of the outer liquid. For large Ca or equivalently, large drops of $R > 27$ μm, Leal and coworkers showed that $m = 4/3$, which agreed with the theoretically expected prediction for a flat or dimpled film drianage [16]. For lower capillary numbers, the value of the exponent m lies in the range $1 < m < 4/3$, as the drops were observed to be predominantly spherical until coalescence [15].

While experimental techniques provide insight into macroscopic properties of drop coalescence, analytical and numerical methods are essential for understanding drainage of the film between the drops and establishing the mechanisms involved. Davis and coworkers [17, 18] focused on the drainage of the film for gravity driven coalescence of drops, and made use of the lubrication approximation while solving the Navier Stokes equations. Later, three-dimensional boundary integral methods were used by Rother, Zinchenko and Davis [19,20] and Rother and Davis [21] to study the effect of local deformations on two drops colliding in linear flows. Yue et al. [22] used diffused interface methods to study the coalescence dynamics of drops imparted with initial velocities directed at each other. Loewenberg and coworkers [23, 24] showed

that the external flow field affects the flow inside the drops which could arrest film drainage and as a result prevent coalescence, thereby demonstrating the contrast between drops coalescing due to an external flow field and drops pushed together by body forces in a quiscent liquid. Janssen et al. [25] and Yoon et al. [26] derived simple scaling relations for the drainage time t_d with Ca and observed good agreement for scaling behavior of drainage times between their boundary-integral simulations and the experiments conducted by Leal and coworkers for large Ca. Recently, Nemer et al. [27] derived scaling relationships for the film thickness with time when the drops undergo small deformations. More recently, Ramachandran and Leal [28] examined the impact of interfacial slip on scaling exponents for film drainage times, in an effort to resolve the discrepancy in experimentally observed trends and simple scaling theories for smaller Ca.

The works mentioned so far have considered creeping flow conditions for the coalescence of drops, since inertia is not expected to play a role for highly viscous liquids approaching each other at vanishingly small velocities, or for extremely small drops of the size of 10 μm or below. However, coalescers and separators present in industry involve flows where inertia is significant, and the assumptions of Stokes flow do not apply. Controlled experiments of flow-induced collisions of liquid drops are still due. Until recently, previous works that considered inertial effects [29] did not capture the dynamics of the interfacial film and its subsequent drainage well. Sambath [30] used a Galerkin finite element framework (G/FEM) to simulate the flow-induced head-on collision and coalescence of two equal sized drops in a compressional flow like that generated by Taylor's four roll mill [10] for liquids of low viscosity. The author demonstrated that the drops rebound on first approach before coalescing on the second approach, as inertia plays a game-changing role in delaying coalescence. Sambath [30] further showed that drainage times computed for such cases do not conform to the scaling theories developed for creeping flow conditons as reviewed above. Furthermore, drop rebound was seen to occur for intermediate Oh values, with drop separation decreasing monotonically without rebound for low Oh or high Oh values,

where $Oh = \mu_1/\sqrt{\rho_1 \sigma R}$ is the ratio of the viscous force to the square root of the product of the inertial and capillary forces.

The goal of this chapter is to revisit the results of Sambath [30] and provide a better understanding of the dynamics that lead to drop rebound before coalescence on subsequent approach. The role played by each liquid's inertia and viscosity in determining whether rebound occurs or not, and to what extent, is examined by means of numerical simulations. The chapter is organized as follows. Section 6.2 describes in detail the problem under consideration and outlines the equations and boundary conditions governing drop coalescence dynamics. Section 6.3 describes the numerical methods employed to solve computationally the aforementioned equations and presents the results of validation tests conducted to verify the accuracy of these methods. Section 6.4 examines the role that liquid inertia plays in causing observed rebound effects and consequent increase in drainage times, while section 6.5 describes the effect of the viscosity ratio on the extent of drop rebound. Finally, section 6.6 concludes the chapter by summarizing the key results and discussing future avenues that can be explored by extending the current analyses.

6.2 Mathematical Formulation

The system consists of two initially spherical drops of radius R of a Newtonian liquid of constant density ρ_1 and viscosity μ_1, suspended in an immiscible Newtonian liquid of constant density ρ_2 and viscosity μ_2. The interfacial tension of the liquid-liquid interface is spatially uniform and constant in time and is denoted by σ, while the Hamaker constant for the liquid-liquid system A_H is constant and positive, signifying that the force between the drops is attractive. The drops are initially separated by a center-to-center distance of $4R$, and pushed towards each other by a compressional flow with a constant strain rate G, identical to that generated by a four-roll Taylor mill [10]. It proves convenient to adopt a cylindrical coordinate system where the origin is located midway between the two drops along the line connecting the centers of the two drops, $\tilde{r}$ and $\tilde{z}$ represent the radial and axial distance from the origin, and

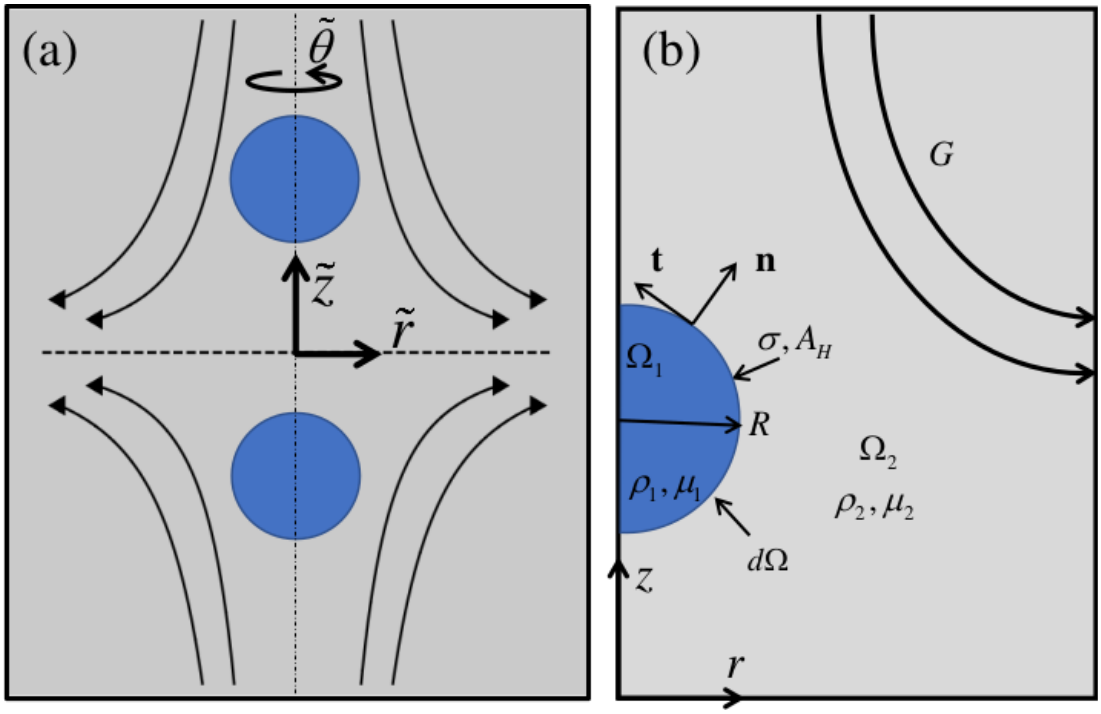

Figure 6.1. In this chapter, we examine the (a) head on collision of two equal-sized drops of a Newtonian liquid immersed in a second Newtonian liquid which are pushed towards each other by a compressional flow similar to Taylor's four roll mill [10]. (b) Domain used for numerical simulations on account of symmetry.

$\mathbf{e}_r$ and $\mathbf{e}_z$ represent orthogonal unit vectors in the radial and axial direction in this cylindrical coordinate system. The computational domain is reduced to one quadrant owing to axisymmetry about the axis $\tilde{r} = 0$ and symmetry about $\tilde{z} = 0$. A detailed schematic is shown in figure 6.1. In what follows, the subscript $()_i$ denotes variables in the drop liquid as $i = 1$ and variables in the outer liquid as $i = 2$.

In this chapter, problem variables are non-dimensionalized using the undeformed drop radius R as the characteristic length $l_c \equiv R$, the inertio-capillary time-scale as the characteristic time $t_c \equiv \sqrt{\rho_1 R^3/\sigma}$, the ratio of the two as the characteristic velocity scale $v_c \equiv l_c/t_c$, and the capillary pressure as the characteristic stress $p_c \equiv \sigma/R$. The flow is then governed by the following dimensionless groups: the Ohnesorge number $Oh = \mu_1/\sqrt{\rho_1 \sigma R}$, which is the ratio of the viscous force to square root of

the product of the inertial and capillary forces, viscosity ratio $m_2 = \mu_2/\mu_1$, density ratio $d_2 = \rho_2/\rho_1$, dimensionless strain rate $U_\infty = G\sqrt{\rho_1 R^3/\sigma}$, and the van der Waals number $A = A_H/(6\pi\sigma R^2)$ which is the ratio of the force due to van der Waals attraction to capillary force. In what follows, variables without tilde ($\sim$) over them denote the dimensionless counterparts of the variables with tilde over them.

The dynamics in the regions $\Omega_1(t)$ and $\Omega_2(t)$ are governed by the continuity and Navier-Stokes equations which are given in dimensionless form by

$$\nabla \cdot \mathbf{v}_i = 0 \tag{6.1a}$$

$$d_i \left(\frac{\partial \mathbf{v}_i}{\partial t} + \mathbf{v}_i \cdot \nabla \mathbf{v}_i \right) = \nabla \cdot \mathbf{T}_i \tag{6.1b}$$

where $\mathbf{T}_i \equiv -p_i \mathbf{I} + m_i Oh \left((\nabla \mathbf{v}_i) + (\nabla \mathbf{v}_i)^T \right)$, and p_i and $\mathbf{v}_i = u_i \mathbf{e}_r + w_i \mathbf{e}_z$ denote the pressure and velocity in liquid i respectively, and $d_1 = m_1 = 1$, while d_2 and m_2 have already been specified. The kinematic and traction boundary conditions are applied at the liquid-liquid interface $d\Omega(t)$, which is unknown a priori, to enforce mass conservation and account for the discountinuity in stress due to interfacial tension and van der Waals forces

$$\mathbf{n} \cdot (\mathbf{v}_i - \mathbf{v}_s) = 0 \tag{6.2a}$$

$$\mathbf{n} \cdot (\mathbf{T}_2 - \mathbf{T}_1) = 2H\mathbf{n} - \frac{A}{h^3}\mathbf{n} \tag{6.2b}$$

where $\mathbf{n}$ represents the unit normal to the interface as shown in figure 6.1, $\mathbf{v}_s$ represents the velocity of the interface, $2H$ represents twice the mean curvature, equal to the surface divergence of the unit normal ($-\nabla_s \cdot \mathbf{n}$). The second term in equation (6.2b) represents van der Waals attraction between the two drops which becomes significant when the axial distance between the interfaces, denoted by $2h$, becomes of the order of a few hundred nanometers, and thus the value of A is typically small [9,31,32]. In the current formulation, h is taken to be equal to the axial coordinate of the in-

terface $d\Omega(t)$, and curvature effects are neglected. Symmetry boundary conditions are applied at the axis of axisymmetry $r = 0$ and plane of symmetry $z = 0$. At the outer boundaries located at $z = k$ and $r = k$, where k is some positive constant, the velocity field in the outer liquid $\mathbf{v}_2$ is given by

$$\mathbf{v}_2(|\mathbf{x}| \to \infty) = U_\infty \left(\frac{r}{2}\mathbf{e}_r - z\mathbf{e}_z\right) \tag{6.3}$$

On account of different characteristic scales used in this chapter and those used by previous researchers to simulate drop coalescence under creeping flow conditions [25–27], it is useful to relate the aforementioned dimensionless groups to the Capillary number Ca and Reynold's number Re

$$Ca = \frac{\mu_2 GR}{\sigma} = m_2 Oh U_\infty \tag{6.4}$$

$$Re = \frac{\rho_2 (GR) R}{\mu_2} = \frac{U_\infty d_2}{m_2 Oh} \tag{6.5}$$

Both these dimensionless groups are defined using the paramters of the outside liquid, as opposed to our scheme, where we use the inside liquid for characteristic values. It is clear that in the creeping flow limit, $Re \to 0$ when $Oh \to \infty$ and $U_\infty \to 0$, but Ca is finite.

The system is initially quiescent and the drops are separated by a center to center distance of 4. At time $t = 0$, the velocity profile of equation (6.3) is imposed along the outer boundaries at $r = k$ and $z = k$.

6.3 Numerical methods and code validation

The governing equations (6.1) subject to the boundary conditions (6.2) for simulating the collision and coalescence of two drops suspended in a second liquid constitute a set of coupled non-linear second-order partial differential equations in space and time. These equations are solved by a fully implicit method of lines algorithm which utilizes an arbitrary Lagrangian-Eulerian scheme, the Galerkin finite element

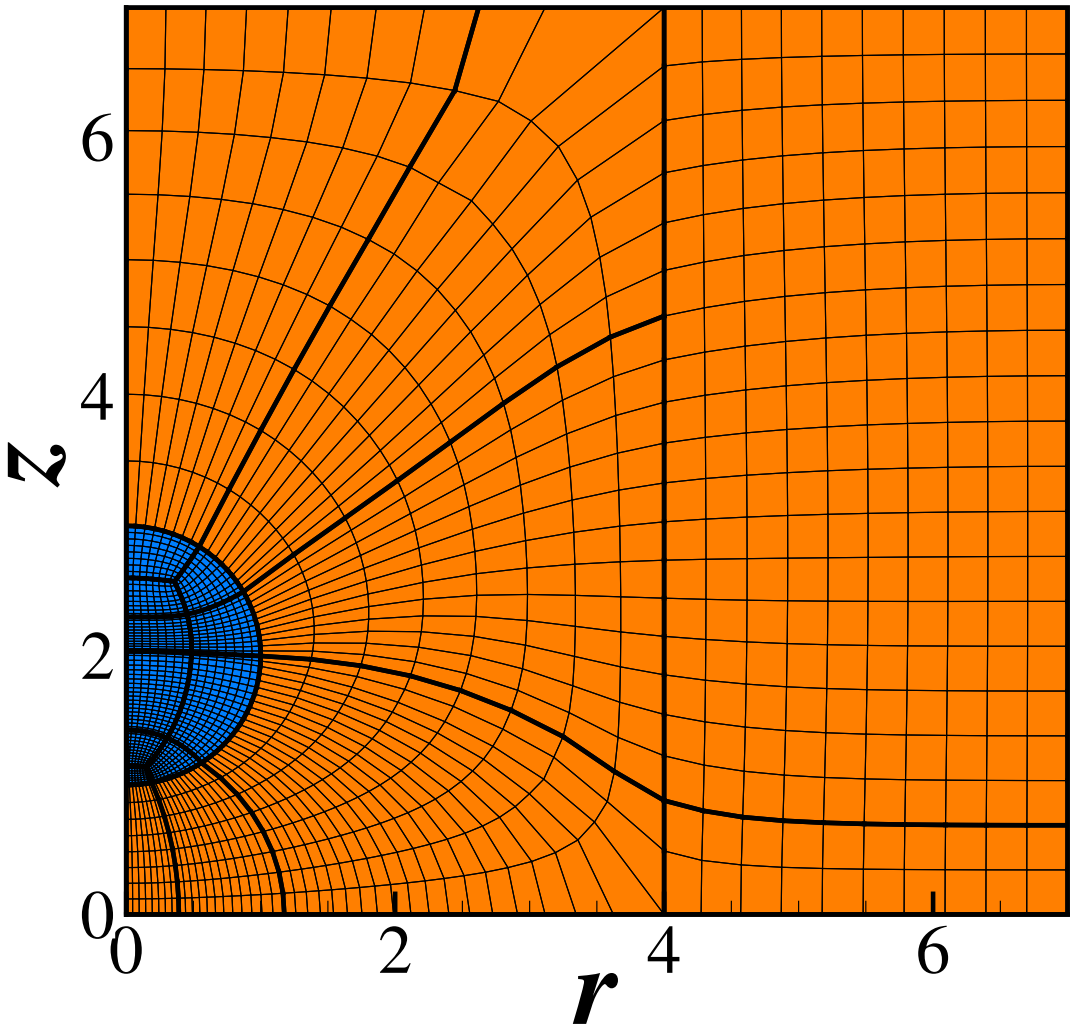

Figure 6.2. Sample mesh generated using the elliptic mesh equations [33] for the computational domain specified in section 6.2. The mesh is weighted towards the region between the drop interface and symmetry plane at $z = 0$ to accuarately capture the thin film dynamics during the mid to latter stages of coalescence. The mesh shown here is very coarse and for illustrative purposes only, as typical meshes used are $10 - 15$ times denser.

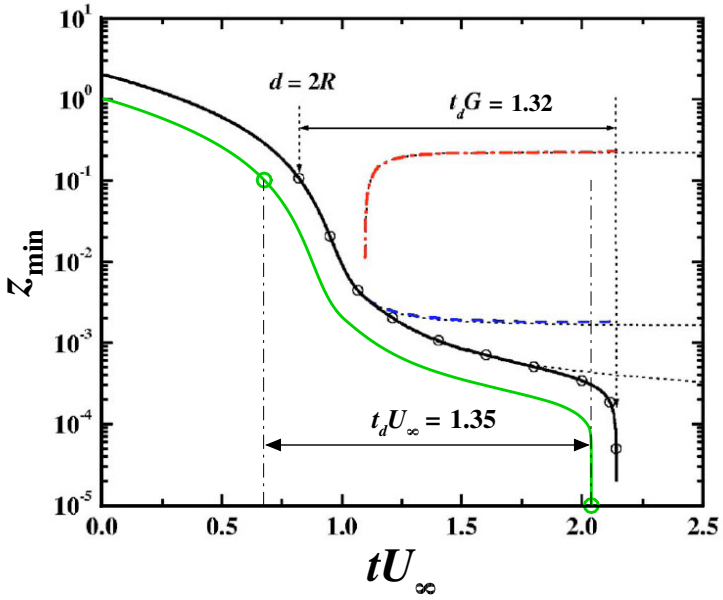

Figure 6.3. Evolution of half the minimum separation between two drops coalescing for parameter values of $Oh = 1.55 \times 10^4$, $m_2 = 5.3$, $d_2 = 1.1$, $U_\infty = 1.81 \times 10^{-7}$, and $A^* = 4.99 \times 10^{-11}$. The green curve shows our simulations while the solid black curve represents boundary element simulations of Yoon et al [26]. The dashed blue and red lines show the position of the centre of mass and radius of the dimple that forms once the drops deform respectively from the simulations of Yoon et al [26]. The dotted lines represent these quantities for when van der Waals forces are artificially turned off, by setting $A^* = 0$.

method for spatial discretization [34, 35] and the adaptive Adams-Bashforth method for time integration [36, 37]. The resulting non-linear algebraic equations are solved iteratively using Newton-Raphson's method where the Jacobian is computed analytically. Complete formulation of residuals and corresponding Jacobians are given in Sambath [30]. As this problem involves deformable liquid-liquid interfaces, special elliptic meshing techniques, originally developed by Christodoulou and Scriven [33], along with algebraic meshing techniques are employed to track the moving boundaries and tessellate the moving domains $(\Omega_1(t) \cup \Omega_2(t))$ into quadrilateral sub-domains at

every point in time when the solution is computed [38]. For all results presented in this chapter, the domain size in radial and axial direction was set such that $k = 7$, as any further increase led in negligible change in the results. Newton-Raphson iterations, which were continued until residual norms fell below 10^{-6}, were found to converge quadratically confirming the correctness of analytically computed Jacobian. Typically, $3 - 4$ iterations were required for solution convergence at each time step. Variants of this algorithm have been used by our group in the past to analyze hydrodynamic singularities that arise during the breakup of filaments [39], rupture of thin films [40], breakup and coalescence of bubbles [41] and drops [42]. A sample coarse mesh is shown in figure 6.2.

To validate our code, we considered the drop coalescence experiments of Yoon et al. [14] conducted in a four-roll Taylor mill apparatus. Yoon et al. [14] studied the coalescence of two polybutadiene (PBD) drops ($\rho_1 = 890$ kg/m^3, $\mu_1 = 5.5$ Pa.s) of size 27.2 μm when immersed in PDMS ($\rho_2 = 965$ kg/m^3, $\mu_2 = 29.3$ Pa.s) with an imposed strain rate which never exceeds $G = 0.08$ s^{-1}. The interfacial tension for this system was measured and its value was $\sigma = 4.6$ mN/m. Yoon et al. [26] performed boundary integral method simulations for this system for simulation parameter values $Ca = 0.015$, $A^* = 4.99 \times 10^{-11}$ and $m_2 = 5.3$. Their results agreed well with Yoon et al. [14] and they reported a drainage time value of $t_d G = 1.32$. Figure 6.3 shows the evolution of half the minimum axial separation between the drops z_{min} as a function of tU_∞ (Yoon et al. [14, 26] use tG, which is identical to tU_∞ since they use the visco-capillary time scale) for head-on collision of two drops such that parameter values are $Oh = 1.55 \times 10^4$, $m_2 = 5.3$, $d_2 = 1.1$, $U_\infty = 1.81 \times 10^{-7}$, and $A^* = 4.99 \times 10^{-11}$. It is clear that our simulations closely follow those of Yoon et al [26] and predict a drainage time of $t_d U_\infty = 1.35$, which is in good agreement with the experimental value of $t_d G = 1.32$ observed by Yoon et al. [14] and later corroborated by Yoon et al. [26]. Having validated the solution algorithm and code, we use it to study the physics involved in the rebound of two liquid drops approaching each other when immersed in a second liquid.

6.4 Role of inertia in drop rebound dynamics

6.4.1 The significance of normal force in causing rebound

Figure 6.4 shows several quantities of interest for two drops brought together in a head-on collision by compressional flow described by equation 6.3 such that parameter values are $Oh = 0.02$, $m_2 = 5.26$, $d_2 = 1.1$, $U_\infty = 0.095$, and $A^* = 4.99 \times 10^{-11}$. The Reynolds number for this case is $Re = 0.99$. Sambath [30] studied this case and observed that the drops rebound upon first approach before coalescing on second approach. The author showed that the inclusion of inertia is essential for drop rebound, as artificially "turning off" the inertial terms results in a monotonic decrease in half the minimum axial separation between the drops z_{min}. Sambath [30] further showed that if inertia were "turned off", the radial velocity in the region of the film in between the drops is always positive, i.e., liquid is always being expelled from the film region such that the drops coalesce without rebounding. The two cases − drop coalescence with inertia considered, referred hereafter to as case 1, and drop coalescence with inertia "turned off" by setting $d_i = 0$ in equation (6.1b), hereafter referred to as case 2 − are shown in figure 6.4. Figure 6.4(b) compares the net force F_z and its components − force due to pressure $F_z{}^p$ (referred to as the normal force) and force due to viscous drag $F_z{}^v$ − in the positive z direction on the drop for both cases, which can be computed by

$$F_z = \int_S \mathbf{n} \cdot \mathbf{T}_2 \cdot \mathbf{e}_z dS \tag{6.6}$$

$$F_z{}^p = \int_S \mathbf{n} \cdot (-p_2 \mathbf{I}) \cdot \mathbf{e}_z dS \tag{6.7}$$

$$F_z{}^v = \int_S \mathbf{n} \cdot m_2 Oh \left(\nabla \mathbf{v}_2 + (\nabla \mathbf{v}_2)^T \right) \cdot \mathbf{e}_z dS \tag{6.8}$$

At time instant t_1, the drops are separated by $z_{min} = 10^{-1}$ for case 1, and the pressure in the film region between the drops is rising. This is evident from the increase in F_z^p in the moments following t_1, and the corresponding increase in CSA. The net

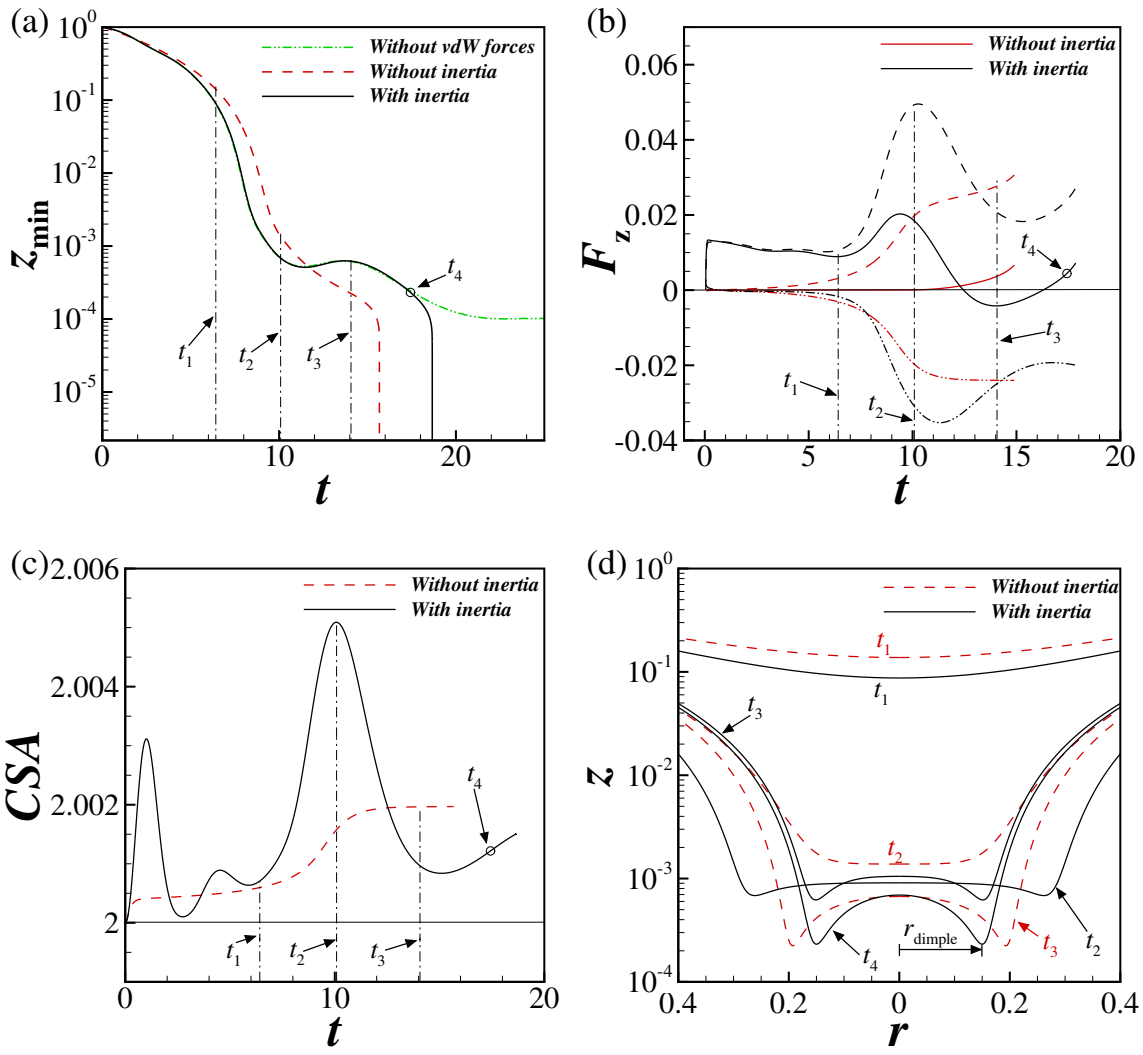

Figure 6.4. Time evolution of (a) half the minimum axial separation between the drops' interfaces z_{min} for three cases: (1) When inertia is considered but van der Waals forces are neglected by setting $A^* = 0$, (2) When inertia is artifically neglected, and (3) when inertia is considered, (b) net force F_z (shown by solid lines), and its components − net force due to pressure F_z^p (shown by the dashed lines) and net force due to viscous drag F_z^v (shown by the dashed-dotted lines) − in the positive z direction determined from equations (6.6 − 6.8) being exterted by the outer liquid on the drop when inertia is considered and when inertia is absent, (c) surface area CSA of the drop when inertia is considered and when inertia is absent for two equal-sized drops immersed in an outer liquid being driven towards each other such that $Oh = 0.02$, $m_2 = 5.26$, $d_2 = 1.1$, $U_\infty = 0.095$, and $A^* = 4.99 \times 10^{-11}$. (d) Drop interface shapes at time instants t_1, t_2, and t_3 represented by the dashed vertical lines in (a),(b), and (c).

force F_z on the drop is positive and increases, thus opposing its motion towards the symmetry plane. In contrast, for case 2, while pressure buildup and flattening of the interface also occurs in the moments following t_1, the increase in both F_z^p and CSA is much smaller, and balanced by a corresponding decrease in F_z^v, so that the net force F_z on the drop for case 2 is zero, and the drop does not experience any deceleration as observed for case 1. At time instant t_2, F_z^p and CSA for case 1 is at a maximum, as a large normal force acts on the flattened drop. The large extent of deformation or large r_{dimple} can be seen in figure 6.4(d). As the interfaces are separated by $z_{min} \sim 10^{-3}$ at this instant, van der Waals forces are unable to cause rupture of the film, and the large positive F_z pushes the drops away from each other, causing outer liquid to flow back into the film region. In the moments following t_2, the drop regains its spherical shape as the normal force decreases. In contrast, the situation is remarkably different for case 2, as the magnitude of F_z^p acting on the drop is much smaller, and consequently the extent of deformation of the interface is much smaller. As the net force F_z is still zero for case 2, the drops continue to approach each other. At time instant t_3, the drops for case 1 have moved apart and the value of r_{dimple} is small. Viscous drag F_z^v, which has so far been sub-dominant, now dominates and results in a net negative F_z, pushing the drops towards each other. This causes the interfaces to deform and CSA to increase for a second time. For case 2, pressure in the film is large enough to dominate over viscous drag, and a net positive F_z begins to cause deceleration of the drop. However, as the separation falls to $z_{min} \sim 2 \times 10^{-4}$, van der Waals forces of attraction become significant. Thus, in the moments following t_3, rapid local rupture of the film separating the drops occurs at the radial location of r_{dimple} for case 2 and the separation reaches molecular lengthscales, or in other words, the drops coalesce. For case 1, interface deformation and increase in CSA occurs for a second time as the drops approach each other again at time instant t_4. However, the deformation of the drop is much smaller during this second approach, as the normal force opposing approach is much lower. The drops are able to get close and $z_{min} \sim 2 \times 10^{-4}$, causing van der Waals driven rupture of the film separating the drops. Thus, for coalescence

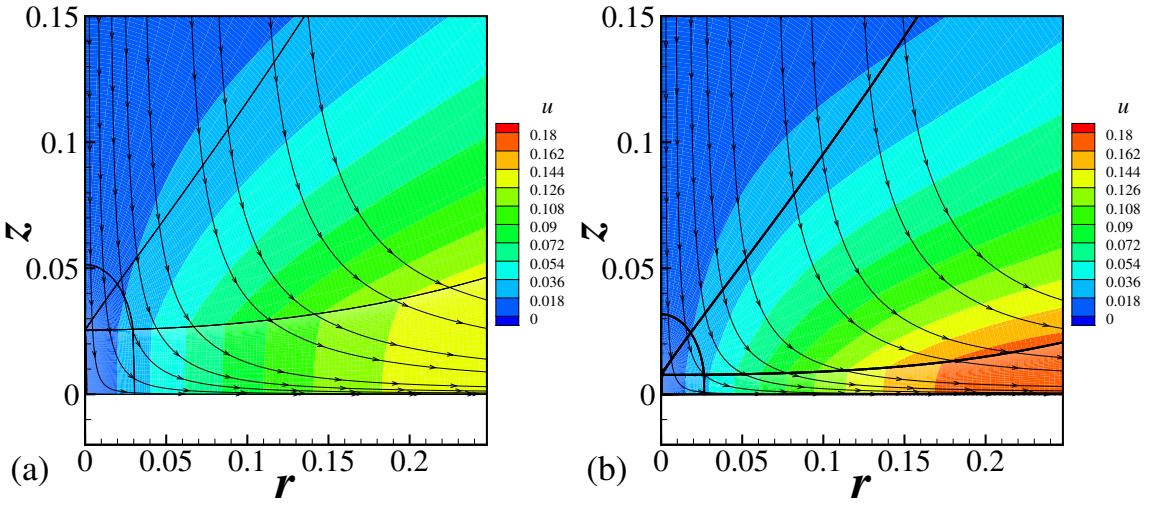

Figure 6.5. Contours of the radial velocity u for two time instants (a) $t = 7.41$ and (b) $t = 7.95$ in the film that forms between the drops. The parameters are identical to those for figure 6.4. The velocity increases in time and r.

at $Re = 1$, inertial effects lead to a net positive F_z acting on the drop through the mid to late stages of coalescence, resulting in a much larger deformation or r_{dimple} in comparison to the "Stokes" case, causing deceleration of the drops and eventual rebound.

6.4.2 Pressure buildup in the film due to inertia

A natural question that arises from the analysis presented in the previous paragraph is why the normal force F_z^p was much larger when the liquids have inertia, in comparison to when inertia is neglected, during the initial approach of the two drops (starting at $t \sim 8$ in figure 6.4). Analyzing the governing equations for the liquid velocities and pressure in the film at $z = 0$ can provide an explanation. The continuity equation in the film of outer liquid can be written as

$$\frac{1}{r}\frac{\partial}{\partial r}(ru_2) = -\frac{\partial w_2}{\partial z} \tag{6.9}$$

Furthermore, assuming that gradients in the axial direction of u_2 are small compared to gradients in the radial direction, or $\partial u_2/\partial z \ll \partial u_2/\partial r$ (which is true for coalescence and similarly, free film dynamics), the r-component of the Navier Stokes equation (6.1b) in the film of outer liquid at the interface is given by

$$d_2\left(\frac{\partial u_2}{\partial t}+u_2\frac{\partial u_2}{\partial r}\right)=-\frac{\partial p_2}{\partial r}+m_2Oh\frac{\partial}{\partial r}\left(\frac{1}{r}\frac{\partial}{\partial r}(ru_2)\right) \tag{6.10}$$

Substituting the result from equation (6.9) into (6.10)

$$d_2\left(\frac{\partial u_2}{\partial t}+u_2\frac{\partial u_2}{\partial r}\right)=-\frac{\partial p_2}{\partial r}-m_2Oh\frac{\partial}{\partial r}\left(\frac{\partial w_2}{\partial z}\right) \tag{6.11}$$

At the symmetry plane $z=0$, $w_2=0$ and thus the z-component of the momentum balance is given by

$$0=-\frac{\partial p_2}{\partial z}+m_2Oh\frac{\partial^2 w_2}{\partial z^2} \tag{6.12}$$

This reduces to $\partial p_2/\partial z=0$ from the continuity equation and our earlier assumption of axial gradients of u_2 being small. Thus, equation (6.11) can be integrated in r from $r=0$ to $r=r_e$ to give

$$\int_0^{r_e} d_2\left(\frac{\partial u_2}{\partial t}+u_2\frac{\partial u_2}{\partial r}\right)\partial r=-p_2|_{r_e}+p_2|_{r=0}-m_2Oh\left[\left(\frac{\partial w_2}{\partial z}\right)_{r_e}-\left(\frac{\partial w_2}{\partial z}\right)_0\right] \tag{6.13}$$

The expression for pressure in the film at the axis $r=0$, denoted by p_0 is then given by

$$p_0=p_2|_{r_e}+\underbrace{m_2Oh\left[\left(\frac{\partial w_2}{\partial z}\right)_{r_e}-\left(\frac{\partial w_2}{\partial z}\right)_0\right]}_{\text{V}}+\underbrace{\int_0^{r_e} d_2\left(\frac{\partial u_2}{\partial t}+u_2\frac{\partial u_2}{\partial r}\right)\partial r}_{\text{I}} \tag{6.14}$$

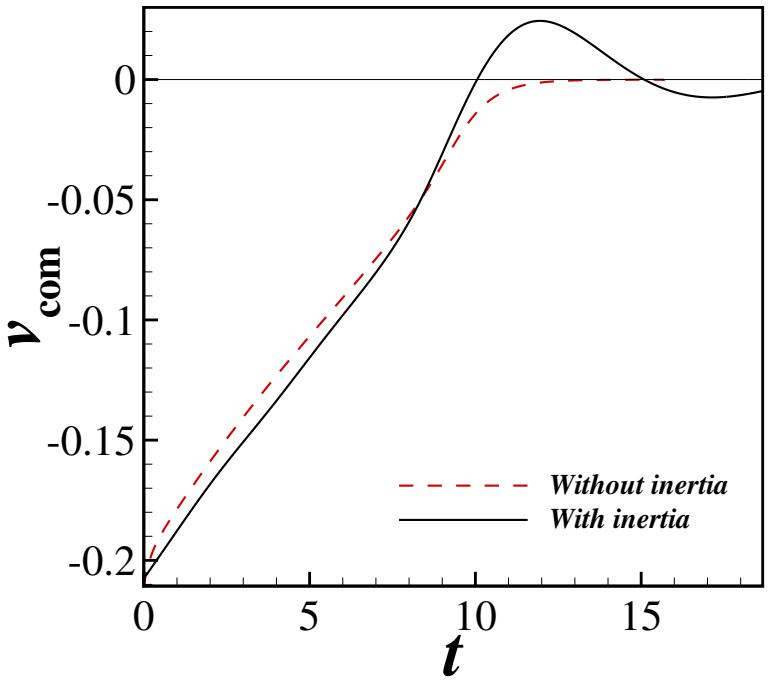

Figure 6.6. Variation of the velocity of the center of mass v_{com} of the drop for two cases: (1) when inertia is considered and (2) when inertia is neglected from the governing equations. The horizontal line represents $v_{com} = 0$.

If one makes a simplyifying assumption to estimate $\partial w_2/\partial z = v_{com}/h$, where h is the local film thickness, then the pressure at the centre of the film is given by

$$p_0 = p_2|_{r_e} + \underbrace{m_2 Oh v_{com}\left[\left(\frac{1}{h}\right)_{r_e} - \left(\frac{1}{h}\right)_{r=0}\right]}_{\text{V}} + \underbrace{\int_0^{r_e} d_2\left(\frac{\partial u_2}{\partial t} + u_2\frac{\partial u_2}{\partial r}\right)\partial r}_{\text{I}} \quad (6.15)$$

The viscous term (V) is positive as the film thickness $h_{r_e} > h_{r=0}$, while v_{com} is negative. Moreover, the inertial term (I) is positive as the drop approaches the symmetry plane, as radial velocity increases both in time and in the radial direction, and is always positive. This is shown in figure 6.5. In contrast, if inertia is excluded

from the governing equations (case 2), the pressure in the film at the axis p_O^{stokes} is now given by

$$p_0^{stokes} = p_2|_{r_e} + \underbrace{m_2 Oh v_{com} \left[\left(\frac{1}{h} \right)_{r_e} - \left(\frac{1}{h} \right)_{r=0} \right]}_{\text{V}} \tag{6.16}$$

In other words, the positive inertial term (I) is added to p_0 for case 1, and thus, the pressure in the film is larger when inertia is included during the initial stages of approach of the drop. Additionally, figure 6.6 shows the variation of velocities of center of mass v_{com} with time for the two cases, and it is clear that the magnitude of the velocity of approach is greater for case 1, until $t = 8$, when the net positive F_z begins to cause drop deceleration for case 1. Thus, the viscous term (V) is also larger when inertia is considered. In conclusion, $p_0 > p_0^{stokes}$. Thus, when inertia is considered, the larger pressure in the film causes the larger normal force on the drop, which in turn leads to the rebound dynamics as explained in the previous paragraph.

6.4.3 The significance of inertia of the drop liquid

We next examine the role each liquid's inertia plays in drop rebound. Figure 6.7(a) shows the variation with time of z_{min} for two liquid drops suspended in a second liquid ($Oh = 0.023$, $m_2 = 1.00$, $d_2 = 1.00$, $U_\infty = 0.05$, and $A^* = 1.00 \times 10^{-10}$) for four cases: (1) inertial effects are considered for both liquids, (2) inertial effects are excluded for the drop liquid, (3) inertial effects are excluded for the outer liquid, and (4) inertial effects are excluded for both liquids (Stokes flow). For case 1, the drops approach each other until $z_{min} \sim 3.5 \times 10^{-3}$, following which the drop rebounds. During rebound, the local interfaces approach each other again, before separating by a much larger distance. The drops finally coalesce when the interfaces approach each other for the third time. On the other end of the spectrum, for case 4, z_{min} decreases monotonically with time for Stokes flow without any rebound, similar to the results for Stokes flow in the previous paragraph. As a result, the drainage time for case

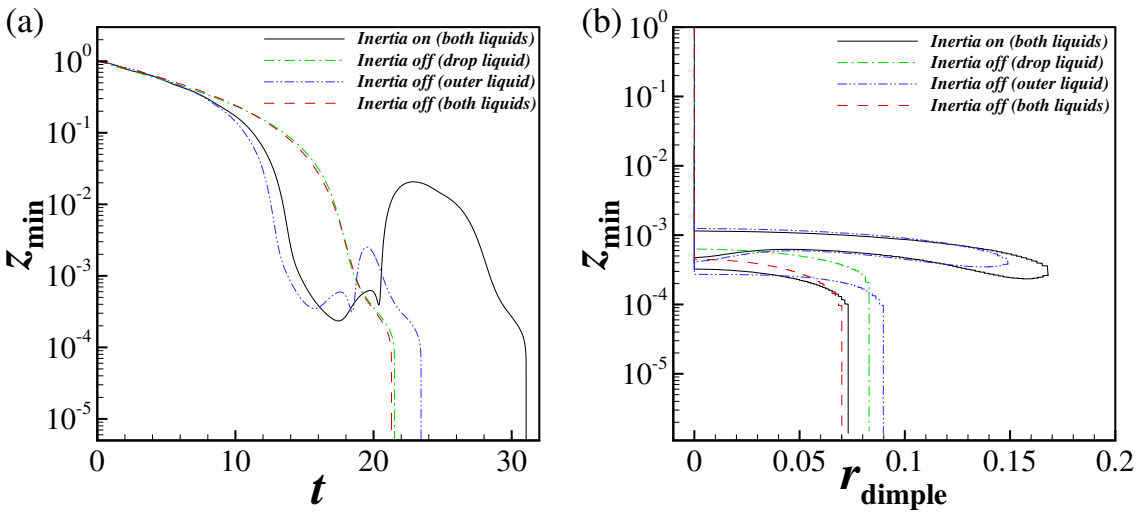

Figure 6.7. (a) Transients of half the minimum separation z_{min} between the two drops for four cases: (1) inertial effects are considered for both liquids, (2) inertial effects are turned off for the drop liquid, (3) inertial effects are turned off for the outer liquid, and (4) inertial effects are neglected for both liquids (Stokes flow). (b) z_{min} vs radius of the dimple r_{dimple} that forms during mid to late stage coalescence, signifying the extent of drop deformation. Here, $Oh = 0.023$, $m_2 = 1.00$, $d_2 = 1.00$, $U_\infty = 0.05$, and $A^* = 1.00 \times 10^{-10}$.

4 is much smaller than drainage time observed for case 1. When inertial effects are only turned off for the drop liquid, the variation of z_{min} with time is identical to that observed for Stokes flow. In other words, excluding inertia of the drop liquid is almost identical to excluding inertia for the entire system, as the coalescence dynamics remain unchanged from those observed for Stokes flow. In contrast, excluding inertial effects for the outer liquid does not lead to such a dramatic impact on the dynamics. Similar to case 1, the drops are observed to rebound upon first approach, and coalesce on the third approach of the interfaces towards each other. The magnitude of rebound is suppressed in this case, with the drainage time smaller than case 1. The absence of inertia in the outer liquid ensures that the viscous drag (F_z^v from equation 6.8) dominates and pushes the drops back together more rapidly, as compared to case 1. Figure 6.7(b) shows the variation of z_{min} with the extent of drop deformation

r_{dimple} for the aforementioned cases. It is evident that both, the z_{min} at which dimple formation begins, and its extent, is much larger for cases 1 and 3. This signifies that the opposing normal force in both cases is large, resulting in the observed rebound. In contrast, for cases 2 and 4 where no rebound was observed, the extent of dimple formation is small, and it begins at a much lower separation of $z_{min} \sim 5 \times 10^{-4}$, where $A^*/h^{-3} \sim O(1)$. Thus, attractive van der Waals forces are large enough to drive the drops to coalesce on first approach. It is clear from the results of figure 6.7 that inertia of the drop liquid is primarily responsible for rebound, as opposed to inertia of the outer liquid. The inclusion of inertia of the drop liquid results in large drop deformation at large separations, causing subsequent slowdown of film drainage, much before van der Waals forces are significant enough to cause local film rupture.

6.5 Role of viscosity in drop rebound dynamics

In this section we examine the role played by liquid viscosity in drop rebound dynamics. Figure 6.8 shows the variation with time t of several quantities of interest for the collision and coalescence of two drops in an outer liquid such that parameter values are $Oh = 0.023$, $d_2 = 1.00$, $U_\infty = 0.05$, and $A^* = 1.00 \times 10^{-10}$, while the viscosity ratio is varied from $m_2 = 0.1-10$. Figure 6.8(a) makes plain that coalescence dynamics are similar for $m_2 = 0.1 - 2.0$ until the minimum separation between the interfaces falls to $z_{min} \sim 3 \times 10^{-3}$, but subseqeuntly, the extent to which the drop rebounds before the drops come together again, and the film between the interfaces ruptures, decreases as m_2 increases. Infact, for $m_2 = 0.1$, or when the outer liquid is 10 times less viscous than the liquid of the drop, the drops approach each other, rebound and then return to their initial state, without coalescence occuring. For $m_2 = 0.5 - 1.0$, the drops coalesce on subsequent approach after rebounding, as the interfaces make contact on their third approach towards each other, while for $m_2 = 2.0$, the interfaces make contact on their second approach towards each other (or in other words, only one rebound is observed). For the largest value of $m_2 = 10.0$, the dynamics of coalescence differ significantly from the aforementioned cases from the

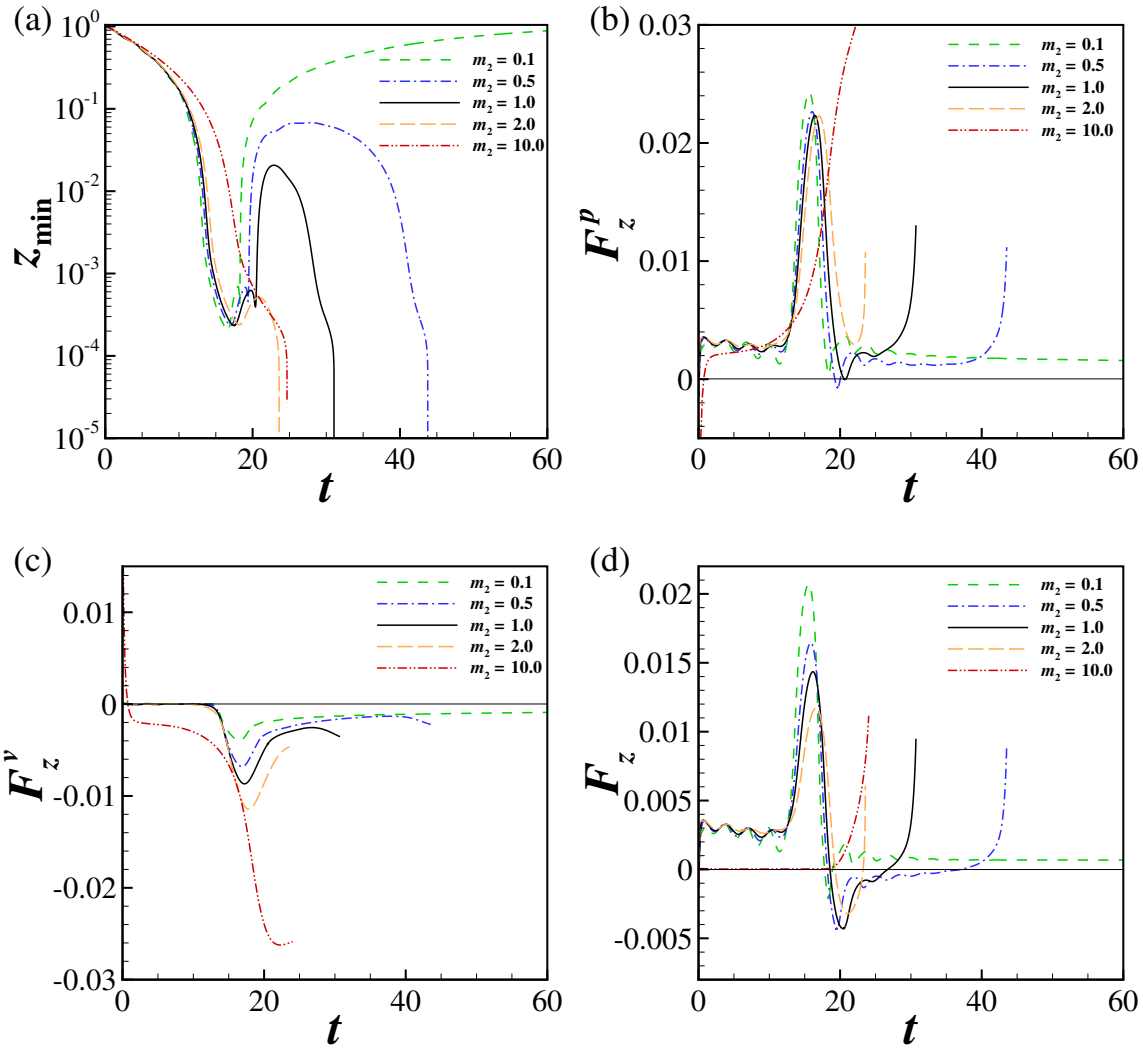

Figure 6.8. Time evolution of (a) half the minimum axial separation between the drops' interfaces z_{min}, (b) net normal force applied by the outer liquid on the drop F_z^p, (c) net viscous drag applied by the outer liquid on the drop F_z^v, and (d) net force applied by the outer liquid on the drop F_z in the positive z direction for the collision and coalescence of two equal-sized drops in an outer liquid such that parameter values are $Oh = 0.023$, $d_2 = 1.00$, $U_\infty = 0.05$, and $A^* = 1.00 \times 10^{-10}$, while the viscosity ratio is varied from $m_2 = 0.1 - 10$.

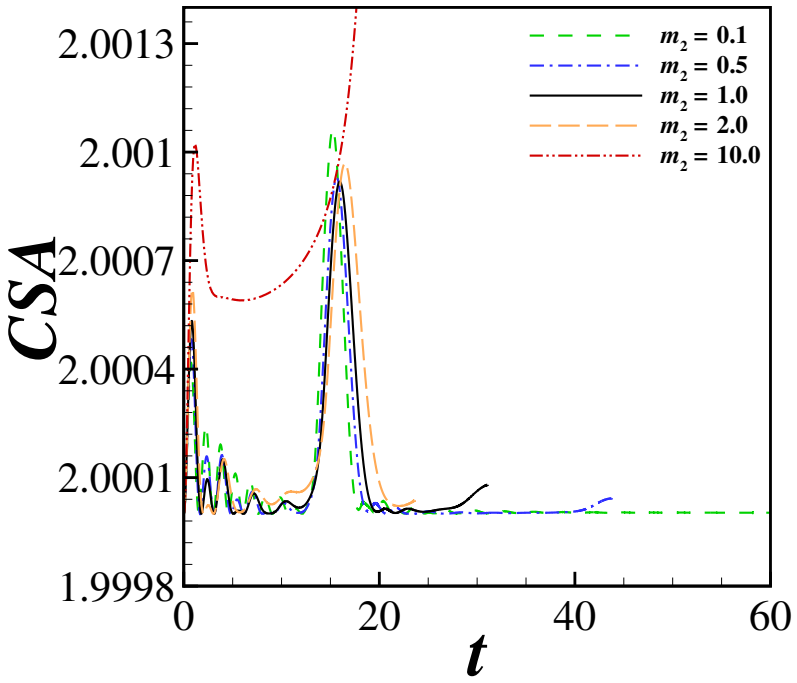

Figure 6.9. Time evolution of the total surface area CSA of the drop for different values of m_2. Fluid parameters are identical to the ones specified in the previous figure. The extent of drop deformation is nearly identical for $m_2 = 0.1 - 2.0$. Thus, normal forces opposing drop motion towards the symmetry plane will be nearly identical for these cases, as seen in the previous figure.

initial stages of approach. The drops are observed to approach each other at a slower rate and coalesce on first approach, without any rebound. It is evident from figure 6.8(b) that the normal force opposing drop motion towards the symmetry plane, F_z^p, attains nearly identical values as the drop deforms upon approach to the symmetry plane, for all values of $m_2 = 0.1 - 2.0$. This is also evident from the extent of drop deformation, which is nearly identical for these cases as seen in figure 6.9. This is expected since liquid parameter values are identical apart from the viscosity of the outer liquid. However, the viscous drag F_z^v in the negative z direction, applied by the outer liquid on the drop, increases as m_2 increases (figure 6.8(c)), and thus the net force opposing drop motion towards each other, F_z, decreases as m_2 increases (figure

6.8(d)). This leads to a smaller rebound, and subsequently, the viscous drag applied by the outer liquid is more effective in bringing the drops together. This result gives further credence to the role played by liquid inertia in enhacing drop deformation; if the liquid inertia is unchanged, the extent of deformation is unchanged. However, it is clear that drop rebound dynamics are also a function of the viscosity ratio of the liquids involved. For cases where drop rebound occurs, the extent of rebound is amplified if the outer liquid is less viscous than the liquid of the drop, on account of lesser viscous drag pushing the two drops together. In contrast, if the outer liquid is more viscous than the drop liquid, rebound is suppressed and the interfaces make contact soon after initial rebound. For even higher values of m_2, coalescence dynamics are significantly different, as seen for $m_2 = 10.0$. At such values, drop coalescence dynamics resemble Stokes flow (as seen in the previous sub-section when inertia is "turned off") as the viscous drag applied by the outer liquid is equal and opposite to the normal force, and results in a net zero force on the drop until van der Waals forces cause film rupture.

6.6 Conclusions and outlook

In this chapter, flow-induced coalescence of two equal-sized drops of a Newtonian liquid immersed in another immiscible Newtonian liquid was studied for low Oh flows. The normal force opposing the motion of the drop towards the symmetry plane was observed to be considerably larger when inertia was included in the governing equations, as opposed to when it was excluded. This caused the drops to deform to a greater extent, much before van der Waals forces become significant, resulting in drop rebound. It was further observed that the inertia of the drop liquid is key for drop rebound to occur, as neglecting it was similar to considering coalescence in Stokes flow conditions. Finally, the effect of the viscosity ratio m_2 on drop rebound dynamics was examined. It was shown that while the viscosity ratio has no impact on the normal force or drop deformation for $m_2 = 0.1 - 2.0$, the change in viscous drag pushing the two drops together causes rebound to be amplified for $m_2 < 1$, to the

extent where the drops may not coalesce at all for very low values of m_2. In contrast, for large values of m_2, rebound is suppressed and coalescence dynamics resemble those observed for Stokes flow.

While the results of Sambath [30] and this chapter establish the crucial role played by drop inertia in causing rebound, further analysis of its role in causing larger deformation of the drops is required. Inertial migration of the neck region in pinchoff of threads of low Oh fluids is a well-known phenomena [43], and is responsible for satellite drop formation in Newtonian threads [44] and beads on a string structures in viscoselastic threads [45]. Moreover, the effect of strain rate G − especially if it is non-constant − on drop rebound dynamics requires further exploration, as local flow patterns in coalescers, separators etc. are non-homogenous.

In many industrial applications where emulsions exist, surface active agents are present at the liquid-liquid interface of the drop and outer liquid [2]. A dramatic increase in drainage times for flow-induced coalescence of drops in the presence of surfactants has been observed experimentally by Yoon et al. [46] and computationally by Dai and Leal [47] for Stokes flow conditions. It is unknown if inertia plays a role during drop coalescence of surfactant-laden low Oh liquids. This is explored in chapter 7. The rate coalescence of drops in emulsions can be enhanced by electric fields [48], provided the field strength is below some critical value [49]. Understanding the dynamics of drop coalescence in the presence of electric fields is crucial for designing electrically enhanced coalescer units [50, 51]. The numerical methods utilized by Collins et al. [52] and Collins et al. [42] for studying electrohydrodynamic tip streaming of charged drops can be combined with the algorithm described in this chapter to study rigorously the head-on collision of two drops in an electric field.

6.7 List of References

[1] Stig Friberg, Kare Larsson, and Johan Sjöblom. *Food emulsions*, volume 132. CRC Press, 2003.

[2] Peter K Kilpatrick. Water-in-crude oil emulsion stabilization: Review and unanswered questions. *Energy & Fuels*, 26(7):4017–4026, 2012.

[3] Rudolf Heusch. Emulsions. *Ullmann's Encyclopedia of Industrial Chemistry*, 1987.

[4] D Moinard-Checot, Y Chevalier, S Briançon, H Fessi, and S Guinebretière. Nanoparticles for drug delivery: Review of the formulation and process difficulties illustrated by the emulsion-diffusion process. *Journal of nanoscience and nanotechnology*, 6(9-10):9–10, 2006.

[5] Howard A Stone. Dynamics of drop deformation and breakup in viscous fluids. *Annu. Rev. Fluid Mech.*, 26(1):65–102, 1994.

[6] Jens Eggers, John R Lister, and Howard A Stone. Coalescence of liquid drops. *J. Fluid Mech.*, 401:293–310, 1999.

[7] J. D. Paulsen, J.C. Burton, S. R. Nagel, S. Appathuri, M. T. Harris, and O. A. Basaran. The inexorable resistance of inertia determines the initial regime of drop coalescence. *Proc. Nat. Acad. Sci.*, 109(18):6857–6861, 2002.

[8] Christopher R. Anthony. *Dynamics of retracting films and filaments near singularities*. PhD thesis, Purdue University, August 2017.

[9] AK Chesters. The modelling of coalescence processes in fluid-liquid dispersions: a review of current understanding. *Chemical engineering research & design*, 69(A4):259–270, 1991.

[10] GI Taylor. The formation of emulsions in definable fields of flow. *Proceedings of the Royal Society of London. Series A*, 146(858):501–523, 1934.

[11] Hong Yang, C Charles Park, Y Thomas Hu, and L Gary Leal. The coalescence of two equal-sized drops in a two-dimensional linear flow. *Phys. Fluids*, 13(5):1087–1106, 2001.

[12] Marcos Borrell, Y Yoon, and L Gary Leal. Experimental analysis of the coalescence process via head-on collisions in a time-dependent flow. *Phys. Fluids*, 16(11):3945–3954, 2004.

[13] L Gary Leal. Flow induced coalescence of drops in a viscous fluid. *Phys. Fluids*, 16(6):1833–1851, 2004.

[14] Y. Yoon, M. Borrell, C. C. Park, and L. G. Leal. Viscosity ratio effects on the coalescence of two equal-sized drops in a two-dimensional linear flow. *J. Fluid Mech.*, 525:355–379, 2005.

[15] Adam S Hsu, Anshuman Roy, and L Gary Leal. Drop-size effects on coalescence of two equal-sized drops in a head-on collision. *J. Rheol.*, 52(6):1291–1310, 2008.

[16] JM Frostad, J Walter, and LG Leal. A scaling relation for the capillary-pressure driven drainage of thin films. *Phys. Fluids*, 25(5):052108, 2013.

[17] S. G. Yiantsios and R. H. Davis. Close approach and deformation of two viscous drops due to gravity and van der Waals forces. *J. Colloid Interf. Sci.*, 144:412–433, 1991.

[18] R. H. Davis. Buoyancy-driven viscous interaction of a rising drop with a smaller trailing drop. *Phys. Fluids*, 11:1016–1028, 1999.

[19] Michael A Rother, Alexander Z Zinchenko, and Robert H Davis. Buoyancy-driven coalescence of slightly deformable drops. *J. Fluid Mech.*, 346:117–148, 1997.

[20] Alexander Z Zinchenko, Michael A Rother, and Robert H Davis. A novel boundary-integral algorithm for viscous interaction of deformable drops. *Phys. Fluids*, 9(6):1493–1511, 1997.

[21] Michael A Rother and Robert H Davis. The effect of slight deformation on droplet coalescence in linear flows. *Phys. Fluids*, 13(5):1178–1190, 2001.

[22] P. Yue, J. F. Feng, C. Liu, and J. Shen. Diffuse-interface simulations of drop coalescence and retraction in viscoelastic fluids. *J. Non-Newtonian Fluid Mech.*, 129:163–176, 2005.

[23] MB Nemer, X Chen, DH Papadopoulos, J Bławzdziewicz, and M Loewenberg. Hindered and enhanced coalescence of drops in stokes flows. *Phys. Rev. Let.*, 92(11):114501, 2004.

[24] MB Nemer, X Chen, DH Papadopoulos, J Bławzdziewicz, and M Loewenberg. Comment on two touching spherical drops in uniaxial extensional flow: Analytic solution to the creeping flow problem. *J. Col. Int. Sci.*, 308(1):1–3, 2007.

[25] P. J. A. Janssen, P. D. Anderson, G. W. M. Peters, and H. E. H. Meijer. Axisymmetric boundary integral simulations of film drainage between two viscous drops. *J. Fluid Mech.*, 567:65–90, 2006.

[26] Y. Yoon, F. Baldessari, H. D. Ceniceros, and L. G. Leal. Coalescence of two equal-sized deformable drops in an axisymmetric flow. *Phys. Fluids*, 19(10):102102, 2007.

[27] MB Nemer, P Santoro, X Chen, J Bławzdziewicz, and M Loewenberg. Coalescence of drops with mobile interfaces in a quiescent fluid. *J. Fluid. Mech.*, 728:471–500, 2013.

[28] A Ramachandran and LG Leal. Effect of interfacial slip on the thin film drainage time for two equal-sized, surfactant-free drops undergoing a head-on collision: A scaling analysis. *Phys. Rev. Fluids*, 1(6):064204, 2016.

[29] M. R. Nobari, Y. J. Jan, and G. Tryggvason. Head-on collision of drops - a numerical investigation. *Phys. Fluids*, 8:29–42, 1996.

[30] Krishnaraj Sambath. *Dynamics of Drop Disintegration and Coalescence with and without Electric Fields*. PhD thesis, Purdue University, August 2013.

[31] P. G. De Gennes. Wetting: statics and dynamics. *Rev. Mod. Phys.*, 57(3):827, 1985.

[32] G. F. Teletzke, H. T. Davis, and L.E. Scriven. How liquids spread on solids. *Chem. Eng. Comm.*, 55(1-6):41–82, 1987.

[33] K. N. Christodoulou and L. E. Scriven. Discretization of free surface flows and other moving boundary problems. *J. Comput. Phys.*, 99(1):39–55, 1992.

[34] Osman A Basaran and Fred K Wohlhuter. Effect of nonlinear polarization on shapes and stability of pendant and sessile drops in an electric (magnetic) field. *J. Fluid. Mech.*, 244:1–16, 1992.

[35] J. Q. Feng and O. A. Basaran. Shear-flow over a translationally symmetrical cylindrical bubble pinned on a slot in a plane wall. *J. Fluid Mech.*, 275:351–378, 1994.

[36] TW Patzek, RE Benner Jr, OA Basaran, and LE Scriven. Nonlinear oscillations of inviscid free drops. *Journal of Computational Physics*, 97(2):489–515, 1991.

[37] Edward D Wilkes and Osman A Basaran. Drop ejection from an oscillating rod. *J. Col. Int. Sci.*, 242(1):180–201, 2001.

[38] Patrick K. Notz and Osman A. Basaran. Dynamics and breakup of a contracting liquid filament. *J. Fluid Mech.*, 512:223–256, 2004.

[39] S. S. Thete, C. Anthony, O. A. Basaran, and P. Doshi. Self-similar rupture of thin free films of power-law fluids. *Phys. Rev. E*, 92(2):023014, 2015.

[40] Vishrut Garg, Pritish M Kamat, Christopher R Anthony, Sumeet S Thete, and Osman A Basaran. Self-similar rupture of thin films of power-law fluids on a substrate. *J. Fluid Mech.*, 826:455–483, 2017.

[41] Christopher R Anthony, Pritish M Kamat, Sumeet S Thete, James P Munro, John R Lister, Michael T Harris, and Osman A Basaran. Scaling laws and dynamics of bubble coalescence. *Phys. Rev. Fluids*, 2(8):083601, 2017.

[42] R. T. Collins, K. Sambath, M. T. Harris, and O. A. Basaran. Universal scaling laws for the disintegration of electrified drops. *Proc. Nat. Acad. Sci. USA*, 110(13):4905–4910, 2013.

[43] Y-J Chen and PH Steen. Dynamics of inviscid capillary breakup: collapse and pinchoff of a film bridge. *J. Fluid. Mech.*, 341:245–267, 1997.

[44] Patrick K. Notz, Alvin U. Chen, and Osman A. Basaran. Satellite drops: Unexpected dynamics and change of scaling during pinch-off. *Phys. Fluids*, 13(3):549, 2001.

[45] P. P. Bhat, S. Appathurai, M. T. Harris, M. Pasquali, G. H. McKinley, and O. A. Basaran. Formation of beads-on-a-string structures during break-up of viscoelastic filaments. *Nat. Phys.*, 6(8):625–631, 2010.

[46] Yosang Yoon, Adam Hsu, and L Gary Leal. Experimental investigation of the effects of copolymer surfactants on flow-induced coalescence of drops. *Phys. Fluids*, 19(2):023102, 2007.

[47] Bing Dai and L Gary Leal. The mechanism of surfactant effects on drop coalescence. *Phys. Fluids*, 20(4):040802, 2008.

[48] Xiaoguang Zhang, Osman A Basaran, and Robart M Wham. Theoretical prediction of electric field-enhanced coalescence of spherical drops. *AIChE Journal*, 41(7):1629–1639, 1995.

[49] WD Ristenpart, JC Bird, A Belmonte, F Dollar, and HA Stone. Non-coalescence of oppositely charged drops. *Nature*, 461(7262):377, 2009.

[50] KJ Ptasinski and PJAM Kerkhof. Electric field driven separations: phenomena and applications. *Separation science and technology*, 27(8-9):995–1021, 1992.

[51] John S Eow and Mojtaba Ghadiri. Electrostatic enhancement of coalescence of water droplets in oil: a review of the technology. *Chemical Engineering Journal*, 85(2-3):357–368, 2002.

[52] Robert T Collins, Jeremy J Jones, Michael T Harris, and Osman A Basaran. Electrohydrodynamic tip streaming and emission of charged drops from liquid cones. *Nature Physics*, 4(2):149–154, 2008.

7. FLOW-INDUCED COALESCENCE OF TWO EQUAL-SIZED LIQUID DROPS IMMERSED IN A SECOND LIQUID IN THE PRESENCE OF INSOLUBLE SURFACTANTS

7.1 Introduction

The fate of liquid-liquid emulsions, which are fine dispersions of drops of one liquid, known as the dispersed phase, in another immiscible liquid is crucial in many industrial applications. The separation of water from water-oil emulsions formed during crude oil extraction is essential to prevent corrosion due to brine accumulation [1, 2]. The timeframe over which the constituent emulsion of many food products is kinetically stable determines their shelf lives [3]. More recently, emulsions of aqueous drops in oil have been utilized to carry out independent reactions e.g., to generate nanoparticles [4]. The interplay of coalescence and breakup of the dispersed drops determines if the emulsion separates into two distinct, immiscible phases, or is kinetically stable over the observed timeframe. While droplet breakup has been investigated thoroughly both theoretically and experimentally [5–7], the coalescence of two drops immersed in a second, immiscible fluid is still poorly understood. The dynamics of two drops coming together and coalescing are studied separately by usually assuming no influence from other drops and particles present in the emulsion. Such studies on coalescence of two drops can again be sub-categorized into two parts: (a) pre-coalescence dynamics − events leading up to the contact of two drops − and (b) post-coalescence dynamics, or the events following contact as the drops merge into one large drop due to capillary forces [8–10]. These constitute either sides of the hydrodynamic singularity event when the two drops come in contact. During pre-coalescence, the two drops approach each other due to a driving force, e.g. gravitational, electric, or buoyancy

forces, or due to imposed flow of the external fluid. As the drops get closer, a thin film of outer liquid forms between the approaching drops, as the drops deform due to the high pressure in this film. The drainage of this film is the rate-limiting step during pre-coalescence, but once the film thickness falls below some critical value, van der Waals forces of attraction destabilize and rupture the film, leading to rapid coalescence of the drops [11].

The presence of surface-active agents in emulsions due to naturally occurring impurities [2], or by design [12], strongly affects coalescence dynamics and the overall properties of the emulsion [13]. Surfactant molecules lower the surface tension where they adsorb onto the liquid-liquid interface [14], leading to gradients in interfacial tension when subject to flow. Surface-tension gradients cause additional tangential stresses along the interface, known as Marangoni stresses [15], that are responsible for well-known phenomena such as tears of wine, Benard cells in films [15], and microthread cascades in pinchoff of surfactant laden threads [16]. In a series of experiments for flow-induced coalescence of two small drops of radius R in a four-roll Taylor mill [17], Leal and coworkers [18–20] observed that the presence of copolymers at the interface, which act as insoluble surfactants, led to an order of magnitude increase in drainage time t_d − defined as the time elapsed between the instant when the center-to-center distance between the drops is twice their undeformed radius R to when the drops make contact − when compared to the surfactant free case. Similarly, the presence of surfactants during drop coalescence with its bulk phase at a flat liquid/liquid interface was observed to cause longer rest times for the drop at the interface in comparison to the clean interface case [21, 22].

Early theoretical and numerical studies of drop coalescence in the presence of surfactants focused on drainage of the film that forms between the drops during the mid to late stages of coalescence. Cristini et al. [23] considered the coalescence of non-deformable spherical drops in the limit of no surface diffusion of surfactant, and showed that as the drops approach each other, surfactant is convected out of the film causing interfacial tension gradients to develop, which led to Marangoni stress

acting in the opposite direction of flow. Thus, coalescence initially evolved at a fast "clean interface" timescale before switching to a slow "rigid interface" timescale as Marangoni stresses became significant, leading to the slow drainage times observed in experiments. Chesters and Bazhlekov [24] considered the coalescence of deformable drops with surface diffusion interacting under a constant force, and observed a similar transition from fast "partially mobile" to slow "immobile" drainage for small surfactant concentrations, as Marangoni stress caused interfacial velocity to become negative and briefly reverse film drainage. Yeo et al. [25] studied film drainage for surfactant laden drops approaching each other at a constant velocity. More recently, two studies examined the role of surfactants in flow-induced coalescence of two equal-sized drops using the boundary integral method, rather than focusing on the drainage of the film alone. Dai and Leal [26] stated that the primary Marangoni effect acted outside the film as the surface gradient of surfactant concentration was larger outside the film, resulting in increase of drainage times for surfactant-laden drops. Vannozzi [27] studied the effect of surface diffusivity and concentration of the surfactant on drainage times, and reported an increase in drainage times for large values of the capillary number $Ca \equiv \mu_2 GR/\sigma_0$, where μ_2 is the viscosity of the outer liquid, G is the strain rate of the imposed compressional flow, and σ_0 is the interfacial tension of the clean interface, due to "oscillating" behavior of the minimum film thickness, similar to that seen by Chesters and Bazhlekov [24].

The aforementioned theoretical and numerical studies considered the interaction [28] and coalescence of two drops immersed in a second liquid in the Stokes limit and the inertia of the system was always neglected. Recently, Sambath [29] showed that inertia plays a significant role in flow-induced coalescence of surfactant-free drops when the inertia and viscosity of the system was comparable, or $Re \sim O(1)$, where $Re \equiv \rho_2 GR^2/\mu_2$ is the Reynold's number, and ρ_2 is the density of the outer liquid. The drops were observed to rebound on first approach before coalescing on subsequent approach due to inertia of the drop liquid, resulting in a significant departure from the observed scaling law for drainage time t_d with Ca, where $t_d \sim Ca^{4/3}$

for drops coalescing in the Stokes limit [30, 31]. The goal of this chapter is to extend the pioneering study of Sambath to consider flow-induced coalescence in the presence of surfactants, when inertial effects cannot be neglected.

The chapter is organized as follows. Section 7.2 describes in detail the mathematical formulation of the problem under consideration and the numerical methods employed to compute its solution. Section 7.3 presents the effect of system parameters on drainage times. Section 7.4 examines the effect of artificially "turning off" Marangoni stress on drainage times, in order to conclusively prove that Marangoni stress is indeed *primarily* responsible for the dramatic increase in drainage times when surfactants are added. Section 7.5 examines the two key mechanisms by which Marangoni stress delays drainage of the film, while section 7.6 examines a remarkable phenomena: multiple instances of Marangoni-induced flow-reversal that occurs for certain parameter values. Finally, section 7.7 concludes the chapter by summarizing the key results and discussing future avenues that can be explored by extending the current analyses.

7.2 Mathematical Formulation

The system consists of two initially spherical drops of radius R of a Newtonian liquid of constant density ρ_1 and viscosity μ_1, suspended in an immiscible Newtonian liquid of constant density ρ_2 and viscosity μ_2, with the surfactant-free tension of the liquid-liquid interface denoted by σ_0. The Hamaker constant A_H for the liquid-liquid system is constant in time and positive, such that the intermolecular force between the drops is attractive. The drops are initially separated by a center-to-center distance of $4R$, and pushed towards each other by a compressional flow with a constant strain rate G, identical to that generated by a four-roll Taylor mill [17]. It proves convenient to adopt a cylindrical coordinate system where the origin is located midway between the two drops along the line connecting the centers of the two drops, $\tilde{r}$ and $\tilde{z}$ represent the radial and axial distance from the origin, and $\mathbf{e}_r$ and $\mathbf{e}_z$ represent orthogonal unit vectors in the radial and axial direction in this cylindrical coordinate system. The

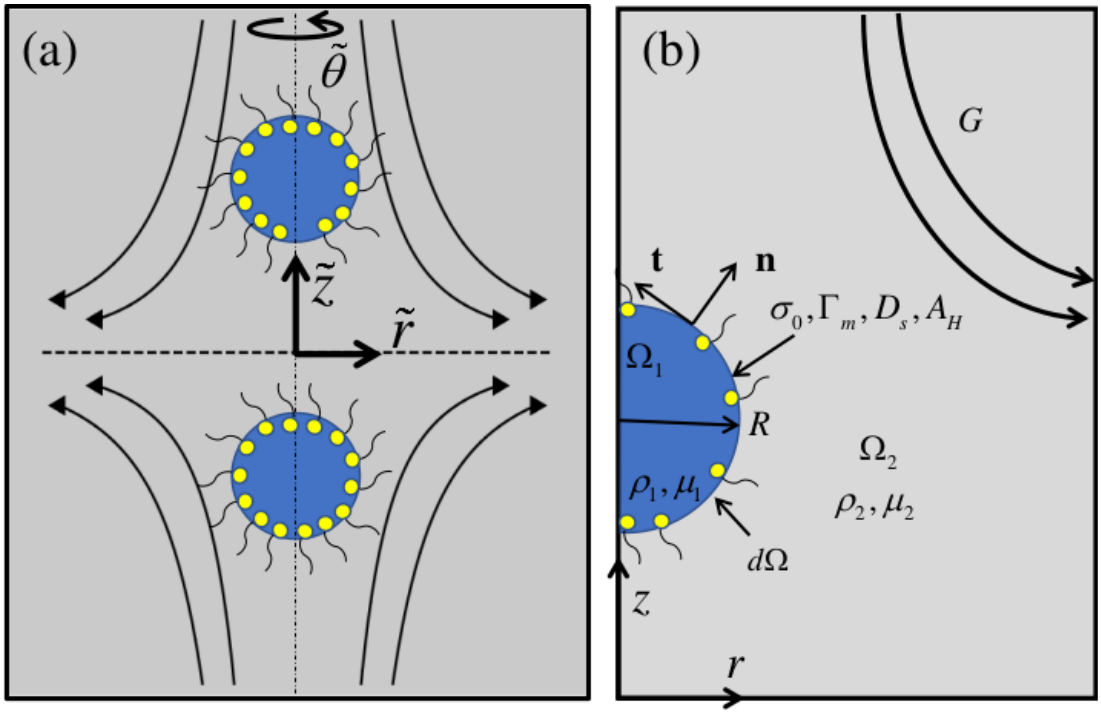

Figure 7.1. In this work, we examine the (a) head on collision of two equal-sized drops of a Newtonian liquid immersed in a second Newtonian liquid which are pushed towards each other by a compressional flow similar to Taylor's four roll mill [17] in the presence of insoluble surfactants. (b) The computational domain under consideration on account of symmetry.

computational domain is reduced to one quadrant owing to axisymmetry about the axis $\tilde{r} = 0$ and symmetry about $\tilde{z} = 0$. A detailed schematic is shown in figure 7.1. In what follows, the subscript $()_i$ denotes variables in the drop liquid as $i = 1$ and variables in the outer liquid as $i = 2$.

In this chapter, problem variables are non-dimensionalized using the undeformed drop radius R as the characteristic length $l_c \equiv R$, the inertio-capillary time-scale as the characteristic time $t_c \equiv \sqrt{\rho_1 R^3/\sigma_0}$, the ratio of the two as the characteristic velocity scale $v_c \equiv l_c/t_c$, the capillary pressure as the characteristic stress $p_c \equiv \sigma_0/R$, the clean interface surface tension σ_0 as the characteristic surface tension, and maximum packing concentration Γ_m as the characteristic surfactant concentration. The

flow is then governed by the following dimensionless groups: the Ohnesorge number $Oh = \mu_1/\sqrt{\rho_1\sigma_0 R}$, which is the ratio of the viscous force to square root of the product of the inertial and capillary forces, viscosity ratio $m_2 = \mu_2/\mu_1$, density ratio $d_2 = \rho_2/\rho_1$, dimensionless strain rate $U_\infty = G\sqrt{\rho_1 R^3/\sigma_0}$, the van der Waals number $A = A_H/(6\pi\sigma_0 R^2)$ which is the ratio of the force due to van der Waals attraction to capillary force, initial surfactant loading $\Gamma_0 \equiv \tilde{\Gamma}_0/\Gamma_m$ and two additional dimensionless numbers described below. In what follows, variables without tilde ($\sim$) over them denote the dimensionless counterparts of the variables with tilde over them.

Flow in the regions $\Omega_1(t)$ and $\Omega_2(t)$ is governed by the continuity and Navier-Stokes equations which are given in dimensionless form by

$$\nabla \cdot \mathbf{v}_i = 0 \tag{7.1}$$

$$d_i \left(\frac{\partial \mathbf{v}_i}{\partial t} + \mathbf{v}_i \cdot \nabla \mathbf{v}_i \right) = \nabla \cdot \mathbf{T}_i \tag{7.2}$$

where $\mathbf{T}_i \equiv -p_i \mathbf{I} + m_i Oh \left((\nabla \mathbf{v}_i) + (\nabla \mathbf{v}_i)^T \right)$, and p_i and $\mathbf{v}_i$ denote the pressure and velocity in liquid i respectively, and $d_1 = m_1 = 1$, while d_2 and m_2 have already been specified. The kinematic and traction boundary conditions are applied at the liquid-liquid interface $d\Omega(t)$, which is unknown a priori, to enforce mass conservation and account for the discontinuity in stress due to interfacial tension and van der Waals forces

$$\mathbf{n} \cdot (\mathbf{v}_i - \mathbf{v}_s) = 0 \tag{7.3}$$

$$\mathbf{n} \cdot (\mathbf{T}_2 - \mathbf{T}_1) = 2H\sigma\mathbf{n} + \nabla_s \sigma - \frac{A}{h^3}\mathbf{n} \tag{7.4}$$

where $\mathbf{n}$ represents the unit normal to the interface as shown in figure 7.1(b), $\mathbf{v}_s$ represents the velocity of the interface, $2H$ represents twice the mean curvature, equal to the surface divergence of the unit normal ($-\nabla_s \cdot \mathbf{n}$), and σ is the dimensionless local tension at the interface. The tangential component of equation (7.4) is non-

zero when gradients of local tension occur along the interface, and $\mathbf{t}.\nabla_s\sigma$ is known as the Marangoni stress [15]. The third term in equation (7.4) represents van der Waals attraction between the two drops which becomes significant when the axial distance between the interfaces, denoted by $2h$, becomes of the order of a few hundred nanometers, and thus the value of A is typically small [11, 32, 33]. In the current formulation, h is taken to be equal to the axial coordinate of the interface $d\Omega(t)$, and curvature effects are neglected. Symmetry boundary conditions are applied at the axis of axisymmetry $r = 0$ and plane of symmetry $z = 0$. The radial and axial boundaries of the domain are located at $r = k$ and $z = k$, where k is some positive constant, and taken to be $k = 7$ for all cases studied in this chapter. Increasing the value of k had no significant effect on the results. At these outer boundaries, the velocity in the outer liquid is described by

$$\mathbf{v}_2(|\mathbf{x}| \to \infty) = U_\infty \left(\frac{r}{2}\mathbf{e}_r - z\mathbf{e}_z\right) \tag{7.5}$$

Surfactants reduce the local tension by adsorbing at the interface. This effect is described by an equation of state that relates the interfacial tension to the local concentration of the surfactant. Here, we use the Szyszkowski equation of state [34] to capture this effect, which is given in dimensionless form by

$$\sigma = 1 + \beta ln\,(1 - \Gamma) \tag{7.6}$$

where $\sigma \equiv \tilde{\sigma}/\sigma_0$ is the dimensionless local interfacial tension, $\Gamma \equiv \tilde{\Gamma}/\Gamma_m$ is the dimensionless local surfactant concentration, $\beta = R_g T_{abs}\Gamma_m/\sigma_0$ is the surfactant strength parameter, R_g is the universal gas constant, and T_{abs} is the absolute temperature of the system. The maximum packing concentration for N-octadecanol chains in water was reported to be 8μ mol/m^2 by Liao, Franses and Basaran [34], and for copolymer surfactants by Yoon et al. [20] as 5.1μ mol/m^2. Thus, a typical value of β is between 0.2 and 0.4. Copolymers [26], long-chain alcohols in water [34], or soluble surfactants where the timescale for diffusion exchange between the bulk and interface is much

larger than the characteristic time of film drainage [24], can be considered insoluble in the bulk fluid. Thus, transport of surfactant occurs only at the interface due to advection of the bulk liquids, diffusion, and stretching or dilatation of the interface. Its concentration along the interface is then governed by the convection-diffusion equation [35], given in dimensionless form by

$$\frac{\partial \Gamma}{\partial t} + \nabla_s \cdot (\Gamma \mathbf{v}_s) - \frac{1}{Pe} \nabla_s^2 \Gamma = 0 \tag{7.7}$$

where $Pe \equiv R^2/t_c D_s$ is the surface Peclet number, and D_s is the surface diffusivity of the surfactant, which is typically anywhere between $D_s = 10^{-12}$ cm^2/s for bulk polymers [27] to $D_s = 10^{-4}$ cm^2/s for low molecular weight surfactants. Thus Pe numbers are typically large for μm to mm sized drops, ranging from 600 to 10^{12}. A symmetry condition is imposed for surfactant concentration at the locations where the interface meets the axis $r = 0$

$$\mathbf{t} \cdot \nabla_s \Gamma = 0 \tag{7.8}$$

where $\mathbf{t}$ is the unit tangent to the interface.

The system is initially quiescent with the flow described by equation (7.5) imposed at $t = 0$ at the outer boundaries $z = k$ and $r = k$. The surfactant concentration along the interface is initially homogeneous and set equal to Γ_0. The reduced interfacial tension is then given by $\sigma_{eq} = 1 + \beta ln(1 - \Gamma_0)$. It is useful to describe relations for the following dimensionless numbers used in past studies in the Stokes limit:

$$Ca = \frac{\mu_2 GR}{\sigma_0} = m_2 Oh U_\infty \tag{7.9}$$

$$Re = \frac{\rho_2 (GR) R}{\mu_2} = \frac{U_\infty d_2}{m_2 Oh} \tag{7.10}$$

Both these dimensionless groups are defined using the parameters of the outside fluid, as opposed to our scheme, where we use the inside fluid for characteristic values. It

is clear that in the creeping flow limit, $Re \to 0$ when $Oh \to \infty$ and $U_\infty \to 0$, but Ca is finite. Details of the numerical methods used to solve numerically the system of equations described above can be found in chapter 6.

7.3 Effect of system parameters on drainage times

In order to understand the effect of surfactants on flow-induced coalescence of two drops, it is important to study the effect of system parameters on the drainage time t_d, defined as the dimensionless time that elapses between half the minimum axial separation of the drops z_{min} attaining a value of $z_{min} = 10^{-1}$, and coalescence. Figures 7.2 - 7.3 shows the variation with time t of z_{min} and drainage times t_d over a range of values of the flow parameter U_∞, and surfactant parameters Γ_0, β, and Pe. For every comparison, coalescence behavior is compared with the clean interface or surfactant-free case with parameter values $Oh = 0.065$, $m_2 = 1$, $d_2 = 1$, $U_\infty = 0.05$, and $A = 10^{-10}$. The Reynold's number for this flow is $Re = 0.77 \sim O(1)$. The drops are observed to coalesce for this surfactant-free case without rebounding, and the drainage time $t_d = 19.71$.

Figures 7.2(a) and 7.2(b) show that increasing the dimensionless strain rate U_∞ leads to a corresponding increase in the drainage time t_d. At strain rates of $U_\infty = 0.05$ and higher, the addition of surfactant causes the drops to rebound at the surfactant parameter values mentioned in figure 7.2, with the extent of rebound increasing as U_∞ is increased. A dramatic increase in t_d is observed for all cases with surfactants as compared to the surfactant-free case.

Figures 7.2(c) and 7.2(d) show that increasing the initial surfactant loading Γ_0 leads to a corresponding increase in t_d. While Yoon et al. [20] observed saturation for drainage times at small values of σ_{eq} and no further increase in t_d upon increasing loading, t_d is observed to depend exponentially on Γ_0 in our simulations. However, Vannozzi [27] notes that additional attractive forces due to copolymer effects were responsible for the saturation in drainage times seen by Yoon et al. [20], and increasing t_d with increasing Γ_0 was observed in simulations when van der Waals forces were the

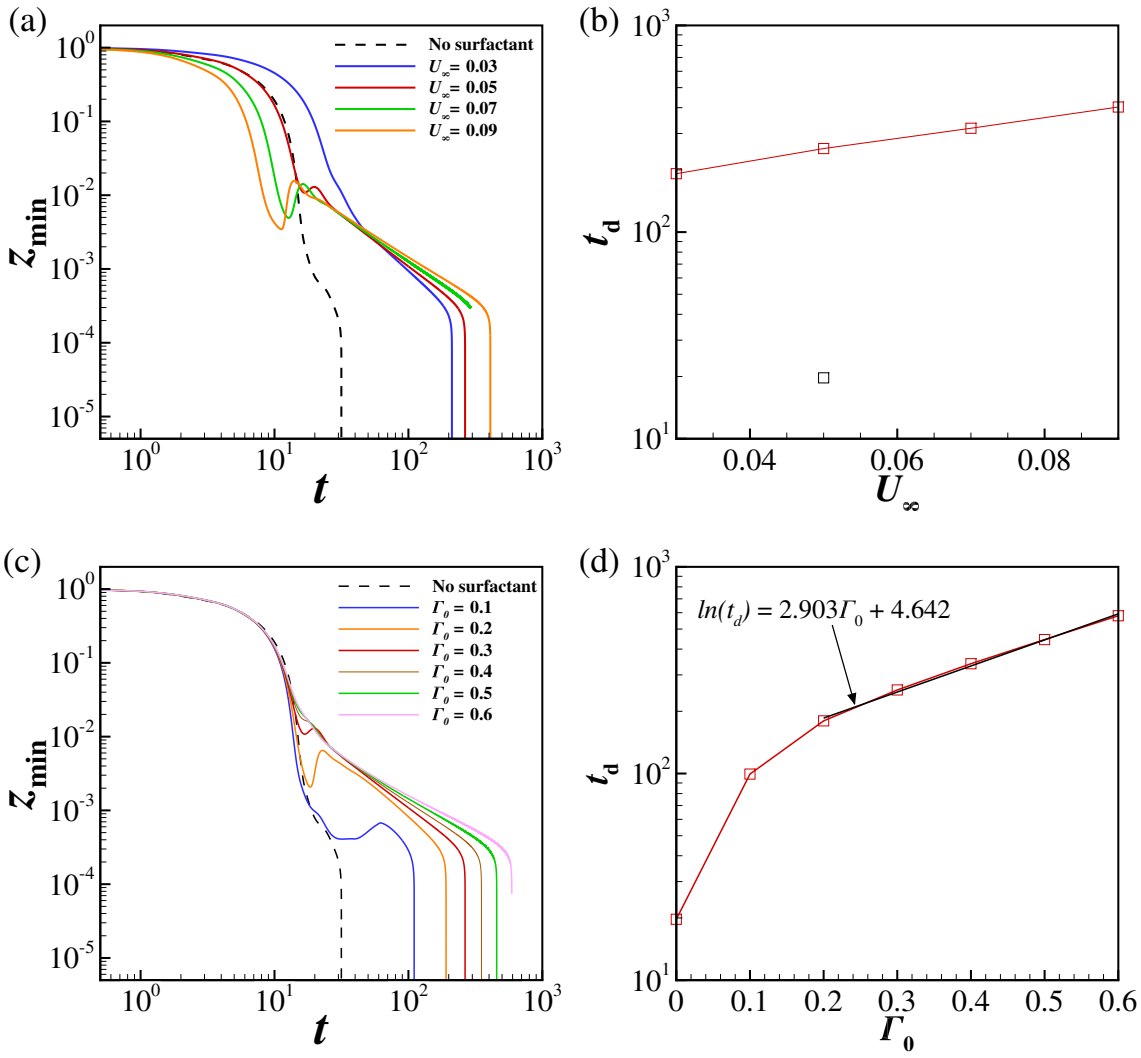

Figure 7.2. (a) Time evolution of half the minimum axial separation between the drops' interfaces z_{min} and (b) variation of drainage time t_d with dimensionless strain rate U_∞ when the value of $\Gamma = 0.3$. (c) Time evolution of z_{min} and (d) variation of t_d with initial surfactant loading Γ when the value of $U_\infty = 0.05$. Parameter values are $Oh = 0.065$, $m_2 = 1$, $d_2 = 1$, $A = 10^{-10}$, $\beta = 0.1$ and $Pe = 1000$.

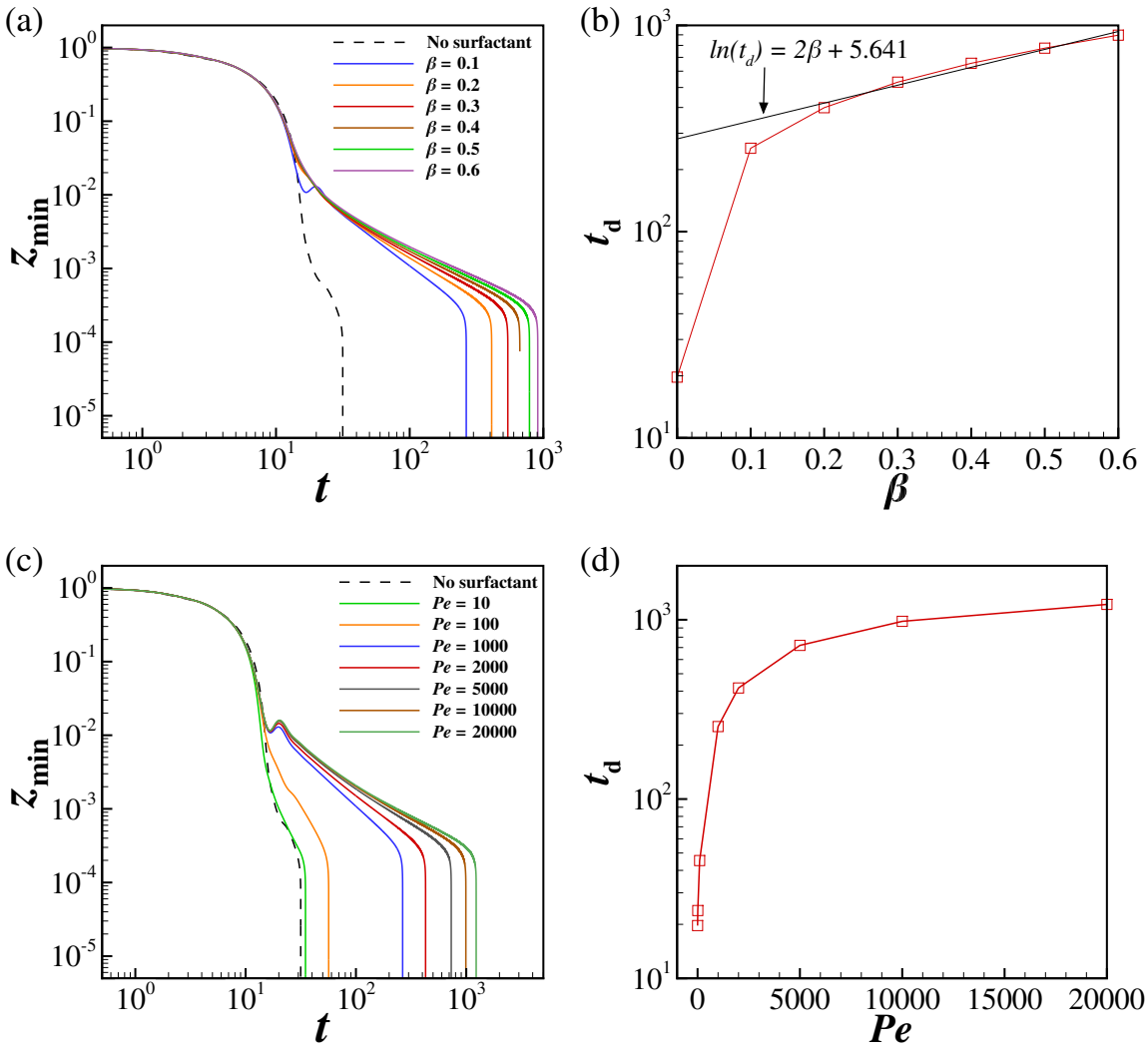

Figure 7.3. (a) Time evolution of half the minimum axial separation between the drops' interfaces z_{min} and (b) variation of drainage time t_d with surfactant strength parameter β when the value of $Pe = 1000$. (c) Time evolution of z_{min} and (d) variation of t_d with Peclet number Pe when the value of $\beta = 0.1$. Parameter values are $Oh = 0.065$, $m_2 = 1$, $d_2 = 1$, $U_\infty = 0.05$, $A = 10^{-10}$, and $\Gamma = 0.3$.

only attractive forces considered in the system [24, 26, 27]. Interestingly, the addition of surfactant causes drop rebound for lower values of loading $\Gamma_0 = 0.1 - 0.3$, while a monotonic decrease in z_{min} is observed for high Γ_0 values.

Figures 7.3(a) and 7.3(b) show that the effect of surfactant strength parameter β is similar to that seen for Γ_0 above, as increasing β leads to a corresponding increase in t_d, and a dramatic increase compared to the surfactant-free case. Again, the addition of surfactant causes rebound of the two drops at the lowest value of $\beta = 0.1$, while larger values lead to a monotonic decrease in z_{min}, and an exponential dependence of t_d on β.

Finally, figures 7.3(c) and 7.3(d) show the effect of Peclet number Pe on coalescence behavior and drainage times. Clearly, for low $Pe = 10$, or when surfactant advection is comparable to diffusion, the effect of adding surfactant is almost negligible and coalescence dynamics are nearly identical to those for the surfactant-free case. This suggests that Marangoni stress plays a crucial role in the dramatic increase in coalescence times in the presence of surfactants, which has been discussed by previous authors [24, 27], as Marangoni stresses only operate for large Pe when the advection of surfactant causes large gradients in concentration. Drainage time saturates as Pe is increased, and asymptotes to a constant value upon further increase in Pe, as large advection in the initial stages of coalescence will lead to a film region devoid of surfactants causing essentially surfactant-free drainage in the film.

7.4 Coalescence dynamics with Marangoni stresses artificially turned off

The parametric study described in section 7.3 hints at the crucial role played by Marangoni stress in causing the dramatic increase in drainage times seen for coalescence in the presence of surfactants. However, it is unclear from the variation of t_d with Γ_0 and β if non-uniform local reduction of interfacial tension plays an additional role in increasing drainage times, as stated by Dai and Leal [26]. To conclusively prove that Marangoni stress is *primarily* responsible for the dramatic increase in drainage times, simulations are perm formed for coalescence in the absence of Marangoni stress,

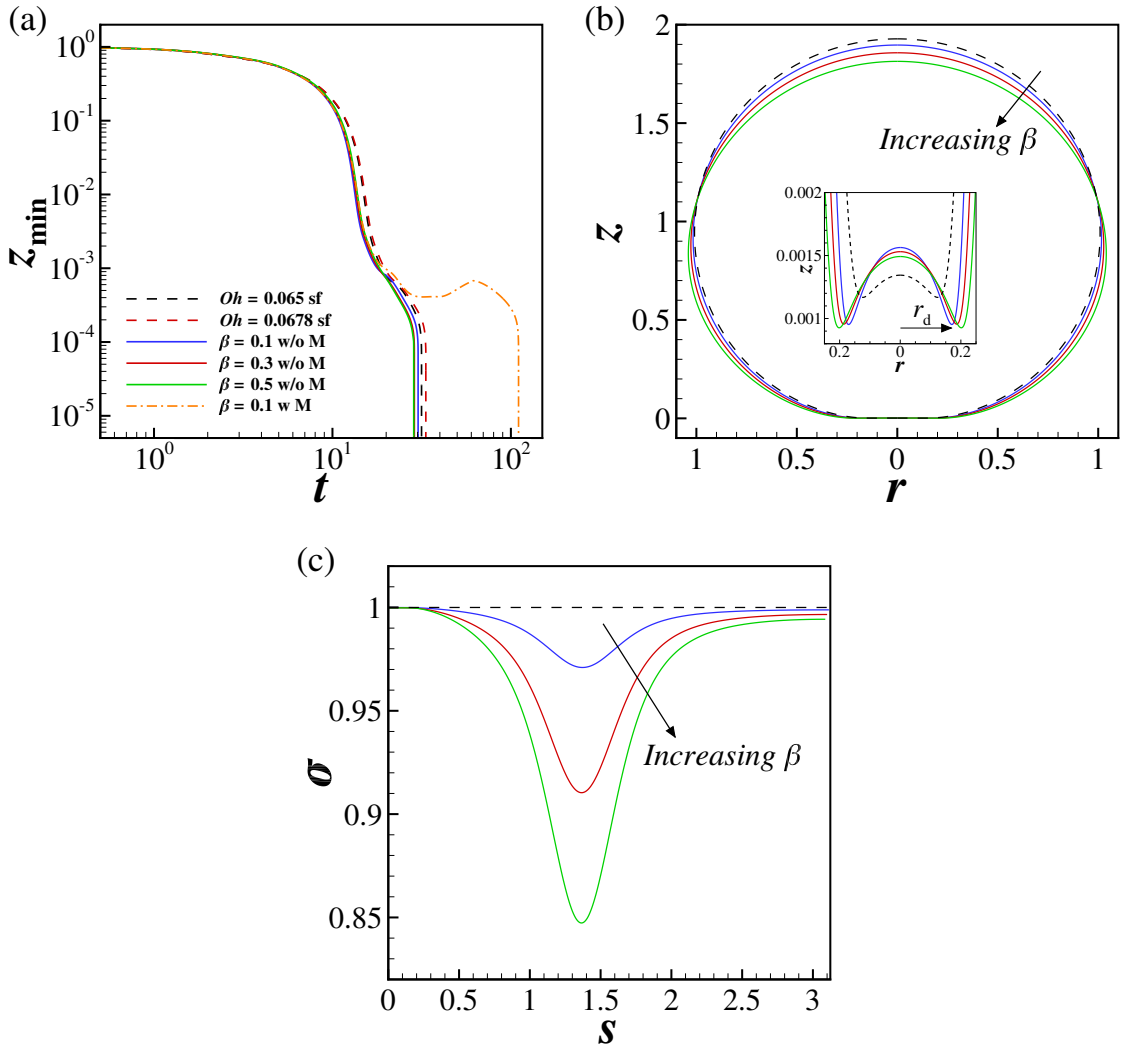

Figure 7.4. (a) Time evolution of half the minimum axial separation between the drops' interfaces z_{min}. The dashed lines represent surfactant-free cases (sf), while the solid lines represent surfactant-laden flows with Marangoni stress artificially "turned off" (w/o M), and the dash-dotted line represents surfactant-laden coalescence with Marangoni stress on (w M). Parameter values are $m_2 = 1$, $d_2 = 1$, $U_\infty = 0.05$, $A = 10^{-10}$ for all cases, and $Oh = 0.065$, $\Gamma_0 = 0.3$, $Pe = 1000$ for the surfactant-laden cases. (b) Drop shapes at $t = 18.3$ for the surfactant-free and Marangoni-free cases for $Oh = 0.065$. The inset shows a zoomed-in view of film shapes and the corresponding extent of the dimple r_d. (c) Interfacial tension σ as a function of arc length s at the same instant for the surfactant-free and Marangoni-free cases for $Oh = 0.065$.

by artificially "turning them off" or setting $\mathbf{t} \cdot \nabla_s \sigma = 0$ in the boundary condition (7.4). Figure 7.4(a) shows the variation of z_{min} with time for a surfactant-free case, three cases where β is progressively increased while Marangoni stress is turned off (Marangoni-free cases), and a surfactant-laden case with Marangoni stress on, for identical fluid parameters $Oh = 0.065$, $m_2 = 1$, $d_2 = 1$, $U_\infty = 0.05$, $A = 10^{-10}$, $\Gamma_0 = 0.3$, and $Pe = 1000$. Additionally, coalescence behavior for a surfactant-free case with $Oh = 0.0678$ where the interfacial tension σ_0 is reduced to match σ_{eq} for $\beta = 0.5$ is also shown. Figure 7.4(a) makes plain that decreasing interfacial tension σ_0 for the surfactant-free case ($Oh = 0.0678$), or a uniform reduction in interfacial tension, leads to an increase in drainage time. This is expected, as the effective Ohnesorge number of the system has increased. However, the increase in drainage time is small, and of the same order of magnitude as the effective change in Oh due to reducing σ_0. Remarkably, for the Marangoni-free cases, values of t_d are *smaller* than those observed for the equivalent surfactant-free case, and decrease as β is increased. The effect of non-uniform local reduction of interfacial tension is opposite to that observed for uniform reduction in tension, if Marangoni stress is artificially turned off.

Figures 7.4(b) and 7.4(c) show the shapes of the drop and interfacial tension σ as a function of arc length s at $t = 18.33$ for the three Marangoni-free cases, in comparison to the surfactant free case. Surfactant is convected from the upper half of the drop, as well as out of the film region, to the lower half of the drop outside the film region. This leads a local minima in σ, with the magnitude of decrease in σ naturally increasing with β . As a result, the shape of the drop at the same time instant is more deformed for larger β, as a higher local curvature is needed at the minima to support the smaller value of σ. This in turn leads to a more pronounced dimple r_d (shown in inset of figure 7.4(b)) for larger β. Thus van der Waals forces become significant earlier for the largest value of β which results in the unexpected trend in drainage times.

These results conclusively prove that Marangoni stress is *primarily* responsible for the dramatic increase in drainage times observed for surfactant laden coalescence of drops, as selectively turning off Marangoni stress leads to an unexpected decrease in drainage times in comparison to the surfactant free case.

7.5 Drop rebound due to addition of surfactants

In section 7.3 it was observed that addition of surfactants led to drop rebound at lower Γ_0 and β values. Previous numerical studies using film drainage models [24] and boundary-integral method simulations [27] have reported "oscillations of the minimum separation", at lower concentrations of surfactants. Here, the mechanism that leads to rebound of the drops in the presence of surfactants is explored first, followed by a study of the effects of inertia and surfactant strength on drop rebound.

7.5.1 Additional mechanism of drainage delay: Drop rebound

Figure 7.5 shows the variation with time of z_{min} and velocity of center of mass of the drop v_{com} for flow-induced coalescence of two drops in an outer liquid when $Oh = 0.065$, $m_2 = 1$, $d_2 = 1$, $U_\infty = 0.05$, and $A = 10^{-10}$ for a surfactant free case (shown by the black dashed line), a surfactant-laden case (blue line) with parameters $\Gamma_0 = 0.3$, $\beta = 0.1$, and $Pe = 1000$, the same case but when inertia of both fluids is "turned off" by setting $d_i = 0$ in equation (7.2) (orange line), and finally, a surfactant-laden case with larger strength parameter $\beta = 0.3$ (red line). Rebound is only observed for the surfactant-laden case with $\beta = 0.1$ when inertia is included, leading to a value of drainage time $t_d = 253.69$, as compared to $t_d = 210.35$ for the inertia-free case, and $t_d = 19.71$ for the surfactant-free case. Additionally, it is clear that rebound, and not "oscillations of h_{min}" (which suggests a phenomena local to the film), occurs for the surfactant-laden case, as v_{com} reverses direction during film thickening, signifying that the drops move away from each other.

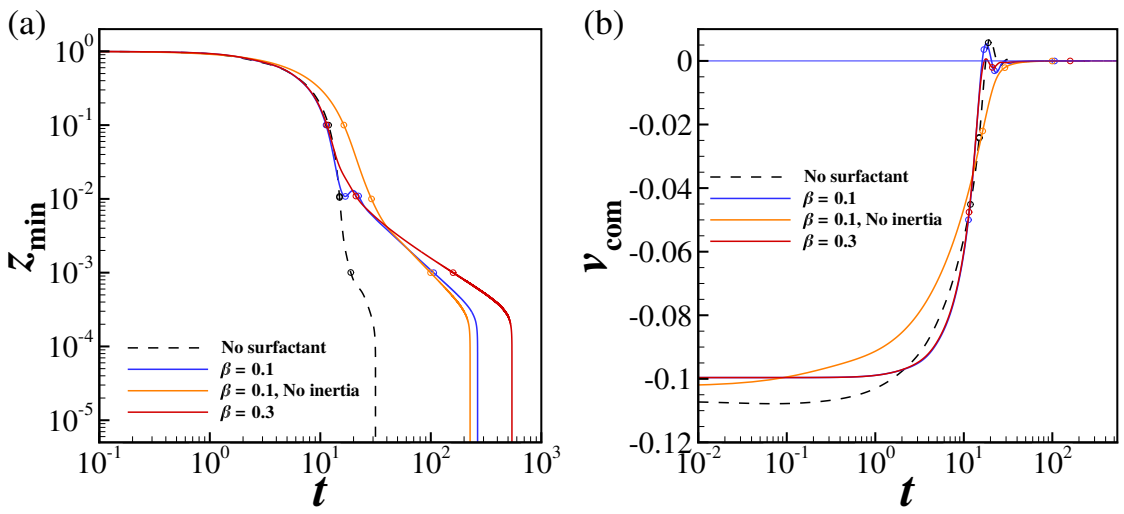

Figure 7.5. (a) Time evolution of half the minimum axial separation between the drops' interfaces z_{min} for a surfactant-free case (black dashed line), a surfactant-laden case with $\beta = 0.1$ with inertia (blue solid line), and with inertia "turned off" (orange solid line), and a surfactant-laden case with $\beta = 0.3$ (red solid line). (b) Velocity of center of mass of the drop for the corresponding cases in (a). Parameter values are $Oh = 0.065$, $m_2 = 1$, $d_2 = 1$, $U_\infty = 0.05$, $A = 10^{-10}$, $\Gamma_0 = 0.3$, and $Pe = 1000$. The open symbols denote time instants for which surface profiles are shown in figures 7.6 - 7.9.

Figure 7.6 shows the surface profiles of several quantities of interest at four time instants for the surfactant-laden case with $\beta = 0.1$. As the drops approach each other, the first row of frames show that surfactant is convected out of the region between the drops and towards the equator due to a positive tangential velocity $v_t = \mathbf{t} \cdot \mathbf{v}_s$ at the interface. The net flux of surfactant, defined as

$$\phi = \mathbf{t} \cdot \left(\mathbf{v}_s \Gamma - \frac{1}{Pe} \nabla_s \Gamma \right) \tag{7.11}$$

is positive up to $s = 0.4$, but negative for $0.4 < s < 3.14$, which is why surfactant begins to accumulate just outside this region between the drops. A negative Marangoni stress $T_{nt} = \mathbf{t} \cdot \nabla_s \sigma$ develops in this region, due to the increase in Γ along

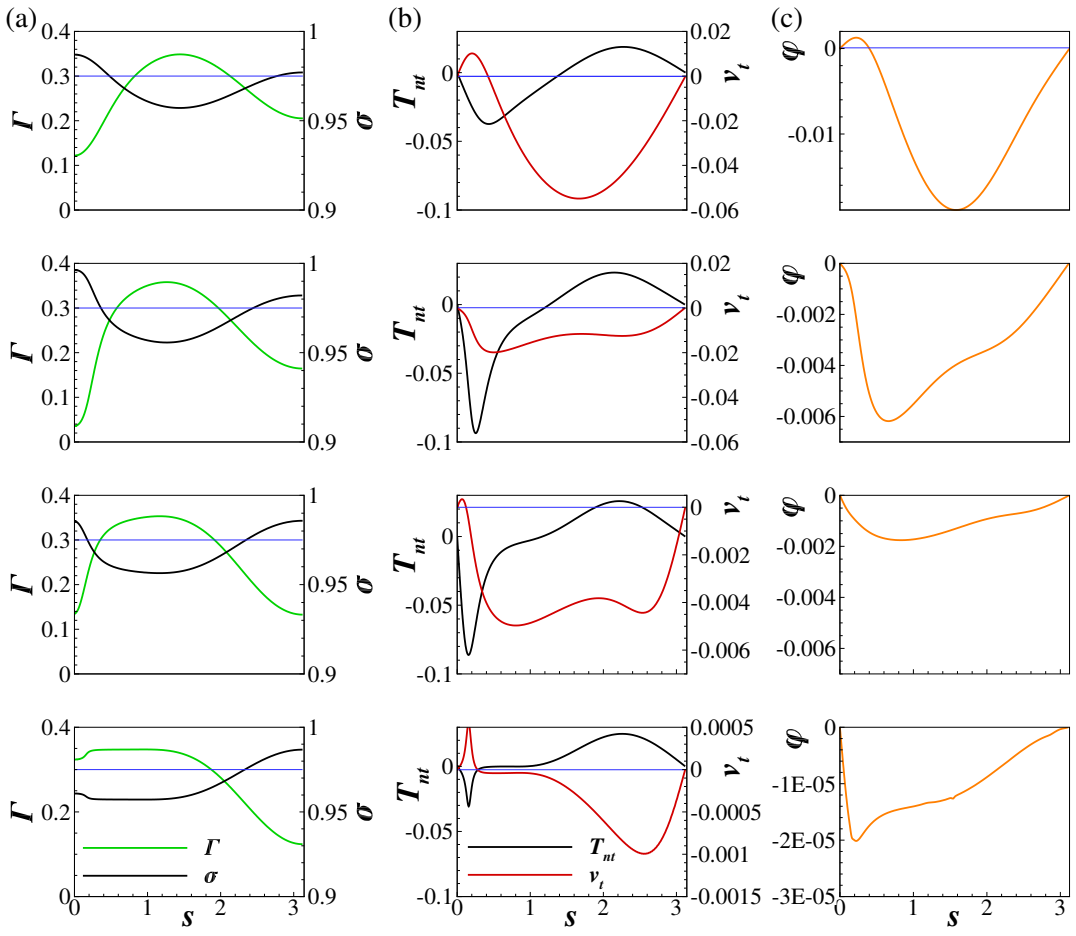

Figure 7.6. Surface profiles of (a) surfactant concentration Γ (green line) and local interfacial tension σ (black line), (b) Marangoni stress T_{nt} (black line) and tangential velocity at the interface v_t (red line), and (c) net flux of surfactant in direction of the tangent $\mathbf{t}$ for the surfactant-laden case with $\beta = 0.1$ where drop rebound occurs. Each row of the figure corresponds to one time instant shown in figure 7.5 by the open symbols. The horizontal blue lines represent the initial state of $\Gamma = 0.3$, $v_t = 0$ and $\phi = 0$. Other parameter values are same as figure 7.5.

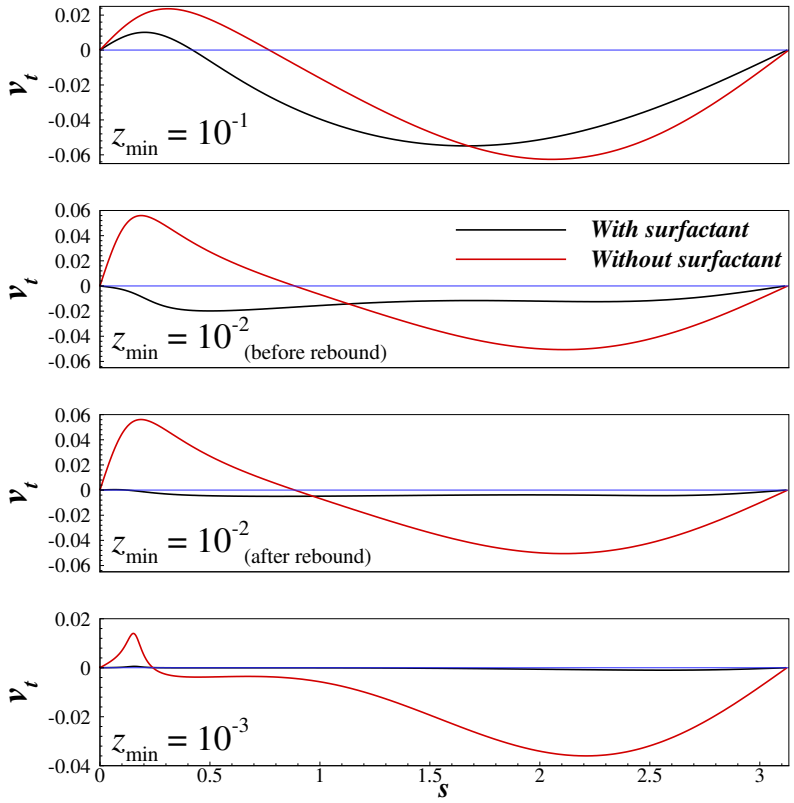

Figure 7.7. Surface profiles of the tangential velocity v_t for the surfactant-free and surfactant-laden case with $\beta = 0.1$ at the z_{min} values shown in each frame. These values correspond to the time instants shown in figure 7.5 by the open symbols. The horizontal blue lines represent $v_t = 0$. Other parameter values are same as figure 7.5.

the arc length s, as one moves from the center of the drop to its equator. An opposite Marangoni stress operates on the top half of the drop, pushing it towards the symmetry plane. As the drops get close such that $z_{min} = 10^{-2}$, more surfactant is convected out of the film that develops between the drops, and towards the equator. The flow-induced gradient in surfactant leads to a large negative Marangoni stress, which opposes the driving pressure gradient in the film and is large enough to cause backflow and reverse flow direction. This is made plain by the negative v_t in the film region (in addition to the rest of the surface) seen in the second row of figure 7.6. Thus, at this instant, drop rebound is initiated, and the film begins to thicken as

the drops move away from each other. The flux of surfactant ϕ is understandably negative, as both advection and diffusion of surfactant occurs into the film region. As the external flow field reverses drop movement and the drop approaches the symmetry plane a second time, its velocity is much smaller. At this instant, while v_t in the film is positive, indicating a convective flux of surfactant out of the film, the velocity is so small that diffusion dominates, and ϕ is still negative in the film. Thus, surfactant concentration is increasing in the film, and Marangoni stress outside the film region keeps decreasing in magnitude. Thus, it is unable to cause reversal of flow a second time. This behavior is maintained as z_{min} falls to 10^{-3}, with diffusion restoring surfactant in the film and the opposing Marangoni stress reducing in magnitude. While Marangoni stresses are small, their magnitude is large enough to cause partial immmobilization of the surface, and slow down drainage of the film. Figure 7.7 compares the tangential velocity v_t at the time instants shown in figure 7.5 for the surfactant-free and surfactant-laden case, and the degree of partial immobilization of the surface for the surfactant-laden case is plain, especially after rebound occurs.

Thus, large negative Marangoni stresses outside the film region initially arrest, and reverse film drainage due to convection of surfactant out of the film during first approach. This is the first possible mechanism that leads to larger drainage times for surfactant-laden coalescence as compared with surfactant-free coalescence, and applies to coalescence for low Γ_0 and β values. Subsequently, diffusion dominates over convection and surfactant is restored in the film until coalescence, leading to diminishing Marangoni stresses which are unable to cause flow reversal again. However, they are sufficient to immobilize the drop surface and thus delay drainage of the film; this is the second mechanism that leads to larger drainage times for surfactant-laden coalescence.

7.5.2 Absence of drop rebound in the absence of fluid inertia

Figure 7.8 shows the surface profiles of several quantities of interest for surfactant-laden coalescence with $\beta = 0.1$ in the Stokes limit, or when the inertia of both the

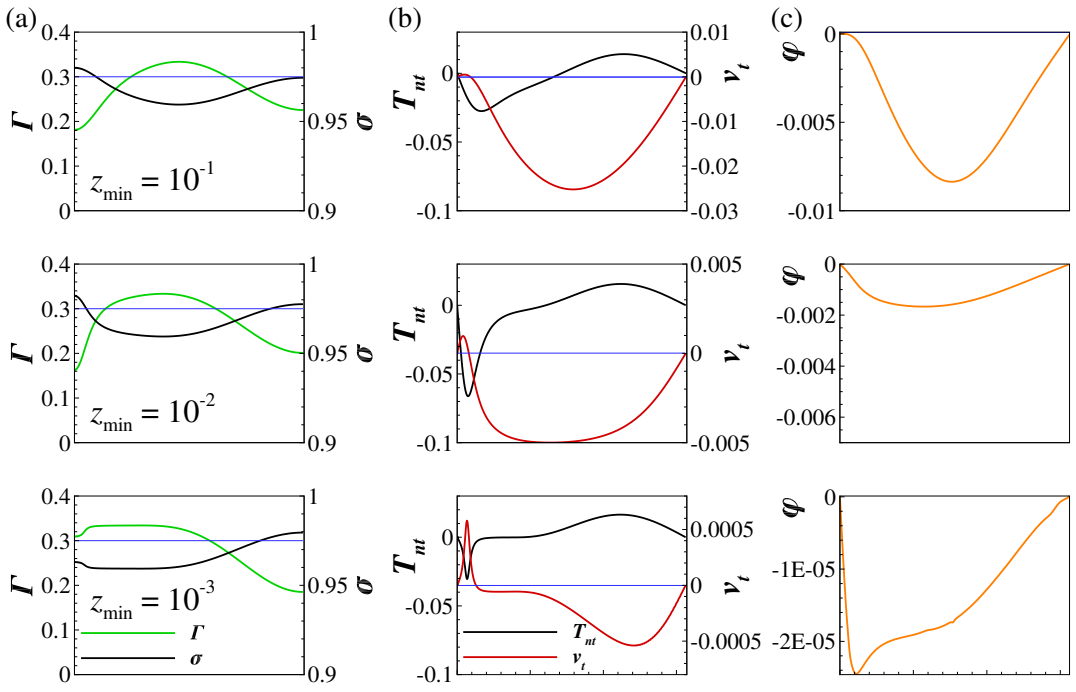

Figure 7.8. Surface profiles of (a) surfactant concentration Γ (green line) and local interfacial tension σ (black line), (b) Marangoni stress T_{nt} (black line) and tangential velocity at the interface v_t (red line), and (c) net flux of surfactant in direction of the tangent $\mathbf{t}$ for the surfactant-laden case with $\beta = 0.1$ when inertia is "turned off". Each row of the figure corresponds to one time instant at the z_{min} value specified in the first frame, and shown in figure 7.5 by the open symbols. The horizontal blue lines represent the initial state of $\Gamma = 0.3$, $v_t = 0$ and $\phi = 0$. Other parameter values are same as figure 7.5.

fluids is "turned off". It is evident that at the same values of z_{min}, the corresponding decrease in Γ in the film is much lesser than corresponding case with inertia. The resulting negative Marangoni stress outside the film is also smaller, and v_t remains positive in the film throughout the process of coalescence, indicating that the film is always draining. The degree of immobilization is higher when inertia is excluded, as v_t is much lower at all instants when compared to the inertial case in figure 7.6. This indicates that increase in drainage time in the Stokes limit in comparison to the surfactant-free case is only due to the second mechanism of surfactant-laden

coalescence, i.e. due to interface immobilization. The occurrence of rebound and drainage delay due to the first mechanism is absent when inertia is neglected from the governing equations. Figure 7.5(b) makes plain that the velocity of approach v_{com} of the drop is lower when inertia is neglected. This is the likely reason for lesser initial convection of surfactant out of the region between the drops, and the subsequent absence of rebound.

7.5.3 Absence of drop rebound at higher β

Figure 7.9 shows the surface profiles of several quantities of interest for surfactant-laden coalescence when the surfactant strength is increased to $\beta = 0.3$. The drops do not rebound for this case but coalesce on first approach. Even as v_{com} briefly reverses direction (figure 7.5), the minimum separation between the drops continues to fall monotonically until the interfaces are close enough for van der Waals forces to become significant. The figure makes plain that the convection of surfactant out of the region between the drops is reduced in comparison to the $\beta = 0.1$ case (figure 7.6). However, due to the larger surfactant strength, the magnitude of Marangoni stress opposing drainage of the film is actually larger for this case at $z_{min} = 10^{-1}$. The larger Marangoni stress acts to reduce v_t faster. Indeed, at the instant when $z_{min} = 10^{-2}$, the magnitude of v_t along the entire surface is much lesser than the $\beta = 0.1$ case. The large Marangoni stresses act to further reduce the tangential velocity as the drops get closer, leading to near immobilization at $z_{min} = 10^{-3}$. Thus, the coalescence of surfactant-laden drops with larger values of β is only delayed by the second mechanism of interface immobilization, in comparison to surfactant-free coalescence, and resembles coalescence of surfactant-laden drops in the Stokes limit shown in the previous sub-section.

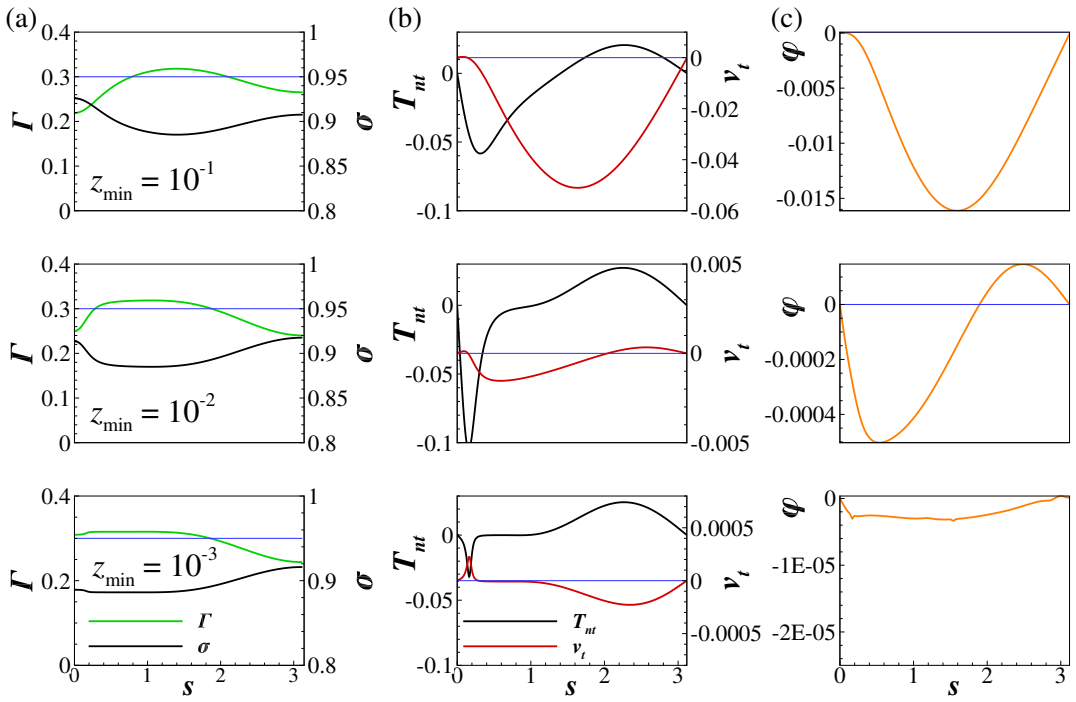

Figure 7.9. Surface profiles of (a) surfactant concentration Γ (green line) and local interfacial tension σ (black line), (b) Marangoni stress T_{nt} (black line) and tangential velocity at the interface v_t (red line), and (c) net flux of surfactant in direction of the tangent $\mathbf{t}$ for the surfactant-laden case with $\beta = 0.3$. Each row of the figure corresponds to one time instant at the z_{min} value specified in the first frame, and shown in figure 7.5 by the open symbols. The horizontal blue lines represent the initial state of $\Gamma = 0.3$, $v_t = 0$ and $\phi = 0$. Other parameter values are same as figure 7.5.

7.6 Multiple instances of Marangoni-induced flow-reversal

For coalescence at the parameter values considered so far in this chapter, drop rebound does not occur for the surfactant-free case. In chapter 6, several instances of drop rebound for surfactant-free coalescence were observed at higher Re, as a result of fluid inertia. As we have observed above that addition of surfactant leads to drop rebound, a natural question arises: What effect does addition of surfactant have on coalescence dynamics when rebound is observed for the surfactant-free case?

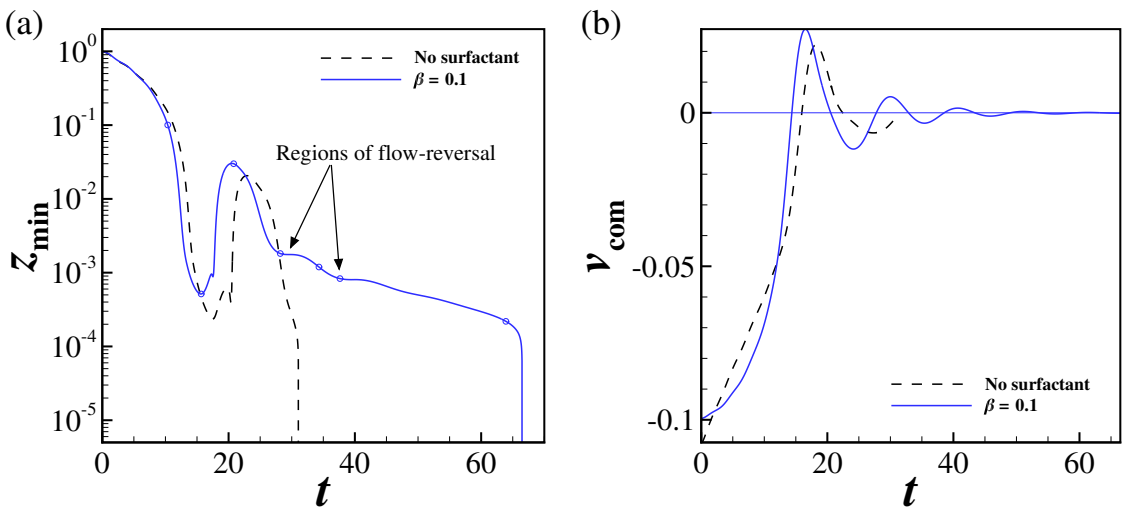

Figure 7.10. (a) Time evolution of half the minimum axial separation between the drops' interfaces z_{min} for a surfactant-free case (black dashed line) and a surfactant-laden case (blue line). (b) Velocity of center of mass of the drop for the corresponding cases in (a). Parameter values are $Oh = 0.023$, $m_2 = 1$, $d_2 = 1$, $U_\infty = 0.05$, $A = 10^{-10}$, $\Gamma_0 = 0.1$, $\beta = 0.1$ and $Pe = 1000$. The open symbols in (a) denote time instants for which surface profiles are shown in figures 7.11.

Figure 7.10 shows the variation with time of z_{min} and v_{com} for flow-induced coalescence when parameter values are $Oh = 0.023$, $m_2 = 1$, $d_2 = 1$, $U_\infty = 0.05$, and $A = 10^{-10}$ when the interface is clean, and when insoluble surfactants are present such that $\Gamma_0 = 0.1$, $\beta = 0.1$, and $Pe = 1000$. The Reynold's number is now $Re = 2.17$. A remarkable phenomena is observed for the surfactant-laden case. In comparison to the surfactant-free case, the extent of the first rebound is enhanced, and additionally, the drops undergo two periods of flow reversal as drainage of the film is arrested and z_{min} stays constant or increases with time. The velocity of the center of mass v_{com} signifies that at these instants the drops undergo flow reversal and are moving away from each other. Figure 7.11 shows the variation of the surfactant concentration Γ, Marangoni stress T_{nt} and tangential velocity at the interface v_t at the instants of time marked by the open symbols in figure 7.10(a). A clear picture of the underlying dynamics emerges from this figure. As the drops approach each other initially,

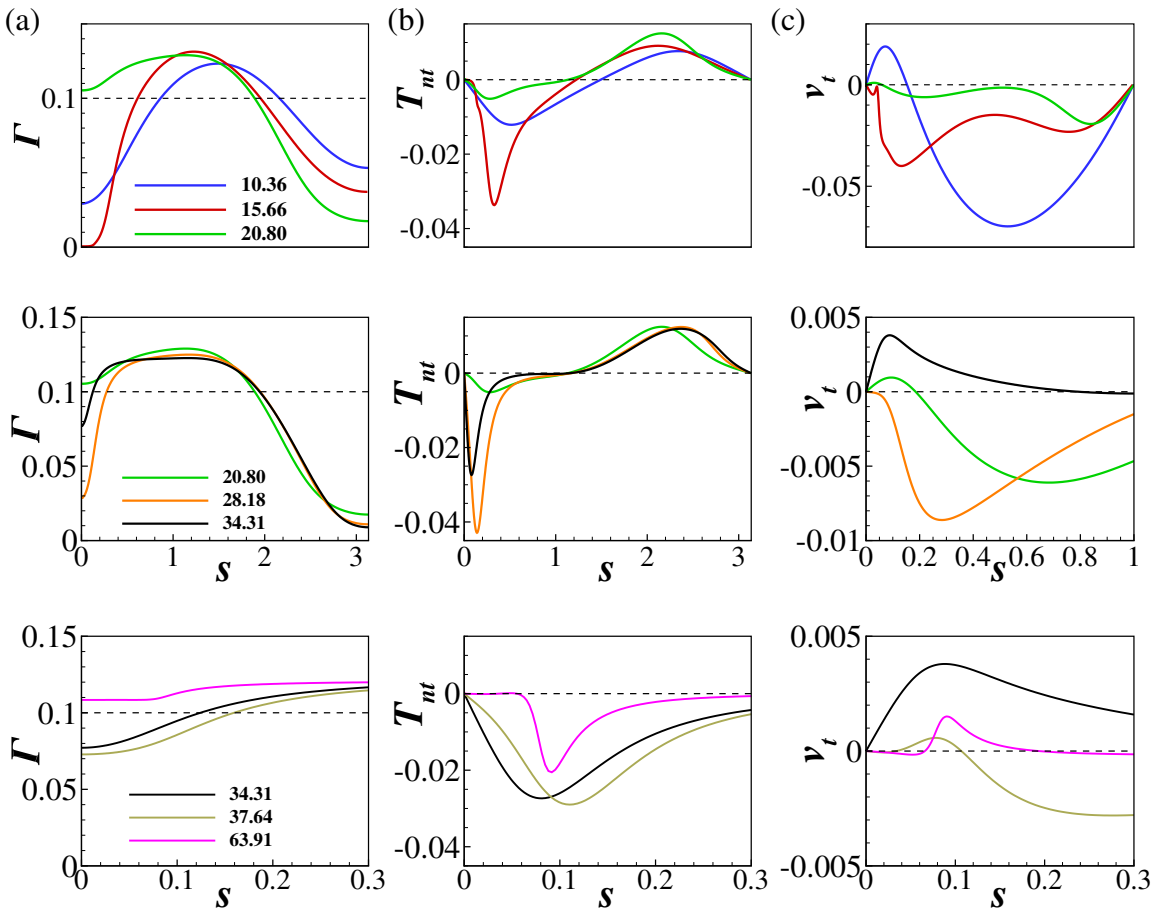

Figure 7.11. Surface profiles of (a) surfactant concentration Γ, (b) Marangoni stress T_{nt}, and (c) tangential velocity at the interface v_t surfactant-laden coalescence with $\beta = 0.1$. Each row of the figure shows the profiles for three time-instants specified in the first frame, and shown in figure 7.10 by the open symbols. The horizontal blue lines represent the initial state of $\Gamma = 0.3$, $T_{nt} = 0$ and $v_t = 0$. Other parameter values are same as figure 7.10.

surfactant is completely convected out of the film that forms between the two drops, and a large negative Marangoni stress promotes backflow into the film. In contrast to earlier cases, Marangoni stress is not solely responsible for flow-reversal and rebound, but adds to the already negative pressure gradient to cause additional backflow. This results in the earlier arrest of film drainage and flow reversal (seen in figure 7.10) and subsequent rebound to a greater extent. However, the compressional flow imposed at the boundaries causes the drops to reverse direction and approach again. In contrast to earlier cases where only one such rebound was observed, surfactant drains from the film again, and a large negative Marangoni stress acts to reverse flow in the film. Surfactant is replenished in the film due to backflow and Marangoni stress is no longer an impediment to drainage, and film drainage resumes. However, the earlier mechanism is repeated for a third time, causing reversal in flow again. Every successive flow reversal clearly diminishes in magnitude, until the interface is nearly immobilized. Following this, slow drainage due to the second mechanism of interface immobilization occurs until the drops are close enough for van der Waals forces to kick in. Thus, in the event of coalescence of surfactant-laden drops where drop rebound occurs for the surfactant-free case, multiple cycles of flow-reversal are observed, which cause additional delay in coalescence of the two drops. Similar phenomena has been observed experimentally [36], where the authors observed "cyclic dimpling" in an aqueous film formed between oil phases in the presence of non-ionic surfactants (Tweens). An attempt to explain this phenomena by means of a lubrication thin film theory [37] was unable to capture the cyclic formation of dimples, which is expected since the multiple flow-reversals observed here are a result of fluid inertia acting in tandem with Marangoni stresses.

7.7 Conclusions and outlook

In this chapter, flow-induced coalescence of two drops in a second immiscible liquid in the presence of insoluble surfactants was studied when the flow Reynold's number $Re \sim O(1)$. A dramatic increase in drainage times in comparison to surfactant-free

coalescence was observed when surfactants were added in even small concentrations, in agreement with previous experiments and numerical studies. Two mechanisms for this delay were discovered: (1) drop rebound that occurs due to Marangoni-stress induced backflow into the region of fluid between the drops, and (2) interface immobilization due to Marangoni stress. Drainage delay due to rebound was only observed when fluid inertia was considered in the governing equations, and turning off inertia led to drainage by the second mechanism alone. Thus, for $Re \sim O(1)$ flows, the inclusion of inertia is essential to capture the additional delay in film drainage due to rebound of the drops. Moreover, this mechanism only operates at low concentrations of low-strength surfactants, as interface immobilization in these cases is low. It must be noted that previous works considering purely lubrication ($Re = 0$) flows [24, 27] have observed drop rebound "oscillations of minimum drop separation". As our simulations show that inertia is essential for Marangoni-induced drop rebound at $Re \sim O(1)$, it is of future interest to study coalescence for vanishingly small U_∞ values. Remarkably, when the surfactant-free drops are known to rebound upon first approach due to inertia, addition of surfactant in small concentrations leads to amplification of this behavior, and additional instances of flow-reversal that delay film drainage.

The rate coalescence of drops in emulsions can be enhanced by electric fields [38], provided the field strength is below some critical value [39]. Understanding the dynamics of drop coalescence in the presence of electric fields is crucial for designing electrically enhanced coalescer units [1,40]. The numerical methods utilized by Collins et al. [41] and Collins et al. [42] for studying electrohydrodynamic tip streaming of charged drops can be combined with the algorithm described in this chapter to study rigorously the head-on collision of two drops in an electric field when the interface is contaminated by surfactants.

7.8 List of References

[1] John S Eow and Mojtaba Ghadiri. Electrostatic enhancement of coalescence of water droplets in oil: a review of the technology. *Chemical Engineering Journal*, 85(2-3):357–368, 2002.

[2] Peter K Kilpatrick. Water-in-crude oil emulsion stabilization: Review and unanswered questions. *Energy & Fuels*, 26(7):4017–4026, 2012.

[3] Sanjeev Kumar, G Narsimhan, and D Ramkrishna. Coalescence in creaming emulsions. existence of a pure coalescence zone. *Industrial & engineering chemistry research*, 35(9):3155–3162, 1996.

[4] Lung-Hsin Hung, Kyung M Choi, Wei-Yu Tseng, Yung-Chieh Tan, Kenneth J Shea, and Abraham Phillip Lee. Alternating droplet generation and controlled dynamic droplet fusion in microfluidic device for cds nanoparticle synthesis. *Lab on a Chip*, 6(2):174–178, 2006.

[5] Howard A Stone. Dynamics of drop deformation and breakup in viscous fluids. *Annu. Rev. Fluid Mech.*, 26(1):65–102, 1994.

[6] Yashodhara Pawar and Kathleen J Stebe. Marangoni effects on drop deformation in an extensional flow: The role of surfactant physical chemistry. i. insoluble surfactants. *Phys. Fluids*, 8(7):1738–1751, 1996.

[7] Petia M Vlahovska, Michael Loewenberg, and Jerzy Blawzdziewicz. Deformation of a surfactant-covered drop in a linear flow. *Phys. Fluids*, 17(10):103103, 2005.

[8] Jens Eggers, John R Lister, and Howard A Stone. Coalescence of liquid drops. *J. Fluid Mech.*, 401:293–310, 1999.

[9] J. D. Paulsen, J.C. Burton, S. R. Nagel, S. Appathuri, M. T. Harris, and O. A. Basaran. The inexorable resistance of inertia determines the initial regime of drop coalescence. *Proc. Nat. Acad. Sci.*, 109(18):6857–6861, 2002.

[10] Christopher R. Anthony. *Dynamics of retracting films and filaments near singularities*. PhD thesis, Purdue University, August 2017.

[11] AK Chesters. The modelling of coalescence processes in fluid-liquid dispersions: a review of current understanding. *Chemical engineering research & design*, 69(A4):259–270, 1991.

[12] Peter Van Puyvelde, Sachin Velankar, Jan Mewis, Paula Moldenaers, and KU Leuven. Effect of marangoni stresses on the deformation and coalescence in compatibilized immiscible polymer blends. *Polymer Engineering & Science*, 42(10):1956–1964, 2002.

[13] Xiaofan Li and C Pozrikidis. The effect of surfactants on drop deformation and on the rheology of dilute emulsions in stokes flow. *J. Fluid. Mech.*, 341:165–194, 1997.

[14] VG Levich and VS Krylov. Surface-tension-driven phenomena. *Ann. Rev. Fluid Mech.*, 1(1):293–316, 1969.

[15] LE Scriven and CV Sternling. The marangoni effects. *Nature*, 187(4733):186, 1960.

[16] Pritish M Kamat, Brayden W Wagoner, Sumeet S Thete, and Osman A Basaran. Role of marangoni stress during breakup of surfactant-covered liquid threads: Reduced rates of thinning and microthread cascades. *Phys. Rev. Fluids*, 3(4):043602, 2018.

[17] GI Taylor. The formation of emulsions in definable fields of flow. *Proceedings of the Royal Society of London. Series A*, 146(858):501–523, 1934.

[18] YT Hu, DJ Pine, and L Gary Leal. Drop deformation, breakup, and coalescence with compatibilizer. *Phys. Fluids*, 12(3):484–489, 2000.

[19] JW Ha, Yosang Yoon, and LG Leal. The effect of compatibilizer on the coalescence of two drops in flow. *Phys. Fluids*, 15(4):849–867, 2003.

[20] Yosang Yoon, Adam Hsu, and L Gary Leal. Experimental investigation of the effects of copolymer surfactants on flow-induced coalescence of drops. *Phys. Fluids*, 19(2):023102, 2007.

[21] TD Hodgson and DR Woods. The effect of surfactants on the coalescence of a drop at an interface. ii. *Journal of Colloid and Interface Science*, 30(4):429–446, 1969.

[22] P Ghosh and VA Juvekar. Analysis of the drop rest phenomenon. *Chemical Engineering Research and Design*, 80(7):715–728, 2002.

[23] Vittorio Cristini, J Bławzdziewicz, and Michael Loewenberg. Near-contact motion of surfactant-covered spherical drops. *J. Fluid. Mech.*, 366:259–287, 1998.

[24] Allan K Chesters and Ivan B Bazhlekov. Effect of insoluble surfactants on drainage and rupture of a film between drops interacting under a constant force. *J. Col. Int. Sci.*, 230(2):229–243, 2000.

[25] Leslie Y Yeo, Omar K Matar, E Susana Perez de Ortiz, and Geoffrey F Hewitt. Film drainage between two surfactant-coated drops colliding at constant approach velocity. *J. Col. Int. Sci.*, 257(1):93–107, 2003.

[26] Bing Dai and L Gary Leal. The mechanism of surfactant effects on drop coalescence. *Phys. Fluids*, 20(4):040802, 2008.

[27] Carolina Vannozzi. Coalescence of surfactant covered drops in extensional flows: effects of the interfacial diffusivity. *Phys. Fluids*, 24(8):082101, 2012.

[28] Michael A Rother, Alexander Z Zinchenko, and Robert H Davis. Surfactant effects on buoyancy-driven viscous interactions of deformable drops. *Colloids and Surfaces A: Physicochemical and Engineering Aspects*, 282:50–60, 2006.

[29] Krishnaraj Sambath. *Dynamics of Drop Disintegration and Coalescence with and without Electric Fields*. PhD thesis, Purdue University, August 2013.

[30] Y. Yoon, F. Baldessari, H. D. Ceniceros, and L. G. Leal. Coalescence of two equal-sized deformable drops in an axisymmetric flow. *Phys. Fluids*, 19(10):102102, 2007.

[31] JM Frostad, J Walter, and LG Leal. A scaling relation for the capillary-pressure driven drainage of thin films. *Phys. Fluids*, 25(5):052108, 2013.

[32] P. G. De Gennes. Wetting: statics and dynamics. *Rev. Mod. Phys.*, 57(3):827, 1985.

[33] G. F. Teletzke, H. T. Davis, and L.E. Scriven. How liquids spread on solids. *Chem. Eng. Comm.*, 55(1-6):41–82, 1987.

[34] Ying-Chih Liao, Elias I Franses, and Osman A Basaran. Deformation and breakup of a stretching liquid bridge covered with an insoluble surfactant monolayer. *Phys. Fluids*, 18(2):022101, 2006.

[35] HA Stone. A simple derivation of the time-dependent convective-diffusion equation for surfactant transport along a deforming interface. *Phys. Fluids A: Fluid Dynamics*, 2(1):111–112, 1990.

[36] Orlin D Velev, Theodor D Gurkov, and Rajendra P Borwankar. Spontaneous cyclic dimpling in emulsion films due to surfactant mass transfer between the phases. *J. Col. Int. Sci.*, 159(2):497–501, 1993.

[37] Krassimir D Danov, Theodor D Gurkov, Tatyana Dimitrova, Ivan B Ivanov, and Daniel Smith. Hydrodynamic theory for spontaneously growing dimple in emulsion films with surfactant mass transfer. *J. Col. Int. Sci.*, 188(2):313–324, 1997.

[38] Xiaoguang Zhang, Osman A Basaran, and Robart M Wham. Theoretical prediction of electric field-enhanced coalescence of spherical drops. *AIChE Journal*, 41(7):1629–1639, 1995.

[39] WD Ristenpart, JC Bird, A Belmonte, F Dollar, and HA Stone. Non-coalescence of oppositely charged drops. *Nature*, 461(7262):377, 2009.

[40] KJ Ptasinski and PJAM Kerkhof. Electric field driven separations: phenomena and applications. *Separation science and technology*, 27(8-9):995–1021, 1992.

[41] Robert T Collins, Jeremy J Jones, Michael T Harris, and Osman A Basaran. Electrohydrodynamic tip streaming and emission of charged drops from liquid cones. *Nature Physics*, 4(2):149–154, 2008.

[42] R. T. Collins, K. Sambath, M. T. Harris, and O. A. Basaran. Universal scaling laws for the disintegration of electrified drops. *Proc. Nat. Acad. Sci. USA*, 110(13):4905–4910, 2013.

APPENDICES

A. STEP CHANGE IN INTACT JET LENGTH FOR LOW VISCOSITY LIQUIDS

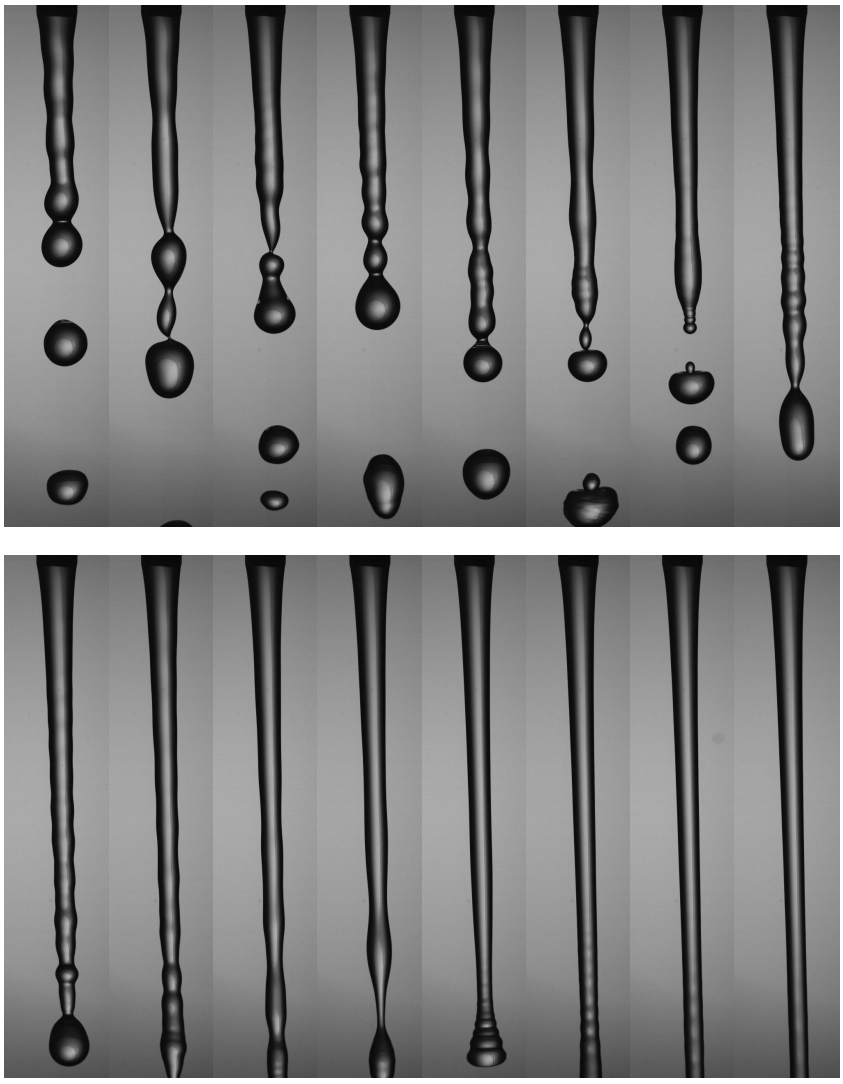

Figure A.1. Experimental images of jetting of DI water from a nozzle of diameter 2.31 mm at a flowrate of 78.5 mL/min. The interval between two timeframes is 22.3 ms. The intact length of the jet undergoes a step change at a Weber number of $We = 1.56$, with the length of the intact jet increasing by as much as 50 times. These images were taken with a Phantom V310 camera at 10000 fps.

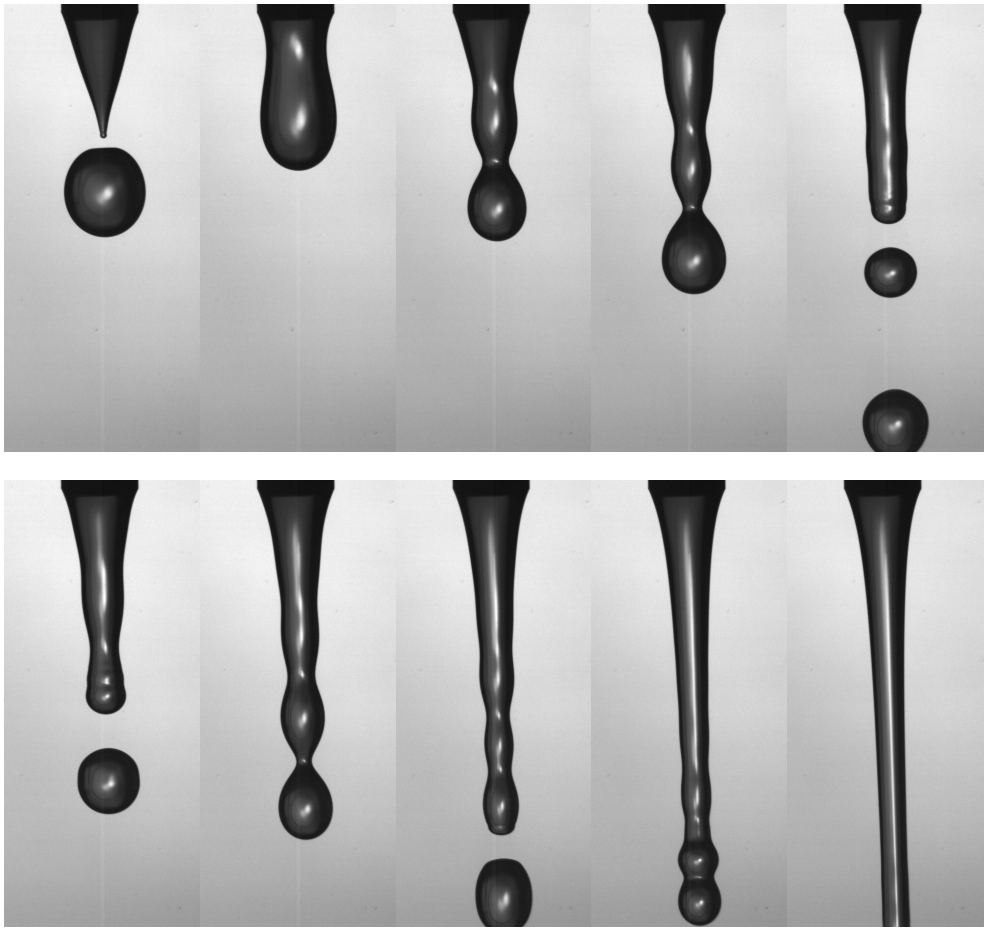

Figure A.2. Experimental images of jetting of a 1% by volume solution of a surfactant laden liquid in DI water from a nozzle of diameter 2.31 mm at a flowrate of 23.5 mL/min. The interval between two timeframes is 59.6 ms. The surface tension of the solution is 28.95 mN/m, while other liquid properties are equal to those of pure water. The intact length of the jet undergoes a step change at $We = 0.34$, a value much lower than that seen for water above. Simulations can provide insight into the role played by surfactants in reducing the critical Weber number at which this step change is observed. These images were taken with a Phanton V310 camera at 8000 fps.

B. FLOW-INDUCED COALESCENCE OF BUBBLES IMMERSED IN A POWER-LAW FLUID

In this appendix, the flow-induced collision and coalescence of two equal sized bubbles immersed in a Newtonian or power-law liquid is described. The size distribution of bubbles in bubble columns is constantly changing due to collision and coalescence of bubbles [1]. The rate of bubble coalescence determines if an aqueous foam can be considered "stable" over the desired timeframe [2], and plays a crucial role in determining the bubble size distribution for deep-water gas/oil spills [3]. The velocity at which two bubbles approach each other is an important parameter in deciding if the collision of the bubbles eventually leads to coalescence [1,4]. Previous works have determined analytically [5], or observed experimentally [4,6], an approximate value of a critical Weber number $We \equiv \rho V^2 R/\sigma$, where ρ is the density of the outer liquid, V is the approach velocity of the two bubbles of radius R, and σ is the surface tension of the gas-liquid interface, above which bubble collision if followed by a rebound, and no coalescence.

B.1 Macroscopic behavior of flow-induced collision of bubbles

Here, we investigate the coalescence dynamics of two equal sized bubbles induced by a compressional flow similar to that generated by a four-roll Taylor mill [7] in a micro-gravity environment, such that buoyancy effects can be neglected. The problem setup is identical to that described in chapter 6, with the "drop" fluid now being treated as an incompressible, isothermal gas with the properties of air at room temperature. The dimensionless problem variables specified in this appendix were

non-dimensionalized using the characteristic scales in chapter 6. It is observed that the critical Weber number of approach We_c above which bubbles rebound and never coalesce is proportional to the square of the viscosity ratio m_2, or $We_c = U_c^2 \propto m_2^2$.

B.2 Self-similarity during rupture of the thin film between coalescing bubbles

For bubbles that approach each other with a vleocity $U_\infty < U_c$ for a given viscosity ratio m_2, the bubbles coalesce on first approach. As the separation between the bubble interfaces falls below a few hundred nanometers, van der Waals forces of attraction between the two bubbles causes rupture of the thin liquid film [8]. The dynamics resemble those of axisymmetric or point rupture of a free film [9–11], and are thus expected to be self-similar during the final stages of coalescence. The related problem of self-similarity during attachment of a bubble to a solid wall was explored in chapter 5. Figures B.6 −B.8 demonstrate self-similarity during coalescence of two air bubbles in a moderately viscous Newtonian or power-law liquid of power-law exponent n. The scaling exponents observed are in excellent agreement with expected values for point rupture of a free film of power-law fluid of corresponding value of n and $Oh \sim O(1)$ (refer to figure 3.11 and Thete et al. [10]). Film Oh numbers are typically $10^{3/2}$ times the Oh number values for our system, as radius of the bubble R is used as the characteristic length here, as opposed to initial film thickness h_0 used in thin film studies. For typical values, $h_0/R \sim 10^{-3}$. The dimensionless time to coalescence is denoted by $\tau \equiv t_c - t$, where t_c is the time instant at which the film of outer liquid between the bubbles ruptures and the interfaces make contact.

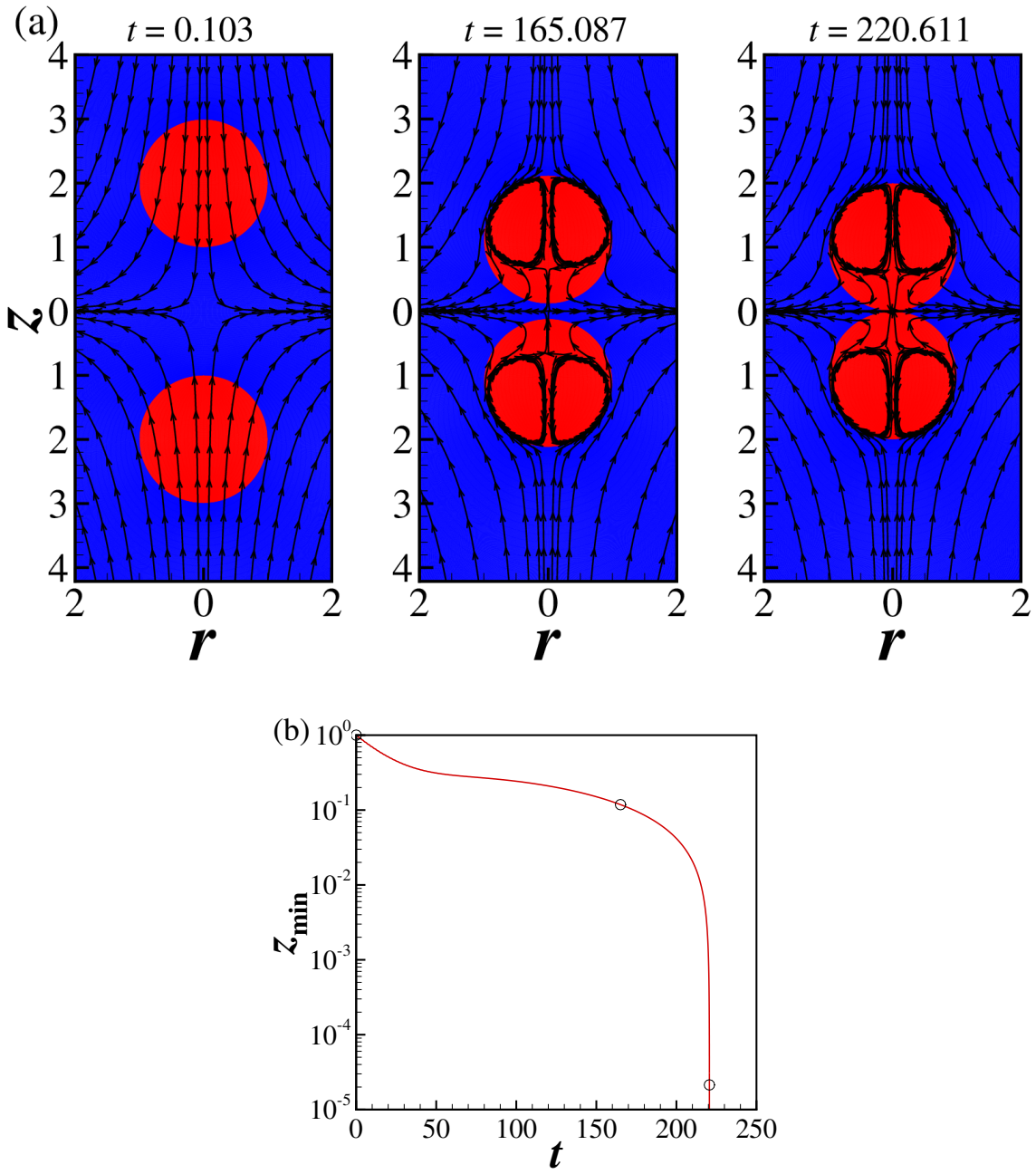

Figure B.1. (a) Shapes and positions of two equal sized air bubbles approaching each other in water such that parameter values are $Oh = 3.736 \times 10^{-3}$, $m_2 = 10^3$, $d_2 = 10^3$, $U_\infty = 0.018$, and $A^* = 7.37 \times 10^{-13}$. (b) Evolution of half the minimum axial separation between the bubbles z_{min} with time t. The symbols denote the time instants at which the shapes and positions are shown in (a). The bubbles coalesce on first approach without any occurence of rebound.

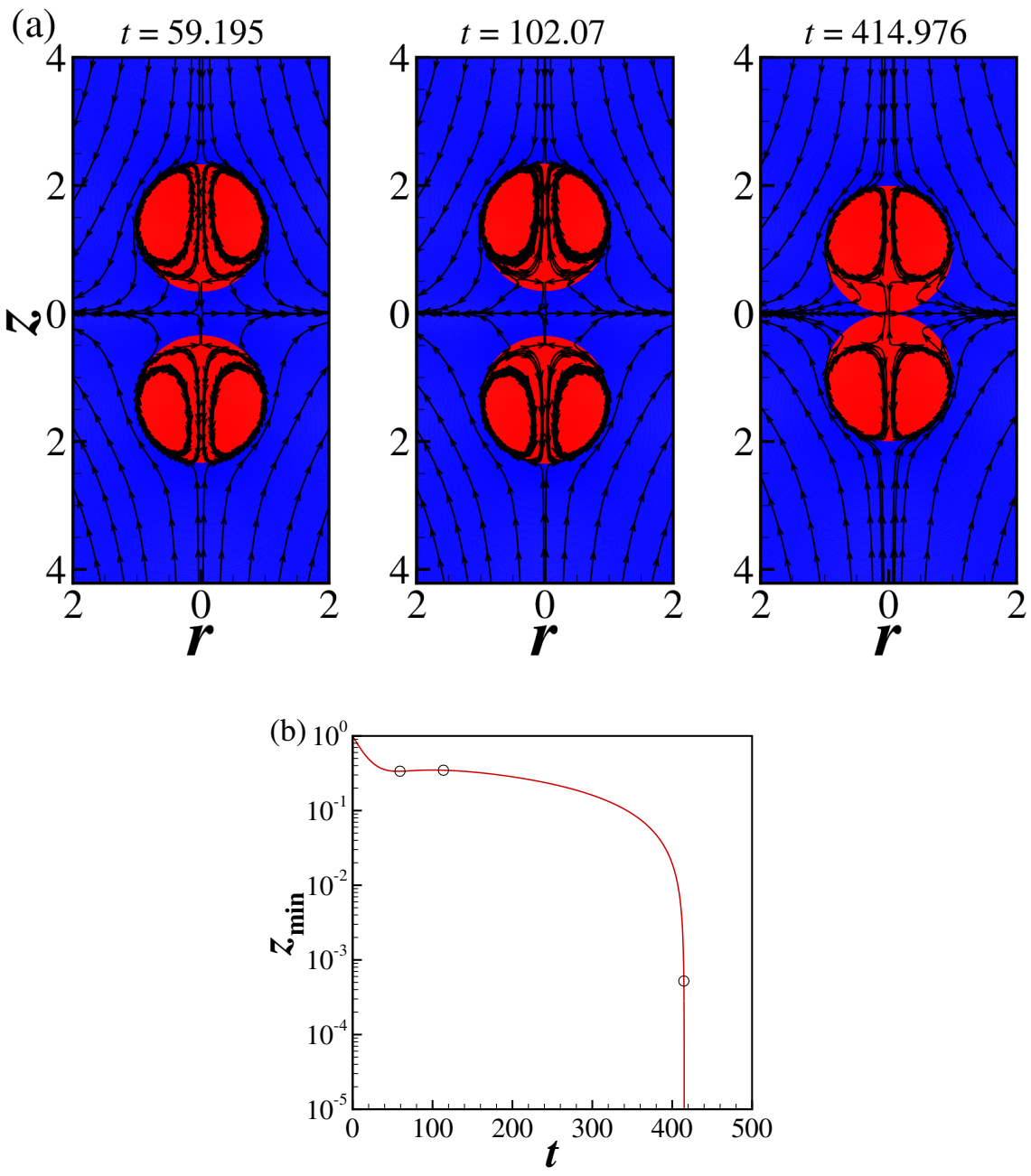

Figure B.2. Parameter values are identical to figure B.2 except $U_\infty = 0.020$. The bubbles rebound between the first two time instants shown, before coalescing on second approach. Larger values of U_∞ lead to rebound without coalescence. Hence, this is the critical value of $U_\infty = U_c = 0.020$.

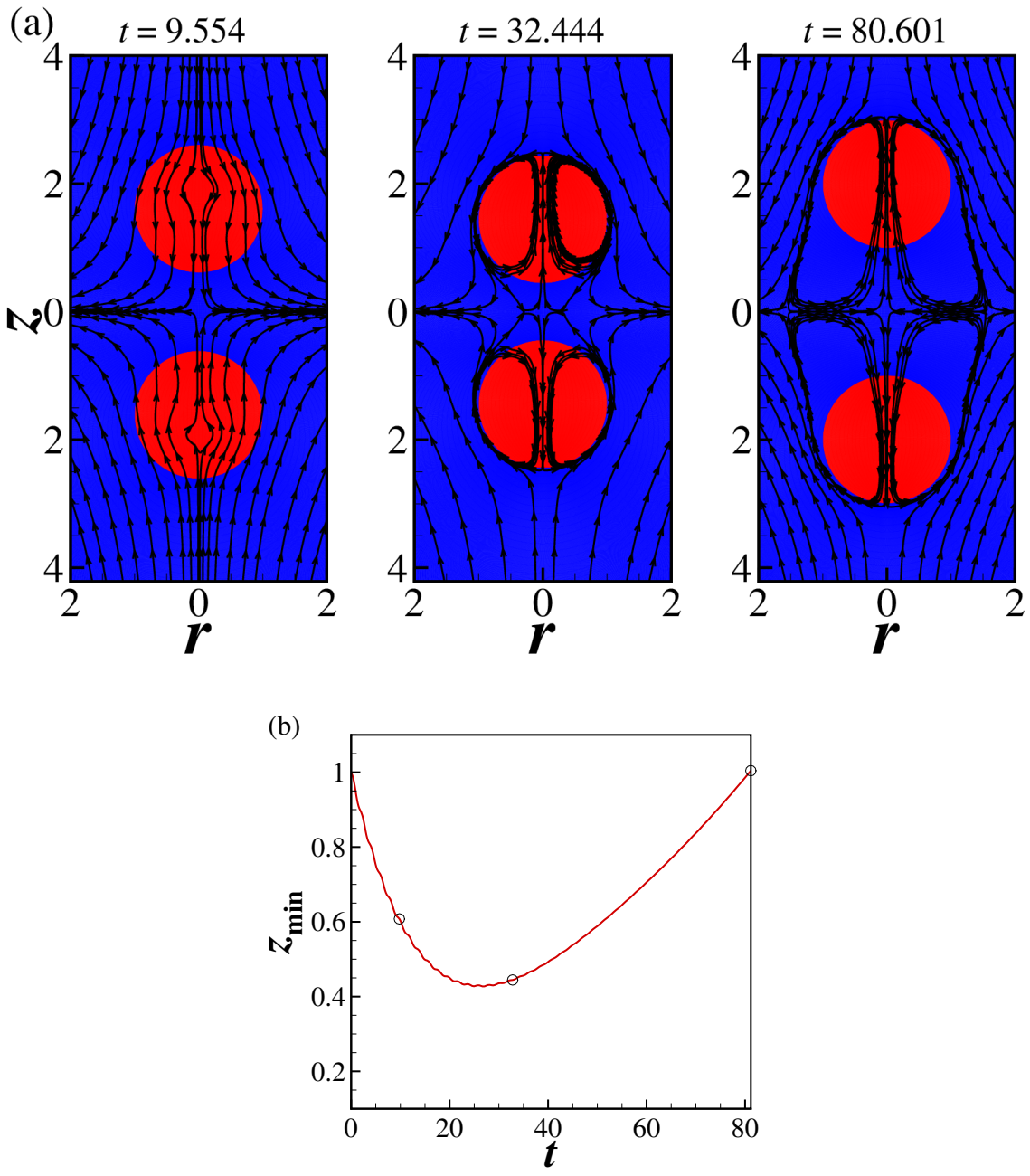

Figure B.3. Parameter values are identical to figure B.2 except $U_\infty = 0.028$. The bubbles rebound and separate from each other, with the circular flow that develops between the bubbles driving them away further than their initial separation.

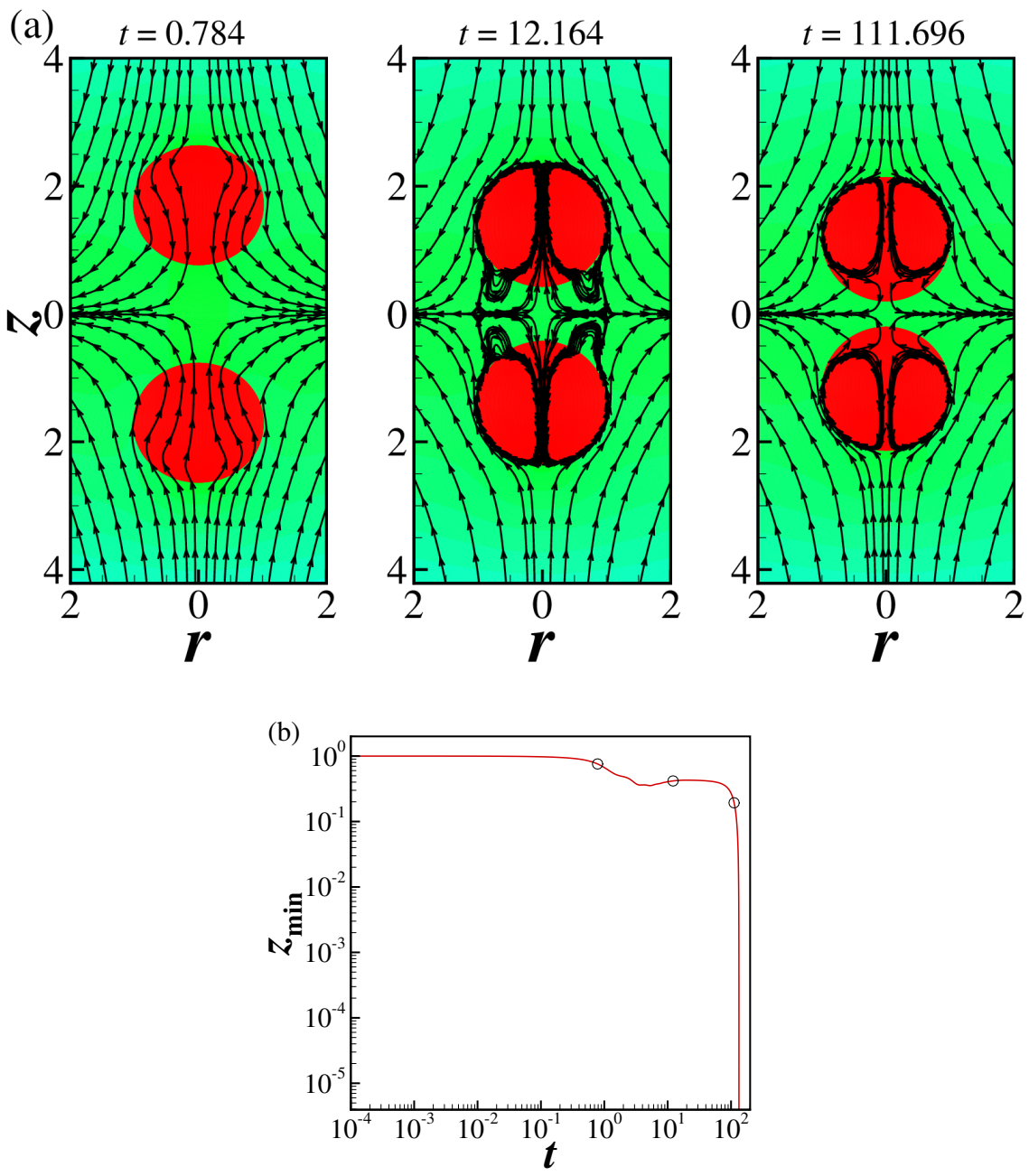

Figure B.4. (a) Shapes and positions of two equal sized air bubbles approaching each other in a viscous liquid such that parameter values are $Oh = 3.736 \times 10^{-2}$, $m_2 = 10^4$, $d_2 = 10^3$, $U_\infty = 0.223$, and $A^* = 7.37 \times 10^{-13}$. (b) Evolution of half the minimum axial separation between the bubbles z_{min} with time t. The bubbles rebound and coalesce on second approach only for this large approach velocity, which is approximately 10 times the critical velocity determined for water in figure B.2.

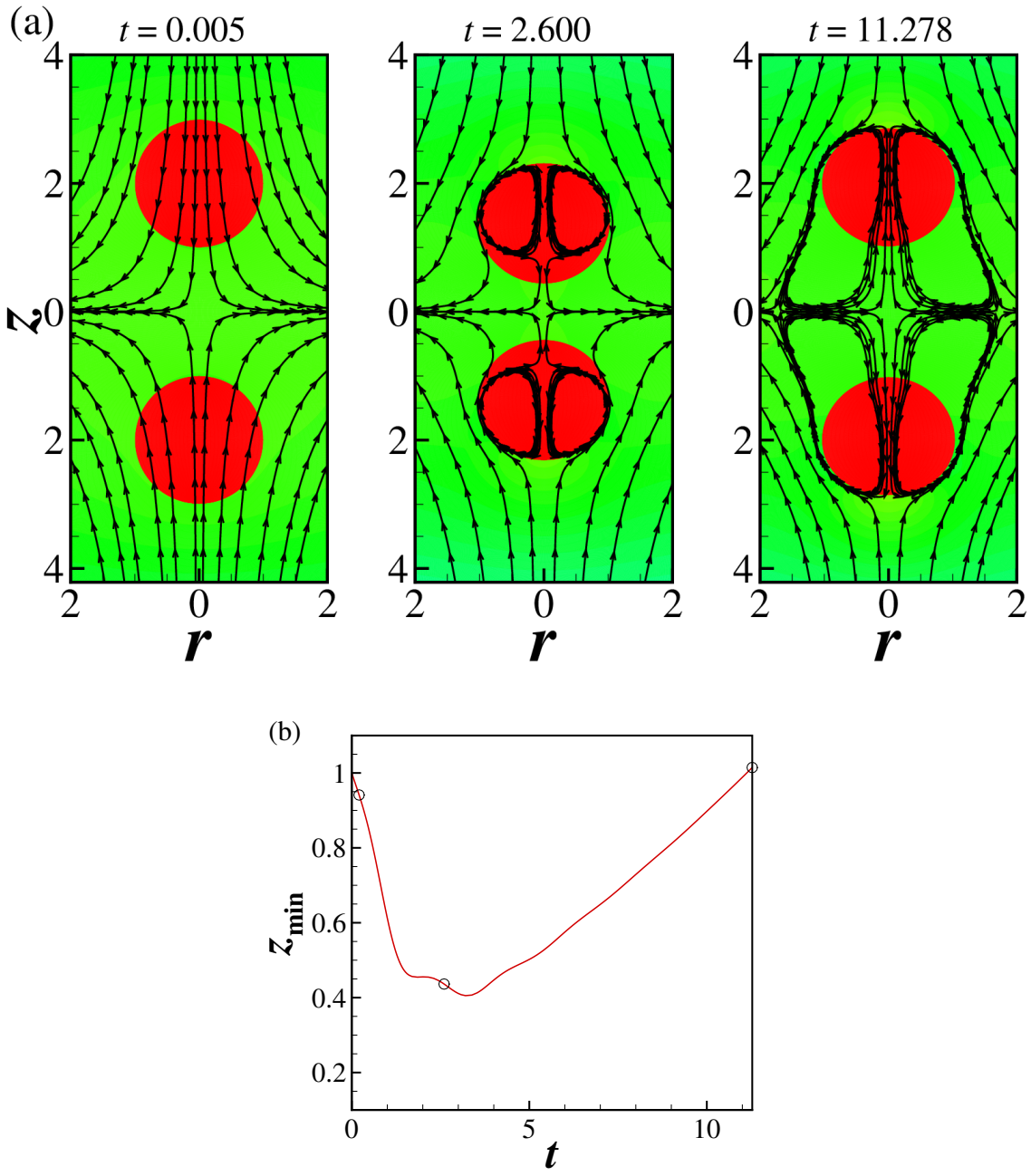

Figure B.5. Parameter values are identical to figure B.4 except $U_\infty = 0.279$. The bubbles rebound and do not coalesce, as the velocity of approach is again higher than U_c for this viscous liquid. Note the deformation of the bubbles as a result of the large velocities and viscosity of the outer liquid. The approach velocity here is 13.95 times the critical velocity determined for water.

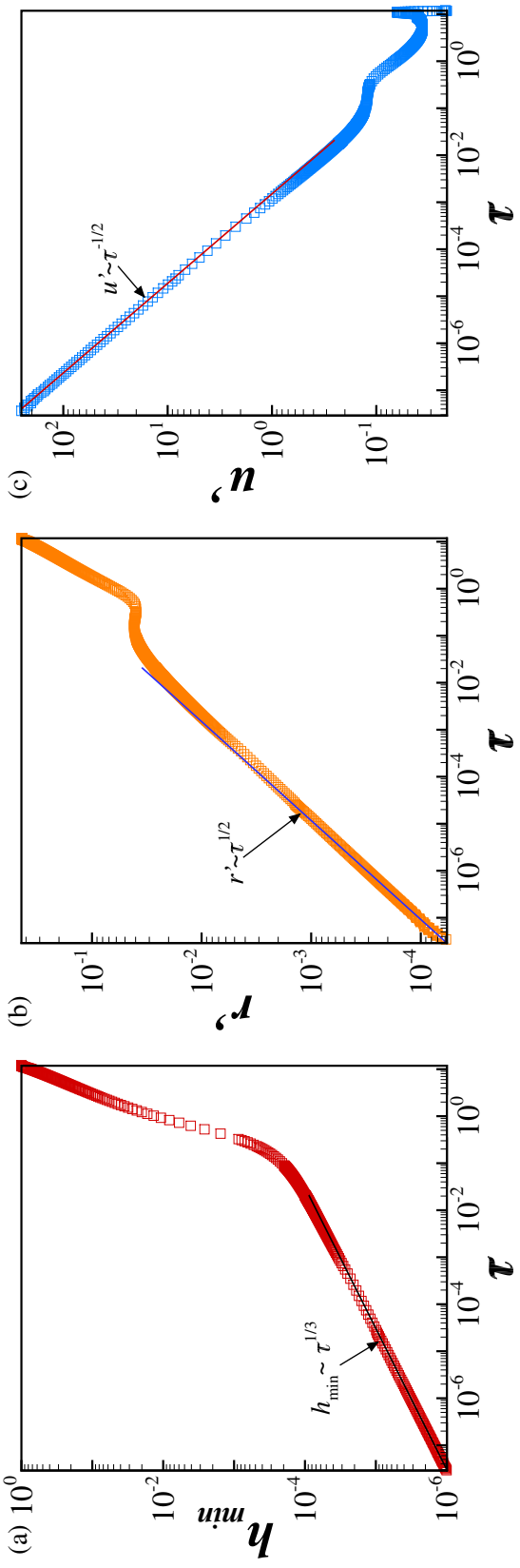

Figure B.6. Scaling behavior for variables during flow-induced coalescence of air bubbles in a Newtonian liquid. Variation with time to coalescence τ of (a) half the minimum axial separation between the bubbles h_{min}, (b) radial length scale r', evaluated at a radial location where half the axial separation between the bubbles is given by $h = 1.05h_{min}$ and (c) radial velocity u' evaluated at the same radial location as that for r'. Simulation results are shown by the data points while the straight lines represent best fit to the data. The inertial-viscous scaling regime for Newtonian free-films [9] is observed here. The parameter values are $Oh = 0.02$, $m_2 = 10^3$, $d_2 = 10^3$, $U_\infty = 0.095$, $A^* = 4.99 \times 10^{-11}$, and $n = 1$.

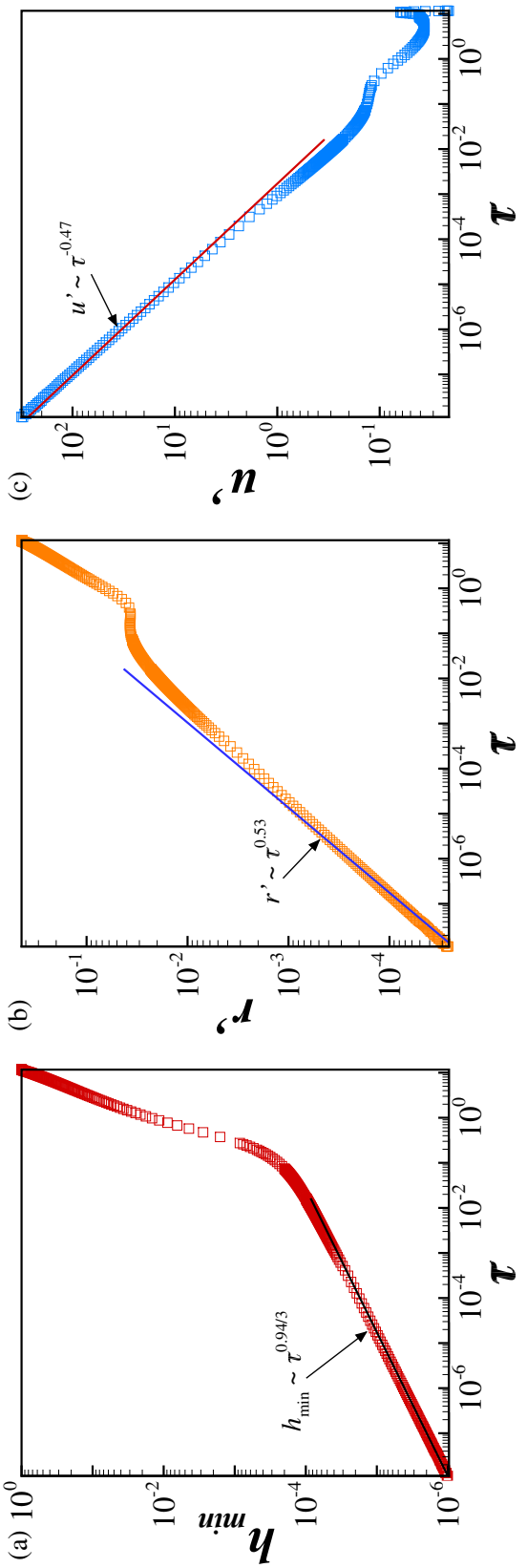

Figure B.7. Scaling behavior for variables for flow-induced coalescence in a power-law liquid with high n. The power-law inertial-viscous scaling regime for power-law free-films [10] is observed here. The parameter values are $Oh = 0.02$, $m_2 = 10^3$, $d_2 = 10^3$, $U_\infty = 0.095$, and $A^* = 4.99 \times 10^{-11}$ and $n = 0.94$.

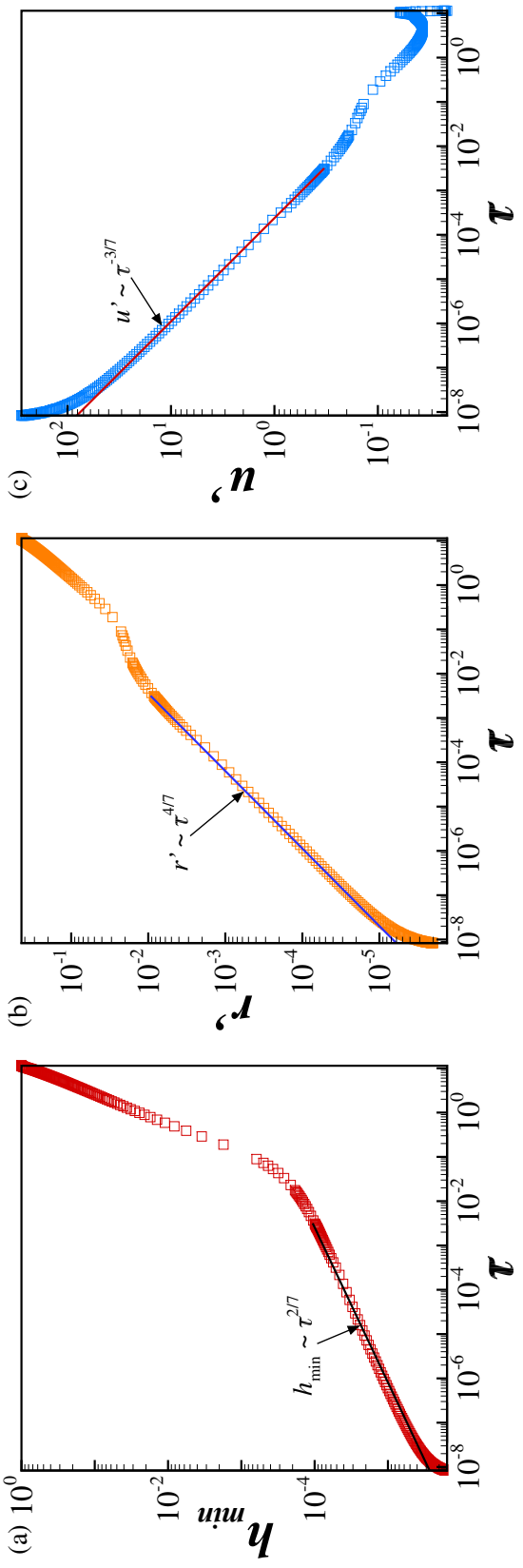

Figure B.8. Scaling behavior for variables for flow-induced coalescence in a power-law liquid with low n. The inertial scaling regime for power-law free-films [10] is observed here. The parameter values are $Oh = 0.02$, $m_2 = 10^3$, $d_2 = 10^3$, $U_\infty = 0.095$, and $A^* = 4.99 \times 10^{-11}$ and $n = 0.60$.

B.3 List of References

[1] RD Kirkpatrick and MJ Lockett. The influence of approach velocity on bubble coalescence. *Chemical Engineering Science*, 29(12):2363–2373, 1974.

[2] S. Cohen-Addad, R. Höhler, and O. Pitois. Flow in foams and flowing foams. *Ann. Rev. Fluid Mech.*, 45(1):241, 2013.

[3] Uditha C Bandara and Poojitha D Yapa. Bubble sizes, breakup, and coalescence in deepwater gas/oil plumes. *Journal of Hydraulic Engineering*, 137(7):729–738, 2011.

[4] PC Duineveld. Bouncing and coalescence of bubble pairs rising at high reynolds number in pure water or aqueous surfactant solutions. In *In Fascination of Fluid Dynamics*, pages 409–439. Springer, 1998.

[5] AK Chesters and G Hofman. Bubble coalescence in pure liquids. In *Mechanics and Physics of Bubbles in Liquids*, pages 353–361. Springer, 1982.

[6] Toshiyuki Sanada, Masao Watanabe, and Tohru Fukano. Effects of viscosity on coalescence of a bubble upon impact with a free surface. *Chemical Engineering Science*, 60(19):5372–5384, 2005.

[7] GI Taylor. The formation of emulsions in definable fields of flow. *Proceedings of the Royal Society of London. Series A*, 146(858):501–523, 1934.

[8] Timothy O Oolman and Harvey W Blanch. Bubble coalescence in stagnant liquids. *Chemical Engineering Communications*, 43(4-6):237–261, 1986.

[9] D. Vaynblat, J. R. Lister, and T. P. Witelski. Rupture of thin viscous films by van der Waals forces: Evolution and self-similarity. *Phys. Fluids*, 13(5):1130–1140, 2001.

[10] S. S. Thete, C. Anthony, O. A. Basaran, and P. Doshi. Self-similar rupture of thin free films of power-law fluids. *Phys. Rev. E*, 92(2):023014, 2015.

[11] S. S. Thete, C. Anthony, P. Doshi, M. T. Harris, and O. A. Basaran. Self-similarity and scaling transitions during rupture of thin free films of Newtonian fluids. *Phys. Fluids*, 28(9):092101, 2016.

C. NOTES ON THINNING AND RUPTURE OF FREE FILMS OF POWER-LAW LIQUIDS

C.1 Sheet rupture due to finite amplitude perturbations

Spontaneous sheet rupture due to van der Waals forces is a long-wavelength problem, as the wavelength of the sinusoidal perturbation required in order to observed spontaeous thinning and rupture is much larger than its initial thickness. For a sheet of initial thickness $2h_0$ and lateral extent λ, if a perturbation is applied to the surface of the film such that its the surface profile is described by

$$\tilde{h}(\tilde{z},0) = h_0\left[1-\chi\cos\left(\frac{2\pi\tilde{z}}{\lambda}\right)\right] \tag{C.1}$$

spontaneous rupture occurs if the extent of the film λ is greater than $\lambda_c = 8h_0^2\sqrt{\pi^3\sigma/A_H}$, for a film with constant surfact tension σ and Hamaker constant A_H. As the initial aspect ratio $\varepsilon = h_0/L \ll 1$, the long-wavelength approximation can be applied to the initial stages of thinning. If $\tilde{h}(\tilde{t})$ and $\tilde{l}(\tilde{t})$ denote the film thickness and lateral length scale at time $\tilde{t}$, we can define the film aspect ratio at this time, which is given by $\varepsilon(\tilde{t}) = \tilde{h}(\tilde{t})/\tilde{l}(\tilde{t})$, and its variation with time is given by

$$\varepsilon(\tilde{t}) = \frac{h_0}{l_c}\tau^{\alpha-\beta} = \frac{h_0}{l_c}\left[\frac{\tilde{h}_{min}(\tilde{t})}{h_0}\right]^{1-\beta/\alpha} \tag{C.2}$$

where $l_c \equiv \left(48\pi h_0^4\sigma/A_H\right)^{1/2} \equiv \sqrt{2}\pi\lambda_c$ is the characteristic length in the lateral direction and α and β are scaling exponents for the film thickness and lateral lengthscale respectively. For all regimes explored in chapter 3, $\beta > \alpha$, and thus the aspect ratio is always increasing as the film thins or $\tau \to 0$. Equation (C.2) can be rewritten as

$$\varepsilon(\tilde{t}) = \frac{d}{\sqrt{24}h_0}\left[\frac{\tilde{h}_{min}(\tilde{t})}{h_0}\right]^{1-\beta/\alpha} \tag{C.3}$$

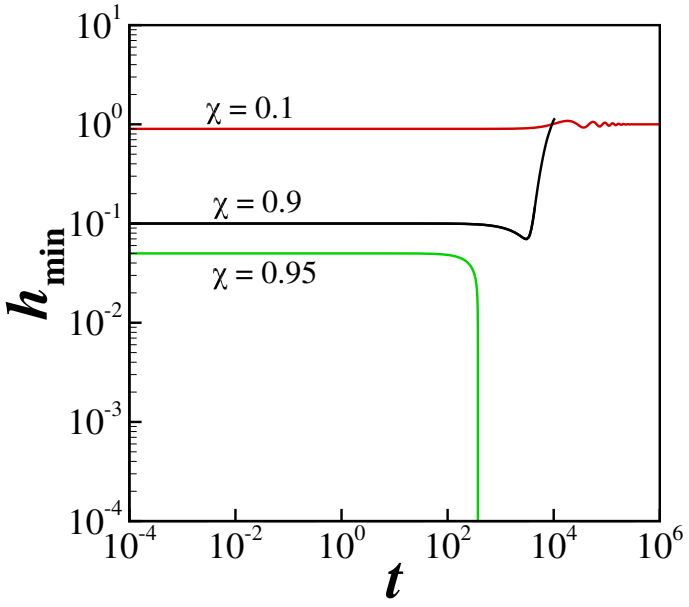

Figure C.1. Variation with time of minimum film thickness h_{min} for thinning of a sheet such that $Oh = 0.085$, $A = 9.21 \times 10^{-8}$, $m = 1/A$, and $n = 0.6$ for different amplitudes of perurbation χ. The lateral extent of the sheet is $\lambda = \lambda_c/25$.

where $d \equiv \sqrt{(A_H/2\pi\sigma)^{1/2}}$ is the molecular lengthscale. The aspect ratio becomes $O(1)$ when

$$\tilde{h}_{min}/d = (1/\sqrt{24})^{1/(\beta/\alpha-1)} \left[\frac{d}{h_0}\right]^{1/(\beta/\alpha-1)-1} \tag{C.4}$$

For the inertial-capillary regime, $\beta = 2\alpha = 4/7$ and hence, the aspect ratio becomes $O(1)$ when $\tilde{h}_{min}/d = 1/\sqrt{24}$. This means that slenderness of the film breaks down long after the minimum film thickness has fallen below the molecular lengthscale, or in other words, after the continuum approximation breaks down. Thus, the long-wavelength approximation is always valid for spontaneous rupture of sheets.

In many natural and industrial situations, the film might experience perturbations of finite amplitudes [1–3]. In such cases, the film might rupture even if its lateral extent is lesser than the critical wavelength required for spontaneous rupture, similar to breakup of an invisicid fluid region observed by Burton and Taborek [4]. Figure C.1 shows the variation with time of the minimum film thickness h_{min} for three

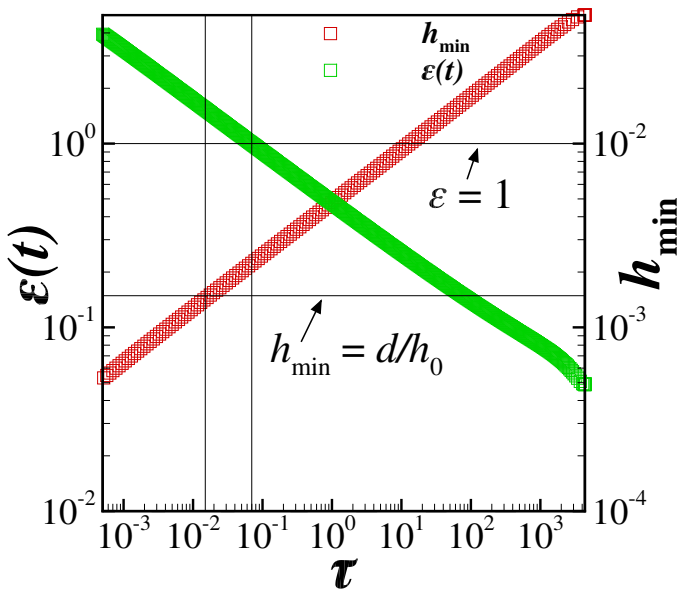

Figure C.2. Variation with time to rupture τ of the sheet aspect ratio $\varepsilon(t)$ and minimum film thickness h_{min} for thinning of a sheet such that $Oh = 0.085$, $A = 9.21 \times 10^{-8}$, $m = 1/A$, and $n = 0.6$. The aspect ratio becomes 1 before h_{min} reaches the molecular lengthscale d/h_0, signifiying that slenderness breaks down before the continuum limit is reached. The lateral extent of the sheet is $\lambda = \lambda_c/25$ while an initial perturbation of amplitude $\chi = 0.95$ is applied to its surface.

values of perturbation χ for a sheet of power-law liquid with parameter values $Oh = 0.085, A^* = 9.21 \times 10^{-8}, m = 1/A$ and $n = 0.6$. The non-dimensionalization and characteristic scales are specified in chapter 3. The lateral extent of the film for all three cases is $\lambda = \lambda_c/25$ which means the film cannot rupture spontaneously due to van der Waals forces. Figure C.1 shows that the film stabilizes and returns to its original unperturbed state of $h(t) = 1$ for both $\chi = 0.1$ and $\chi = 0.9$. However, for an even larger amplitude of $\chi = 0.95$, van der Waals forces dominate over surface tension to cause eventual rupture. In this case, the lengthscale of the film is defined by $l_c = \lambda_c/25$, and the variation with time of its aspect ratio is given by

$$\varepsilon(\tilde{t}) = \frac{h_0}{\lambda_c/25}\tau^{\alpha-\beta} = \frac{25d}{\sqrt{48\pi^2 h_0}}\left[\frac{\tilde{h}_{min}(\tilde{t})}{h_0}\right]^{1-\beta/\alpha} \tag{C.5}$$

Again, for the inertial-capillary regime, when $\beta = 2\alpha$, the aspect ratio is $O(1)$ when

$$\frac{\tilde{h}_{min}}{d} = \frac{25}{\sqrt{48\pi^2}} > 1 \tag{C.6}$$

Thus, for finite amplitude perturbations, the long-wavelength approximation can break down before the continuum limit is reached, in which case the system of transient two-dimensional partial differential equations will have to be solved for thinning of sheets. Figure C.2 shows the variation with time remaining to rupture τ of the aspect ratio $\varepsilon(t)$ and minimum film thickness h_{min}, and makes plain that $\varepsilon(t)$ becomes $O(1)$ before $h_{min} = d/h_0$, or before the continuum limit is reached. Figure C.3 shows that the variation with τ of h_{min}, lateral length scale z' and lateral velocity v' is in excellent agreement with the expected inertial-capillary regime for this case.

C.2 Relations between series coefficients of scaling functions

In chapter 3 solutions of the self-similar spatially one dimensional ordinary differential equations (ODEs) for thinning and rupture of power-law fluids in the Stokes limit are obtained. The set of self-similar ODEs are given by

$$-\frac{n}{3}H + \beta\xi\frac{dH}{d\xi} + \frac{d\left(HV\right)}{d\xi} = 0 \tag{C.7}$$

$$\frac{3}{H^4}\frac{dH}{d\xi} + \frac{4}{H}\frac{d}{d\xi}\left[\left|2m_1\frac{dV}{d\xi}\right|^{n-1} H\frac{dV}{d\xi}\right] = 0 \tag{C.8}$$

where β is the scaling exponent for the lateral length scale, ξ is a similarity varibale, H and V are the scaling functions for the film thickness and lateral velocity respectively, n is the power-law index for the fluid and m_1 is the characteristic deformation rate for the fluid. The scaling functions are subsequently expanded in a Taylor series about $\xi = \xi_0$ such that they are given by

$$H\left(\xi - \xi_0\right) = \sum_{k=0}^{\infty} H_k \left(\xi - \xi_0\right)^k \tag{C.9}$$

$$V\left(\xi - \xi_0\right) = \sum_{k=0}^{\infty} V_k \left(\xi - \xi_0\right)^k \tag{C.10}$$

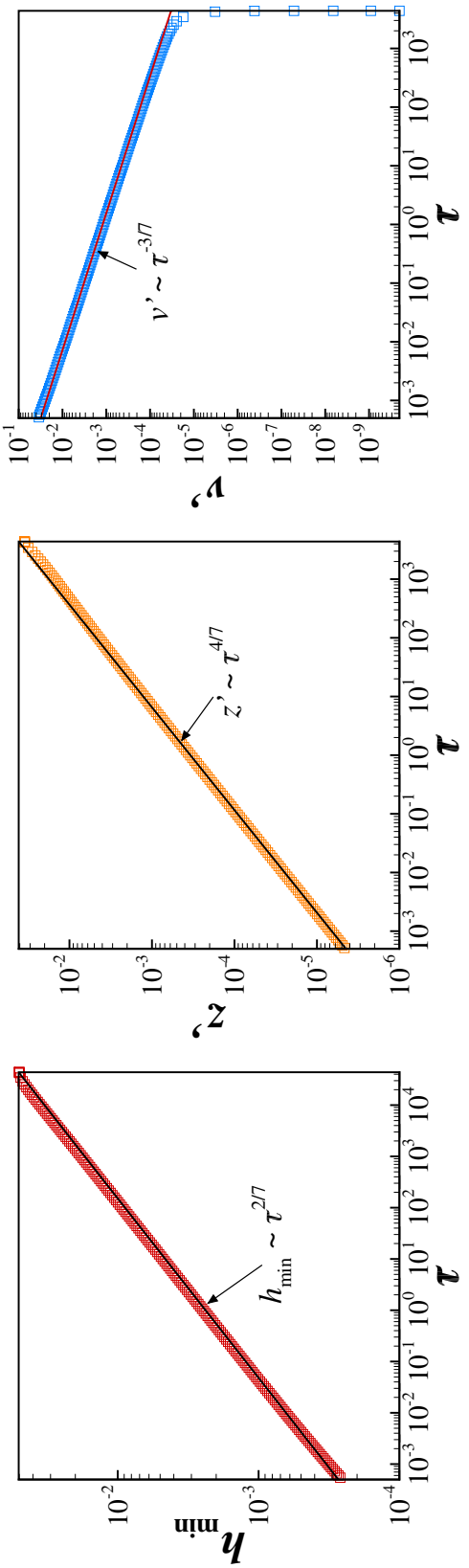

Figure C.3. Scaling behavior of variables in the rupture zone during thinning of a sheet such that $Oh = 0.085, A = 9.21 \times 10^{-8}$, $m = 1/A$, and $n = 0.6$. The variation with time to rupture τ for (a) minimum film thickness h_{min}, (b) lateral length scale z', evaluated at a lateral location where the film thickness is given by $h = 1.05 h_{min}$ and (c) lateral velocity v' evaluated at the same lateral location as that for z'. Simulation results are shown by the data points while the straight lines represent best fit to the data. The lateral extent of the sheet is $\lambda = \lambda_c/25$ while an initial perturbation of amplitude $\chi = 0.95$ is applied to its surface.

By substituting these expansions into the self-similar ODEs (C.7) and (C.8) the following recursion relations are obtained between series coefficients for H and V

$$\left[(k+1)H_0\right]V_{k+1} + \left[k\left(\frac{n}{3}+\beta\right)\right]H_k = Q_{k+1} \tag{C.11}$$

$$\left[4\theta nk(k+1)H_0^4\right]V_{k+1} + \left[3+\frac{4\theta n}{3}H_0^3\right]kH_k = R_k \tag{C.12}$$

where Q_{k+1} and R_k are functions of β, H_{k-1}, V_k, and other lower order coefficients, given by

$$Q_{k+1} = \begin{cases} 0, & \text{for} \quad k=1 \\ -(k+1)\sum_{i=2}^{k} V_i H_{k-i+1}, & \text{for} \quad k \geq 2 \end{cases}$$

and

$$R_{k+1} = \begin{cases} 0, & \text{for} \quad k=1 \\ R_k\left(H_i^a H_j^b, \beta\right), & \text{for} \quad k \geq 2 \end{cases}$$

such that $ai+bj = k, i, j \neq 0$ and $i, j \leq k$. For higher order coefficients to be non-zero, the following condition must hold for some $k = j$

$$H_0 = \left(\frac{9}{n\theta(4nj+12\beta j-4)}\right)^{1/3} \tag{C.13}$$

where $\theta = (2m_1 n/3)^{n-1}$. Thus, we have

$$H_1 = H_2 = \cdots = H_{j-1} = 0, H_j \neq 0 \tag{C.14}$$

$$V_0 = -\beta\xi_0, V_1 = n/3, V_2 = V_3 = \cdots = V_j = 0 \tag{C.15}$$

and, finally

$$V_{j+1} = -jH_j\left[\frac{\beta+n/3}{(j+1)H_0}\right] \tag{C.16}$$

The expansions for the scaling functions can now be given by

$$H\left(\xi-\xi_0\right) = H_0 + \sum_{k=0}^{\infty} H_{j+k}\left(\xi-\xi_0\right)^{j+k} \tag{C.17}$$

$$V\left(\xi-\xi_0\right) = V_0 + V_1\left(\xi-\xi_0\right) + \sum_{k=0}^{\infty} V_{m+k+1}\left(\xi-\xi_0\right)^{m+k+1} \tag{C.18}$$

Using the recursion relation (C.11), it can be seen for $k = j + 1$,

$$[(j+2)H_0]\,V_{j+2} + \left[(j+1)\left(\frac{n}{3}+\beta\right)\right] H_{j+1} = -(j+2)\,[V_2 H_j + V_3 H_{j-1} + \cdots + V_{j+1} H_1] \tag{C.19}$$

However, from equations (C.14) and (C.15), we know that the right hand side of this equations is zero, thus

$$[(j+2)H_0]\,V_{j+2} + \left[(j+1)\left(\frac{n}{3}+\beta\right)\right] H_{j+1} = 0 \tag{C.20}$$

A solution to this equation is given by

$$H_{j+1} = V_{j+2} = 0 \tag{C.21}$$

Next, we seek a solution for when $k = j + 2$,

$$[(j+3)H_0]\,V_{j+3} + \left[(j+2)\left(\frac{n}{3}+\beta\right)\right] H_{j+2} = -(j+3)\,[V_2 H_{j+1} + V_3 H_{j-1} + \cdots + V_{j+2} H_1] \tag{C.22}$$

Again, the right hand side of this equation reduces to zero, by substituting in equations (C.14 - C.15) and (C.21). Thus, we obtain

$$H_{j+2} = V_{j+3} = 0 \tag{C.23}$$

Similarly, the values of successive coefficients can be shown to also be zero

$$H_{j+1} = H_{j+2} = \cdots = H_{2j-1} = 0 \tag{C.24}$$

$$V_{j+2} = V_{j+3} = \cdots = V_{2j} = 0 \tag{C.25}$$

However, when $k = 2j$

$$\begin{aligned}[(2j+1)H_0]\,V_{2j+1} \;=\; & -\left[2j\left(\frac{n}{3}+\beta\right)\right] H_{2j} - (2j+1)[V_2 H_{2j-1} + V_3 H_{2j-2} + \\ & \cdots + V_{j+1} H_j + V_{j+2} H_{m-1} + \cdots + V_{2j} H_1]\end{aligned} \tag{C.26}$$

which can be simplified to

$$[(2j+1)H_0]\,V_{2j+1} + \left[2j\left(\frac{n}{3}+\beta\right)\right] H_{2j} = -(2j+1)\,[0 + \cdots + V_{j+1} H_j + \cdots + 0] \tag{C.27}$$

And thus,

$$V_{2j+1} = -2jH_{2j}\frac{n/3+\beta}{(2j+1)H_0} - V_{j+1}\frac{H_j}{H_0} \tag{C.28}$$

Now, since $H_j \neq 0$ and $V_{j+1} \neq 0$, it thus follows that $H_{2j} \neq 0$ and $V_{2j+1} \neq 0$. Similarly, one can show that $H_{kj} \neq 0$ and $V_{kj+1} \neq 0$ where k is any positive integer. Thus, the series expansion for the scaling functions reduces to

$$H\left(\xi - \xi_0\right) = \sum_{k=0}^{\infty} H_{jk}\left(\xi - \xi_0\right)^{jk} \tag{C.29}$$

$$V\left(\xi - \xi_0\right) = -\beta\xi_0 + \sum_{k=0}^{\infty} V_{jk+1}\left(\xi - \xi_0\right)^{jk+1} \tag{C.30}$$

C.3 Invariance of self-similar equations to variable transformations

If the variable ξ and scaling function V is transformed such that $\xi \to \phi\xi$ and $V \to \phi\xi$, where ϕ is a non-zero constant, and substituted into the self-similar ODEs (C.7) and (C.8) we get

$$-\frac{n}{3}H + \beta(\phi\xi)\frac{dH}{d(\phi\xi)} + \frac{d\left(H(\phi V)\right)}{d(\phi\xi)} = 0 \tag{C.31}$$

$$\frac{3}{H^4}\frac{dH}{d(\phi\xi)} + \frac{4}{H}\frac{d}{d(\phi\xi)}\left[\left|2m_1\frac{d(\phi V)}{d(\phi\xi)}\right|^{n-1} H\frac{d(\phi V)}{d(\phi\xi)}\right] = 0 \tag{C.32}$$

It is clear that ϕ can be cancelled out of both equations and we recover the original self-similar ODEs (C.7) and (C.8), signifying that the equations are invariant to variable transformations of the type $\xi \to \phi\xi$ and $V \to \phi\xi$. Since the series expansion for H is given by

$$H\left(\xi\right) = H_0 + H_j\left(\xi\right)^j + H_{2j}\left(\xi\right)^{2j} + \ldots \tag{C.33}$$

if $\xi_0 = 0$, we can rearrange terms to get

$$H\left(\xi\right) = H_0 + \frac{H_j}{\phi^j}\left(\phi\xi\right)^j + \frac{H_{2j}}{\phi^{2j}}\left(\phi\xi\right)^{2j} + \ldots \tag{C.34}$$

where ϕ is a non-zero constant. Let us require that $H_j/\phi^j = 1$, which gives us $\phi = H_j^{1/j}$. If we say the solution exists such that $H_j = 1$, then

$$H\left(\xi\right) = H_0 + \left(\xi\right)^j + H_{2j}\left(\xi\right)^{2j} + \ldots \tag{C.35}$$

Let us also say that the solution exists when $H_j = 0.1 = 10^{-1}$, then

$$\begin{aligned} H(\xi) &= H_0 + 10^{-1}(\xi)^j + H_{2j}(\xi)^{2j} + \dots \\ &= H_0 + \left(\frac{\xi}{10^{1/j}}\right)^j + H_{2j}10^2\left(\frac{\xi}{10^{1/j}}\right)^{2j} + \dots \\ &= H_0 + \eta^j + H_{2j}10^2\eta^{2j} + \dots \end{aligned} \tag{C.36}$$

where $\eta = \xi/10^{1/j}$. Since the equations are invariant for $\xi \to \phi\xi$, this proves that the value of H_j has no effect on the similarity solution obtained from solving the ODEs in similarity space and is thus set to be $\phi^{1/m}$ in chapter 3.

C.4 Axisymmetric or point rupture of free films

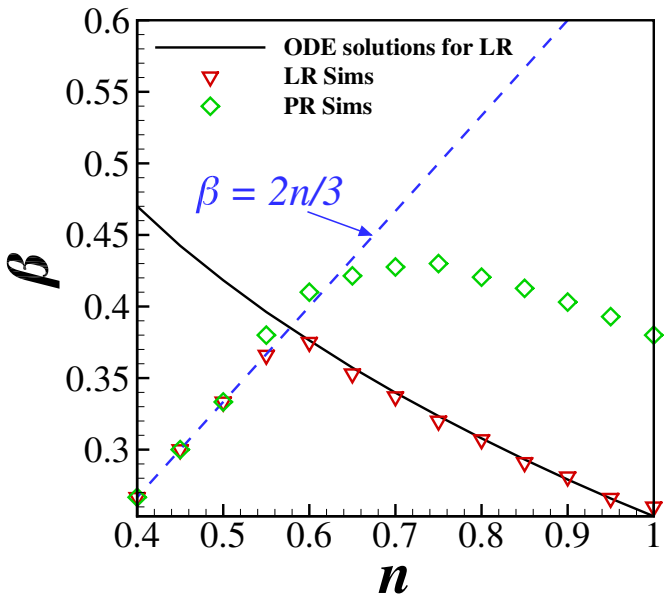

Figure C.4. Variation with power-law exponent n of the scaling exponent for the lateral lengthscale β for thinning and rupture of free films of power-law fluids in the Stokes limit for both two-dimensional line rupture (LR) and three-dimensional axisymmetric or point rupture (PR). The values for β when the film thins in the power-law viscous (PLV) regime are significantly different based on the geometry of the problem but converge to the line $\beta = 2n/3$ when dynamics lie in the power-law capillary viscous (PLCV) regime.

C.5 List of References

[1] Thomas Brooke Benjamin and Fritz Joseph Ursell. The stability of the plane free surface of a liquid in vertical periodic motion. *Proc. R. Soc. Lond. A*, 225(1163):505–515, 1954.

[2] R. V. Craster and O. K. Matar. Dynamics and stability of thin liquid films. *Rev. Mod. Phys.*, 81(3):1131, 2009.

[3] Rabibrata Mukherjee and Ashutosh Sharma. Instability, self-organization and pattern formation in thin soft films. *Soft Matter*, 11(45):8717–8740, 2015.

[4] JC Burton and P Taborek. Two-dimensional inviscid pinch-off: An example of self-similarity of the second kind. *Phys. Fluids*, 19(10):102109, 2007.

VITA

VITA

Vishrut Garg was born in New Delhi, India on October 18, 1991 to parents Cmde P.K. Garg and Dr. Vigya Garg. From the age of one month, his and brother Shreyas' childhood was a myriad of different schools in various towns and cities of India as their father's job in the Indian Navy kept the family on the move. A voracious appetite for books and traveling cultivated by his parents, and an aptitude for science encouraged by his grandfather were the only constants during his schooling years. One of such moves involved a year spent in the Andaman and Nicobar islands during grade X, where he placed first in the state in the national high school examinations, earning a gold medal from the Governor. He joined the Indian Institute of Technology, Bombay (I.I.T. Bombay) in Mumbai, India to pursue a B.Tech. degree in Chemical Engineering. During the summer of 2011, he worked as an intern in the marine engines division of General Electric's John Welch Technology Center in Bengaluru, India. During the summer of 2012, he completed an internship at FMP Technology GmbH, Erlangen, Germany under the supervision of Prof. Franz Durst, where he studied twin-jet fuel injectors. He did his B.Tech honors project with Prof. Sanjay M. Mahajani on underground coal gasification, and graduated from IIT Bombay in 2013.

During the Fall of that year, he began his Ph.D. studies at the Davidson School of Chemical Engineering at Purdue University, joining Prof. Osman Basaran's fluid dynamics research group. Along the course of his Ph.D. he presented research at several meetings for the American Physics Society's Division of Fluid Dynamics as well as meetings of Purdue Process and Safety Assurance Center (P2SAC). During the summer of 2017, Vishrut worked as a graduate intern in the Computational Modeling Center at Air Products and Chemicals, Inc., Allentown, PA, under the supervision of

Dr. George Harriott and Dr. Sanjay Mehta. He has published one paper in a peer-reviewed journal and has four papers under various stages of development. During the later three years of his Ph.D., Vishrut was an active member of the Purdue Cycling Club and Purdue Photography Club, and combined these two hobbies to document the collegiate and domestic racing seasons of the Purdue Cycling Club with his camera. After completing his graduate studies, Vishrut expects to return to Air Products and Chemicals, Inc. to work full-time as a Ph.D. Career Development Engineer at their headquarters in Allentown, PA.